UNIVERSITY OF SOUTHAMPTON

FACULTY OF ENGINEERING AND PHYSICAL SCIENCE

Electronics and Computer Science

Analogue Radio Over Fiber Aided Wireless MIMO Downlink System Design

by

Yichuan Li

Thesis for the degree of Doctor of Philosophy

Supervisors:

Dr. Mohammed El-Hajjar

and Prof. Lajos Hanzo

March 20, 2019

Dedicated to my parents

UNIVERSITY OF SOUTHAMPTON

ABSTRACT

FACULTY OF ENGINEERING AND PHYSICAL SCIENCE

Electronics and Computer Science

Doctor of Philosophy

ANALOGUE RADIO OVER FIBER AIDED WIRELESS MIMO DOWNLINK SYSTEM DESIGN

by Yichuan Li

In this thesis, we design cost-efficient high-performance communication systems employing analogue radio over fiber (A-RoF) techniques combined with wireless multiple-input-multiple-output (MIMO) techniques. Our objective is to exploit the A-RoF design for reducing complexity of MIMO signal processing, without degrading the MIMO gains attained.

Explicitly, we propose four novel systems involving both A-RoF and wireless MIMO schemes. Firstly, we conceive a novel A-RoF aided beamforming technique beneficially exploiting the fiber's potentially harmful non-linearity, in order to circumvent the excessive insertion loss of electronic phase-shifters. In this system, the phased array antenna elements are fed by the output of the highly non-linear fiber (HNLF), resulting in a beneficial angular beamsteering range depending on the length of the HNLF used, which can be exploited by sophisticated cloud/centralised radio access networks (C-RANs) for reducing the co-channel interference. Secondly, we propose an A-RoF aided spatial modulation (SM) scheme, where the SM's antenna indices are conveyed by the optical side-bands. Furthermore, we experimentally demonstrate the feasibility of our proposed concept by a prototype system using two-antenna based SM, realising an A-RoF aided SM system supporting a downlink rate of 2 Gbps. Then, we further developed the A-RoF aided wireless MIMO design to conceive an adaptive C-RAN system, where both the modulation format and the number of connected remote radio heads are selected depending on the channel conditions.

Additionally, inspired by our previous designs of amalgamating beamforming and SM using A-RoF, we extend our vision to multi-functional MIMO (MF-MIMO) systems. We subsequently conceive a novel A-RoF system design relying on the sophisticated multi-set space-time shift keying (MS-STSK) concept, which is capable of combining diversity and SM. This flexible MF-MIMO design carries out its signal processing tasks in a central unit and it is capable of achieving a rate of 10 Gbps using 16QAM.

The above-mentioned three systems rely on using single-mode silicon fiber for outdoor cellular systems, while in our fourth study, we propose an architecture for indoor scenarios in order to meet the increasing demands for in-home services. Thus, we design an all-optical processing aided wireless MF-MIMO architecture employing plastic optical fiber (POF), where both diversity and beamforming gains can be attained. Explicitly, we aim for realising a MF-MIMO system by using radio over POF techniques for RF operating in the 2.4 GHz band. Specifically, Alamouti's twin-antenna space-time block coded symbols are transmitted using a single Mach-Zehnder modulator (MZM). The attainable angular beamsteering range is 150°. We also show that this concept can be extended to a multi-user system using mode division multiplexing (MDM).

Our research described in this thesis demonstrates the feasibility and the benefits of using A-RoF aided MIMO signal processing, in terms of both its cost-reduction and performance-improvements.

Contents

List of Symbols

General notation

- The superscript * represents complex conjugate.
- The superscript ^{T} represents matrix transpose operation.
- The superscript ^{H} represents complex conjugate transpose operation.
- The operator $\circ$ represents the Hadamard product.
- The operator $J_n(.)$ represent the Bessel functions of the first kind and order n.

Special Symbols

Chapter 2

τ	Time delay
d	Distance between the adjacent antenna elements
c	Speed of light
θ	Beamsteering angle around the axis of antenna array orientation
ϕ	Phase shift
f	Signal frequency
$AF(\phi)$	Array factor
M	Number of antenna elements
k	Wave number

λ_{RF}	Radio signal wavelength in vacuum
λ	Bragg wavelength
n_{eff}	Model index
Λ	Grating period
A	Amplitude of the input optical signal
α	Fiber loss
z	Fiber length
β_2	The second order dispersion parameter in the fiber
γ	Fiber non-linearity parameter
$\hat{D}$	Differential operator that denotes the fiber loss and dispersion
$\hat{N}$	Non-linearity operator
ω	Angular frequency
h	Each step size of symmetric split-step Fourier method
x	The input signal
N_t	The number of transmitter antennas in each RRH
N_r	The number of receive antennas per user
$\mathbf{y}$	The received signal vector by the user in the C-RAN system
β	A-RoF-system-induced distortion
$\mathbf{w}$	The combining vector of size $N_r \times 1$
$\mathbf{H}$	Semi-correlated channel with L paths
$\mathbf{f}$	The beam steering vector of size $N_t \times 1$
$\mathbf{n}$	The complex Gaussian noise
ϕ_r, ϕ_t	The angle of arrival and departure
$\mathbf{a}_t$, $\mathbf{a}_r$	The response vectors for uniform linear arrays

Chapter 3

$\hat{x}_1$	Spatial modulation antenna selection bits
$\hat{x}_2$	Spatial modulation modulated bits
x_2	Spatial modulated symbols
s_1	Spatial modulation symbols for transmitter antenna 1 of Fig. 3.3
s_1	Spatial modulation symbols for transmitter antenna 2 of Fig. 3.3
λ_i	LD's optical carriers

$\mathbf{B}$	Input bit sequence of Fig. 3.11
$\hat{\mathbf{B}}$	Detected bit sequence at receiver
b_1	Classic modulated bit sequence
b_2	Implicit data
b_{21}	Implicit data for phase-difference selection
b_{22}	Implicit data for drive frequency selection
S	Classic modulated symbol
S_1	STBC symbol to the corresponding transmitter antennas of Fig. 3.11
$\mathbf{H}$	MIMO channel matrix
$\mathbf{Y}$	Received symbol matrix
$\mathbf{X}$	Transmitted SM-STBC matrix
$\mathbf{N}$	Additive white Gaussian noise matrix
f_{drive_i}	MZM's drive frequency

Chapter 4

$\hat{x}_1$	Implicit bits
$\hat{x}_2$	Classic modulated bits
x_1	Implicit symbols
x_2	Classic modulated symbols
f_{RF}	RF frequency for radio carrier modulation
f_{drive}	Drive frequency of MZM
λ_n	Optical wavelengths
V_π	MZM switching voltage
V_{dr}	MZM drive voltage
ω_{LO}	Angular center frequency of MZM drive signal
ω_{RF}	Angular center frequency of f_{RF}
E_{in}	Input optical signal of MZM
E_{MZM}	Output optical signal of MZM
P_{laser}	LD's output power
ω_{oc}	Optical carrier's angular frequency
N_t	Number of transmitter antennas
N_r	Number of receiver antennas

M	STSK space dimension
Q	Number of dispersion matrix
T	STSK time slots
$\mathcal{L}$	PSK/QAM constellation size
B_1	Antenna selection bits of MS-STSK
B_2	Dispersion matrices selection bits of MS-STSK
B_3	Classic modulated bits of MS-STSK

Chapter 5

x_1	Alamouti's STBC symbol fed into TAA1
x_2	Alamouti's STBC symbol fed into TAA2
E_{dm}	Output field of the direct-modulated LD
P_{laser}	LD power
f_{oc}	Optical carrier frequency
E_{MZM}	Output field of MZM
V_π	Switching voltage of MZM
V_{dr}	MZM's drive voltage

List of Publications

1. **Y. Li**, M. El-Hajjar and L. Hanzo, "Future Analogue Radio Over Fiber Based C-RAN System Design for MIMO Downlink", IEEE Vehicular Technology Magazine (In preparation).

2. **Y. Li**, K. Satyanarayana, M. El-Hajjar and L. Hanzo, "Analogue Radio Over Fiber Aided MIMO Design for the Learning Assisted Adaptive C-RAN", in IEEE Access, vol. 7, pp. 21359-21371, Feb. 2019.

3. **Y. Li**, S. Ghafoor, K. Satyanarayana, M. El-Hajjar and L. Hanzo, "Analogue Wireless Beamforming Exploiting Fiber-Nonlinearity of Radio Over Fiber Based C-RAN", IEEE Transactions on Vehicular Technology, vol. 68, no. 3, pp. 2802-2813, March 2019.

4. **Y. Li**, Q. Yang, I. Hemadeh, M. El-Hajjar, C. Chan, and L. Hanzo, "Experimental Characterization of the Radio Over Fiber aided Twin-antenna Spatial Modulation Downlink", in Optics Express, vol. 26, no. 10, pp. 12432-12440, May 2018.

5. **Y. Li**, M. El-Hajjar and L. Hanzo, "Joint Space-Time Block-Coding and Beamforming for the Multiuser Radio Over Plastic Fiber Downlink", in IEEE Transactions on Vehicular Technology, vol. 67, no. 3, pp. 2781-2786, March 2018.

6. **Y. Li**, I. A. Hemadeh, M. El-Hajjar and L. Hanzo, "Radio Over Fiber Downlink Design for Spatial Modulation and Multi-Set Space-Time Shift-Keying", in IEEE Access, vol. 6, pp. 21812-21827, March 2018.

Declaration of Authorship

I, **Yichuan Li** , declare that the thesis entitled **Analogue Radio Over Fiber Aided Wireless MIMO Downlink System Design** and the work presented in the thesis are both my own, and have been generated by me as the result of my own original research. I confirm that:

- this work was done wholly or mainly while in candidature for a research degree at this University;
- where any part of this thesis has previously been submitted for a degree or any other qualification at this University or any other institution, this has been clearly stated;
- where I have consulted the published work of others, this is always clearly attributed;
- where I have quoted from the work of others, the source is always given. With the exception of such quotations, this thesis is entirely my own work;
- I have acknowledged all main sources of help;
- where the thesis is based on work done by myself jointly with others, I have made clear exactly what was done by others and what I have contributed myself;
- parts of this work have been published as shown in the list of publications:

Signed:.....

Date:.....

Acknowledgements

I would like to express my gratitude to my supervisors Dr Mohammed El-Hajjar and Prof. Lajos Hanzo, who guide me to the glorious hall of science and schooling me with their patience and enthusiasm. Their insights and advices have always encouraged and enlightened my PhD life and will definitely be my life-long treasury. I will constantly remember the day and night we prepared our ideas, discussed our future research plans and drafted our papers, which bring abundant fruition with us. Again, thanks for their open-minded suggestions and selfless contributions especially during my struggling days.

I also give my sincere appreciations to my fellow PhD friends, also co-authors, Katla Satyanarayana, Dr Salman Ghafoor, Dr Ibrahim Hemadeh and Qianmei Yang, who dedicated their superior intellects and precious time to our research collaborations, without them, my PhD would be much less valuable. Besides, I thank Prof. Calvin Chun-Kit Chan from CUHK, Prof. Fasong Wang from Zhengzhou University and my MSc tutor Prof. Lie-liang Yang for their genuine help and support. Special thanks to my room mates during my stay in Soton, to my colleagues in NGW group for their company, and to the university staff who help me handle my daily issues. Moreover, I wish to thank my close friend, the Dr.-to-be Teerasak Lee and my girlfriend, Miss Yingyang Chen, who communicate and interact with me frequently and patiently, letting me feel at home always.

Lastly and most importantly, I would like to express my strongest gratitudes to my father, Aihua Li, who dedicated his life and love to my success in my life, supporting me endlessly and selflessly, leading me to a bright future, and my mother, Lihua Duan, who contributes her encouragement and faith to me, nurturing and supporting me. I am forever grateful they bring me into this world and let me follow my dream.

Chapter 1

Introduction

1.1 Motivation

Our life-style has been radically changed by the information revolution. As exemplified by the innovative iPhones and the Android-based smart phones, to the rabidly evolving artificial intelligence, hardware innovations are capable of supporting more reliable communication system designs. In communication system design, we have to carefully consider the performance-cost trade-off, where the performance is typically quantified in terms of the bit error ratio (BER), signal-to-noise ratio (SNR) and the achievable throughput. By contrast, the total cost of ownership (TCO) takes into account both the Capital Expenditure (CAPEX) and the Operating Expenditure (OPEX)[1]. Generally, the frequency, space, time, code and polarisation domains etc. can be exploited as the fundamentals for supporting a multiplicity of users and for reducing BER as well as the interferences and increasing the SNR, thus enhancing the channel capacity [2]. Meanwhile, in order to support more users, the mobile network is perpetually upgraded for the provision of low-cost reliable communication links [1]. Although, numerous techniques can be used for substantially boosting the network performance attained [3–5]. Striking an appropriate performance vs cost trade-off is always of importance.

[1]CAPEX comprises the expenditure for network construction, whist OPEX sums the cost for operating the communication network [1].

Wireless communication is facing an ever-increasing thirst for high-quality data transmission. But this also imposes high demands on the core networks, hence optical fiber has been widely used in access networks, such as both for the backhaul and fronthaul as well as even for indoor communication systems [6].

Thus, the capacity demands of emerging technologies test the limits of current access communication systems. Some of their critical issues are summarised as follows:

1. **Outdoor cellular system**

   (a) **Issue 1:** The need for deploying a large number of base stations is quite pressing for the sake of serving more users, especially in densely populated areas. This trend results in substantial energy- and cost-consumptions [7].

   (b) **Issue 2:** Given the shortage of frequency allocated for civil usage, the achievable spectral efficiency is deemed a crucial design metric [8].

   (c) **Issue 3:** Both the inter-channel and co-channel interferences are aggrevated as a result of supporting more users involved [9].

2. **Indoor communications**

   (a) **Issue 4:** The Internet of Thing (IoT) supporting smart homes requires a large bandwidth for serving the ever-increasing number of connected devices, which the traditional copper based network struggles to handle [10].

   (b) **Issue 5:** Both the copper based and the glass optical fiber (GOF) based indoor communications rely on trained engineers for installation and on expensive test equipment for network monitoring [11, 10].

Then, considering the performance vs cost, the above-mentioned issues can be addressed by the following solutions:

1. **Outdoor cellular system**

   (a) **Issue 1** is concerned with the expenditure of deploying more base station towers designed for supporting more users. Centralised networks based on radio over fiber (RoF)[2] aided distributed antennas are capable of splitting

[2]Unless we specify the fiber type, the fiber here is referred to as single-mode fiber.

the functions of the traditional base station between the central unit (CU) and the remote radio head (RRH), hence significantly reducing the TCO by beneficially lowering the OPEX, when it counts to networks upgrade, management as well as site rental. A 10% CAPEX and a 50% OPEX saving may be attainable compared to traditional base stations [1, 12].

(b) **Issue 2** and **Issue 3** are related to the spectral efficiency and to the deleterious effects of interferences, which are related to the achievable throughput and system reliability. Multiple-antenna based multiple-input-multiple-output (MIMO) techniques are capable of supporting beamforming and of providing both the diversity and multiplexing gains[3] by exploiting the degrees of freedom, in the space, time and frequency domains for improving the spectral efficiency without invoking extra bandwidth and for mitigating the interferences with the aid of novel transceiver designs.

2. **Indoor communications**

(a) The above-mentioned MIMO-assisted spectral efficiency improvements are also advocable in indoor communications provided that carefully designed solutions are conceived. Furthermore, **Issue 4** emphasises the bandwidth limitation of the traditional copper based indoor communications, which are expected to be gradually superseeded by RoF techniques, due to fiber's low loss and rich bandwidth [13].

(b) Multi-mode GOF and large-core plastic optical fiber (POF) potentially address **Issue 5**, with the aid of easing the installation procedure by introducing the "do-it-by-yourself" connections [10]. As a further benefit, POF solutions rely on inexpensive test equipment for further reducing the overall cost.

In a nutshell, as it transpires from Fig. 1.1, MIMOs and RoF techniques contribute to performance-improvement and cost-reduction respectively, while POF solutions are capable of further reducing the system installation cost in indoor communications. Considering the performance vs cost trade-off of the access network, we integrate the sophisticated MIMO schemes with RoF aided centralised systems, where we aim for a

[3]In this thesis, we refer to the beamforming, diversity and multiplexing which employ multiple antennas as MIMO schemes.

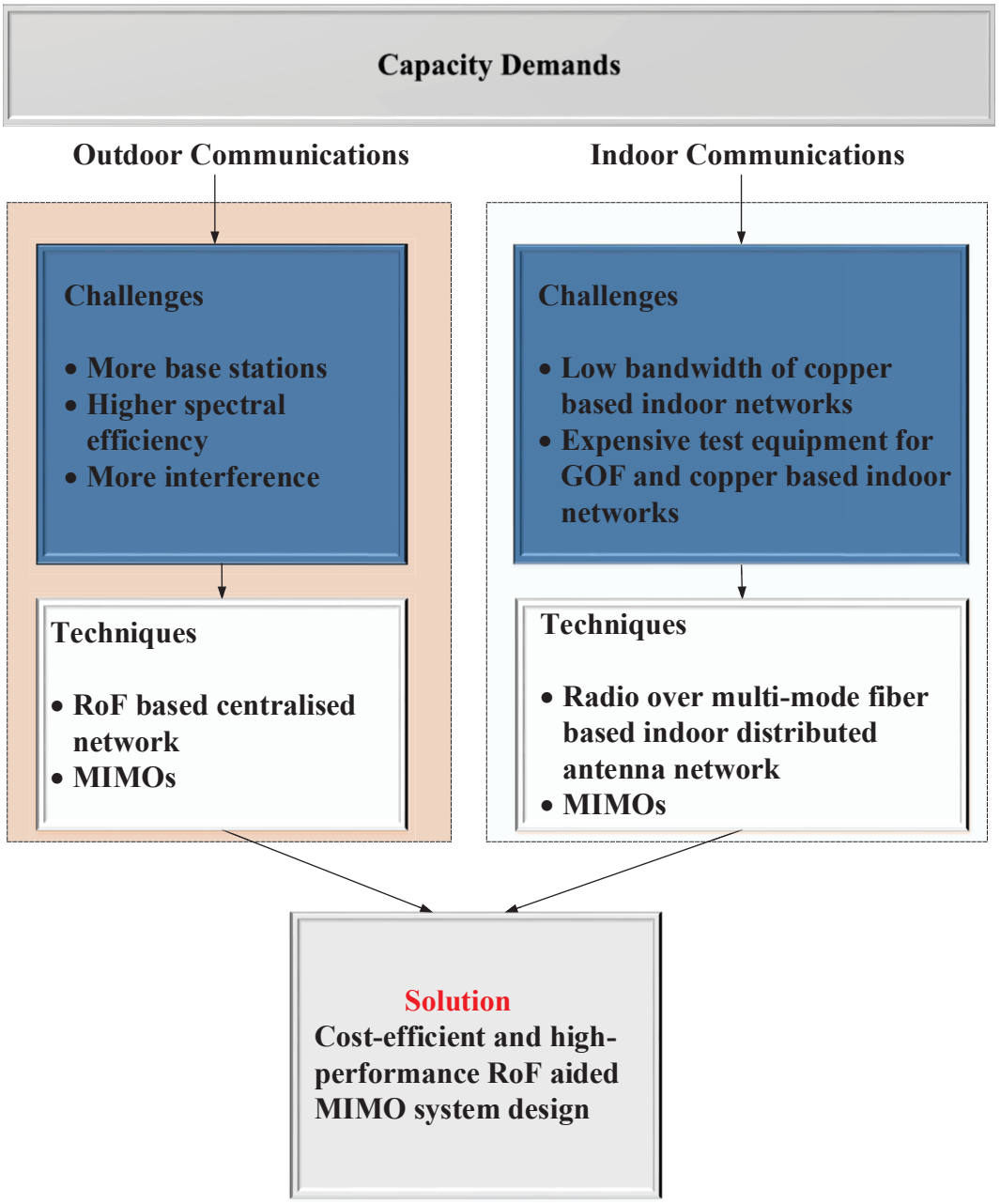

Figure 1.1: Motivation of the research conducted.

high-performance yet low-cost communication system design, capable of striking a compelling performance vs cost trade-off. Explicitly, in this thesis, we propose a RoF aided MIMO concept, where the performance is improved using MIMO schemes and the TCO is reduced by beneficially exploiting the RoF's capability of centralising most of the signal processing.

Thus, in Chapters 2, 3 and 4, we invoke single-mode GOF for our RoF based radio

access network. More specifically, beamforming and spatial modulation (SM) are implemented optically in the low-cost RoF aided centralised/cloud radio access network (C-RAN) advocated, followed by a low-cost multi-functional MIMO-assisted and RoF aided C-RAN system design. Furthermore, by exploiting the low-cost deployment of POF in short-distance applications such as indoor communications, Chapter 5 intrinsically amalgamates the state-of-the-art multi-functional MIMO (MF-MIMO) concepts with POF aided indoor communications for realising a RoF-MIMO aided high-performance yet low-cost local area network (LAN) for multi-user communications.

Prior to detailing the new contributions of the thesis, we briefly introduce the system component of RoF aided MIMOs, the prevalent C-RAN system and the multi-mode fiber based indoor communication scenarios, followed by highlighting their rationale and challenges.

1.2 Background

1.2.1 Radio Over Fiber System

RoF systems convey RF signals in the optical frequency band over fiber. They can be used in many scenarios, such as cable television (CATV) [13] by exploiting the wide bandwidth of the optical fiber [13]. Similarly, the ground station of satellite communication systems may invoke RoF transmissions for centralising the signal processing in a central station whilst flexibly positioning the antenna at the best location [14, 15]. On a similar note, outdoor cellular networks and indoor distributed antenna networks can potentially benefit in the same way from having distributed antennas and central processing, hence, substantially boosting the OPEX savings [16]. In this section, the two classic RoF systems, namely the digitised RoF (D-RoF) and analogue RoF (A-RoF) concepts are introduced and compared. Finally, we will opt for A-RoF for our MIMO designs since it reduces both the remote site's hardware implementation cost as well as the total power-consumption.

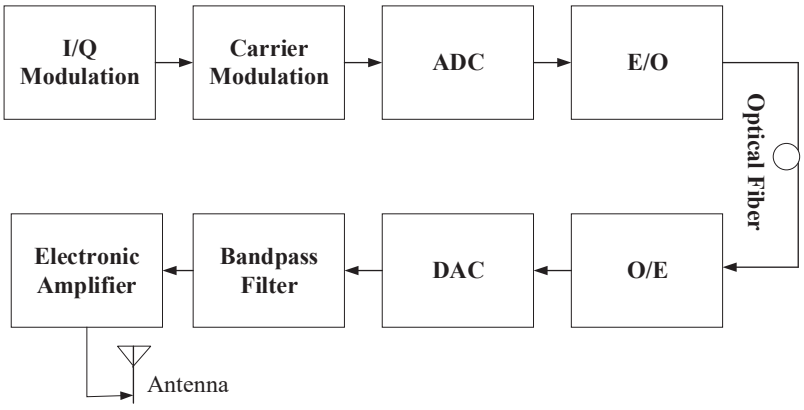

Figure 1.2: A general D-RoF system.

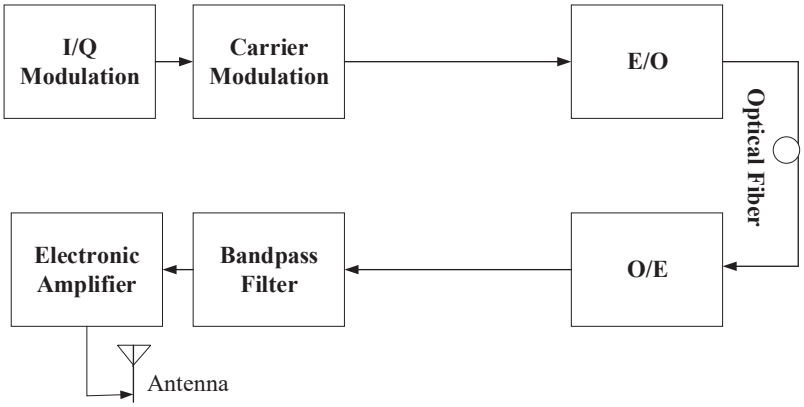

Figure 1.3: A general A-RoF system.

1.2.1.1 Digitised RoF Solutions

The D-RoF concept is capable of substantially improving the system performance whilst simultaneously reducing the OPEX and CAPEX cost [17]. As shown in Fig. 1.2, the in-phase/quadrature (I/Q)-modulated symbols are up-converted by the RF carrier [18], followed by the digitisation of the modulated RF signals before electro-to-optic (E/O) conversion. The discrete-time, discrete-amplitude RF signal is then conveyed by optical modulation. Then, the optical signal carrying the digitised RF signals is then conveyed by the optical fiber to the remote antenna site. The optic-to-electro (O/E) conversion subsequently maps the modulated optical signal to the digitised RF signal, prior to digital-to-analogue conversion (DAC). The recovered RF signal will then be transmitted

over the ether by carrying out some basic radio functions such as filtering and amplification without sophisticated digital signal processing. It has even shown that D-RoF transmission improves the link's dynamic range, defined as the ratio of the strongest to the weakest RF signals transmitted over the fiber without distortion [16]. Furthermore, the signal processing centralisation substantially reduces the OPEX [16]. Moreover, the digital optical link is capable of improving the system performance as a benefit of combating the fiber impairments.

However, since D-RoF relys on the digitisation of high-frequency RF, it requires a high sampling frequency and a high resolution analogue-to-digital conversion (ADC) [16, 17]. This problem is potentially alleviated by bandpass sampling. As a design-alternative, A-RoF dispenses with digitisation altogether as well as with power-thirsty ADC and DAC, hence it is capable of supporting broadband services by invoking lower-bandwidth optical transmitters [12, 18]. Next, we briefly describe the rationale of A-RoF solutions.

1.2.1.2 Analogue RoF Solutions

Fig. 1.3 shows the schematic of a general A-RoF downlink system, where the ADC and DAC used for digitising/recovering the RF of D-RoF in Fig. 1.2 are removed. Explicitly, as seen in Fig. 1.3, the modulated RF signal is E/O-converted by using an optical transmitter before being transported over a fiber link to the remote antenna site. Then, the optically carried RF signal is photo-detected (i.e. O/E conversion), filtered by a bandpass filter (BPF) and amplified by an electronic amplifier (EA), before being directly transmitted over the air. The only substantial difference between A-RoF and D-RoF is the eliminated digitisation process. Hence, A-RoF requires a lower-bandwidth optical transmitter, resulting in a reduced fiber load and reduced power-consumption at the remote antenna site [16]. However, A-RoF exhibits poor dynamic range and it is susceptible to the fiber's non-linearity and fiber dispersion, hence limiting the attainable fiber length to a few kilometers [16]. Therefore, A-RoF techniques have been primarily used in millimeterWave (mmWave) systems [12, 19], in C-RAN systems [7] and in indoor LANs [15, 20] for short-distance transmission. Furthermore, as mentioned in Section

1.1, A-RoF and MIMOs may be beneficially amalgamated into a cost-efficient high-performance centralised systems. Hence, we will briefly highlight the associated MIMO schemes in the next section.

1.2.2 MIMO Techniques

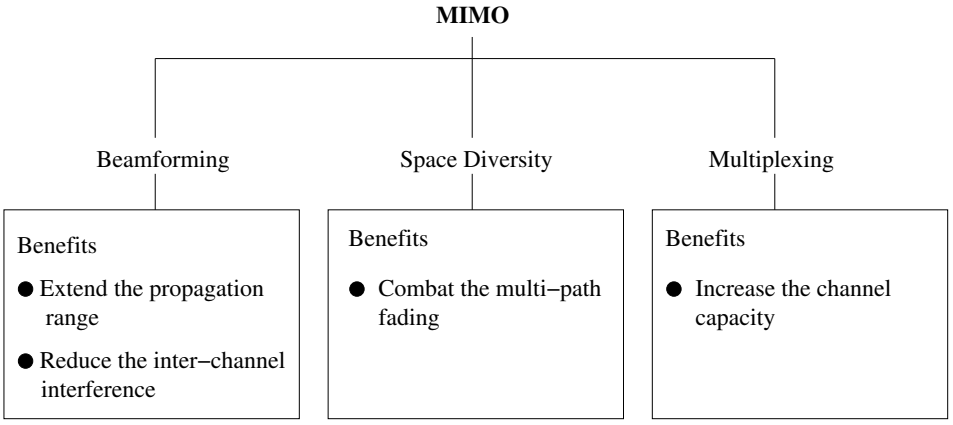

Figure 1.4: MIMO schemes and their benefits.

By exploiting the extra degree of freedom provided by the spatial dimension, multiple-antenna techniques substantially improve the system performance [21]. In MIMO systems, multiple transmit and receive antennas act in unison in order to achieve beamforming-based SNR gains, multiplexing-assisted capacity gains and diversity gains [2]. As shown in Fig. 1.4, we list the three popular MIMO families and their corresponding benefits in terms of improving the system's performance. As seen in Fig. 1.4, beamforming is capable of extending the propagation range as well as reducing the inter-user interference by forming an analogue receive beam. By contrast, space diversity is designed for combating fading channel. Finally, multiplexing improves the channel capacity. For further information on MIMO techniques please refer to [22].

1.2.2.1 Multi-functional MIMO Systems

Again, as shown in Fig. 1.4 and in Fig. 1.5, beamforming is capable of extending the propagation range and reducing the inter-channel interference whilst space diversity mitigates the fading effects and multiplexing is capable of increasing the channel capacity.

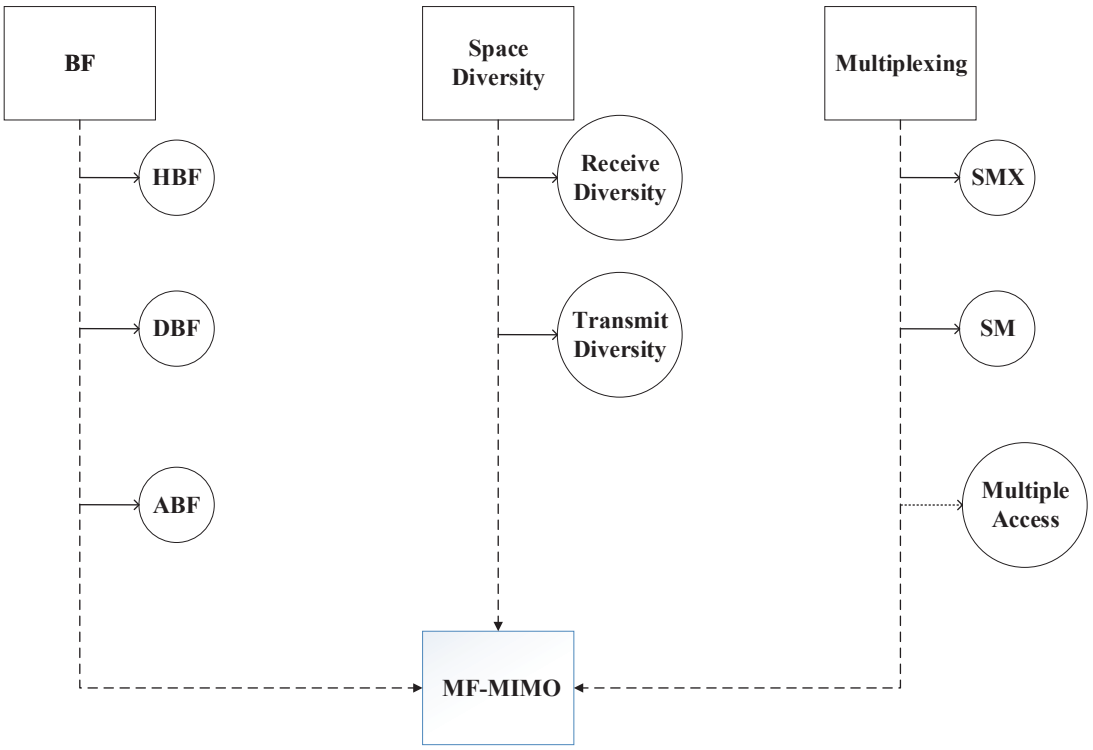

Figure 1.5: MF-MIMO concept. HBF: Hybrid Beamforming, DBF: Digital Beamforming, ABF: Analogue Beamforming, SMX: Spatial Multiplexing, SM: Spatial Modulation, MF-MIMO: Multi-functional MIMO. (Note that we refer to beamforming as analogue beamforming, unless stated otherwise.)

However, both the reliability and the throughput are crucial considerations, which motivates combining two or more MIMO schemes within a single communication system. This leads to the concept of MF-MIMO schemes, aiming for achieving a combination of beamforming, diversity and multiplexing gains. We will provide a brief review of MF-MIMO concepts in Chapter 4.

1.2.3 Centralised Network Based On A-RoF

1.2.3.1 Cloud/Centralised Radio Access Networks

In the second-generation global system of mobile communications as GSM, each base station accommodates both the baseband unit and the radio unit, with the antennas located only few meters-away. This concept evolved further in the W-CDMA system based 3G, where the functions of baseband signal processing carried out in the baseband

unit/central unit (BBU/CU) and the tasks of the radio function carried out in the remote radio head (RRH) were separated[4] [9, 23]. Then, in the fast-paced 4G and 5G era, the RAN architecture mentioned above was redesigned by conceiving a centralised RAN, where all the BBUs serving the individual RRH became housed in the same place, therefore improving the energy efficiency resulted by relying on further simplified RRHs as well as on the advanced coordinated multi-point (CoMP) and load balancing techniques of [1].

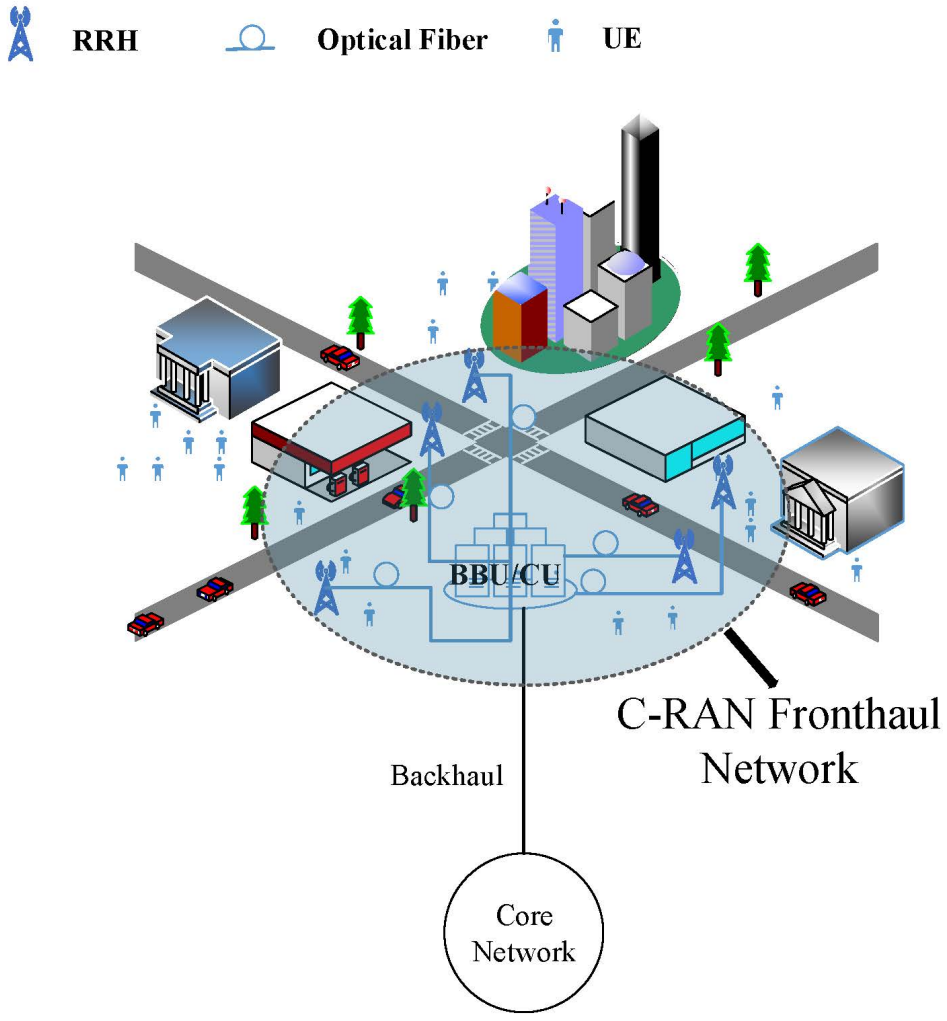

Figure 1.6: RoF aided C-RAN system.

[4]1. In general, as shown in Fig. 1.7, the baseband unit performs in-phase and quadrature (I/Q) modulation, pulse shaping, digital modulation etc., while the RRH is only responsible for the low-complexity radio function of filtering, amplification and transmission. 2. The terminologies of BBU and CU in this thesis are interchangeable.

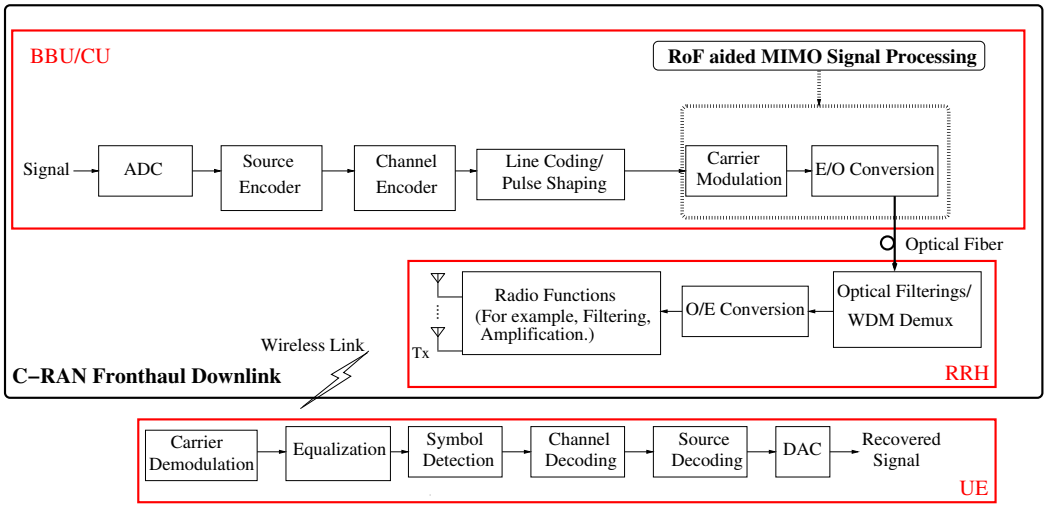

Figure 1.7: A-RoF aided MIMO signal processing in the C-RAN downlink.

The A-RoF aided C-RAN downlink is depicted in Fig. 1.6, where the backhaul connects the core networks and the BBU/CU, while the C-RAN fronthaul links the BBU/CU to the RRHs using optical fibers. Thus, a single BBU/CU is capable of supporting several RRHs with the aid of a cost-efficient, high-flexibility centralised RoF downlink design. To be more specific, a detailed functional map of the A-RoF aided MIMO signal processing conceived for the C-RAN downlink is provided in Fig. 1.7, where we show the digital processings blocks of ADC, source coding, channel coding, line coding/pulse shaping and some RF processings, such as for example, carrier modulations followed by E/O conversion, which are centralised in the BBU/CU. Furthermore, as shown in Fig. 1.7, the RRH is substantially simplified to the low-complexity functions of optical filtering, O/E conversion as well as some RF functions, such as filtering and amplifications. The wireless link is considered to be that of a cellular system.

Thus, the C-RAN is capable of reducing both the OPEX and the CAPEX as discussed in [1] and of supporting CoMP for enhancing the system performance attained. Given the capability of centralising the signal processing, A-RoF conveniently supports the C-RAN fronthaul design, which we will rely on MIMO designs in the following chapters.

1.2.3.2 Multi-mode Fiber Based Indoor Communications

The above-mentioned C-RAN system is capable of providing a seamless connection for outdoor users. However, due to the fact that indoor activities dominate our daily use of

the Internet and owing to the proliferation of smart-home devices, these diverse services require reliable yet low-cost indoor communication [24]. On the other hand, conventional indoor transmission media, such as coaxial cable, twisted copper pairs, power line communications etc., suffers from a limited bandwidth, high attenuation as well as strong electro-magnetic interferences, which optical fibers are fairly immune to. Furthermore, as a benefit of its lower-cost installation than that of single-mode fiber, multi-mode fiber continues to be installed in indoor scenarios, with standardised 62.5/125 μm (OM1) and conventional 50/125 μm multi-mode fiber (OM2) aiming for a rate of 1 Gbps, while laser-optimised 50/125 μm multi-mode fiber OM3 and OM4 achieving 10 Gbps for short-distance transmissions within 300 meters [25, 26].

Thus, as mentioned above, A-RoF is capable of centralising the signal processing for the sake of arriving a low-cost system design. It can also be combined with multi-mode fiber, where radio over multi-mode fiber (RoMMF) techniques are typically invoked for indoor communication system design, faciliatating replacement of separate access points in each room by a central RG as well as enabling the centrally controlled system to benefit from coordinated communications [26]. To elaborate a little further, in Fig. 1.8, we portray a general multi-mode fiber (MMF) aided indoor system relying on A-RoF, where a residential gateway (RG) is connnected to the Internet and centralises most of the signal processing. Then the downlink signal is carried by an optical signal over a MMF link to each room to provide multimedia services. This architecture significantly simplifies the radio port to low-complexity radio function, such as O/E conversion, filtering and amplifications. Again, by beneficially accommodating A-RoF transmissions in a MMF based indoor system, the resultant structure can also be seen in Fig. 1.7, where the BBU/CU and RRH functions are represented by the RG and by the radio ports, respectively. Furthermore, the deployment of POF indoor is capable of drastically reducing the installation cost as mentioned in [24]. Hence, we will extend our A-ROF aided MIMO design also to a POF based indoor system. The detailed design for our POF based indoor system will be covered in Chapter 5. Let us now detail the main contributions of the thesis.

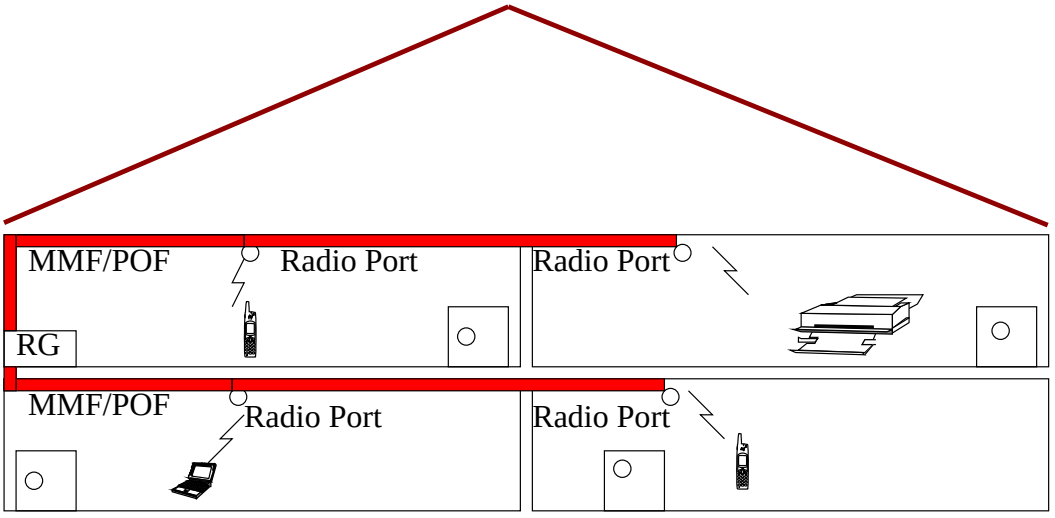

Figure 1.8: A-RoF aided indoor system.

1.3 Main Contributions and Chapter Arrangements

1.3.1 Novel Contributions

Contributions 1 [Publication 3 [27] on Page VIII; Chapter 2]: A novel phase shifting network beneficially exploiting potentially detrimental fiber non-linearity is proposed for analogue wireless beamforming, which is investigated in the context of a C-RAN system. Explicitly, the power-dependent optical phase information is translated into a particular beamsteering pattern using our A-RoF design. It is shown that the beamforming angles may be conveniently configured to cover a range of about 90°. Our system can be centrally controlled using our novel highly non-linear fiber (HNLF) aided tunable beamforming scheme, which can also be utilised for the C-RAN fronthaul. Furthermore, a 10 Gbps quadrature-phase-shift-keying (QPSK) signal transmitted in the downlink of a C-RAN system implementing our HNLF aided beamforming scheme is characterised, where the BER performance shows only a modest degradation compared to that additionally using conventional electronic phase-shifters, which impose an undermined insertion loss.

Contribution 2 [Publications 4 [28] on Page VIII; Chapter 3] : We design an all-optical processing based A-RoF-aided SM scheme. An experimental demonstration of our novel A-RoF-aided twin-antenna SM system is detailed, simplifying the transceiver design and reducing the power consumption of the conventional SM switches. The SM

concept is implemented in the optical domain and our centralised A-RoF-aided SM using Mach-Zehnder modulator's (MZM's) side-band selection was analysed and verified by experiments. This design can be beneficially invoked in C-RAN as well as in small-cell fronthaul solutions. The experimental results show that our 2 Gbps system exhibits only marginally degraded BER performance compared to those operating without RoF, while benefiting from centralised SM encoding and dispensing with radio access point (RAP) switches.

Contribution 3 [Publication 2 [29] on Page VIII; Chapter 3]: We propose an A-RoF aided SM-space-time block coding (SM-STBC) scheme using a MZM and optical side-band selection, which is invoked in an adaptive C-RAN system, where appropriately selected number of transmitter antennas can be used. As a benefit of this solution, the power thirsty ADC and DAC are eliminated, hence resulting in an energy-efficient and cost-efficient mobile access network. The BER performance of the entire system operating with the aide of A-RoF is only marginally affected compared to the conventional wireless SM-STBC scheme. Moreover, we invoke the K-nearest neighbourhood (KNN) algorithm for the sake of adapting both the number of selected RRHs and the modulation format, for achieving the highest possible data rate.

Contribution 4 [Publication 6 [7] on Page VIII; Chapter 4]: We conceive a powerful A-RoF aided SM/multi-set-space-time shift keying (SM/MS-STSK) downlink solution, where the associated SM and MS-STSK schemes are implemented in a centralised processing fashion. This design is capable of substantially reducing the complexity of the RRH, when intrinsically amalgamated with SM or MS-STSK. Our SM/MS-STSK design is capable of achieving optical upconversion to mmWave carriers, whilst relying on optical fiber aided phase-shifting in support of sophisticated beamforming. Additionally, we achieve a bit rate of 10 Gbps for 16QAM and 10 km dispersion-shifted fiber (DSF) in our MS-STSK fiber based A-RoF network, where the BER performance shows only marginal degradation compared to its pure wireless counterpart operating without fiber networks.

Contribution 5 [Publication 5 [19] on Page VIII; Chapter 5]: A novel all-optical processing aided multi-functional wireless MIMO system is designed by exploiting the MZM's non-linearity and chirped fiber Bragg grating (CFBG), where POF is used for

supporting a multi-user system. Furthermore, a novel tunable microwave generator is conceived for feeding the MZM's drive signal as a more cost-efficient solution than its commercial counterpart. The optical double side-band (ODSB) encoded STBC signal is realised by using a combination of two laser diodes (LDs) and two BPFs, where the associated multi-wavelength generation is based on the MZM's beneficially exploiting undesired non-linearity. Our design achieves a beamforming angular range of upto 150° with a small time delay step of 6 ps, which is suitable for indoor communications.

1.3.2 Thesis Structure

As seen in Fig. 1.9, we consider three low-cost high-performance A-RoF aided MIMO designs, namely where beamforming, SM and MF-MIMO are investigated. Furthermore, Chapters 2, 3 and 4 aim for outdoor communications over single-mode silicon fiber, where in Chapter 5 we invoke POF for indoor transmission. Explicitly, the chapter

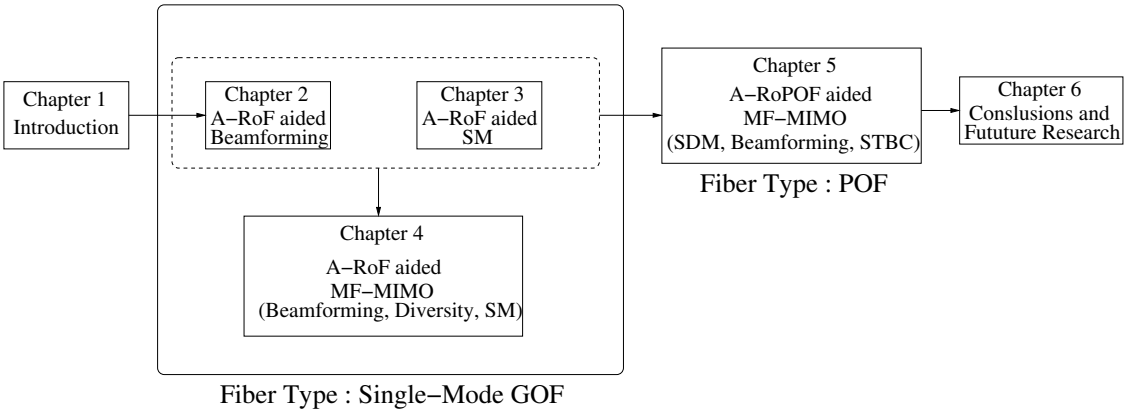

Figure 1.9: Thesis outline.

arrangement of this thesis is highlighted as follows:

Chapter 2: This chapter investigates A-RoF aided beamforming in the context of a centralised signal processing system. The motivation of designing A-RoF aided beamforming is presented in Section 2.1. Then, the basics of phased array aided beamforming and a comprehensive review of the recent RoF-based beamforming technique are introduced in Sections 2.2 and 2.3. In Section 2.4, we conceive a novel optical fiber aided beamforming technique based on turning the fiber's undesired non-linearity into a benefit. Explicitly, in our proposed technique, the PAA elements are fed by the phase-shifted

signals introduced by our HNLF aided phase-shifting solution, which results in an angular beamsteering range of around 90°. This can be exploited by sectorization in cellular networks to reduce the co-channel interference imposed. Furthermore, we exploit the proposed A-RoF-aided phase shifting technique in C-RAN, where our proposed system takes advantage of the centralised signal processing capability of the RoF system to conceive an all-optical processing based tunable beamforming system. While our flexible HNLF-aided phase-shifting process is confined to the CU of the C-RAN, the end users of C-RAN cellular networks are capable of flexibly choosing the serving RRHs and employing diverse wireless transmission techniques. Upon integrating our HNLF-aided phase-shifting design into the proposed C-RAN, we impose as little as 0.1 dB SNR degradation compared to its traditional electronic processing based conventional wireless counterpart, which requires extra phase-shifters. Finally, our conclusions are offered in Section 2.5.

Chapter 3: This chapter studies optical processing aided SM encoding in the context of an A-RoF assisted C-RAN system. The background and a brief review of wireless SM are provided in Sections 3.1 and 3.2, followed by our novelty statement in Section 3.3. Then, in Section 3.4, we present the design and the experimental demonstration of an A-RoF network relying on the state-of-the-art SM, that activates one out of multiple antennas, where the optical single side-band signal generated by a MZM is used for both the antenna selection and for the classic modulated symbol selection processes of SM. The SM encoding is optically processed in a centralised fashion, aiming for the reduction of power consumption and for enabling cost-effective maintenance and management, which can be employed in the context of a C-RAN and a small-cell fronthaul. Furthermore, a 20 km standard single-mode fiber (SSMF) is used for transmission. In this experiment, we conceive and characterise a 2 Gbps transmission link relying on two transmit and two receive antennas imposing less than 1 dB SNR degradation compared to those operating without RoF. Subsequently, inspired by the feasibility study of Section 3.4, in Section 3.5, we propose an A-RoF aided MIMO techniques for a learning assisted adaptive C-RAN system, where the SM concept is combined with STBC using optical processing. The number of connected RRHs is readily controlled by the CU. Furthermore, to improve the attainable throughput, we conceive adaptive modulation with adapting the number of streams by relying on using KNN algorithm. Our simulation results show that the

BER performance of the A-RoF aided link is just marginally degraded compared to the pure wireless system operating without A-RoF, while benefiting from the energy- and cost-efficient C-RAN design. Moreover, the learning assisted KNN-based transceiver adaptation is capable of outperforming the classic threshold-based adaptation in terms of its achievable rate. Section 3.6 concludes this chapter.

Chapter 4: This chapter proposes a new A-RoF for MF-MIMO signal generation concept, which can be exploited in C-RAN architectures. Sections 4.1 and 4.2 briefly introduce the concepts of MF-MIMO and its development, followed by our novelty statement in Section 4.3. In Sections 4.4 and 4.5, we propose an A-RoF downlink networking solution relying on SM and MS-STSK combined with beamforming and up-conversion to mmWave carrier frequencies, whilst using all-optical processing. In the proposed A-RoF system, most of the digital processing of the baseband SM and MS-STSK is carried out by the CU and the implicitly carried bits of SM/MS-STSK, such as the antenna index selection and dispersion matrix selection bits, are recovered by the RRH of our A-RoF network for creating a MIMO arrangement. The classic modulated bits are conveyed by the radio signal, without requiring any additional ADC and DAC before transmission from the antennas. Moreover, A-RoF-aided techniques are invoked for carrying out optical processing aided beamforming and optical up-conversion to a mmWave carrier frequency. Thus, we invoke A-RoF techniques for the generation of our SM/MS-STSK signal with the aid of optically up-converted mmWave beamforming without using any electronic oscillators, mixers or phase shifters. Furthermore, our A-RoF-aided system's BER performance is similar to that of the conventional all-electronic SM/MS-STSK wireless scheme. Finally, this chapter is concluded in Section 4.6.

Chapter 5: This chapter describes the design of a new POF based indoor communication system, where we invoke A-RoF and MF-MIMO for a low-cost high-performance system design. Section 5.1 introduces POF and details its advantages over GOF based communications. Then, a review of POF communication is given in Section 5.2. Furthermore, a channel model popularly used for POF transmission in briefly touched upon in Section 5.3. In Section 5.5, we propose an architecture, where the twin-antenna Alamouti space-time block coded symbols are transmitted using a single MZM over a POF. The signal is then transmitted through a set of FBGs for attaining the appropriate phase shifts required for beamforming, followed by transmission over the wireless

channel. The attainable angular beamsteering range is about 150°, where beamsteering is realised without the need for a large number of complex electronic phase shifter networks. The tuning of the beamsteering angle can be readily implemented by carefully controlling the drive voltage in the MZM, where we use MZM aided multi-wavelength generation for supporting a large number of antennas. Lastly, we conclude this chapter in Section 5.6.

Chapter 6: This chapter summarises this thesis, followed by our thoughts on potential future research.

Chapter 2

Analogue Radio Over Fiber Aided Beamforming

As discussed in Chapter 1, analogue radio over fiber (A-RoF) is capable of centralising signal processing at the central unit (CU) of the cloud/centralised radio access network (C-RAN) system, thus supporting C-RAN at a reduced cost- and energy-consumption. Meanwhile, multiple-input-multiple-output (MIMO) systems significantly improve the diveristy and/or multiplexing gain. As a beneficial MIMO arrangement, analogue beamforming (BF) relies on radio frequency (RF) phase shifting of the appropriately delayed signals of the $\lambda/2$-spaced neighbouring antennas in order to steer the beam, for reducing the co-channel interference (CCI) as well as increasing the signal-to-interference-plus-noise ratio (SINR) gain [30]. We portray the C-RAN structure from the perspective of the physical layer in Fig. 1.7 of Chapter 1, where we replace the MIMO signal processing block by our new A-RoF aided beamformer of Fig. 2.1. In this chapter, we will investigate the potential of deploying BF in an A-RoF based C-RAN for the sake of removing high-insertion-loss RF phase shifter, for designing a cost-efficient mobile access network.

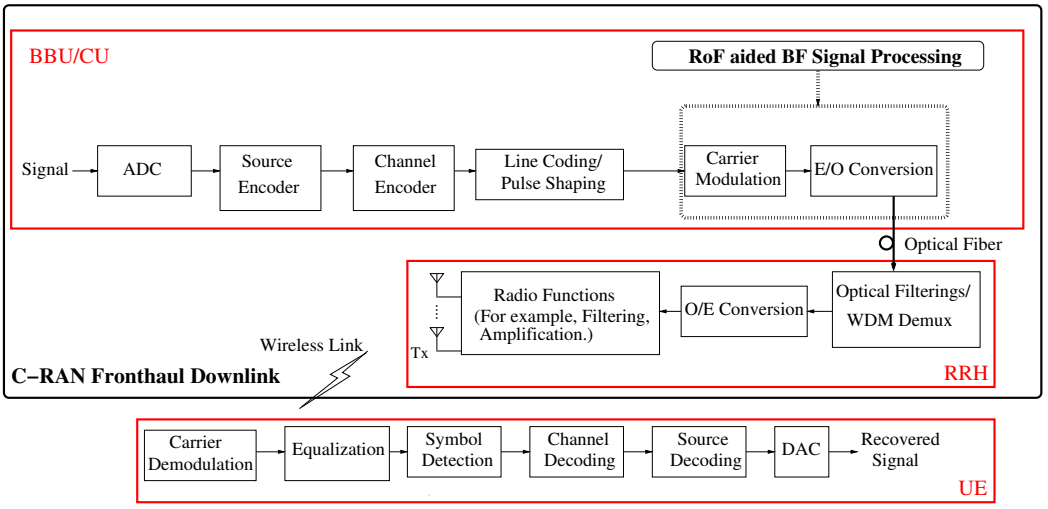

Figure 2.1: A-RoF aided beamforming for C-RAN downlink.

2.1 Motivations

Next generation networks require an ever-increasing capacity [9]. The small cells of the emerging dense networks are expected to support more users [31]. In this context, beamforming techniques relying on phased antenna arrays (PAA) [32], which steer the signal beams in a desired direction are widely used for cell-sectorization, hence they are capable of substantially reducing the CCI, and improving the overall system performance [33].

On the other hand, we invoke a C-RAN system, where a CU housing the centralised baseband signal processing [23] serves multiple low-complexity and low-cost remote radio heads (RRHs). The proposed C-RAN [1] invokes A-RoF [12] transmissions to the RRHs for supporting the emerging small-cell technologies [12, 1].

The fiber-based C-RAN fronthaul has been widely advocated for employment in future wireless networks as a benefit of the fiber's high capacity, low attenuation, immunity to electromagnetic interference, etc [34, 35]. Indeed, beamforming constitutes a promising application of the emerging large-scale MIMO system relying on numerous antennas, owing to their high power efficiency, excellent cell-edge coverage and reduced CCI in cellular network [33]. In this context, it is beneficial to investigate the feasibility of using optical fiber to assist beamforming by circumventing the employment of a large number of electronic RF phase-shifters, which have a high insertion loss. Fig. 2.2 shows

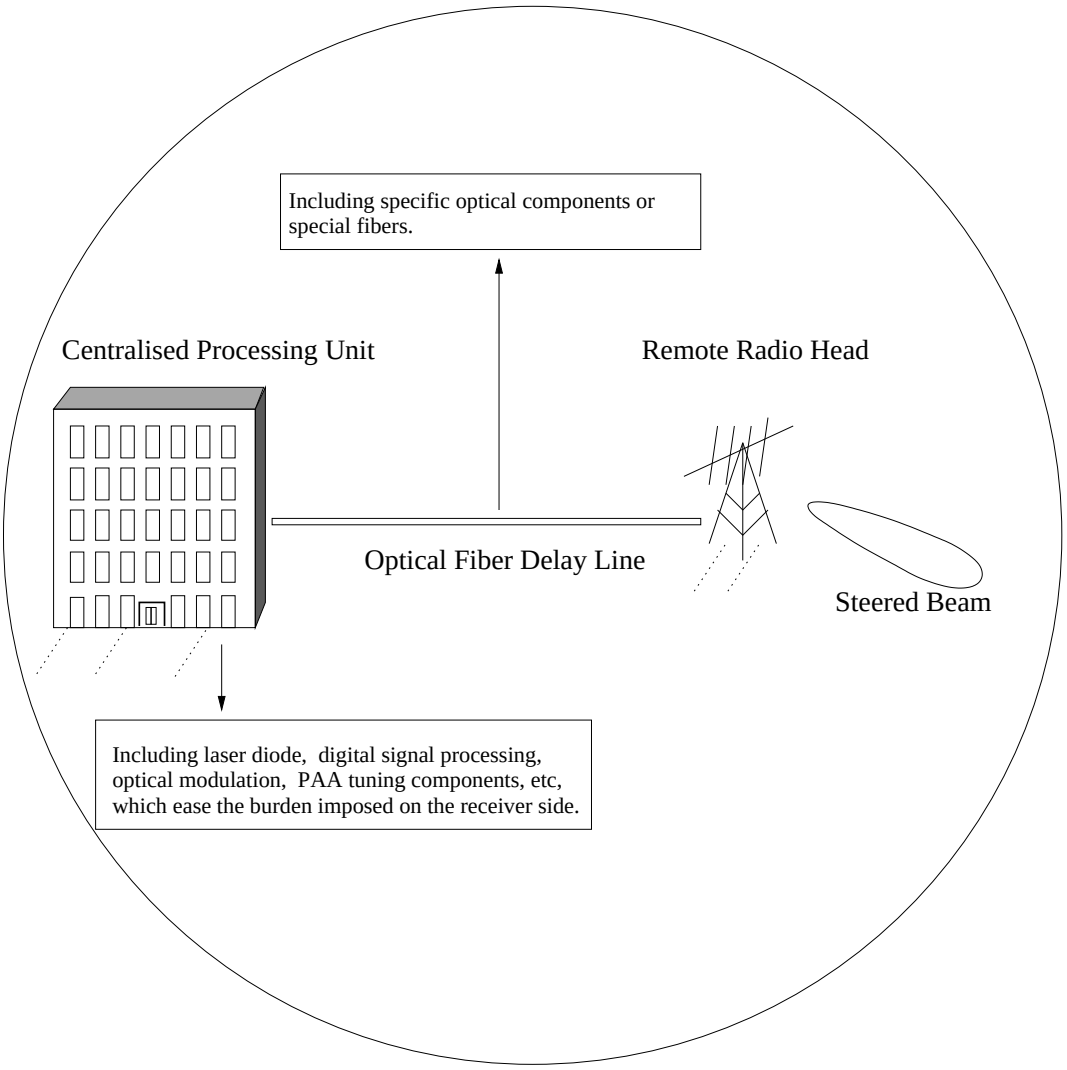

Figure 2.2: Basic concept of A-RoF aided beamforming.

an A-RoF aided beamforming system, which utilises an optical fiber based delay line for beamforming, where an appropriately phased signal is fed into the PAA, with the aid of a centralised processing unit. These A-RoF aided beamforming solutions have several benefits compared to the traditional RF solutions in the context of beamforming, which are listed as follows:

1. Using the optical fiber, fiber-based fronthaul networks can share the optical transmitter or optical receiver. In this case, an all-optical system can be constructed, which does not require additional components for down-conversion or up-conversion in the context of satisfactory beam steering.

2. By separating the function of the traditional base stations (BS) into a signal processing unit known as the CU and a transmission unit known as RRH, such as in C-RAN, the fronthaul configuration carries out the digital signal processing (DSP) tasks in a CU in order to ease the burden imposed on the RRH, which considerably simplifies the system [36]. The low-complexity fronthaul network design aims for reducing the complexity by exploiting the fiber's properties-induced phase shift for beamsteering, hence eliminating any additional processing, which would otherwise be required for carrying out the beamforming-specific phase shift. Thus, cost-efficient centralised processing can be used. The C-RAN has multiple basbeband units (BBUs) in a CU, where optical fiber is an ideal fronthaul transmission medium as a benefit of its large capacity [23, 1].

3. A lower insertion loss is imposed by a fiber-based phase-shifter compared to its electronic counterpart. Explicitly, traditional RF phase-shifters suffer both from a high insertion loss and from an increased noise figure, which is proportional to the number of RF phase-shifters [37]. Although replacing the traditional phase-shifting waveguides by carefully selected and switched lengths of electrical cables is the most common method, again, this suffers from a high loss and bulky construction, hence making the optical solution an attractive design proposition [38].

4. The fiber has well-known advantages compared to copper cables, such as its high operating bandwidth, its immunity to electronic-magnetic interference and low loss [34, 35].

In optical fiber communication systems, beamforming is typically achieved by appropriately customizing the refractive index of the fiber, for example by applying fiber Bragg grating (FBG). This technique has grown in popularity in recent years [39–50, 34]. The beamforming techniques based on the FBG utilise a number of uniform FBGs [51–53] or a single tunable linear chirped FBG [54, 42, 47]. There are two major challenges for the FBG. Using parallel transmission lines by invoking several uniform FBGs has a high complexity, especially when a narrow beamsteering angle is needed, while the chirped FBG suffers from group delay fluctuations, which correspond to phase-non-linearity and hence would degrade the beamforming directivity[1] [55]. Furthermore, other fiber-based

[1]Directivity is referred to as a term to describe the ratio of the power radiated by the designed antenna and the isotropic antenna in a given direction.

beamforming techniques, such as a dispersive switched fiber delay line relying on optical switches for connecting different fiber delay lines of different lengths to obtain the desired time delay corresponding to the specific phase-response have also been investigated [56, 57]. Other solutions, such as optical demultiplexing relying on a specific configuration of multiple ports [58], on photonic crystal fibers [32], on optical ring resonators [59, 60], and on spatial light modulators [61–63] have also been researched.

As alluded to above, non-linear fibers may be characterised by their specific phase responses [64]. Moreover, there is a paucity of relevent A-RoF aided beamforming solutions based on highly non-linear fibers (HNLFs) [65–67]. In [65], a photonic phase-shifter based on stimulated Brilloin scattering was proposed, which requires a table pump source in order to control the phase shift of the output to be fed into the PAA elements. By contrast, in [66] a phase-shifter based on cross-phase modulation was illustrated. In [67], a phase-shifter based on the non-linear polarisation rotation imposed by a HNLF was invoked for the PAAs. However, requiring an excessive number of phase-shifters for realising a high directional beamforming pattern makes the techniques reported in [65–67] somewhat impractical. *As a compelling proposition, we jointly design the non-linearity of the optical fiber and a power control unit so that a linear phase response is constructed from the carefully conceived combination of self-phase modulation (SPM) and cross-phase modulation (XPM).*

The fundamental objective of our proposed technique is to take advantage of the phase shift imposed by SPM and XPM, where the non-linearity-induced phase shift caused by SPM and XPM is highly dependent on the power profile of the optical source. After transmission through a short parallel HNLF, the optical signal is then fed into a dispersion-shifted fiber (DSF) for data transmission, which exibits low dispersion in our wavelength region [13]. After this stage the received optical signal is photo-detected and converted to the corresponding phase-shifted RF signal. After acquiring the phase information, a set of signals subjected to linear phase shift is extracted by a filter and fed into the PAA elements. Our design requires a multi-wavelength source using a single fiber. *To the best of our knowledge, this is the first time that HNLF transmission line based technique is conceived for supporting tunable phase-shifting using SPM and XPM, hence substantially simplifying the photonic phase-shifting arrangement required.* When the PAA elements are fed by the photo-detected signals, the proposed technique achieves

a beamsteering angular range of about 90°. As an application of our HNLF-based phase-shifting beamforming system, a C-RAN network exploiting our design is analysed, where the end users may connect to one or several RRHs, depending on the channel conditions.

In this treatise, we propose employing a HNLF transmission line, which exploits the XPM-SPM-induced phase shifts to build an A-RoF aided beamforming system. In the proposed system, beam steering is carried out in the optical domain using a centralised processing unit. A 10 Gbps system is conceived and investigated.

Compared to the previously proposed fiber-aided beamforming techniques, the advantages of our design using HNLF and the novel contributions can be summarised as follows:

1. We conceive for the first time a beamformer relying on short parallel HNLF lines, which forms a centrally controlled beamforming system designed for the C-RAN fronthaul of low-cost small-cell networks. Meanwhile, the BER performance of the proposed system is maintained in comparison with that of the electronic phase-shifter aided beamforming schemes.

2. A tunable HNLF transmission line based on jointly harnessing the SPM and XPM has never been used for beamforming before. Explicitly, we exploit the unavoidable fiber-non-linearity for phase-shifting-based beamforming, instead of relying on conventional extra phase-shifters.

3. We present a design example using four antenna elements. However, our solution is not limited to the design example employing four antenna elements in Section 2.4. Explicitly, it allows us to increase the number of wavelengths and to employ shorter HNLFs in order to increase the PAA's angular selectivity, making it flexibly scalable.

4. We transmit a quadrature-phase-shift-keying (QPSK) signal at 10 Gbps data rate as an example for demonstrating that our design can be employed in the C-RAN designed in [68], where non-line-of-sight (NLOS) wireless communication is applied.

The rest of this chapter is organised as follows. In Section 2.2, the related PAA basics are described, which are followed by a comprehensive review of the A-RoF aided PAA

beamforming review in Section 2.3. Subsequently, in Section 2.4, the system model of our all-optical phase shifting technique and its application in a C-RAN system are presented, followed by our conclusions in Section 2.5.

2.2 Phased Array Aided Beamforming Basics

Given a single antenna, the signal is transmitted in an omni-directional fashion, while having an N-element antenna allows us to transmit the signal in a directional manner, based on the true-time-delay or phase shift amongst the signals fed into the adjacent PAA elements, as detailed in this section.

Explicitly, there are two major techniques of supporting the PAA: the true-time-delay based and the phase-shifter aided solutions. As for a single frequency, the neighbouring inter-element phase shift of the PAA would remain constant, as long as the time delay of the element is identical.

2.2.1 Phase-shifters

Here, a brief discussion of the PAA aided beamforming concept based on the phase-shifter solution will be presented. In our example of Fig. 2.3, five antenna elements form a PAA. By feeding single-tone signals subjected to a linear phase shift into the five PAA elements, which have a constant distance between them, the output signal of the PAA can be adaptively steered in a specific direction. This is because when a

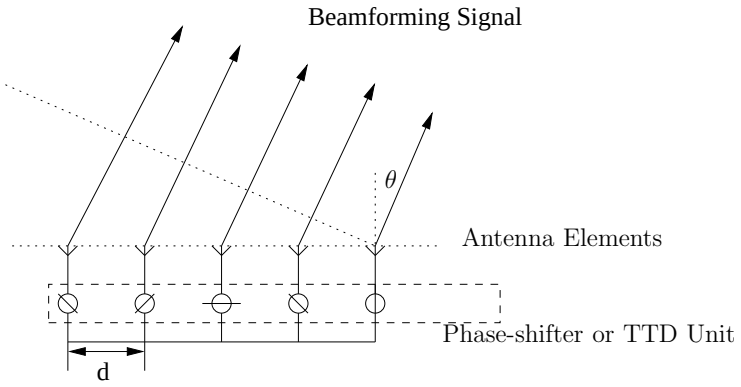

Figure 2.3: A five-element PAA.

required distance d (half the wavelength) and the linear phase shift among the antenna elements are achieved, the five output signals would constructively interfer to strengthen the signal power in a specific direction, while destructively interfer to attenuate the power transmitted in the remaining directions [69]. By controling the phase shift, the beamsteering direction may be tuned. The time delay τ resulting from the phase shift between the adjacent elements can be shown to be [37]:

$$\tau = \frac{dcos(\theta)}{c}, \tag{2.1}$$

Based on Fig. 2.3, where c is the speed of light and θ is the beamsteering angle around the axis of the antenna array orientation. It is clearly seen from Equation (2.1) that the beamteering angle θ is dependent both on the time delay τ and on the distance d. Since the time delay only has a relationship with the phase shift as shown below:

$$\phi = 2\pi f\tau = 2\pi f\frac{dcos(\theta)}{c}. \tag{2.2}$$

When single frequency is applied, the beamsteering angle is directly affected by the phase shift ϕ.

In Equation (2.2), f denotes the signal frequency and ϕ is the corresponding phase shift. This frequency-dependent phase shift impacts the family of broadband systems differently, as detailed in the next section.

In PAA, the beamforming pattern is influenced by two factors: the radiation pattern, which is jointly determined by the type of the radiation source and the array factor[2], which is dependent on external influences, such as the phase progression, number of elements and the carrier frequency [69]. Here, in order to simplify the analysis, an isotropic radiator transmitting in all directions, is exploited. Thus, it is the array factor which predominately affects the beamforming angle. Explicitly, the array factor (AF) is depicted as [69]:

$$AF(\psi) = \frac{sin(M\psi/2)}{Msin(\psi/2)}. \tag{2.3}$$

[2]According to [69], the total field strength radiated by an antenna array is equal to that of a single element positioned at the origin of the array multiplied by a factor, which uniquely and unambiguously defines the array factor.

Then, ψ can be expressed from Equation (2.3) as:

$$\psi = kdcos(\theta) + \phi, \tag{2.4}$$

where M is the number of antenna elements contributing to the beamsteering, while k is the wave number given as $k = 2\pi/\lambda_{RF}$ [70].

As mentioned above, for a single frequency, a constant TTD represents a constant phase shift. However, for a wideband beamforming system the neighbouring inter-element phase shift depends on the frequency, as shown in [69]. This may result in beam misalignment. Thus, using TTD system may be a better design alternative for broadband communication.

2.2.2 The True-time Delay Concept

As in Equation (2.3) and Equation (2.4), the array factor relies on the neighbouring inter-element phase shift ϕ. Thus, for specific frequency, the beamsteering angle can be controlled by tuning the phase shift ϕ. However, for a wide bandwidth, it remains a challenge to form the same beamforming pattern for every frequency component by simply tuning the phase-shifter, unless the distance between adjacent elements can be changed flexibly. However, in practice, the element spacing can not be readily reconfigured. In this case, according to Equations (2.2), (2.3) and (2.4), if we keep d and ϕ fixed, varying f would result in the variation of the beamsteering angle, which is referred to as beam-squinting [38]. Thus, TTD devices are required for achieving free beam-squinting, since the beamsteering angle is directly related to the time delay between the antenna elements, regardless of the frequencies, as seen in Equation (2.1).

Thus, the relationship between the time delay and phase shift is given by Equation (2.2). Technically, the phase-shifter is a special case of TTD in the context of narrowband communications [37], when frequency difference can be neglected.

Specifically, in narrow-band communications, beam-squinting can be more or less avoided, as detailed in Section 2.3. By contrast, in wideband communication, the beam-squinting would severely degrade the beamsteering performance. Thus, a true-time delay beamformer is required for achieving accurate beamforming angle [71]. In the following

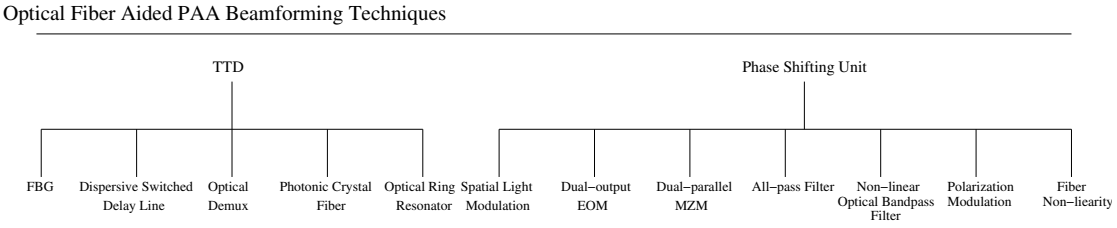

Figure 2.4: A-RoF Aided PAA beamforming review.

Year	Author	Contribution
2002	Wilson *et al,* [62]	Proposed a phase-shifting based beamformer relying on the space light modulator concept, which is suitable for large PAA.
2005	Loayssa *et al,* [65]	Presented a tunable RF photonic phase-shifter based on stimulated Brillion scattering.
2006	Vidal *et al,* [63]	Described a beam-squinting reduction assisted beamformer relying on a combination of parallel SLMs and on optical TTD lines.
	Chan and Minasian [72]	Proposed a photonic RF phase-shifter by applying a single dual-output modulator, two switches and attenuators.
2007	Dong *et al,* [66]	Suggested a phase-shifter concept based on the combination of a Mach-Zehnder modulator (MZM) and a HNLF
2008	Adams and Madsen [73]	Described a novel broadband phase-shifter based on an all-pass filter.
2012	Chan *et al,* [74]	Presented a photonic phase-shifter concept by utilising the dual-parallel MZM to control the DC bias voltage.
2013	Wang *et al,* [75]	Proposed a phase-shifting beamformer based on a non-linear optical bandpass filter.
2014	Li *et al,* [67]	Presented a phase-shifter based on the non-linear polarisation rotation effects taking place in the HNLF.

Table 2.1: A history of phase-shifter based techniques

section, a review of photonic phase-shifter and TTD solutions conceived for A-RoF aided PAA will be presented.

2.3 A-RoF Aided Phased Antenna Array Beamforming Review

Due to the proliferation of fiber-based backhaul/fronthaul networks and the low-loss properties of optical fiber, A-RoF aided PAA beamforming techniques are capable of significantly reducing both the cost and the complexity of electronic beamsteering [36]. Again, there are two major research areas in the context of A-RoF aided PAA beamforming techniques, namely the family of phase-shifter aided systems and TTD aided systems, which will be described in the following sections.

2.3.1 Phase-shifter Aided Systems

Most of the optical phase-shifters are based on generating either a pair of RF sideband signals [74] or a single side-band signal [76] combined with carrier modulation and then varying the relative phase of the sideband and of the optical carrier in order to control the phase of the photo-detected RF signal. This relative phase is then photo-detected at the receiver [76].

The spatial light modulator (SLM) is emminently suitable as a single optical phase-shifter, replacing a number of phase-shifters [77], which is an optical amplitude and phase modulator capable of controlling the phase of the light beams [61], relying on the architecture of Fig. 2.5. As detailed in [63], the refractive index of a specific axis corresponding to a particular polarisation of the light passing through each pixel[3] of the SLM will be controlled by the voltages imposed onto them. Thus, the phase of a specific polarisation component of the transmitted light perpendicular to this axis of the SLM relies on the voltage imposed on the SLM, while the orthogonal component which is parallel to that axis is independent of the voltage applied and has a constant phase. Thus, when different light is fed into each pixel, it becomes feasible to control the phase of the perpendicular polarization component, while keeping the phase of the other one fixed to get a readily controllable phase.

In Fig. 2.6, the parallel-SLM (PAL-SLM) based beamforming phase-shifter of [63] feeding the PAA is shown. The modulated optical signal will then be power-divided and fed into a different strand of fiber. As a result, the SLM will act as a pixelated component, where each output of the line will be transmitted to different pixels. The PAL-SLM of Fig. 2.6, is invoked before photo detection, where the phase shift is controlled by feeding a single side-band and an optical carrier associated with orthogonal polarisations into the same pixel, hence allowing the phase of the RF photo-detected signal to be controlled continuously. This technique avoids having multiple high-complexity phase-shifter configurations, but still faces some fabrication challenges, such as mitigating the temperature sensitivity of the device [78].

Other methods have also been proposed for achieving the relative phase control, such as applying a single dual-output electro-optic modulator (EOM), two switches and

[3]Each pixel can be viewed as a waveguide made of liquid crystal.

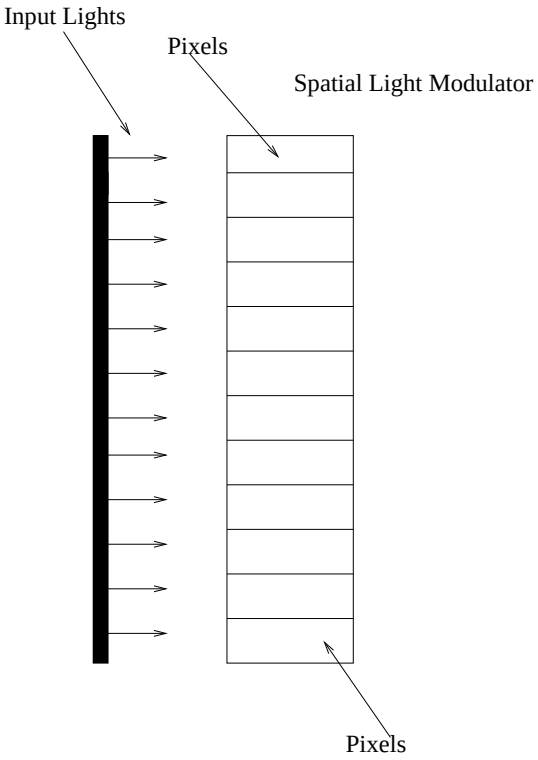

Figure 2.5: A SLM architecture.

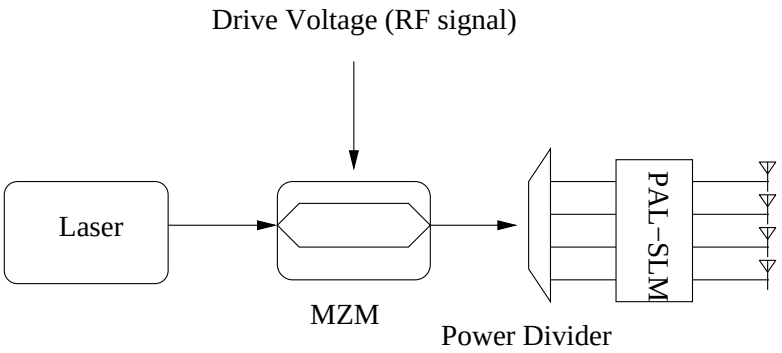

Figure 2.6: A SLM application © B.Vidal *et al.* [61].

attenuators [72], dual-parallel MZM by controlling the DC bias voltage [74], allpass filter [73] and a non-linear optical bandpass filter [75]. The basic concepts behind these techniques rely on varying the phase between the optical carrier and the side-band. However, these methods are not suitable for large arrays due to requiring a large number of phase-shifters. Nonetheless, there are a few examples of phase shifting techniques relying on exploiting the fiber's non-linearity. Specifically, in [65], a RF photonic phase-shifter based on stimulated Brilloin scattering was proposed, which requires a table pump source in order to appropriately tune the phase shift of the output to be fed into the PAA elements. By contrast, in [66] a phase-shifter based on the combination

Year	Author	Contribution
1994	Ball *et al.* [52]	Provided a serial uniform FBG based beamforming technique.
1996	Molony *et al.* [51]	
1997	Molony *et al.* [41]	Proposed a chirped FBG based TTD delay line with a single laser source.
	Minasian and Alame [34]	Presented a chirped FBG beamforming network through the introduction of a photodiode array to eliminate the optical interference.
1998	Corral *et al.* [79]	Suggested a chirped FBG based TTD aided beamforming network with several tunable laser sources.
1999	Corral *et al.* [80]	Compared the performance of different modulation techniques applied in the FBG based delay line.
2000	Ortega *et al.* [81]	Concluded that single side-band plus carrier based modulation imposes no RF frequency limitation and has an excellent performance in the chirped FBG based TTD System.
	Ortega *et al.* [53]	Presented a microwave delay line with a fixed wavelength combined with parallel uniform FBG.
2002	Yao *et al.* [42]	Proposed a tunable chirped FBG delay line with a tunable multi-wavelength laser source.
	Liu *et al.* [47]	Suggested a tunable TTD aided beamforming network based on a tunable chirped FBG by changing its chirp rate via a supported beam.
	Lee *et al.* [57]	Proposed a dispersive switched fiber delay line based on MEMS fast switches.
	Vidal *et al.* [82]	Presented a highly dispersive switched digital delay line for PAA beamforming at 40 GHz.
2005	Italia *et al.* [44]	Suggested a tunable TTD aided beamforming network based on a tunable chirped FBG by applying temperature perturbations to parallel chirped FBGs.
2006	Hunter *et al.* [54]	Demonstrated a multi-channel FBG based TTD beamforming network.
2007	Raz *et al.* [58]	Proposed a TTD aided beamforming network based on Demuxes, where different outputs of a single demux connect different sets of fiber with different fiber lengths.
2008	Subbaraman *et al.* [32]	Presented a TTD aided beamformer relying on the wavelength-dependent photonic crystal fiber delay lines.
	Fakharzadeh *et al.* [60]	Suggested a TTD based solution by applying tunable parallel optical ring resonators.

Table 2.2: A history of TTD based techniques

of a Mach-Zehnder modulator (MZM) and a non-linear optical loop using HNLF was conceived. In [67], a phase-shifter based on non-linear polarisation rotation captured by the HNLF acted as the PAAs. However, the requirement of numerous phase-shifters makes these previous techniques excessively complex, especially when lots of antenna elements are needed for realising a narrow beamforming pattern.

2.3.2 True-time Delay Based Solutions

When the bandwidth reaches a paticular threshold, the beam-squinting problem becomes more severe compared to the true-time delay, which is efficient when the insertion loss

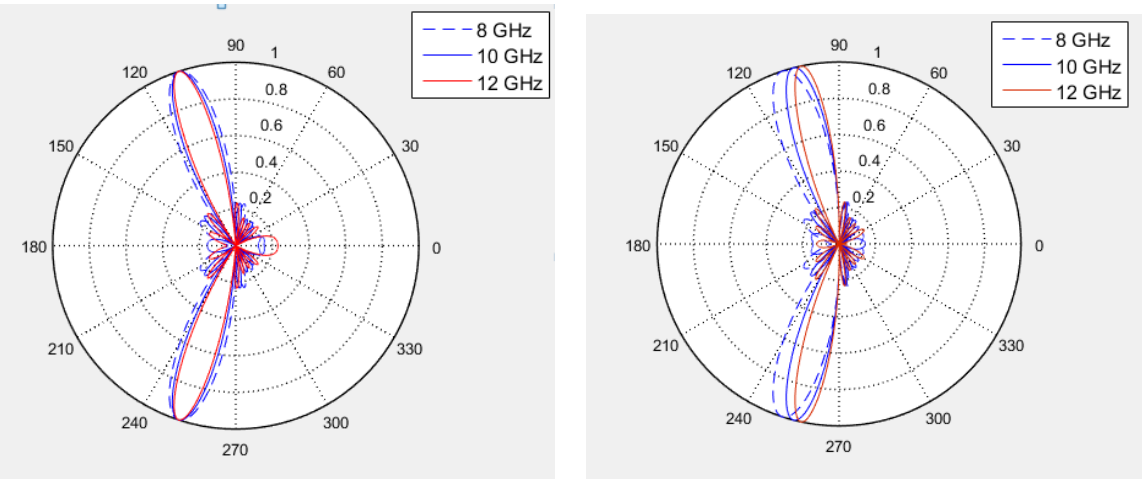

Figure 2.7: Beam-squinting phenomenon: (Left) TTD: the time delay between adjacent elements is 15.6 ps. (Right) Phase-shifter: phase shift (PS) between adjacent elements is $\pi/4$.

and delay of TTD are acceptable [61]. Beam-squinting is caused by the beam misalignment, owing to imposing the same constant phase at different frequencies, as mentioned in Section 2.2. Fig. 2.7 portrays the beampattern of a phase-shifter, explicitly showing the beam-squinting phenomenon, when the transmitted frequencies are 8, 10 and 12 GHz with the aid of seven antennas, while the TTD exhibits nearly no beam-squinting. Next, we present the state-of-the-art of A-RoF aided TTD beamforming.

2.3.2.1 Fiber Bragg Grating Based Techniques

FBG is also often referred to as a wavelength filter in the RoF literature [12], by creating a periodic variation of the refractive index in the fiber core, termed as the grating period [13]. In the uniform FBG, the grating period is uniform along the fiber length, while it is chirping in chirped FBG fiber, as shown in Fig. 2.8 and Fig. 2.9, where Λ denotes the grating period.

FBG reflects a specific wavelength, which is related to the modal index and to the grating period, which is formulated as follows:

$$\lambda = 2\hat{n}\Lambda, \tag{2.5}$$

where λ is the Bragg wavelength (reflected wavelength), $\hat{n}$ is the average modal index and Λ is the grating period.

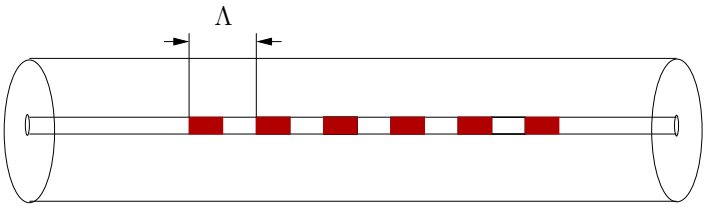

Figure 2.8: Uniform FBG.

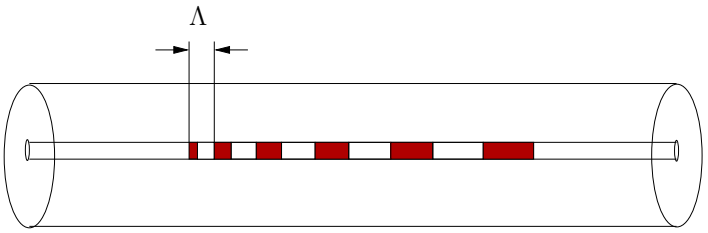

Figure 2.9: Chirped FBG.

By varying the temperature or strain imposed on the fiber, the modal index or grating period changes and hence the wavelength reflected will also be tuned [83]. Again, the uniform FBG solution is shown in Fig. 2.8 to rely on a constant grating period, which will only reflect a specific wavelength. By contrast, Fig. 2.9 shows the chirped FBG, where the grating period is increasing along the fiber length, thus resulting in the reflection of different wavelengths from different locations [13]. By incorporating FBG, when transmitting multi-wavelength optical signals, a linear time delay is imposed based on the chirped properties of FBG. Three main types of FBG solutions have been researched in the context of beamforming: the parallel and serial uniform FBG based delay line as well as the single chirped FBG based delay line.

Fig. 2.10 shows the serial uniform FBG system, where the optical signal having the wavelengths $\lambda_1 ... \lambda_n$ will be reflected by the corresponding uniform FBG. Thus, the time delay is dependent on the distance of the neighbouring FBG sections. By contrast, Fig. 2.11 shows the parallel uniform FBG system. The uniform FBG of each line will be set appropriately to reflect the required wavelength, hence achieving the desired time delay. Finally, the chirped FBG of Fig. 2.12 was specifically constructed for reflecting

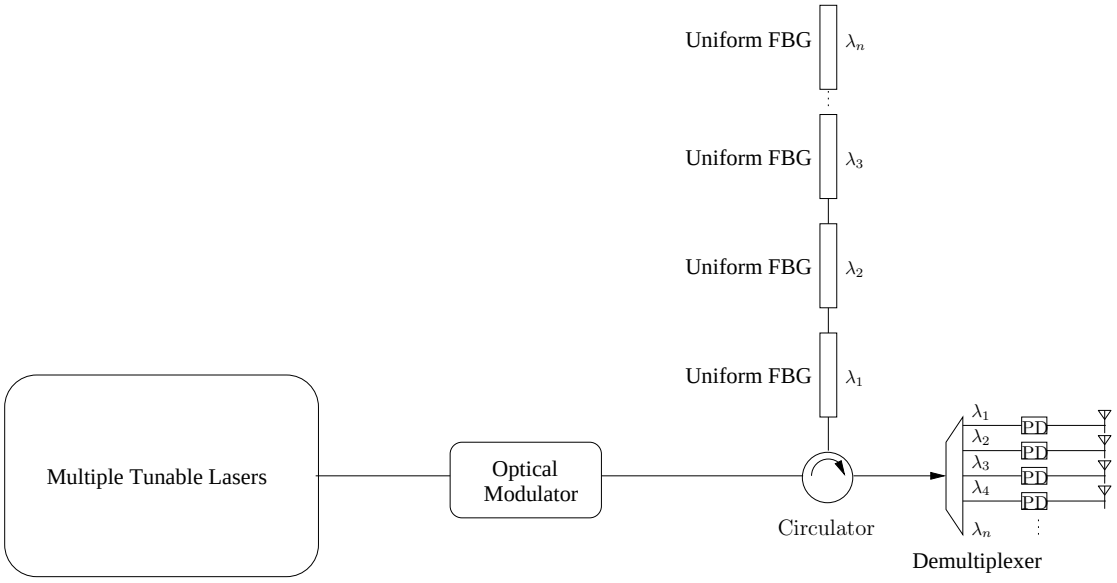

Figure 2.10: Serial uniform FBG based PAA system.

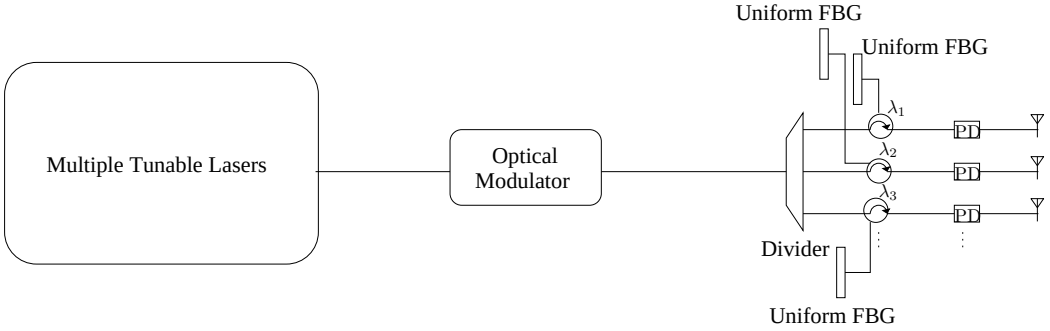

Figure 2.11: Parallel uniform FBG based PAA system.

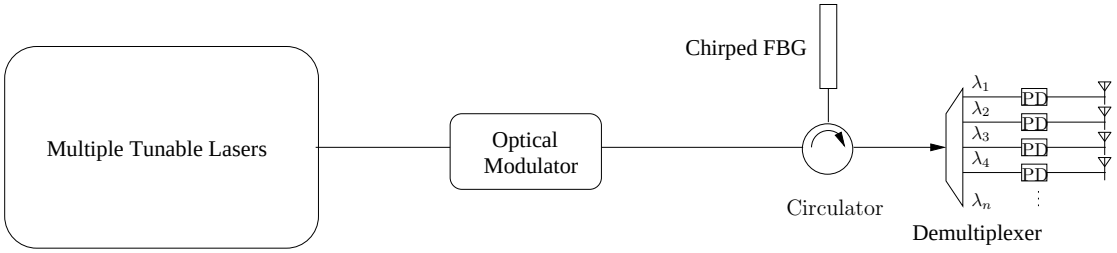

Figure 2.12: Chirped FBG based PAA system.

the different wavelengths at different locations along the fiber-length by appropriately adjusting the grating period or modal index [13].

Research on the family of serial uniform FBG based TTD techniques has been presented in [51, 52], which rely on the basic concepts shown in Fig. 2.10, but with a limited time delay range of less than 20 ps. Then, a fixed wavelength based parallel uniform

FBG solution was further developed for making it tunable for PAA beamforming [53]. This was achieved by simplifying the correponding PAA system [53], which is based on the schematic of Fig. 2.9.

To overcome the limitations of the discrete time-delay and limited time-delay range of uniform FBG, a chirped FBG delay line has been applied for achieving a delay in the range spanning from 40 fs to 59 ps, but unfortunately it exibited a high delay error due to the associated uncontrollable process [41]. In order to invoke the chirped FBG fiber by the PAA system, a chirped FBG network was implemented in [79], which relies on several tunable laser sources for supporting the operation of several phased array elements. However, the solution of [79] suffers from a large group delay ripple, hence the authors mitigate the RF power degradation by applying single side-band plus carrier modulation.

A chirped FBG beamforming network was investigated in [34], which was conceived for eliminating the optical interference through the introduction of a photodiode array, hence making it suitable for a larger time delay range. Subsequently, different modulation techniques were compared in [80], presenting the trade-offs amongst different modulation schemes, including double side-band plus carrier modulation, single side-band plus carrier modulation and self-heterodyne modulation. As a further advance, the authors of [81] showed that single side-band plus carrier modulation imposes no RF frequency limitations and attains a high performance.

The techniques above are all based on using several laser sources, which complicates the system, especially when large arrays of PAA are required. To avoid the complexity of implementing large numbers of uniform FBG as well as to further simplify the system relying on chirped FBG and to satisfy the tunability requirements, based on the schematic of Fig. 2.12, it was proposed in [42] to generate tunable multi-wavelength signals through tuning the chirped FBG within the laser source. Instead of tuning the multi-wavelenth source, tunable chirped FBG can also be realised by changing the chirp rate of chirped FBG via a supported beam [47] or by applying uniform temperature pertubations to parallel chirped FGBs [44]. Furthermore, the authors of [54] substantially reduced the length of FBG by using a single multi-channel FBG.

There are two major challenges in the conception of FBG fiber beamformers. Firstly, the high dispersion caused by the FBG [81, 84] shows that utilising single side-band solutions is essential for the FBG beamforming network. Then, the group delay ripple is mainly caused by the fabrication of the FBG, which should be mitigated [85, 86], because it gravely degrades the PAA beamforming accuracy. Next, another popular beamforming aided technique relying on dispersive switched fiber will be surveyed.

2.3.2.2 Dispersive Switched Fiber Delay Lines

The traditional TTD beamforming technique is based on varying the length of the fiber delay line [38], but this suffers from the inflexibility caused by difficulties of reconfiguring the fixed network. In this case, tunable optical switches would be necessary, which are fast enough for reacting to the signal emission, hence reducing the delay error amongst neighbouring antennas. Using a dispersive switched fiber delay line constitutes a popular method of realising the TTD. The basic concept of this technique is to either vary the length of the standard single-mode fiber or that of the dispersive fiber with the aid of optical switches. To elaborate, on the employment of optical switches, according to the specific length of different fiber-based delay lines, it becomes feasible to generate signals subjected to linearly increasing time delays with the aid of prompt switching, which are then connected to the corresponding antenna elements.

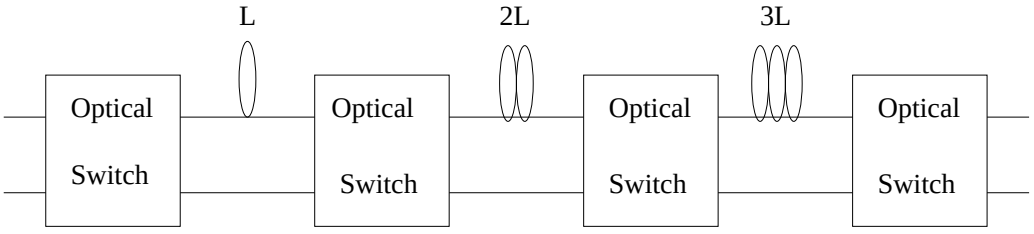

Figure 2.13: A fiber delay line with optical switch.

To elaborate a little further, in Fig. 2.13, a general optical delay line relying on a dispersive fiber is shown, where L represents the dispersive fiber, generatating various delays with the aid of optical switches. In the case of Fig. 2.13, each switch has two input ports and controls two output ports, where the output ports are connected to fibers of length L, $2L$ and $3L$. Thus, by appropriately configuring each switch, we have different fiber-lengths introducing different delays. Based on Fig. 2.13, in [82] an optical

switch combined with a highly dispersive delay line was configured to construct a digital delay line for realising PAA beamforming. In order to achieve a low switching time as well as low insertion loss, a micro electro mechanical system (MEMS) based switch was used [57].

Prompt, low-delay switching is one of the main issues in traditional fiber delay line based beamforming networks. After the issue is that the optically switched fiber delay line should have the shortest possible length to simplify the network deployment. In the next section, we will focus our attention on how fiber can be utilised in the optical demultiplexer for constructing PAA beamforming.

2.3.2.3 Optical Demultiplexing Aided Techniques

Optical demultiplexing (Demux) splits the optical signal into its components having separate wavelengths. Assuming that it is possible to attach different fiber lengths different ports of a Demux, a TTD can be readily realised.

In [58], it was proposed to use a TTD system having several Demux scheme in each channel, which connects different sets of fiber with different fiber lengths, hence each Demux scheme feeds a different antenna. Again, different wavelengths will be input into the specific ports. Thus, by setting fiber length increment of the corresponding port for the same wavelength in neighbouring channels to be constant, a TTD can be realised. However, the practicality of this technique critically hinges on the size of the optical Demux, especially when large arrays are required. As another design option, the photonic crystal fiber may also be invoked for PAA beamforming, as detailed in the next section.

2.3.2.4 Photonic Crystal Fiber

Photonic crystal fiber (PCF), which is referred to as micro-structured fiber relies on tiny hollow tubes along the fiber length for confining the light [87]. As seen in Fig. 2.14. To elaborate a little further, PCF is designed to be phase-matched at the specific wavelength λ_0, hence there is no dispersion at this wavelength. However, as indicated in [32], when the transmitted wavelength obeys $\lambda < \lambda_0$, most of the signal energy would be

confined within the inner core, while for $\lambda > \lambda_0$ if would be, confined to the outer core. Thus, any transmitted wavelength other than λ_0 would experience a high dispersion due to the variation of the refractive index caused by the redistribution of the signal energy in the PCF.

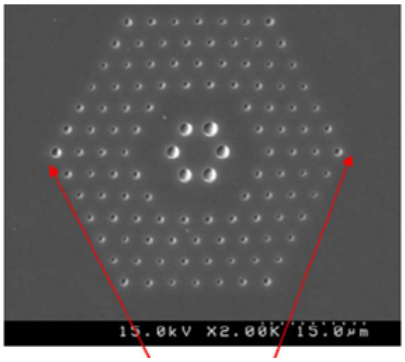

Figure 2.14: The cross-section of PCF showing the hollow tubes along the fiber length provided for confining light ©Harish Subbaraman *et al.* [32].

The reason for using PCF [32] is that the dispersion of PCF is 33 times higher than that of the standard single-mode fiber (SMF), which hence substantially reduces the fiber length required, therefore making the beamforming network more compact. Subbaraman *et al.* [32] designed a PCF aided TTD system relying on feeding multiple laser sources with different RF drive voltages into an electro-optic modulator (EOM), and then transmitting it through several PCF delay lines. Then, by exploiting the wavelength-dependent time delay increment between the adjacent delay lines, it allows the beamforming angle to be controlled by the optical carrier frequency. This system is hence capable of substantially reducing the length fiber used for beamforming, but again, numerous PCFs have to be employed if large arrays of PAA are needed.

2.3.2.5 Optical Ring Resonator

The optical ring resonator is formed of a closed optical loop of fiber and a waveguide. Optical ring resonator couples the optical signal into the resonator from the waveguide through directional coupler or multi-mode interference coupler [88], where because of constructive interference or total internal reflection, a particular wavelength will be retained with the aid of filtering upon travelling through the ring after several round-trips in the loop [59]. In [60], a parallel optical ring resonator was designed for PAA,

which was shown to overcome the challenge of accurate TTD time delay line tunability, where a thermo-optic phase-shifter is used for changing the coupling coefficient of the power from waveguide to the closed loop in order to control the time delay. By tuning the thermo-optic phase-shifter to appropriately adjust the coupling coefficient, in [60] a robust, fast and accurate algorithm was designed for tuning the coupling coefficient of the optical ring resonator for solving the problem of slow time delay tunability, thus becoming capable of achieving different time delays based on the coupling coefficient. However, this scheme required several closed loop for achieving scalable time delays, which is not cost-efficient.

In a nutshell, the techniques discussed above constitutes the state-of-the-art on fiber aided PAA beamforming. In conclusion, the FBG TTD technique is deemed to be the most scalable technique, which exhibit feasible tunability, low loss, short fiber length and a less complex system configuration than invoking several delay lines. Having said that, FBG TDD is by no means flawless. The group delay ripple for example is a key issue to be further researched. Hence in the next section, we will present a beneficial HNLF aided PAA beamforming design.

2.4 All-optical Phase Shifting Technique Beneficially Exploiting the Harmful Fiber Non-linearity for Beamforming

In this treatise, we conceive a novel A-RoF aided beamforming technique based on the fiber's non-linearity to be applied in C-RAN. In our proposed technique, the PAA elements are fed by the phase-shifted signals introduced by our HNLF aided phase-shifting solution, which results in an angular beamsteering range of around 90°, which can be exploited by sectorization in cellular networks to reduce the co-channel interference imposed. Furthermore, we exploit the proposed A-RoF-aided phase shifting technique in C-RAN, where our proposed system takes advantage of the centralised signal processing capability of the A-RoF system to conceive an all-optical processing based tunable beamforming system. While our flexible HNLF-aided phase-shifting process is confined

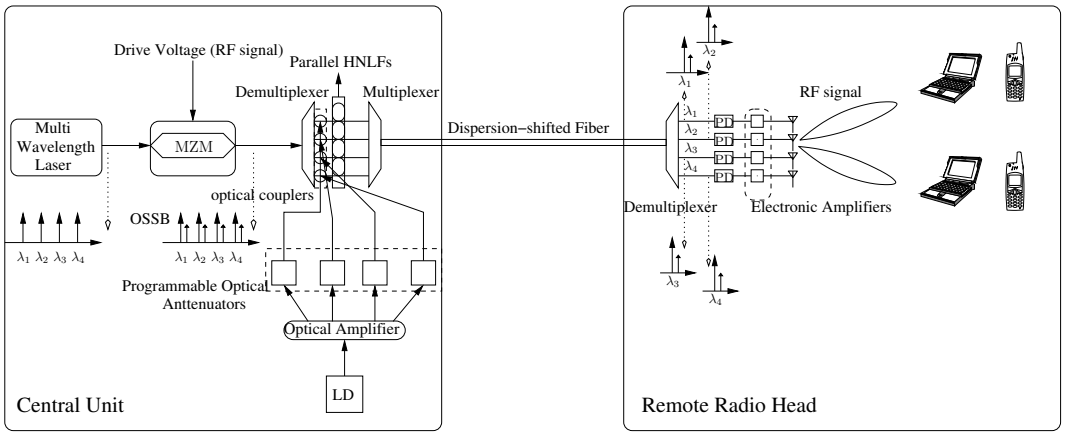

Figure 2.15: Schematic of a four-element beamformer based on HNLF-RoF system.

to the CU of the C-RAN, the end users of C-RAN cellular networks are capable of flexibly choosing the serving RRHs and employing diverse wireless transmission techniques. Upon integrating our HNLF-aided phase-shifting design into the proposed C-RAN, we impose as little as 0.1 dB SNR degradation compared to its traditional electronic processing based conventional wireless counterpart, which requires extra phase-shifters.

Our system exploits the power-controlled fiber-non-linearity-induced phase shifts, where the phase shift of each antenna element of Fig. 2.15 is controllable through a programmable optical attenuator in a centralised processing unit at the input of the fiber, which significantly reduces the complexity imposed on the RRHs at the fiber's output. Note that our proposed design is applicable in cellular sectorization scenarios, with a cell sector range of 90° [89]. To the best of our knowledge, HNLF parallel transmission line based phase shifting has not been used for MIMO beamforming before.

2.4.1 System Overview

Fig. 2.15 shows the block diagram of our proposed beamformer utilising both HNLF and wavelength evolution in each step. Assuming that only a single wavelength λ_1 is transmitted in this system, the associated wavelength landscape-evolution displayed in Fig. 2.15. Then, the wavelength having the designed power is modulated by a MZM modulator to obtain an optical single side-band signal. Afterwards, the modulated signal is injected into a short HNLF having a length below 1 km along with a control signal

generated by the LD of Fig. 2.15. A power-dependent phase shift is imposed and tuned by the XPM induced by the control signal, whose power is tuned by a controllable optical attenuator, as shown in Fig. 2.15. Then, the output power of the HNLF will be fed into the DSF, where the zero-dispersion wavelength is shifted to the vicinity of 1550 nm [13] for transmission to a remote radio port. The phase is then retained after coherently photo-detecting the RF signal. Thus, based on the power-dependent phase shift of the wavelength transmitted in the HNLF which will be detailed in Section 2.4.1.1, the power controller will adjust the power level of the control signal for adjusting the corresponding phase shift.

Relying on the above discussions related to the conception of a tunable phase-shifting aided beamforming system, our design philosophy is now extended to the tunable multi-wavelength source seen in Fig. 2.15 and using four wavelengths as a design example[4]. Then, the multi-wavelength source injects the optical signal into a MZM to generate a optical single side-band (OSSB) signal driven by a binary phase shift keying (BPSK) modulated electronic signal. As seen at the bottom of Fig. 2.15, four optical attenuators are used for tuning the power of the four individual control signals fed into each HNLF. The HNLF is used for imposing different phase shifts for each wavelength due to the XPM induced by the control signal, as detailed below. After transmission through the HNLF, a wavelength multiplexer combines the optical signal into a wavelength division multiplexing (WDM) signal of λ_1 λ_2 λ_3 λ_4 for feeding it into a DSF, where the zero-dispersion wavelength is in the vicinity of 1550 nm. The WDM signal is then split into four branches by a demultiplexer in the example of Fig. 2.15. Then each branch is fed into a coherent photo detector (PD) for converting the optical signal to an RF signal, which is fed into an electronic amplifier. Finally, the amplified RF signal is fed into each antenna at the same power level for ensuring a satisfactory directivity. In other words, each output of the electronic amplifier feeds a PAA element employing uniform linear arrays with each element being fed by linearly delayed RF signals, which allows the scheme to steer the RF signal in the desired direction, which is an explicit benefit of combining the appropriately phased signals fed into the antenna elements. Finally,

[4]For lager size of MIMO system, we need more wavelengths and more short HNLF, but this can be readily realised by tuning multi-wavelength laser source and increasing the number of the deployed short HNLFs.

corresponding to the specific locations of the mobile users, the beamsteering angle can be controlled by the specific phase shift between the adjacent antenna elements.

Next, we provide our simulation-based results to verify our proposed design. Generally, the signal transmitted through the optical fiber suffers from fiber attenuation, fiber dispersion and fiber non-linearity [13, 90]. The fiber attenuation causes power-loss, while the fiber dispersion induces pulse broadening and inter-symbol-interference. Fiber non-linearity engenders stimulated Brillouin scattering (SBS), stimulated Raman scattering (SRS), SPM, XPM and four-wave-mixing (FWM), which yield frequency chirping and phase shifting. These effects are often considered in fiber-optic communication systems. However, in our system, the SRS, SBS and FWM can be neglected due to having a low input optical power and phase-mismatch [90], which will be elaborated on in the next section.

Thus, considering the fiber impairments above, the mathematical principle of the HNLF channel model based on the symmetric split Fourier method (SSFM) with XPM and SPM will be presented.

2.4.1.1 Symmetric Split-step Fourier Method Associated with XPM and SPM

The SSFM is widely used in single-mode fiber (SMF) simulations both for pulse based signals [90] and for continuous wave transmission [90].

To study the impact of SPM and XPM, a simplified form of the non-linear Schrödinger equation is used [90]:

$$i\frac{\partial A}{\partial z} + \frac{i\alpha}{2}A - \frac{\beta_2}{2}\frac{\partial^2 A}{\partial t^2} + \gamma|A|^2 A = 0, \tag{2.6}$$

where A is the amplitude of the input optical signal, z is the fiber length, α denotes the fiber loss, β_2 is the second order dispersion parameter, which accounts for the chromatic dispersion and γ is the non-linearity parameter [91]. Upon taking into account the impact of SPM first, based on the SSFM, we arrive at [90]:

$$\frac{\partial A}{\partial z} = (\hat{D} + \hat{N})A, \tag{2.7}$$

where $\hat{D}$ is a differential operator that represents both the fiber loss as well as the dispersion and $\hat{N}$ is the non-linearity operator representing the SPM. Combining Equations (2.6) and (2.7), yields:

$$\hat{D} = -\frac{\alpha}{2} - \frac{i\beta_2}{2}\frac{\partial^2}{\partial t^2}, \tag{2.8}$$

$$\hat{N} = i\gamma|A|^2. \tag{2.9}$$

To elaborate briefly, the SSFM splits the fiber into numerous short segments of length h, over which the fiber may be deemed linear. There are three operations for each step, in which the first and third step represent the linear operations calculating the attenuation and dispersion, while the second operation represents the non-linear operations. The first operation occurs in the first half interval of length $h/2$ and can be described as:

$$A(\omega, z + \frac{h}{2}) = exp[\frac{h}{2}\hat{D}(i\omega)]A(\omega, z), \tag{2.10}$$

where $A(\omega, z + \frac{h}{2})$ is the Fourier transform of $A(t, z + \frac{h}{2})$ and the differential operator $\partial/\partial t$ is replaced here by $i\omega$. Then, for the second operation taking place during the middle of the step, the non-linearity would be accounted for as follows [90]:

$$A'(t, z + \frac{h}{2}) = A(t, z + \frac{h}{2})exp(h\hat{N}), \tag{2.11}$$

where $A'(t, z + \frac{h}{2})$ is the input signal for the next half step after the non-linear operation [92, 90]. Finally, the third operation, which occurs during the second half step repeats the first process. This procedure can be expressed as [90]:

$$A(t, z + h) = exp(\frac{h}{2}\hat{D})exp(h\hat{N})exp(\frac{h}{2}\hat{D})A(t, z). \tag{2.12}$$

Self-phase modulation occurs, when a single optical beam transmitted through the fiber. More specifically, the reason for the phase shift caused by SPM is that in HNLF, a high-intensity optical signal may induce the optical Kerr effect [90], which changes the refractive index of the optical fiber. This results in slowing down the speed of light beam in the fiber. In contrast to the self-induced phase modulation occuring in a single channel, XPM is caused by having more than one optical beams [13]. Thus, the refractive index affecting the optical beam in HNLF is dependent both on the intensity of its own and those of others. The SSFM described above only handles the effects of SPM, while

for characterising the combination of XPM and SPM, Equation (2.9) should be modified as follows:

$$\hat{N} = i\gamma(|A_i|^2 + 2\sum_{k\neq i}|A_k|^2), \tag{2.13}$$

where A_i is the amplitude of the transmitted optical signal and A_k is that of the co-propagating optical signal. Obviously, from Equation (2.13), that the change of refractive index will be higher when XPM is encountered. Furthermore, Leibrich and Rosenkranz [92] conceived an efficient improvement of the SSFM subjected both to XPM and SPM, making it possible to reduce the required number of simulation steps by a factor of up to 20 without degrading the accuracy of the channel model. In our design, the Leibrich-Rosenkranz method is utilised for the simulation of the HNLF.

Additionally, RoF systems are affected by fiber attenuation, fiber dispersion and fiber non-linearity. Hence, our channel model includes the effects of fiber attenuation, fiber dispersion and SPM-XPM-induced fiber non-linearity are encountered, but that the SBS, SRS and FWM can be neglected. SBS and SRS may indeed significantly degrade the system by reflecting and shifting the transmitted wavelength, when a high optical power is imposed [13]. However, we can ignore these two effects, since the input power of the transmitted wavelength is kept as low as 0.1 milliWatt (mW). This is far below the threshold of the given HNLF, since the corresponding SRS threshold is approximately 270 mW and that of SBS is 42.5 mW based on the theoretical analysis of [13]. Furthermore, we also note that the popular non-linearity-inducing technique of FWM can be readily neglected due to the presence of phase mismatch in our system. This is because the effects of FWM only become significant, when the phase mismatch in the fiber vanishes [90]. Thus, as a benefit of conveniently controlling the chromatic dispersions for our HNLF, the FWM can indeed be neglected by carefully tailoring the chromatic dispersion with the objective of avoiding the phase match of the transmitted wavelengths in our HNLF [93]. Thus, SPM and XPM constitute the main contributions to phase variations in the HNLFs in our design.

To validate the feasibility of our parallel HNLF-aided beamforming, we investigate its performance in the context of a C-RAN, where the CU houses the parallel HNLF-aided components of Fig. 2.16 and the RRHs are connected to it using fibers. To elaborate further, we utilise two RRHs in Fig. 2.16. Explicitly, a single-user C-RAN design relying

on two RRHs is considered, where a pair of fibers is used for fronthaul access. In this scenario, the user may connect to either one or both RRHs to achieve beamforming or beamforming combined with either diversity or multiplexing gains, depending on the wireless channel quality.

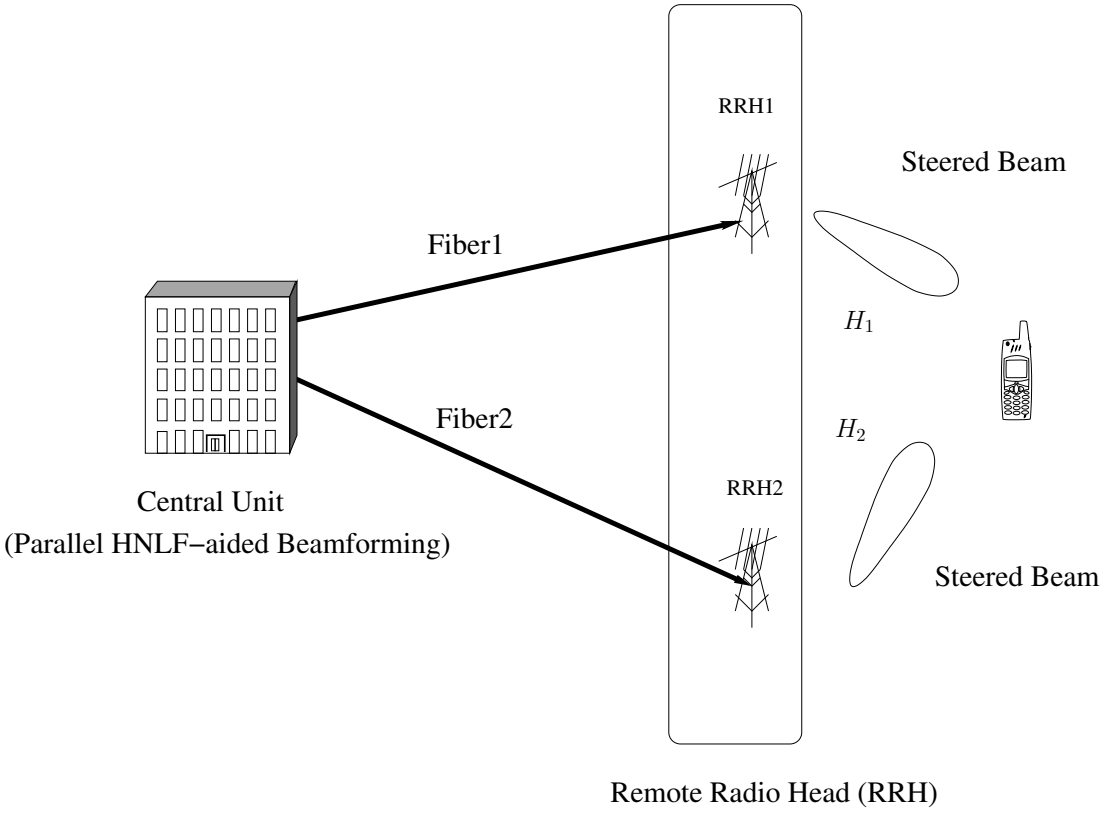

Figure 2.16: C-RAN beamforming system model.

2.4.1.2 C-RAN System Model

In this section, we briefly describe the C-RAN system, which will be used for the verification of our HNLF aided PAA beamforming system, as shown in Fig. 2.16. Beamforming substantially improves the SNR gain, thereby increasing the throughput [33]. Hence, instead of using phase-shifters for beamforming in the RRHs, we invoke the proposed all-optical processing based beamforming system, where HNLF aided phase shifting assisted beamforming is applied in Fig. 2.16.

The C-RAN architecture can flexibly serve the end users in the cellular network [68], enabling them to achieve either diversity or multiplexing gains. As shown in Fig.

2.16, the C-RAN fronthaul is fiber-based, where our HNLF aided PAA technique is employed for achieving beamforming, whilst simultaneously connecting the CU to the RRHs. Naturally the link between the RRH and the end users is wireless.

In this C-RAN system, we adopt the approach of [68], where end users may be connected to one or several RRHs, depending on the prevalent channel conditions, as follows.

1. If the wireless channels between the user equipment (UE) and both RRH1 as well as RRH2 of Fig. 2.16 are favourable, then the UE may be connected to both RRH1 and RRH2, where either multiplexing or diversity gain is attained in addition to beamforming employed at each RRH.

2. On the other hand, when one of the wireless links is in deep fade, the UE is connected to only one of the RRHs, exploiting the better channel, thereby attaining an improved SNR [68]. In this case, the UE may be connected to either RRH1 or RRH2 of Fig. 2.16.

In our design, we investigated both cases using our HNLF aided PAA beamforming technique for demonstrating the flexibility of our design. Thus, we integrated our HNLF-aided beamforming into a C-RAN system.

Let us now consider the network of Fig. 2.16, where the user is equipped with N_r received antennas and each RRH is equipped with N_t transmit antennas. Furthermore, the user is positioned at an angle of ψ_1 and ψ_2 with respect to RRH1 and RRH2, respectively. In the scenario where the user is connected to only one RRH, say RRH1, the received signal vector after combining is given by

$$\mathbf{y} = \beta \mathbf{w}^H \mathbf{H} \mathbf{f} x + \mathbf{w}^H \mathbf{n}, \tag{2.14}$$

where $\mathbf{f}$ is the beam steering vector of size $N_t \times 1$ formulated by the fiber, x is the input signal stream, $\mathbf{n}$ is the complex Gaussian noise of mean 0 and variance σ^2, $\mathbf{w}$ is the combining vector of size $N_r \times 1$, β is the A-RoF-system-induced distortion, while $\mathbf{H}$ is

the semi-correlated channel with L paths, which is given by

$$\mathbf{H} = \sqrt{\frac{N_r N_t}{L}} \sum_{l}^{L} \alpha_l \mathbf{a}_r(\phi_r^l)\mathbf{a}_t^T(\phi_t^l), \tag{2.15}$$

so that $\mathbb{E}[\|\mathbf{H}\|_F^2] = N_t N_r$. Furthermore, $\mathbf{a}_r$ and $\mathbf{a}_t$ are the response vectors and for uniform linear arrays (ULA) they are expressed as:

$$\mathbf{a}_r(\phi_r) = [1 \; e^{j\frac{2\pi}{\lambda}d\cos(\phi_r)} \ldots e^{j\frac{2\pi}{\lambda}(N_r-1)d\cos(\phi_r)}]^T, \tag{2.16}$$

$$\mathbf{a}_t(\phi_t) = [1 \; e^{j\frac{2\pi}{\lambda}d\cos(\phi_t)} \ldots e^{j\frac{2\pi}{\lambda}(N_t-1)d\cos(\phi_t)}]^T, \tag{2.17}$$

where ϕ_r and ϕ_t are the angle of arrival and departure, respectively, while α_l is complex Gaussian distributed whose amplitude is Rayleigh and phase is uniformly distributed.

On the other hand, when the user is served by 2 RRHs, the signal vector received in the downlink is given by

$$\mathbf{y} = \beta \mathbf{W}^H \mathbf{H}\mathbf{F}\mathbf{x} + \mathbf{W}^H \mathbf{n}, \tag{2.18}$$

where $\mathbf{H}$ and $\mathbf{F}$ are now expressed as $\mathbf{H} = [\mathbf{H}_1 \quad \mathbf{H}_2]$ and $\mathbf{F} = \text{diag}\,(\mathbf{f}_1, \mathbf{f}_2)$, respectively. To elaborate further, $\mathbf{H}_i (i = 1, 2)$ is the sub-channel[5]matrix of size $N_r \times N_t$ of the link spanning from the i^{th} RRH to the UE as shown in Fig. 2.16, while $\mathbf{f}_i (i = 1, 2)$ is the beam steering vector of size $N_t \times 1$ employed at the i^{th} RRH. The weights of the vector $\mathbf{f}_i$ are those of a zero-forcing beamformer, where the weights of the vector $\mathbf{f}_i$ is tuned for mitigating the interference caused by other RRHs, i.e. it can null the interference caused by a signal arriving from different angles. Furthermore, $\mathbf{x}$ is the signal vector of size 2×1, while $\mathbf{W}$ is now a matrix of size $N_r \times 2$. The signal transmitted by the beamforming at the RRHs is received by the UE, where the signal is downconverted and processed digitally in the baseband using the combiner matrix $\mathbf{W}^H$. Hence, the linear minimum mean squared (LMMSE) solution[6] is chosen as the combiner matrix $\mathbf{W}^H$. This design can be interpreted as a sub-array architecture, which was depicted and discussed in great detail in [94]. A similar approach can be followed here for multiple RRHs association.

[5]It is instructive to note that, in this case, when two RRHs are used for transmission, $\mathbb{E}[\|\mathbf{H}\|_F^2] = 2N_t N_r$.

[6]Any combiner solution can be employed. We have considered LMMSE as a simplifying solution.

Modulation format	Quadrature phase shift keying
Multi-wavelength	1549.4 (λ_4), 1549.6 (λ_3), 1549.8 (λ_2), 1550 (λ_1) nm (frequency spacing 25 GHz) Output power of each wavelength: 0.1 mW
Control signal	1549.2 nm
Control power range (LD)	0.1 mW-60.1 mW
Optical modulator	Dual-Drive MZM
HNLF fiber length	1 km
Dispersion-shifted fiber length	10 km
Bit rate	10 Gbps
RF carrier frequency	6 GHz
HNLF attenuation	2.13 dB/km
HNLF dispersion parameter	$-1.7 \cdot 10^{-12}$ s^2/km
HNLF fiber non-linearity	18 w^{-1}/km

Table 2.3: Simulation parameters.

Next, our simulation results characterising the power-controlled phase shifts are presented, while the system performance of Fig. 2.16 is analysed and compared to that of the system using traditional electronic phase-shifters without our RoF aided beamforming.

2.4.2 Simulation Results and Discussions

In this section, we will first discuss the attainable phase shifts using our HNLF-aided beamforming scheme. Then, we characterise our fiber-based C-RAN system and benchmark it against that relying on traditional phase-shifters.

2.4.2.1 Highly-non-linear-fiber-aided Phase-shifting System

A HNLF channel transmitting QPSK modulated electronic signals of a multi-wavelength laser source has been simulated using MATLAB. The parameters used are shown in Table 2.3.

More explicitly, a laser source having the four wavelengths of 1549.4, 1549.6, 1549.8 and 1550 nm is modulated by an RF signal having the centre frequency of 6 GHz, where the MZM of Fig. 2.15 is used for generating OSSB to reduce the influence of fiber dispersion. As for the optical fiber properties, the HNLF has an attenuation of 2.13 dB/km, a dispersion parameter of $-1.7 \cdot 10^{-12}$s^2/km and a fiber non-linearity of 18 w^{-1}/km [95] and we rely on a 10 km DSF for signal transmission. In our design example we assume that each HNLF fiber has a length of 1 km.

Since the XPM- and SPM-induced phase shifts fed into our four antenna elements are dependent both on the power level of the four control signals of the LD and on that of the data signals, we used the four optical attenuators of Fig. 2.15 as the power controller for varying the power of each control signal having the same wavelengths to obtain the desired power. After the MZM, the quadruple-wavelength optical signal is demultiplexed, combined with each control signal and then fed into each HNLF. After transmitting through the HNLF and experiencing XPM-SPM-induced phase shift depending on the specific power level of both the modulated data signal and on that of each amplified control signal, we multiplex the output of the four HNLF and transmit the resultant WDM signal over a DSF, which exhibits zero dispersion in the wavelength region of 1550 nm.

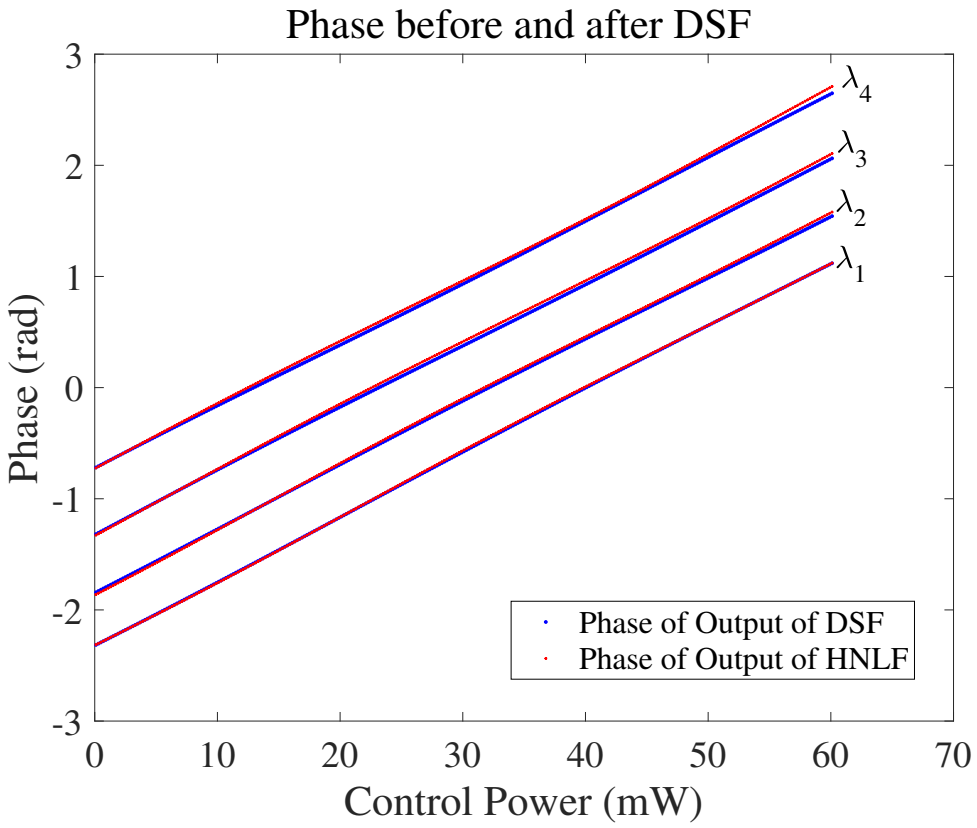

Figure 2.17: Phase before and after DSF of the 10 Gbps system.

In order to characterise the effect of each wavelength on the phase shift of the different signals, we fixed the input power for each wavelength to 0.1 mW and varied the tunable power of the control signal from 0.1 mW to 60.1 mW with a step-size of 0.2 mW. Thus, the SPM maintains the same effect for each wavelength, implying that the phase shift

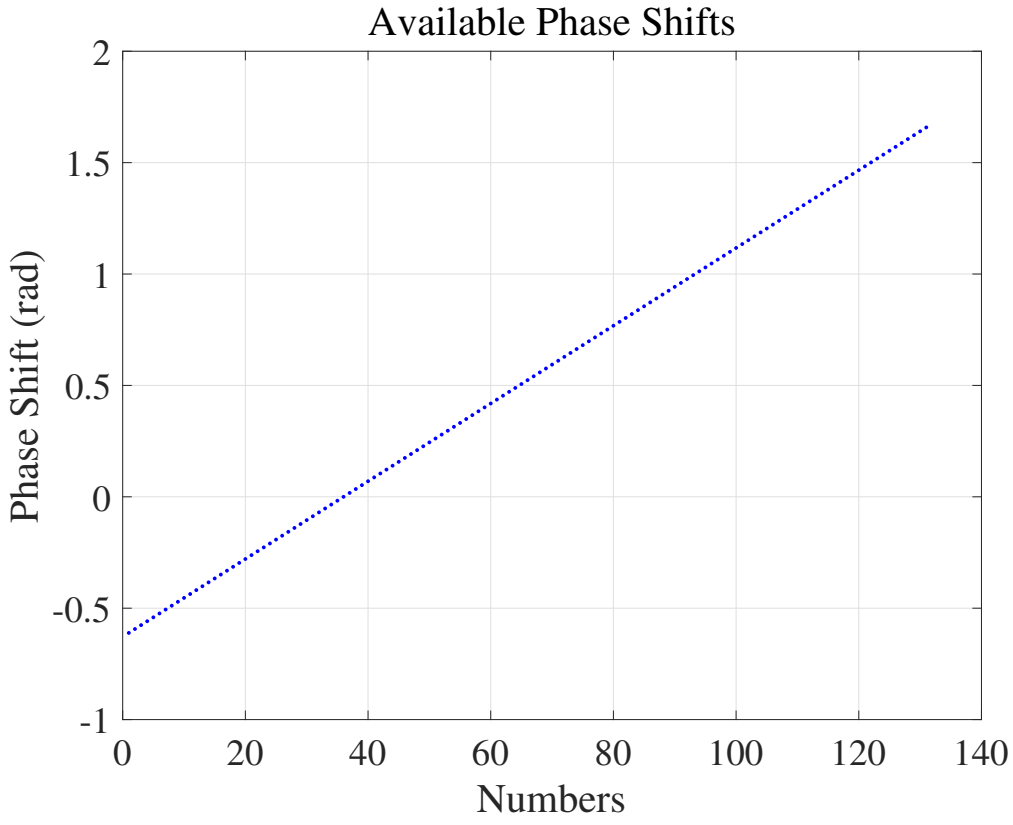

Figure 2.18: Attainable phase shifts of the 10 Gbps system.

between each wavelength would only be affected by the XPM induced by the variation of the control signals' power. As a result, we obtained 301 power levels corresponding to the four separate wavelengths. Then each optical wavelength was demodulated with the aid of coherent photo detection, yielding the photo-detected RF signal associated with a constant phase shift between the different photo-detected RF signals. This was then translated into specific beamforming angles after being radiated from the PAA. Again, by collecting phase values corresponding to the above-mentioned power levels, we have attempted to identify the specific power for the particular optical wavelengths at which we have a constant phase shift between the four PAA elements. Furthermore, each control signal power associated with each wavelength can be tuned separately with the aid of four individual optical attenuators, thus granting us substantial flexibility, as shown in Fig. 2.15.

To obtain a narrow-angle beamforming pattern, a PAA having a constant phase shift between the adjacent antenna elements is required [69]. However, it is a challenge to

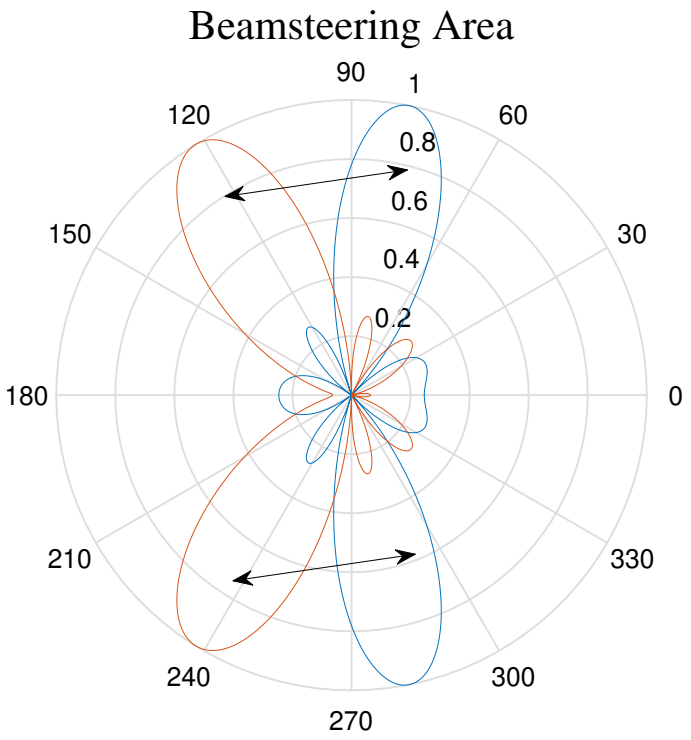

Figure 2.19: Beam pattern of the 10 Gbps system.

maintain a constant phase shift between each and every element. Thus, our design offers us a continuous phase tuning flexibility.

In our example, we used four parallel HNLFs to introduce phase shifts, while employing a DSF for transmitting the data to the RRHs. The measured phases of the four wavelengths at the outputs of both the HNLF and of the DSF are sketched in Figure 2.17, showing that they are nearly constant and hence indicating that our 10 km DSF only has a modest impact on the phase. Again, we can generate the required phase shifts based on the outputs of the parallel HNLF. Thus, we can simply test the parallel HNLFs and then design a codebook, storing the desired beamsteering directions and the corresponding level of the control powers required. Fig. 2.18 shows the range of phase shifts available, which spans from -0.6 rad to 1.6 rad[7]. As a result, Fig. 2.19 portrays the corresponding angular directions, where a continuous scanning range of 90° is attained using a four-element PAA. Thus, we applied our proposed system for a

[7]The x-axis in Fig. 2.18 refers to the number of phase shifts that can be attained, with each corresponding to a specific control power combination.

cellular sectorization of a range below 90°, where a full range of scanning angle is not required.

It was shown in [96] that having a phase error standard deviation for a four-element PAA system below 0.32 rad (18.33°) is suitable for guaranteeing a good beamforming performance. Based on the attainable phase shifts seen in Fig. 2.18, we are able to keep the phase shift differences among the antenna elements within 0.01 rad, which may be deemed almost negligible. Hence our technique is capable of maintaining accurate directivity, outperforming the family of FBG techniques [70, 79, 84]. This is because the accuracy of the FBG family is determined by the fabrication imperfections of FBG, which potentially introduces group velocity ripples, hence potentially degrading the directivity accuracy.

To briefly conclude the impact of XPM and SPM on the beamforming pattern, we extract specific power combinations corresponding to the beamsteering angles required for specific cell-sectorization angles. As explained in Section 2.4.1.1, the optical power induces fiber-non-linearity, which can then cause the phase variation of each transmitted wavelength as verified by Equation (2.12). The phase variations are then exploited for obtaining a relationship between the optical power and the attainable constant phase shift of the adjacent antennas as portrayed by Fig. 2.18, according to which we can form the specific beampattern of Fig. 2.19. As an example, Table 2.4 shows some of the power combinations of the four control signal powers required for particular constant phase shifts for supporting the desired beam directions. These codebooks can be directly used by practitioners to design the sectorization patterns required.

Beamforming direction	Power combination (mW)				Phase shifts (rad)
	Power 1	Power 2	Power 3	Power 4	
80°	55.9	38.5	19.9	0.1	-0.54
85°	42.1	29.3	15.3	0.1	-0.28
90°	27.5	19.5	10.3	0.1	0
95°	13.3	9.9	5.1	0.1	0.28
100°	0.1	1.3	1.5	0.5	0.54
105°	0.1	6.1	11.1	15.5	0.82
110°	0.1	10.7	20.3	29.7	1.08
115°	0.1	14.9	29.3	42.9	1.33
120°	0.1	19.1	38.1	55.5	1.57

Table 2.4: Power combinations required for obtaining different beamforming directions.

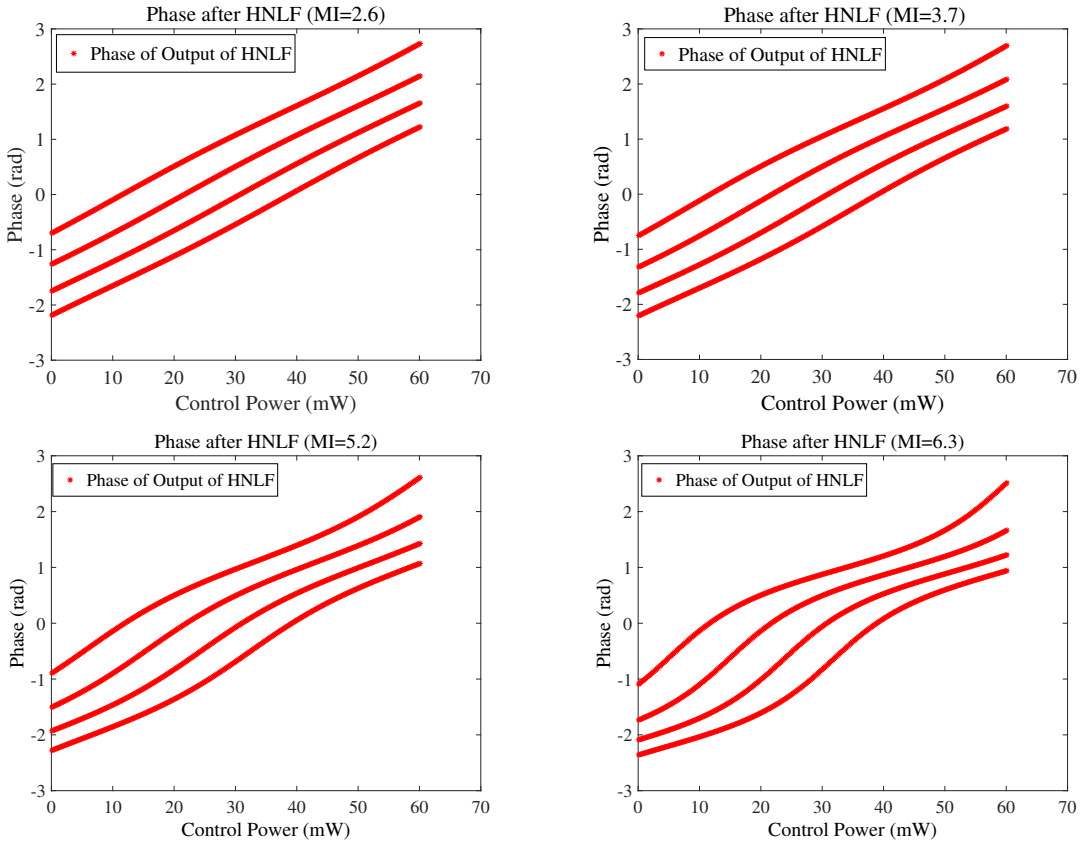

Figure 2.20: Output phase of HNLF with various MI.

As mentioned in Section 2.4.1, the fiber impairments of SBS, SRS, FWM can be neglected, provided that we invoke SSFM for modelling the fiber-non-linearity aided beamforming. Furthermore, there are other system parameters that affect our system performance and here we consider the MZM's non-linearity, the optical input power and the HNLF length.

MZM's non-linearity: The MZM's non-linearity is caused by the high amplitude of the MZM's drive voltage. As analysed in [97, 12], the MZM's non-linearity generates higher-order harmonics, which can potentially degrade our system performance. The MZM's modulation index (MI) $\frac{\pi V_{dr}}{V_\pi}$ determines the MZM's non-linerity[97]. V_{dr} is the amplitude of the drive voltage of the MZM of Fig. 2.15 and V_π is the switching voltage of the MZM. By controlling the amplitude V_{dr} to vary the modulation index according to 2.6, 3.7, 5.2 and 6.3, we obtained the output phase of the HNLF shown in Fig. 2.20, while in the results reported in Fig. 2.17, we fixed the MI to 0.5 to eliminate any harmonics. It is clearly shown that the phases obtained are fluctuated compared to the

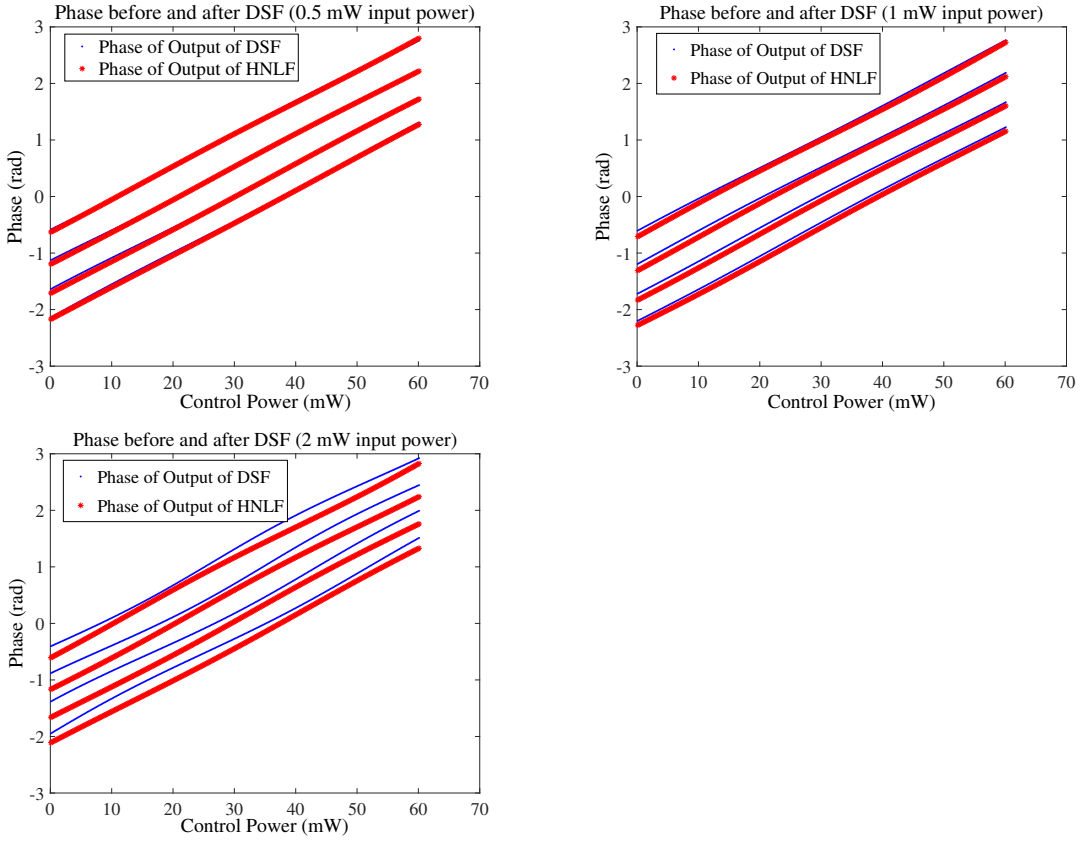

Figure 2.21: Output phase before and after the DSF with various input optical power.

output phase of the HNLF seen in Fig. 2.17 and the fluctuation becomes increasingly severe upon increasing the modulation index. In our proposed system, a MI of 0.5 is used for removing the second-order and higher-order side-bands caused by the MZM's non-linearity.

The optical input power: In the performance study of Section 2.4.2.1, we fixed the optical input power of the HNLF to 0.1 mW, which substantially reduced the SPM that might shift the phase in the transmitted DSF of Fig. 2.15. To further characterise the impact of the optical input power, we vary the transmitted optical power according to 0.5, 1 and 2 mW and we compare the output phase of the HNLF and of the DSF of Fig. 2.15. The results of Fig. 2.21 indicate significant degradations when the power is increased to 2 mW, where the signal associated with the optical input power of 0.5 mW exhibits a similar performance to Fig. 2.17 while the phase of two outputs divert marginally when the power is 1 mW. Thus, varying the optical input power for

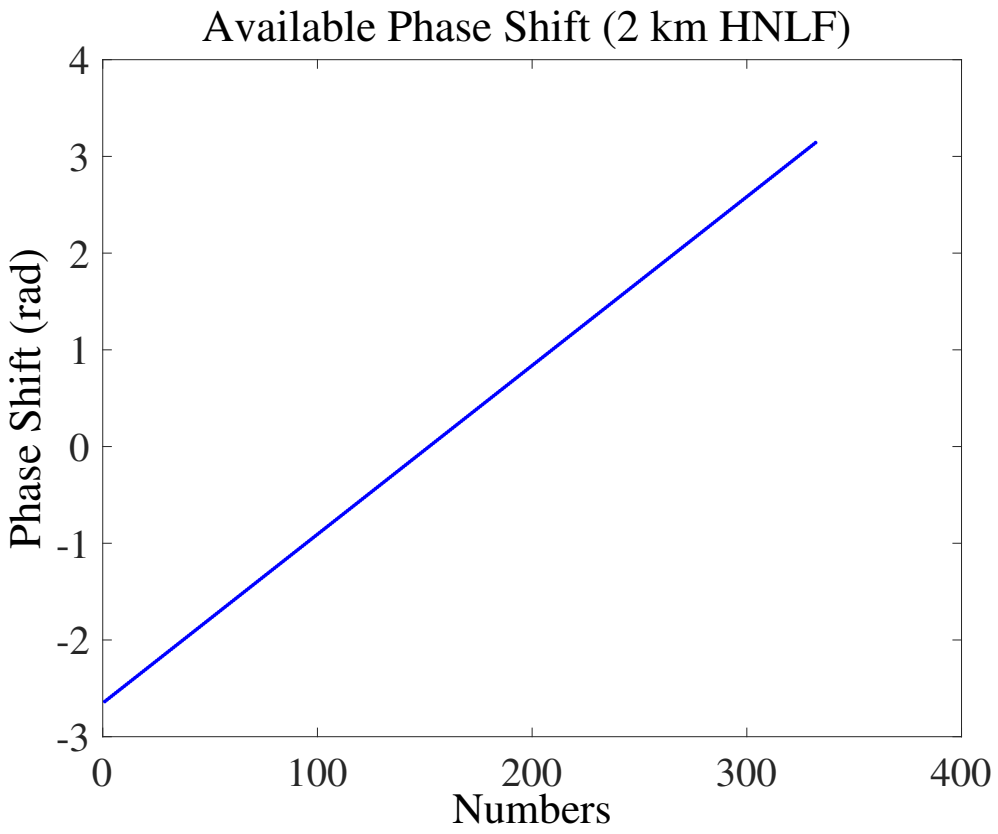

Figure 2.22: Attainable phase shifts with HNLFs fiber length of 2 km.

each wavelength feeding the HNLF will affect the corresponding beamforming direction instructed in the codebook shown in Table 2.4.

The HNLF fiber length: In our example, we proposed parallel HNLF fibers with each fiber length being 1 km for the sake of having a cost-efficient system design. However, we also noted that the achievable beamforming scanning range is limited to 90°. Thus, we increase our HNLF fiber length to 2 km to broaden the achievable range. Fig. 2.22 shows that the achievable phase shifts have a range of -2.6 rad to π rad, implying that a beamforming scanning range of nearly 360° can be realised at the cost of having a longer fiber. Note that the longer fiber can be readily implemented by a cable drum, which can be accommodated without requiring larger space. Alternatively, a highly nonlinear chalcogenide fiber having a non-linearity of 50,000 times that of the standard silica fiber [98] can also be used in our system for the sake of reducing the overall fiber length to a few meters.

The above-mentioned parameters are likely to affect the A-RoF system and should

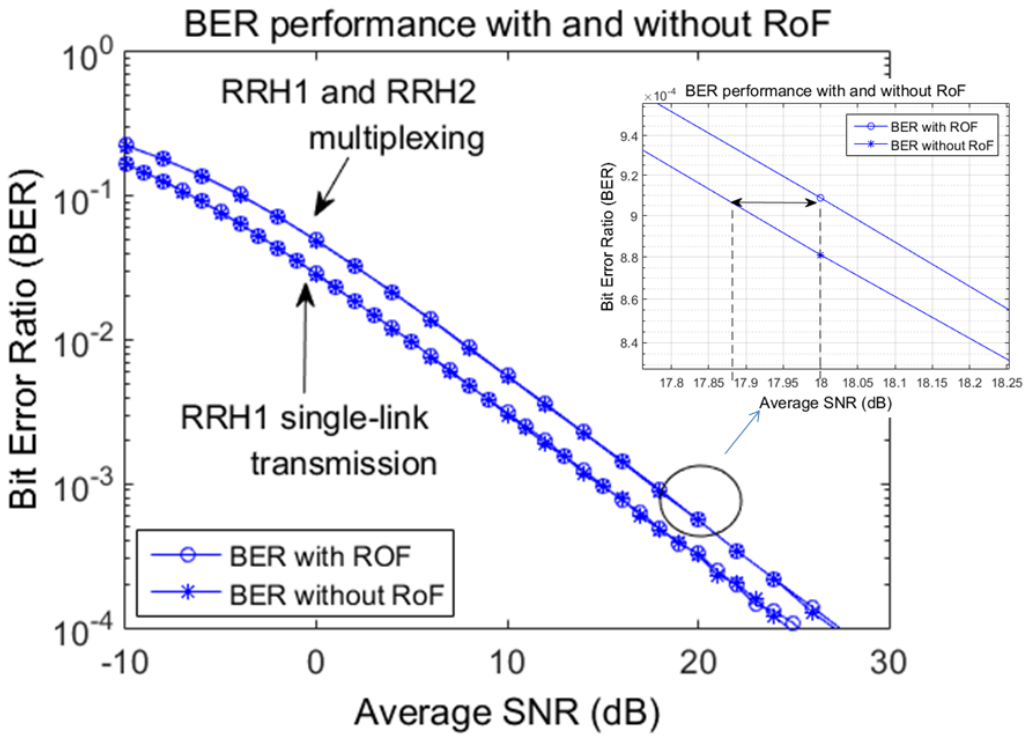

Figure 2.23: BER performance with and without A-RoF.

be carefully tailored. Since our system is designed for cellular sectorization, a beamforming scanning angle within 90° is satisfactory. Our C-RAN application is based on the codebook given by Table 2.4 designed for cellular sectorization.

2.4.2.2 C-RAN BER Performance

We have indicated in Section 2.1 and 2.4.1 that our system is capable of simplifying the electronic phase-shifter based conventional beamforming transceiver system implemented in the conventional base station by beneficially exploiting the fiber-non-linearity aided beamforming technique. C-RAN is widely recognised as a cost- and energy-efficient mobile access network for reducing the total cost of ownership (TCO) [1], such as the management and maintenance fee, by centralising most of the digital signal processing in a CU. More specifically, regarding the analogue beamforming system design, we centralise the beamforming pattern control in the CU, while exploiting fiber non-linearity to shape the phase response. Hence we eliminate the need for the analogue phase shifters.

For example, as discussed in [37], the number of electronic phase-shifters of a conventional analogue beamforming system is a linear function of the number of transmitter antennas. Thus, a four-transmitter-antenna aided beamforming system requires four RF phase shifters and four RF chains, which are housed in the RRHs. In the proposed fiber-non-linearity aided beamforming system, actively-powered phase-shifters, power-thirsty analogue-to-digital converter (ADC) and digital-to-analogue converters (DAC) are totally eliminated, while invoking four short HNLFs of 1 km length in the CU to obtain the designed beamforming phase response. The beamforming angle control is confined to the CU, where the complexity of the conventional base station imposed by the beamforming is substantially reduced. Furthermore, the CU is capable of steering the beam transmitted from multiple RRHs, which will be discussed in this section.

Since the codebook of Table 2.4 can be used for generating specific beams, the centrally power-controlled beamsteering scheme is capable of supporting our C-RAN system, which relies on low-complexity RRHs. Here, to validate that our proposed system can be exploited in a C-RAN system, we have discussed the amalgamation of A-RoF and C-RAN in Section 2.4.1.2. The associated performance results are presented in this section. Based on the C-RAN system of Fig. 2.16 and on the discussions of Section 2.4.1.2, the UE of Fig. 2.16 can be connected either only to RRH1 or to both RRH1 and RRH2, depending on the prevalent channel conditions as detailed in Section 2.4.1.2. We consider both cases and show the BER performance attained in Fig. 2.23.

Fig. 2.23 shows the BER performance of the A-RoF aided beamformer and of the beamformer using conventional phase-shifters without A-RoF as a bench marker. As discussed in [68], when one of the RRHs of Fig. 2.16 is in deep fade, the C-RAN system is capable of switching to another RRH (e.g. RRH1 of Fig. 2.16) for transmission. The corresponding BER curve of the single-link RRH1 is shown in Figure 2.23, which shows only modestly degraded BER results compared to those using conventional electronic phase-shifters without A-RoF[8].

On the other hand, when the UE is connected to both RRH1 and RRH2[9], two

[8]The SNR in Fig. 2.23 represents the wireless SNR, where the measured signal power is the normalised output power of the PAAs and the noise power is the wireless AWGN power.

[9]As mentioned, using a longer fiber or a fiber with higher non-linearity factor, it is possible to extend the coverage angle of the antenna array in each RRH to 360°. In this example, where the coverage angle is 90°, it is possible to employ four antenna arrays at the same RRH, where each antenna array can cover a different 90° area and hence the RRH will be able to cover the entire 360° area.

independently fading spatial streams are transmitted to the user positioned at angle 105° and 120° from RRH1 and RRH2 of Fig. 2.16 invoked for spatial multiplexing, respectively [99]. It can be seen from Fig. 2.23 that the A-RoF aided beamformer shows a negligible 0.1 dB SNR degradation compared to that of the beamsteering using conventional phase-shifters without A-RoF. This is due to the phase noise introduced by A-RoF system. Furthermore, due to the interference introduced by multiplexing shown in Fig. 2.23, we achieved a better performance for the RRH1-based single-link transmission than that for multiplexing. Thus, as evidenced by Fig. 2.23, our A-RoF aided beamforming technique is capable of supporting a C-RAN system, whilst reducing the cost- and energy-consumption compared to the conventional electronic phase-shifter aided beamforming system.

Hence our solution may be readily invoked for sectorization of a C-RAN cellular network to improve the SNR gain attained.

2.5 Conclusions

In this chapter, a review of A-RoF aided PAA beamforming and a novel phase shifting network based on the fiber non-linearity are presented and discussed in detail. In Sections 2.2 and 2.3, the PAA basics and the development of A-RoF aided beamforming PAA have been elaborated. In Section 2.4, we conceive a novel A-RoF aided beamforming technique based on the fiber's non-linearity to be applied in C-RAN. In our proposed technique, the PAA elements are fed by the appropriately phase-shifted signals introduced by our HNLF aided phase-shifting solution, which results in an angular beamsteering range of around 90°. This can be exploited by sectorization in cellular networks to reduce the co-channel interference imposed. Furthermore, we exploit the proposed A-RoF-aided phase shifting technique in a C-RAN, where our proposed system takes advantage of the centralised signal processing capability of the A-RoF system to conceive an all-optical processing based tunable beamforming system. While our flexible HNLF-aided phase-shifting process is confined to the CU of the C-RAN, the end users in the C-RAN cellular networks are capable of flexibly choosing the serving RRHs and employing diverse wireless transmission techniques. Through integrating our HNLF-aided phase-shifting design into the proposed C-RAN, we impose as little as 0.1 dB SNR degradation

compared to its traditional electronic counterpart, but the latter requires extra phase-shifters. Furthermore, future work can be focused on the C-RAN response time and sum-rates, which are prevalent C-RAN topics.

Chapter 3

Analogue Radio Over Fiber Aided Spatial Modulation

CHAPTER 2 invoked analogue radio over fiber (A-RoF) aided analogue wireless beamforming in the context of a centralised small-cell and cloud/centralised radio access network (C-RAN), which was achieved without any phase shifters. As mentioned in the context of Fig. 1.9, in this chapter, we will investigate the benefits of the spatial modulation (SM) concept in the A-RoF aided C-RAN system.

To elaborate a little further, in C-RAN, the base station at the central unit (CU) feeds the remote radio heads (RRHs), using A-RoF techniques for supporting the cellular network [17, 1, 12, 100]. This chapter will focus on designing A-RoF for SM aided multiple-input-multiple-output (MIMO) systems without having to use actively-powered switches. More explicitly, the A-RoF aided MIMO signal processing of Fig. 1.7 will be replaced by SM as seen in Fig. 3.1. In contrast to the analogue beamforming, which is a MIMO based technique conceived for improving the signal-to-noise ratio (SNR) and for reducing the inter-channel interference (ICI), SM constitutes a low-cost and low-complexity MIMO scheme, which is capable of improving the spectral efficiency (SE) vs energy efficiency (EE) trade-off [8].

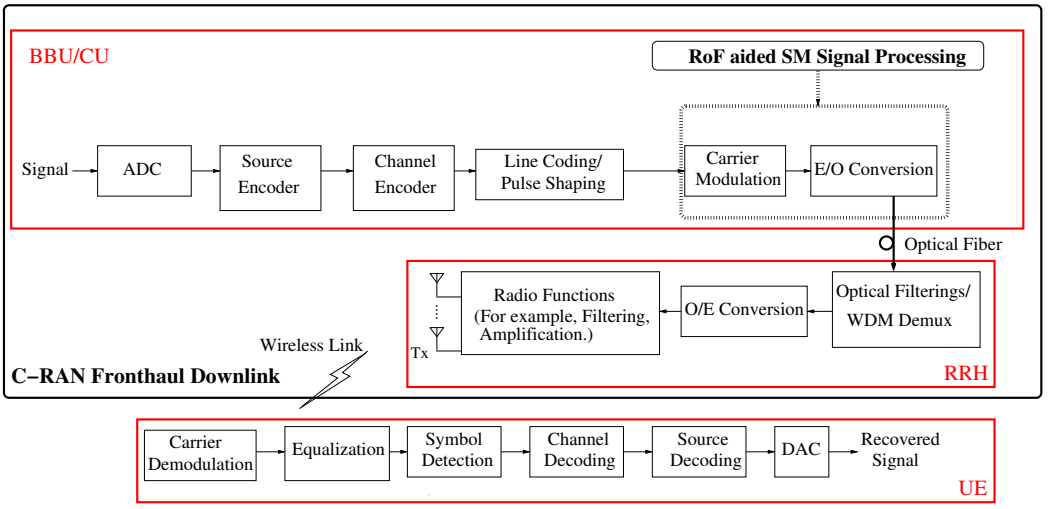

Figure 3.1: A-RoF aided SM for the C-RAN Downlink.

Prior to highlighting our contributions, we will briefly introduce the relevant background and the related SM topics. Then, we will establish the connection between the SM and the A-RoF aided C-RAN fronthaul downlink design.

3.1 Background

Meeting the demands of seemless, low-latency communication requires the exploration of hitherto unused carrier frequencies and employing more small-cell base stations for improving the area spectral efficiency by reducing the ICI [2]. Given the shortage of radio frequencies, the operational cellular network is unable to meet the mobile subscribers' ever-increasing throughput demand, hence there is an urgent need for more small-cell base stations. The deployment of extra base stations allows serving more users but suffers from more drastically fluctuating ICI [2] in addition to the fact that it significantly increases the cost. Thus, the C-RAN concept [101, 1] has been proposed as a novel mobile architecture revolutionising the functions of conventional base stations. Accordingly, most of the baseband signal processing is migrated to a CU, while the main radio functions of the conventional base station, such as the optic-to-electro (O/E) conversion, amplification, electronic filtering and radio transmission, are migrated to the RRHs, hence resulting in a cost- and power-efficient solution [102, 9, 28]. The novel concept of coordinated multi-point (CoMP) [1, 103] aided communications can also be established with the aid of the C-RAN's centrally controlled processing.

Moreover, by exploiting the fiber's low antenuation, its substantial bandwidth and its immunity to electro-magnetic interference [12], the A-RoF based C-RAN system is capable of simplifying the functions of the RRHs, since both the modulation as well as the analogue-to-digital conversion (ADC) and digital-to-analogue conversion (DAC) operations are carried out by the CU, while the passive optical processing components and antennas used at the RRHs only impose a modest cost [102, 16]. This results in an energy-efficient mobile access network relying on centralised MIMO schemes [19].

The most popular spatial multiplexing technique [104] is the classic Bell laboratories layered space-time (BLAST) scheme, where independent signals are transmitted from independent antennas for improving the SE. However, spatial multiplexing aims for imposing the SE without taking into account the overall energy efficiency as well as the complexity. By contrast, SM is characterised by striking an attractive compromise between the SE and EE, whilst relying on a single-RF chain based solution for multiplexing the classically modulated data and the antenna index based stream [105]. Furthermore, it was shown [105] that at a given SE, the receiver complexity is substantially reduced when compared to the Vertical BLAST (V-BLAST).

To elaborate a little further, SM is a low-cost MIMO technique, where only a single one or a small fraction of the transmitter antennas is activated at a time [8, 106, 105, 107]. Apart from the advantage of relying on a single-RF chain, single-antenna based receiver activating a single antenna results in an ICI-free design [108].

3.2 A Brief Review of Wireless Spatial Modulation

Again, SM is a cost-efficient MIMO technique, dating back to the year 2001 [109], although it is closely related to other so-called combinatorial modulation schemes. For a detailed historical perspective, please refer to [104]. In this context, Chau *et al.* [109] advocated the space shift keying (SSK) concept, where only the antenna index carries any data. Based on a twin-transmitter-antenna scheme and activating one or both of the antennas at a time, the SSK scheme proposed in [109] is capable of transmitting the signal purely using the antenna index, while substantially reducing the receiver's complexity [109]. Then, the early theoretical analysis of SM, where the data is carried

by both the classic RF signal and the antenna index, was carried out by Mesleh *et al.* [105].

In the ensuing era, substantial research efforts have been focused on designing SM-aided MIMO systems for improving their performance. Sugiura *et al.* [110] proposed the concept of generalised space-time shift keying (STSK). As a further develepment, link-adaptation was also invoked in the context of SM systems [111], where the system performance was considerably improved compared to the conventional SM systems. To further reduce the receiver complexity by dispensing with any channel state information both at the transmitter and receiver, Bian *et al.* [112] conceived differential spatial modulation (DSM), which exhibited a compelling performance vs complexity trade-off. Furthermore, Basnayaka *et al.* [113] carried out the capacity analysis of SM in the context of massive MIMO scenarios, demonstrating a comparable capacity to that of the open-loop MIMO. Moreover, Wu *et al.* showed in [114] that pre-coding aided SM is capable of improving the secrecy of wireless communication systems.

Given the considerable research efforts invested in SM, a number of surveys have also contributed to the advances in SM [115, 104, 8]. Thus, as mentioned in Chapter 1, to support the potential deployment of A-RoF-based C-RANs, improving the EE vs SE trade-off, we provide an overview of SM adopting a holistic system-oriented perspective. More specifically, the existing SM-MIMO schemes heavily depend on the employment of actively-powered switches. However, with the aid of the A-RoF technique using optical side-band selection, we are capable of removing the SM switches while designing an adaptive C-RAN.

3.3 New Contributions

In this chapter, we aim to solve the following challenges encountered by the conventional SM schemes:

1. SM switches have a high power-consumption, especially when massive MIMO is employed [28].

2. If SM is to be deployed in the C-RAN system, the number of high-speed switches needed for SM is a linear function of the number of RRHs, which together with the RF chains in the RRHs substantially increases the cost of the SM-aided cellular mobile network.

Hence, to solve the above-mentioned pair of challenges, this chapter provides several A-RoF-based SM downlink designs in the context of C-RAN, where we present an experimental demonstration of the A-RoF aided twin-antenna SM scheme to verify the feasibility of using optical single side-band selection for mapping the antenna index, which can replace the actively-powered SM switches. Then we propose a more general A-RoF aided SM design that can support any arbitrary number of transmitters while adaptively choosing the number of the RRHs connected to the users.

Explicitly, we firstly propose a prototype design for an A-RoF aided twin-antenna SM scheme complemented by its experimental characterisation, where a 20 km standard single-mode fiber (SSMF) is used for transmission. In this experiment, a 2 Gbps SM employing two transmit and two receive antennas is investigated, which imposes less than 1 dB SNR degradation at a BER of 10^{-4} compared to those operating without A-RoF. Then, having verified the feasibility of the proposed A-RoF aided SM scheme experimentally, we proceed by proposing a more scalable C-RAN system, where optical processing aided SM capable of supporting an arbitrary number of transmitter antennas. Machine learning is invoked for controlling the system's adaptation, where the objective function is based on improving the achievable data rate. Meanwhile, to mitigate the multi-path interference and to increase the diversity gain attained, an optical space-time-block-coding-SM scheme is introduced. To clearly demonstrate our ideas, this chapter is structured as follows:

Section 3.4 proposes the A-RoF aided twin-antenna SM downlink, followed by its experimental characterisation, where the MZM's side-band selection is carried out by phase shifting the drive voltage of the MZM for replacing the conventional circuit-based switch originally used for antenna selection of the wireless SM. In this design, the SM scheme's antenna selection concept is represented by the side-band selection process of an optical single side-band (OSSB) signal generated by a dual-drive Mach-Zehnder modulator (MZM). More specifically, we assign an index to the OSSB location using

the specific phase-shifting techniques proposed in [116, 117] for realising an optical processing aided low-cost SM encoding, where only a single RF chain is required to serve a single RRH. Thus, in the proposed design, the SM encoding operation takes place in a CU, while the RRHs are responsible for optical filtering, O/E conversion, electronic amplification and transmission. As a benefit, there is no need for agile switches at the wireless transmitter.

Our contributions in Section 3.4 are summarised as follows:

1. We design an energy-efficient A-RoF network relying on twin-antenna SM encoding at the CU, where the SM switches are eliminated, hence significantly simplifying the transceiver design and reducing both the complexity as well as the power consumption of the RRHs of the conventional architecture relying on actively-powered SM switches. This design can also be used in the context of both C-RANs and small-cell fronthauls for facilitating cost-effective management and site maintenance.

2. The sophisticated SM encoding philosophy is intrinsically integrated into our A-RoF design, where we view the optical side-band's frequency position as the antenna selection index, thus realising an all-optical central processing aided SM system architecture. The single-RF chain advantage of SM reduces the complexities of both the CU and of the RRHs.

3. We experimentally characterise the critical elements of our system by demonstrating the underlying principles using a 2 Gbps A-RoF-aided binary phase shift keying (BPSK) SM system combined with convolutional coding, where we show that the SNR performance is less than 1 dB away from that of the conventional wireless system operating without the A-RoF.

4. Our design example employs 3 GHz radio carrier frequency. However, our proposed system design is scalable of operating at any practical carrier frequency, which is determined by the drive frequency of the MZM.

Section 3.5 presents an adaptive A-RoF based C-RAN system, in which the CU of the C-RAN can be adaptively connected to multiple RRHs. Meanwhile, extended

by the feasibility study of the A-RoF aided twin-antenna SM encoding presented in Section 3.4, we conceive a general optical processing SM side-band selection arrangement combined with space-time block coding (STBC). Explicitly, this is achieved with the aid of controlling both the drive frequency and the phase-difference of the dual-drive MZM, supporting any arbitrary number of transmitter antennas in the A-RoF based C-RAN. Furthermore, we invoke a learning algorithm referred to as the K-nearest neighbourhood (KNN) algorithm for adapting both the number of RRHs connected to a single user and its modulation techniques employed. This is attributed to the intrinsic capability of the link adaptation exploited in our proposed C-RAN system.

Due to A-RoF schemes' capability of centralising both the digital and radio processing [7], SM-STBC can be beneficially implemeted centrally in the A-RoF aided C-RANs considered. *In Section 3.5, we propose an A-RoF aided SM-STBC scheme based on Alamouti code in the C-RAN's CU, which transmits the STBC signal from a pair of wireless transmitters.*

More explicitly, the SM-STBC operations are carried out optically via optical side-band selection, where the drive frequencies and their phase shifts between each arm of the dual-drive Mach-Zehnder modulator (DD-MZM) utilised are mapped to the STBC-activated antenna indices[1], where the switches and the power-thirsty DAC and ADC required in the RRHs for the conventional SM are eliminated, hence realising an energy-efficient A-RoF based C-RAN system relying on an optical processing aided SM-STBC scheme. To elaborate a little further, the STBC signal is directly modulated with the aid of several sets of laser diodes (LDs), and then it is fed into a DD-MZM, where the transmitting optical side-band is selected by the optical index of the drive-frequency and phase-shifters at each STBC symbol period[2]. Then, the modulated signal is carried over standard single-mode fiber (SSMF) and dispersion-compensation fiber (DCF), where the optical signal is passed to an erbium-doped fiber amplifier (EDFA) before being mapped to different antennas by the passive optical components of a wavelength-division-multiplexing demultiplexer (WDM-Demux), fiber Bragg grating (FBG) and then photo-detected to generate the electronic signal. Thus, each SM-STBC signal is processed in the CU using optical indices. We will detail the specifics of this design in Section 3.5.1.

[1]For Alamouti's code, a STBC-activated antennas is a pair of antennas for transmitting STBC symbols.

[2]In Alamouti's code, a STBC symbol period refers to two symbol periods.

Thus, the proposed system amalgamates the SM-STBC scheme with A-RoF techniques, hence constituting an adaptive C-RAN system controlled by the KNN algorithm. The novel contributions of this section are as follows:

1. We propose an A-RoF aided optical processing based SM-STBC encoding schemes where an optical index constituted by the DD-MZM's drive frequency and their phase shifts eliminates the need for any actively-powered switches, which would be inevitably required by the wireless SM scheme as well as dispensing with the power-thirsty DACs and ADCs in the RRHs.

2. Our system may be readily invoked for adapting the number of RRHs supporting a single user, simply using a laser bank. Furthermore, the proposed adaptive C-RAN system is controlled by a learning-assisted technique, capable of near-instantaneously adapting the number of RRHs as well as the modulation techniques employed. Moreover, the proposed system is capable of achieving a higher data rate than that of the classic threshold-based adaptation.

3. The proposed system concept was inspired by our A-RoF aided twin-antenna SM experimental study of Section 3.4 [28]. However, the system advocated is capable of supporting MIMO having a variable number of antennas by using direct modulation and extra optical indices, where any arbitrary number of transmitter antennas can be supported, while STBC is invoked for the sake of achieving transmit diversity.

The aim of this chapter is to design a low-cost and low-complexity A-RoF aided SM arrangement, where we invoke optical signal processing for implementing SM encoding supporting our C-RAN system design.

3.4 Experimental Characterisation of the Radio Over Fiber Aided Twin-Antenna SM Downlink

3.4.1 Proposed A-RoF-aided SM System

In this section, we will introduce our A-RoF-aided twin-antenna SM system design and present our simulation-based performance analysis. This can be considered as a potential application of C-RAN for enabling simplified and energy-efficient SM. The C-RAN application will be discussed in Section 3.5, followed by the feasibility study of this section.

3.4.1.1 Conventional Twin-antenna SM Scheme

In the conventional SM scheme, the transmitted data is firstly split into two streams, as shown in Fig. 3.2, where the upper stream corresponds to the implicitly conveyed information used for antenna selection, while the lower stream to the classic modulated symbol transmission, namely quaduature amplitude modualation/phase shift keying (QAM/PSK). As shown in Fig. 3.2, the switch activating the specific antenna used for wireless transmission relies on the antenna selection information assigned to the upper stream of Fig. 3.2. For example, a twin-antenna SM scheme requires one-bit of information to control the switch-option, where a logical 1 can activate antenna 1 while a logical 0 activates antenna 2 corresponding to the lower side-band and upper side-band in our system to be elaborated on in the next section. Generally speaking, a classic N-bit information symbol can be conveyed over the lower stream of Fig. 3.2. At the receiver side, the classic symbols as well as the antenna selection symbols can be jointly interpreted by maximum likelihood (ML) detection [118].

Instead of implementing the SM encoding scheme at each RRH, which adds extra complexity constituted by the antenna-switches, we propose an A-RoF system, which optically encodes the SM symbols in a CU with the aid of centralised processing, where the actively-powered switches are replaced by the passive optical components of the RRHs. As a benefit, we can dispense with power-thirsty high-precision DAC and ADC in the RRHs. Note that the number of passive optical components required in the

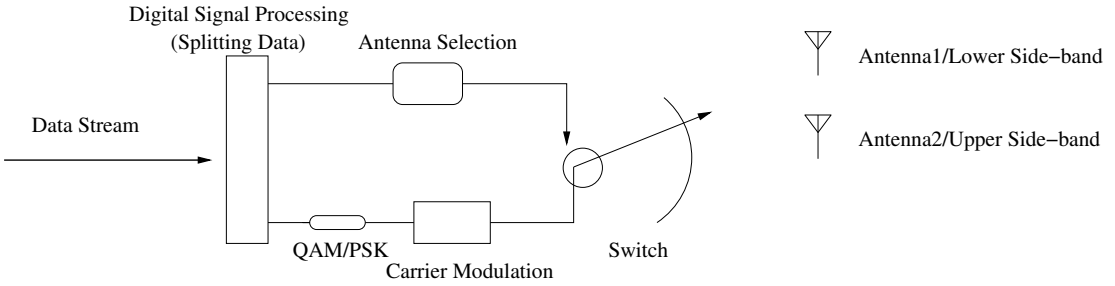

Figure 3.2: Conventional twin-antenna SM scheme adapted to side-band-switching.

RRHs increase linearly with the number of RRHs, however, as a benefit of the low-power RRHs proposed, we conceive an energy-efficient and cost-efficient A-RoF-aided fronthaul system. Next, we detail our A-RoF-aided system design and characterise it.

3.4.1.2 Proposed A-RoF-aided SM Design

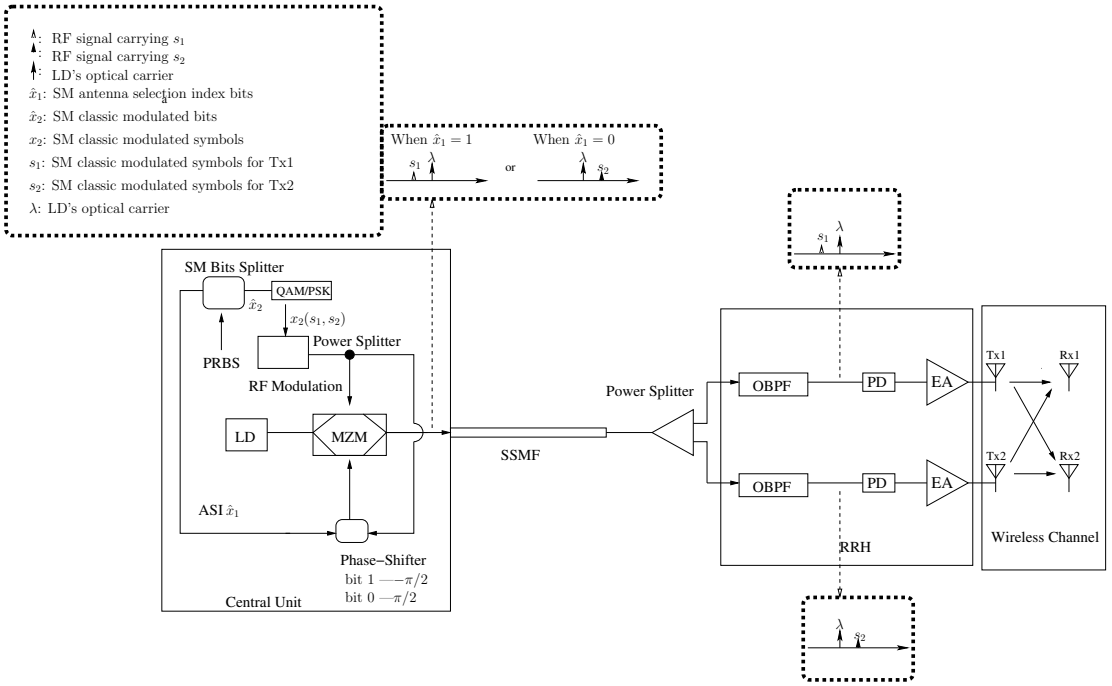

Figure 3.3: System schematic of A-RoF-aided twin-antenna SM downlink system. PRBS: Pseudorandom Binary Sequence, ASI: Antenna Selection Information, DSP: Digital Signal Processing, LD: Laser Diode, RF: Radio Frequency, MZM: Mach-Zehnder Modulator, OBPF: Optical Bandpass Filter, PD: Photo Detector, EA: Electronic Amplfier, RRH: Remote Radio Head, Tx: Transmitter, Rx: Receiver.

Let us now consider our A-RoF-aided twin-antenna SM system shown in Fig. 3.3, where we show both the A-RoF link and the wireless link. In our system, we externally modulate the radio frequency (RF) signal into the optical carrier (OC) generated by a LD using a dual-drive MZM, which can be set to operate in a specific OSSB mode during each symbol period. The OSSB signal can be generated by setting the phase difference of the RF signal in both arms of the MZM to $\pi/2$ or $-\pi/2$, where one of the first-order side-bands would be suppressed [116, 117]. Specifically, to centralise the SM encoding, phase-controlled side-band suppression is exploited. As discussed and experimentally verified in [116, 117], by imposing a phase-difference of $\pi/2$ or $-\pi/2$ between each arm of a DD-MZM, one of the first-order side-bands of the modulated optical signals will be suppressed. We exploit a dual-drive MZM to interpret specific side-band used as the antenna selection index of SM. As shown in Fig. 3.3, a phase-shifter is employed to change the phase-difference of the MZM's arms of Fig. 3.3 to either $-\pi/2$ or $\pi/2$.

In our design, as shown in Fig. 3.3, a pseudorandom binary sequence (PRBS) input is split into the SM antenna selection index bits $\hat{x}_1$ and the SM classic modulated bits $\hat{x}_2$, where $\hat{x}_1$ controls the phase-shifter of Fig. 3.3 and $\hat{x}_2$ is mapped to the classic QAM/PSK symbols x_2. The symbols x_2 are then carried by a RF signal, which is power-split to both MZM arms and used as the drive voltages of the dual-drive MZM of Fig. 3.3. Furthermore, the side-band selection process, which corresponds to the antenna selection in conventional wireless SM, is detailed in Fig. 3.4. As shown in Fig. 3.4, when the antenna selection bit 1 is transmitted, the phase shift $-\pi/2$ is chosen, which maps the QAM/PSK-modulated RF signal to the lower side-band, while the antenna selection bit 0 encodes it to the upper side-band of the optical carrier generated by the LD of Fig. 3.3, which corresponds to a phase shift of $\pi/2$.

Following the SM encoding and the transmission of the signal through a SSMF, the optical signal is power-split and fed into two different lines, where the upper line retains the lower side-band and the bottom line obtains the upper side-band using an optical bandpass filter (OBPF), as shown in Fig. 3.3. Then, the filtered optical signal of each line will be converted to the corresponding electronic signal and passed through electronic amplifiers (EAs) for amplification, where the symbols s_1 conveyed by the lower side-band are carried by an RF signal and feed the transmitter (Tx) antenna 1 (Tx1), while the symbols s_2 conveyed by the upper side-band feed the Tx antenna 2

(Tx2). Subsequently, the SM symbols mapped to the RF signals are transmitted over the wireless channel without any signal processing in the RRHs of Fig. 3.3. Thus, our SM antenna selection information selects the antennas using our new side-band selection technique, while classic symbols are mapped to the corresponding side-band and converted to RF signals. To elaborate a little further, Figs. 3.5 and 3.6 shows the OSSB power spectral density (PSD) of the A-RoF-aided SM signal after each OBPF of the RRH of Fig. 3.3, where the left plot corresponds to the bit-1-selected lower side-band conveying information to Tx1 of Fig. 3.3, while the upper side-band shown in the right plot is the bit-0-selected signal conveying information to Tx2. The central frequency of 200 GHz shown in Fig. 3.5 and 3.6 is selected for the convenience of simulation, which is relative to 193.1 THz.

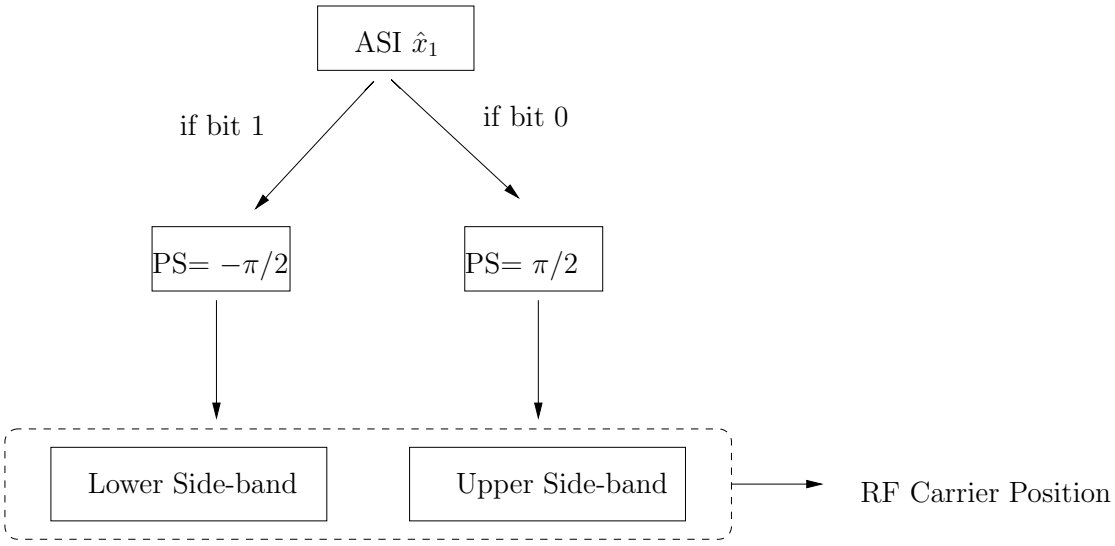

Figure 3.4: Side-band selection. ASI: Antenna Selection Information, PS: Phase Shift.

As a benefit, any electronic digital signal processing as well as SM encoding switches can be completely eliminated in the RRHs of Fig. 3.3. Furthermore, the OBPFs on each line of the RRHs of Fig. 3.3 are utilised to select the required side-band for each antenna. Through side-band filtering, the output of each branch in the RRH of Fig. 3.3 is passed to the corresponding antennas for SM transmission. Thus, the passively preset OBPFs of Fig. 3.3 are capable of replacing the function of actively-powered switches, hence substantially reducing both the system complexity and the power consumption imposed on the RRHs.

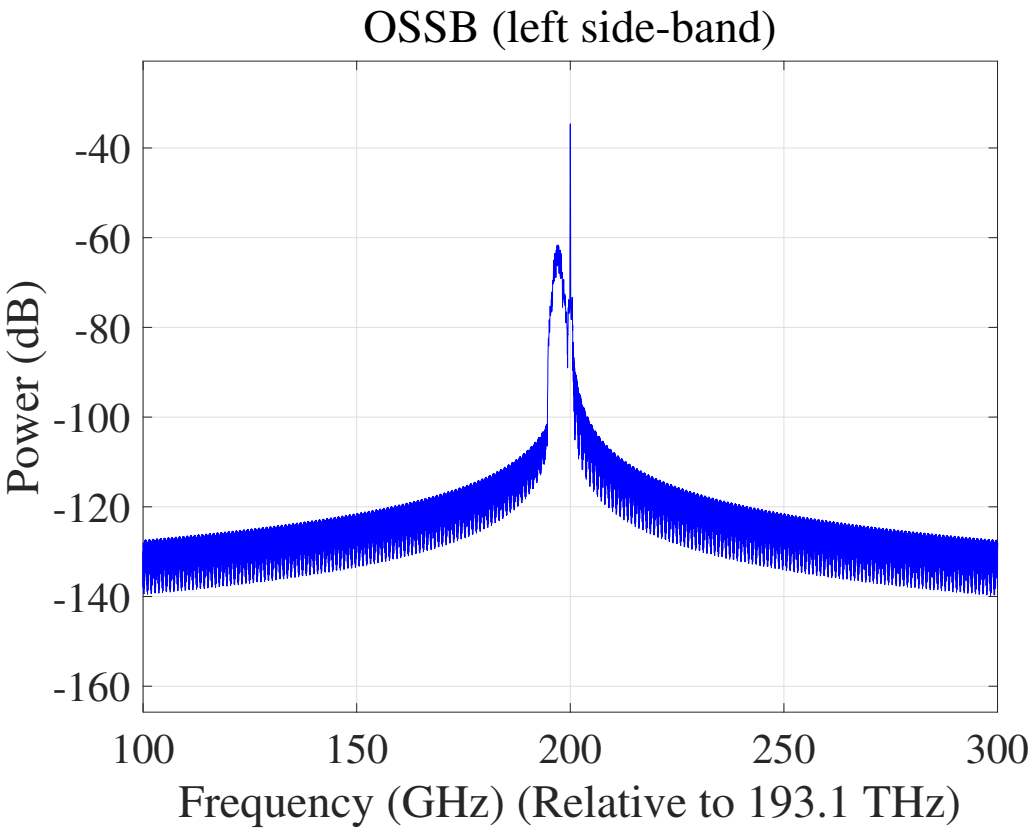

Figure 3.5: PSD of the OSSB for side-band selection (Left Side-Band).

3.4.1.3 Performance Characterisation

Prior to experimental verification, the proposed system was simulated using MATLAB. In our simulations, an RF frequency of 3 GHz was externally modulated by an optical carrier of 1550 nm. The split-step Fourier method was used as our channel model [90].

A convolutional code having a code rate of 1/2, a constraint length of 7 and generator polynomials of (171,133) (in octal) was used. As shown in Fig. 3.3, the classic modulated bits are mapped to BPSK symbols. The classic modulated BPSK symbol is then mapped to the lower side-band of the LD's optical carrier of Fig. 3.3 when a logical one antenna-selection information is applied and vice versa. This is carried by controlling the phase-shifter of Fig. 3.3 by $\pi/2$ or $-\pi/2$. Then, the SM encoded optical signal is transmitted over a 20 km SSMF, where a power splitter is imposed after the fiber transmission in order to extract the side-band information for mapping to the corresponding antennas. Afterwards, the preset OBPF, photo detection (PD) and EA filters the signal and converts the optical signal to 3 GHz RF signal. Thus, the RF signal carrying the

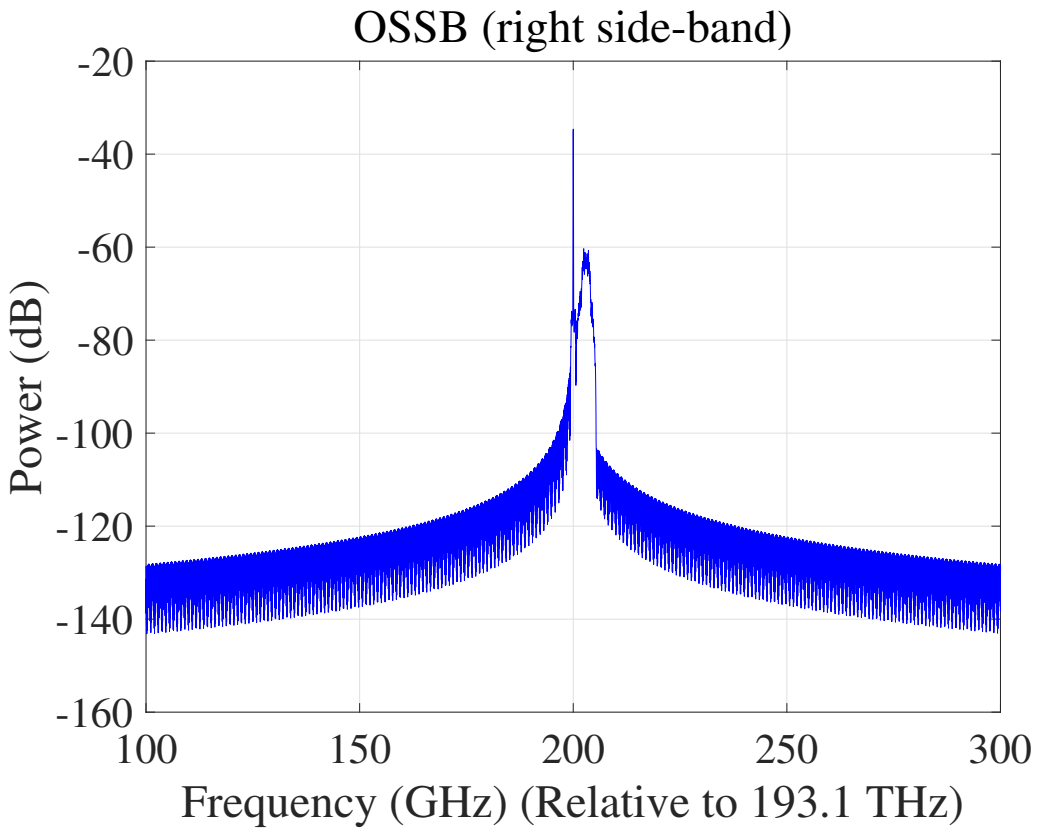

Figure 3.6: PSD of the OSSB for side-band selection (Right Side-Band).

SM symbols is transmitted from the two antennas. In the wireless link, we simulated a Rayleigh-fading channel and we employed ML detection [118].

Fig. 3.7 shows the bit error ratio (BER) performance of a 2×2 SM scheme employing our A-RoF-aided design, which is compared to a 'wireless-only' SM scheme operating without the A-RoF link for the sake of showing the feasibility of intrinsically amalgamating SM with our proposed A-RoF system. The 'wireless-only' SM scheme represents the conventional SM scheme, when only wireless transmission is considered and no A-RoF link is involved. The wireless channel used is a Rayleigh-fading channel. The SNR indicated in Fig. 3.7 is the wireless SNR, where we show that our A-RoF-aided SM system has modest impact on the system's performance. Additionally, our 2×2 SM prototype scheme can be readily extended to an arbitrary number of receive antennas. Based on the analysis above, we will experimentally characterise our system and the experiment will be detailed in the next section.

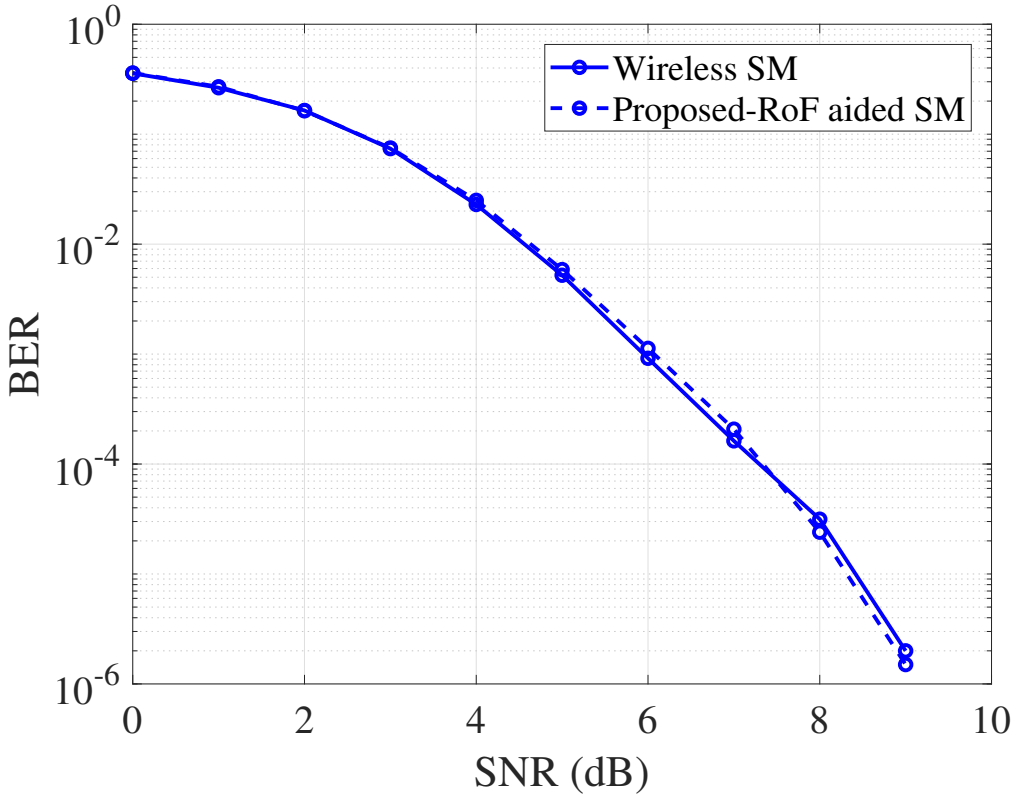

Figure 3.7: Simulated BER performance of proposed A-RoF-aided twin-antenna SM system.

3.4.2 Experimental Setup

To further verify our proposed system, we have demonstrated our system design as shown in Fig. 3.8. The dual-drive MZM used is of 40 Gbps relying on the Model T.DEH1.5-40PD-ADC from SUMITOMO OSAKA CEMENT. A SSMF of 20 km is utilised. The input power of the fiber is 1.5 dBm.

In our experiment, the RF signals are fed into the MZM of Fig. 3.8 for side-band selection, which are processed in MATLAB offline on a computer and then generated by an arbitrary waveform generator (AWG). Specifically, we generated a pair of BPSK-modulated RF carriers at 3 GHz in MATLAB. Then, one of the RF signals is phase shifted by $\pi/2$ or $-\pi/2$ according to the SM antenna selection bits $\hat{x_1}$, with both of the offline-processed signals being entered into an AWG operated at 12 GSamples/s to drive each arm of the dual-drive MZM for the sake of side-band selection. As a result, the signal driving the bottom arm of Fig. 3.8 is phase-shifted off-line in MATLAB for SM

Parameter	Value
Bit rate	2 Gbps (with convolutional code)
RF drive signal	3 GHz
LD center wavelength	1550.134 nm
Optical power before MZM modulation	9.35 dBm
MZM DC bias	2.68 V
Input power of fiber	1.5 dBm
Fiber type	Standard single-mode fiber at 1550 nm
Fiber length	20 km
Modulation type	BPSK
OBPFs central wavelength	1550.174 nm and 1550.094 nm
OBPFs 3 dB bandwidth	0.114 nm
PD data bandwidth	10 Gbps
LPF cutoff frequency	3.9 GHz
Wireless channel	Rayleigh-fading Channel
Wireless detection	Maximum likelihood detection

Table 3.1: Experimental Parameters.

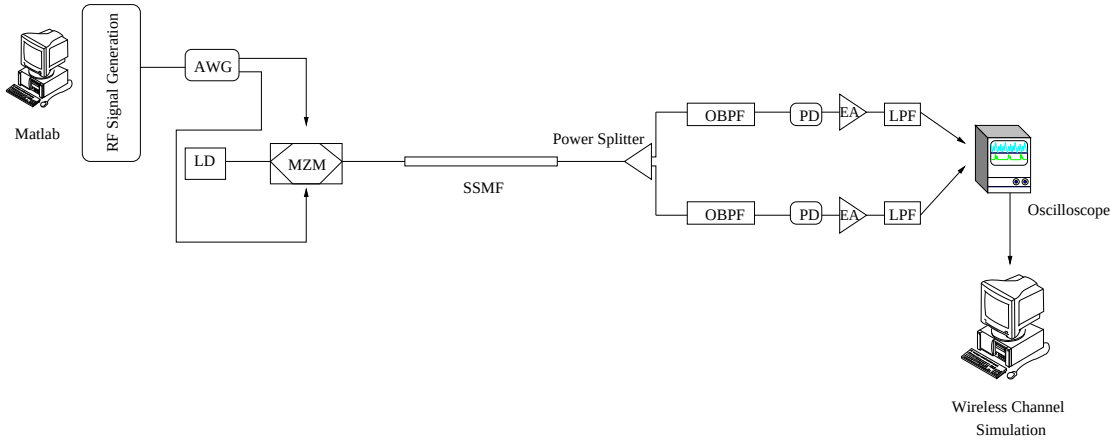

Figure 3.8: Experimental setup.

encoding, thus ensuring that the phase-difference of the drive signal of each arm remains either $\pi/2$ or $-\pi/2$. After the side-band selection by MZM of Fig. 3.8, the signal is transmitted over a 20 km SSMF. At the fiber's receiver side, after OBPF, PD, EA and a low pass filter (LPF), the signal of each branch of Fig. 3.8 is passed to an oscilloscope, where we visualise the output signal for a 2×2 SM MIMO analysis. The normalised signal of the oscilloscope is exploited as the wireless input signal simulated in MATLAB. Again, the wireless channel is simulated as a Rayleigh-fading channel and ML detection is used at the wireless receiver side. The stylized real-world implementation is portrayed in Fig. 3.3. In our experiment, we opted for implementing the critical components of our proposed design, while the associated large-scale wireless system and some of the

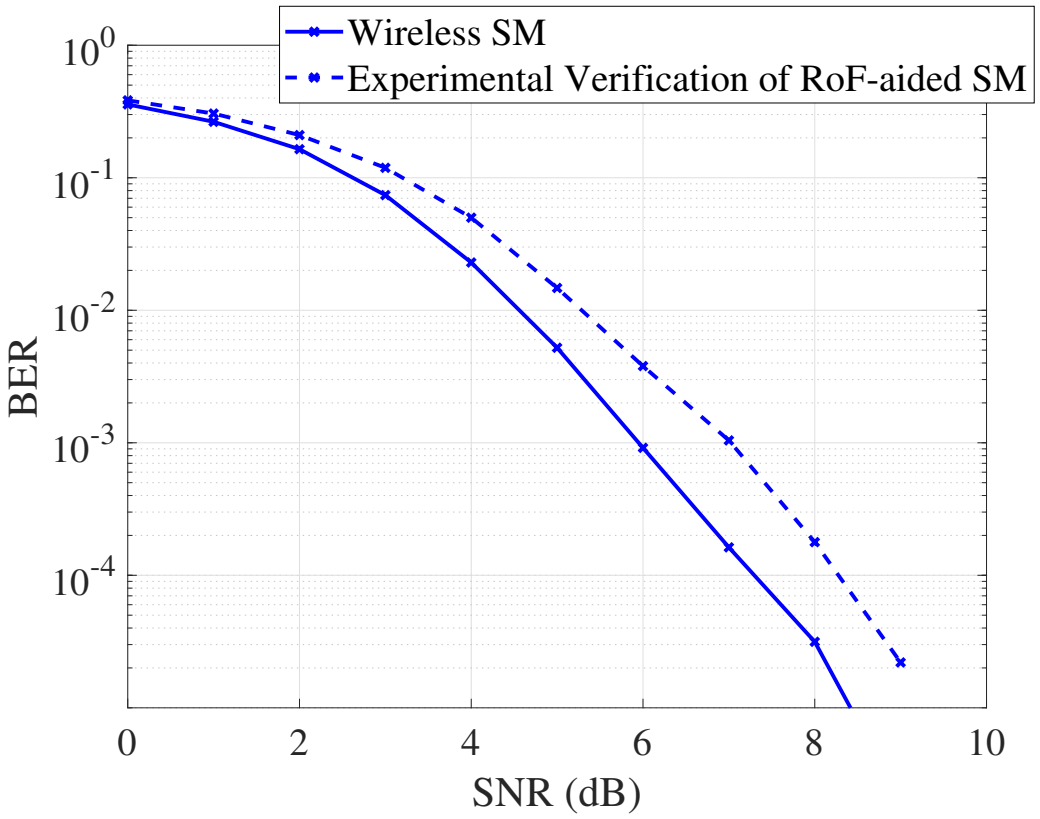

Figure 3.9: Experimental demonstration BER of proposed A-RoF-aided twin-antenna SM BER performance.

electronic devices, such as the phase-shifter of Fig. 3.3, were simulated in MATLAB. The parameters of this experiment are shown in Table 3.1 and the demonstration system is portrayed in Fig. 3.8.

As demonstrated in Table 3.1, a convolutional code having a code rate of 1/2, a constraint length of 7 and generator polynomials of (170,133) (in octal) is used in our system. To show the effect of our proposed system on the BER performance, we also plotted in Fig. 3.9 the 'wireless-only' SM BER curve as well as the experimental A-RoF-aided twin-antenna SM system BER, where we show that the experimental results exhibit about 1 dB degradation at the BER of 10^{-4} compared to the simulation results of the 'wireless-only' SM without A-RoF as well as that with A-RoF of Fig. 3.7. This disparity is partially caused by the phase noise introduced by the optical components and by the frequency leakage of the OBPFs used. Nonetheless, given that only 1 dB degradation is observed at BER of 10^{-4}, we realised a A-RoF-aided twin-antenna SM

system, dispensing with both digital processing and with actively-powered SM switches in the RRH, resulting in an energy-efficient A-RoF-aided SM system.

In the next section, we extend the above scheme, where a scalable SM-STBC scheme is implemented in a learning-assisted adaptive C-RAN system.

3.5 Analogue Radio Over Fiber Aided SM-STBC for the Learning Assisted Adaptive C-RAN Downlink

In Section 3.4, we proposed and experimentally verified the operating principle of our A-RoF aided SM scheme by using a side-band selection philosophy, which was restricted to two transmitter antennas. As described in Section 3.3 and inspired by the proposed OSSB selection method conceived for SM antenna index mapping, we propose another side-band selection aided SM encoding in Section 3.5.1, which is capable of supporting any arbitrary number of SM transmitter antennas per RRH, where we implemented Alamouti's STBC for improving the diversity gain attained. As a further benefit of our flexible design, in Section 3.5.2 we design an adaptive system, where the number of RRHs supporting a single user as well as the modulation technique employed can be adaptively adjusted, where we also invoke a learning algorithm, namely the KNN for controlling the adaptation.

3.5.1 Proposed A-RoF Aided C-RAN System Model

In the context of our C-RAN and MIMO deployment, SM-STBC can be considered a cost-efficient technique of achieving a high throughput and a beneficial diversity gain. To dispense with the power-thirsty antenna switches as well as with the DAC and ADC in the RRHs of the C-RAN system, in this section, we present our A-RoF aided SM-STBC scheme conceived for a C-RAN, where the SM-STBC processing is carried out optically relying on the optical carrier index. Fig. 3.10 shows a generic fiber-based C-RAN system, where a CU performs most of the signal processing, while the RRHs contain some passive optical components for supporting the associated radio functions.

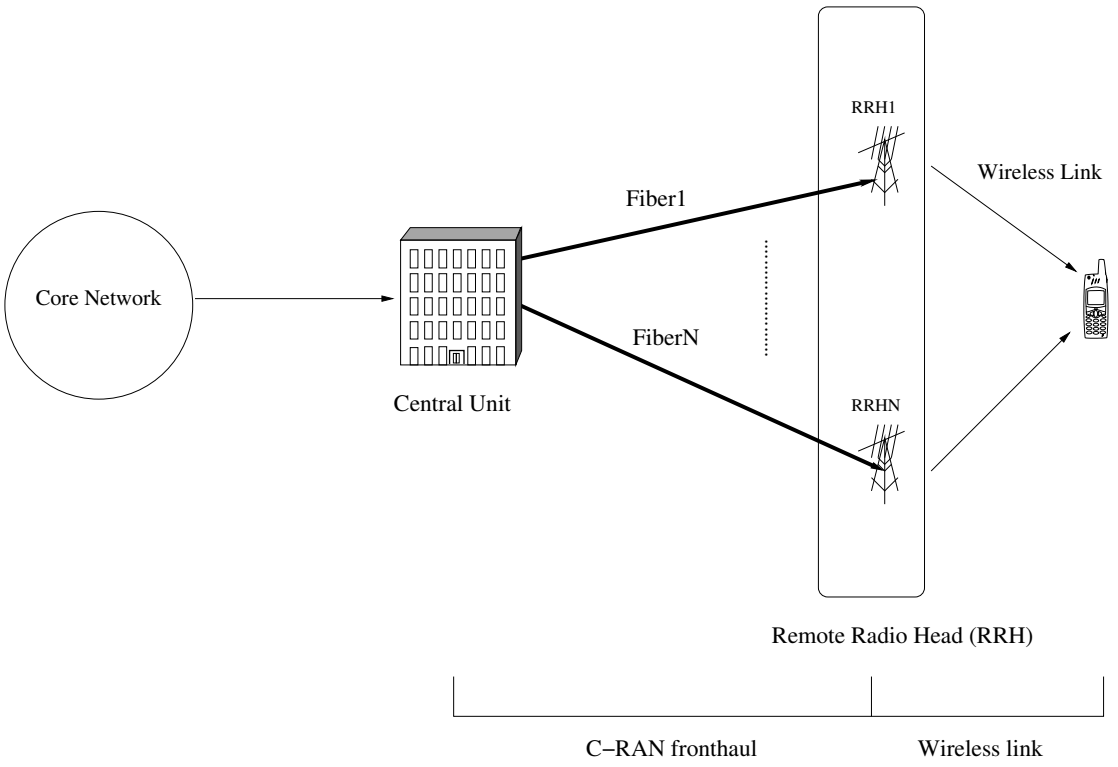

Figure 3.10: An A-RoF aided C-RAN system.

Let us now consider a C-RAN system, employing our A-ROF aided SM-STBC design shown in Fig. 3.11, where the schematic of our C-RAN fronthaul design and the wireless link are shown. The proposed system relies on an optical solution for selecting the specific side-band which corresponds to different STBC-activated antennas. This is achieved without employing any actively-powered SM switches and power-thirsty ADCs and DACs. Hence, as shown in Fig. 3.11, the STBC signal is directly modulated by a set of LDs referred to as a laser bank, resulting in an optical double side-band (ODSB) signal, where each side-band carrying Alamouti's STBC streams[3] is mapped to each antenna of each RRH. Explicitly, each of the STBC symbols is carried by one of the side-bands of the ODSB-STBC signal, which is then mapped to an antenna at the RRH. Then, with the side-band selection[4] performed by controlling the drive-frequency and the phase shifter of the DD-MZM of Fig. 3.11, only a single ODSB-STBC signal carrying the Alamouti's code will be transmitted over the fiber at each STBC symbol period,

[3]Here, we refer to the directly modulated ODSB signal carrying the STBC symbols in this stage as the **ODSB-STBC signal** for clarifying our side-band selection process.

[4]To clarify, the "side-band" in this side-band selection refers to a single ODSB-STBC signal generated by direct modulation of Fig. 3.11, because the ODSB-STBC signal would be viewed as the side-band of an optical carrier after MZM modulation.

where the side-band selection process would be detailed later in Section 3.5.1.2. At the fiber receiver of Fig. 3.11, an EDFA is invoked for optical amplification, while some passive optical components such as a WDM-Demux and FBG are used for side-band to antenna mapping. The WDM-Demux separates each ODSB-STBC signal, and the FBG divides each side-band of the ODSB-STBC signal carrying Alamouti's STBC stream and then passes it on for optic-to-electro (O/E) conversion and electronic amplification (EA). Then, each side-band of the ODSB-STBC signal carrying Alamouti's code is mapped to each STBC-activated antenna of Fig. 3.11. Note that owing to the side-band selection's capability to transmit a single ODSB-STBC signal at each SM-STBC symbol period, only a pair of the STBC-activated antennas of Fig. 3.11 would transmit the modulated data during each SM-STBC symbol period, while the remaining antennas remain inactive.

Additionally, we propose an adaptive design, where the number of RRHs supporting a user as well as the modulation technique used per user is adapted. As shown in Fig. 3.11, the block performing both the STBC scheme and the direct modulation (DM) scheme, where in Fig. 3.11 we refer to as "STBC & SD (SD)", is capable of adapting the number of connected RRHs by assigning the STBC symbols to each SD_RRHx, hence realising a flexible adaptive C-RAN system, which we will control by invoking a learning algorithm in Section 3.5.2. This section will only elaborate on our A-RoF aided C-RAN design.

In the proposed design of Fig. 3.11, the CU performs digital modulation, optical processing aided SM-STBC encoding, radio carrier modulation, electro-to-optic (E/O) conversion and C-RAN RRHs adaptation control, while the RRH implements the associated radio functions (filtering, O/E conversion, photo detection, amplifying and radio transmission), thereby substantially simplifying the transceiver design in the RRH by beneficially centralising the digital processing in the CU.

3.5.1.1 Wireless SM-STBC Scheme

Prior to discussing our proposed C-RAN design, we will introduce the wireless SM-STBC architecture. SM is a cost-efficient MIMO scheme, where only one of the transmit antennas is activated each symbol period, thus commensurately reducing both the number

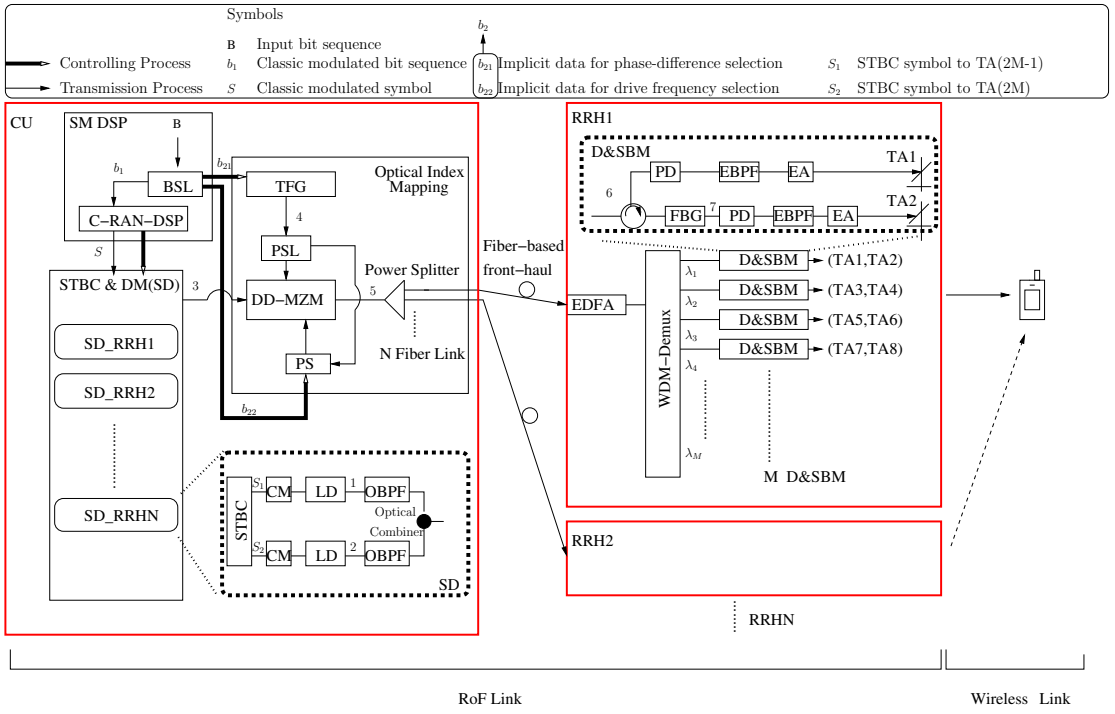

Figure 3.11: Proposed A-RoF aided adaptive C-RAN system.

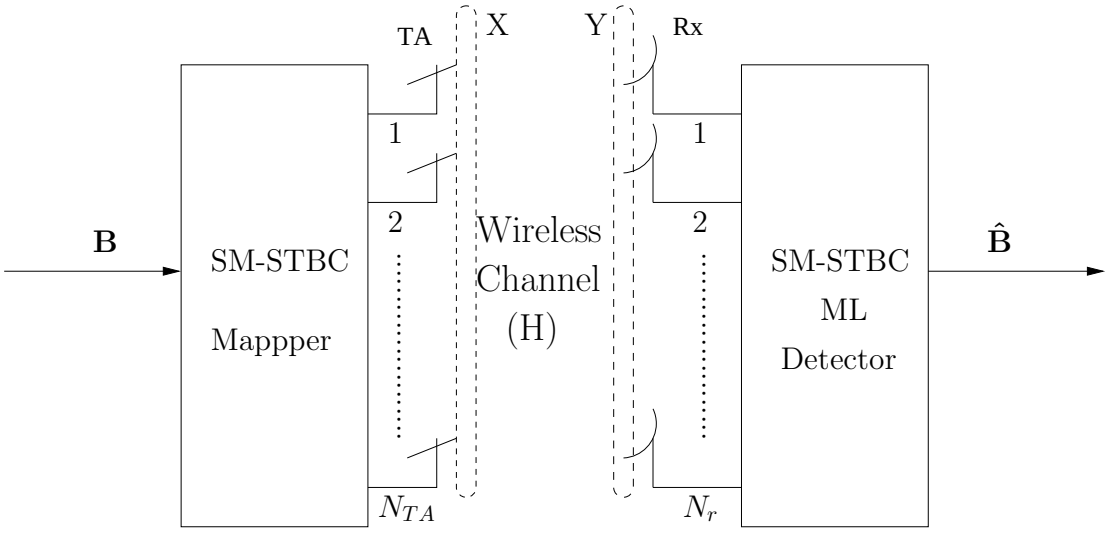

Figure 3.12: Wireless SM-STBC scheme.

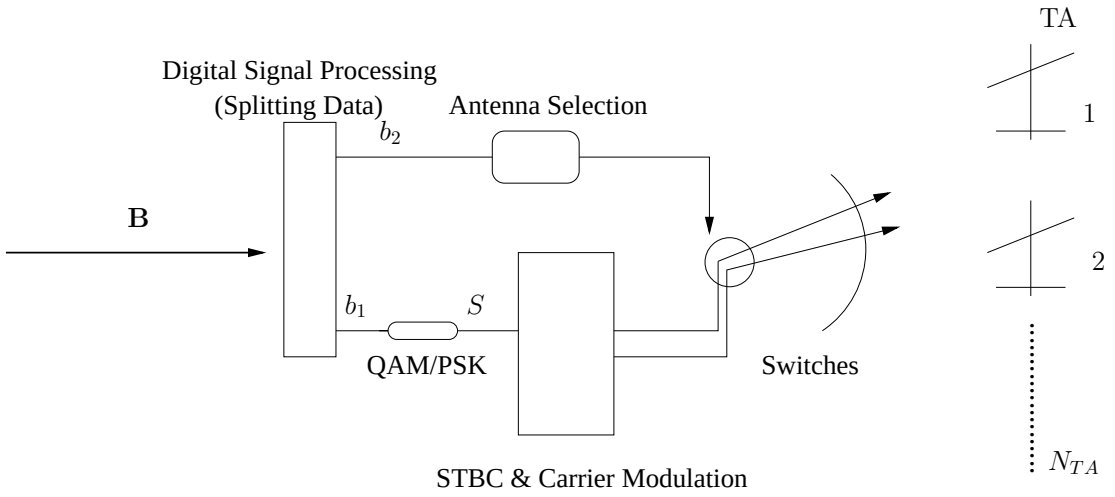

Figure 3.13: Wireless SM-STBC mapper.

of RF chains and the ICI. The antenna index and the transmitted symbols are jointly detected at the receiver. In this context, STBC is amalgamated with SM for the sake of attaining a diversity gain. Fig. 3.12 shows the wireless SM-STBC scheme, where $\mathbf{B}$ is the transmitted input bit sequence, $\hat{\mathbf{B}}$ is the detected bit sequence, N_{TA} is the number of transmitter antennas (TA) and N_r is the number of receiver antennas (RAs). In this section, an Alamouti STBC stream is transmitted by activating a pair of the TAs of Fig. 3.12 during two consecutive symbol periods, jointly forming an STBC symbol period. The statistical SM-STBC model is as follows:

$$\mathbf{Y} = \mathbf{HX} + \mathbf{N}, \tag{3.1}$$

where $\mathbf{H}$ is the MIMO channel matrix of size $(N_r \times N_{TA})$, $\mathbf{X} = [\mathbf{x_1}, \mathbf{x_2}]$ is the transmitted input SM-STBC matrix of size $N_{TA} \times 2$ with the ith column $\mathbf{x_i}$ denoting the symbol vector transmitted over the ith symbol time of a STBC block[5]. Furthermore, $\mathbf{N} = [\mathbf{n_1}, \mathbf{n_2}]$ denotes the $N_r \times 2$ noise matrix, with the ith column $\mathbf{n_i}$ denoting the receiver noise vector over the ith symbol period of a STBC symbol period. $\mathbf{Y}$ is the received symbol matrix of size $Nr \times 2$, where $\times 2$ denotes two symbol periods. To elaborate a little further, Fig. 3.13 shows the SM-STBC mapping process, where the input data vector $\mathbf{B}$ is split into two streams, namely b_1 and b_2, where the classic modulated data b_1 is QAM/PSK-modulated for transmission and the antenna selection index b_2 performs the antenna switching to the corresponding TAs [105, 7]. The classic modulated symbols S

[5]Each STBC block utilises two symbol periods and we refer to this as STBC symbol period.

are transmitted to the corresponding pair of TAs after the STBC processing and radio carrier modulation. For example, if $\mathbf{B} = \{b_1, b_2\} = \{1, 0, 0\}$, we obtain $b_1 = \{1, 0\}$, which is BPSK-modulated to $S = \{1, -1\}$, while $b_2 = 0$ is used for simultaneously selecting TA1 and TA2 for transmission within a STBC symbol period. Explicitly, after STBC encoding, at the first symbol period, symbol 1 feeds TA1 while -1 feeds TA2. At the second symbol period, symbol -1 feeds TA1 and symbol -1 feeds TA2. Given that at least two RF chains are required to feed a pair of TAs in the proposed SM-STBC scheme, a switch is required to simultaneously control the selected two TAs, enabling the SM-STBC mapping. Following the SM-STBC antenna selection, the vector $\mathbf{X}$ of Equation 3.1 is denoted by:

$$\begin{bmatrix} 0 & 0 \\ 0 & 0 \\ . & . \\ . & . \\ s_1 & -{s_2}^* \\ s_2 & {s_1}^* \\ 0 & 0 \\ . & . \\ 0 & 0 \end{bmatrix},$$

where

$$\begin{bmatrix} s_1 & -{s_2}^* \\ s_2 & {s_1}^* \end{bmatrix}$$

represents an Alamouti STBC transmitted from the SM-STBC activated-TAs. Furthermore, at the receiver, the classic optimal ML detection [118] is used for jointly detecting both the antenna selection index and the transmitted data.

Based on the above SM-STBC scheme and the C-RAN system, we invoke A-RoF techniques for optically processing the SM-STBC using the optical carrier index mapped to each TA of Fig. 3.11, where the power-thirsty SM switches, DAC and ADC are eliminated in the RRHs. This concept results in an energy-efficient C-RAN system combined with optical processing aided MIMO signal generation. Next, we will detail the proposed A-RoF aided C-RAN fronthaul design.

3.5.1.2 A-RoF Aided C-RAN Fronthaul Design Using SM-STBC

In this section, we present our system as an energy-efficient and low-complexity mobile fronthaul solution capable of maintaining the BER performance of the above-mentioned wireless SM-STBC scheme.

Fig. 3.11 shows the schematic of our proposed system design, comprising both a RoF link and a wireless link. In this section we focus our attention on the fiber-based fronthaul design. The SM-STBC encoding process is confined to the CU of Fig. 3.11, where the ODSB-STBC signal controlled both by the optical index of the phase-shifter and by the drive frequencies of the DD-MZM of Fig. 3.11 is mapped to each of the activated STBC antennas of Fig. 3.11. As shown in Fig. 3.11, the fiber-based fronthaul connects the CU and the RRHs.

To be more explicit, the CU is constituted by three modules, namely the SM scheme's digital signal processing (SM-DSP), the STBC and direct modulation (STBC and DM) and the Optical Index Mapping. At the RRHs, the actively-powered switches used in Section 3.5.1.1 are replaced by a set of passive optical components, which will be detailed later in Section 3.5.1.2. In the following, we will describe our system based on an eight-TA system per RRH as an example.

SM Digital Signal Processing This module carries out the digital processing operations of SM signal generation, splitting the input bit sequence into index bit sequence for side-band selection and the classic transmitted bit sequence for generating STBC symbols. As shown in Fig. 3.11, the input bit sequence $\mathbf{B}$ is fed into a bit splitter (BSL) that outputs the pair of bit sequences b_1 and b_2, where b_1 is used for QAM/PSK classic modulation and b_2 controls the optical index of the side-band which corresponds to each TA of the RRH. In our proposed system b_2 is further split into b_{21} and b_{22}. In contrast to the antenna index b_2 of Fig. 3.13 used in the wireless SM-STBC described in Section 3.5.1.1, the optical index is related to the phase shift between each arm as well as to the drive frequency of the DD-MZM of Fig. 3.11, which are controlled by b_{22} and b_{21}, respectively. For example, if we aim for an eight-TA SM-STBC scheme transmitting $\mathbf{B} = \{b_1 = \{0, 1\}, b_2 = \{1, 1\}\}$, where $\mathbf{B}$ is a binary sequence, b_1 is BPSK-modulated into $S = \{-1, 1\}$, which is processed for STBC transmission, while b_2 is further split

into $b_{21} = \{1\}$ and $b_{22} = \{1\}$ for the sake of tuning the drive frequency of the tunable frequency generator (TFG) of Fig. 3.11 and controlling the phase-shifter (PS) of Fig. 3.11 for ODSB-STBC signal side-band selection corresponding to eight different TAs. Note that the SM-STBC system employing eight antennas will require two bits to select one out of the four possible twin-antenna combinations, hence b_{21} and b_{22} are constituted by a single bit[6]. The C-RAN-DSP of Fig. 3.11 performs the classic QAM/PSK modulation and centrally processes the data stream transmitted to each RRH using the laser bank in the STBC & DM block of Fig. 3.11. The mapping rule and its rationale will be discussed in the Paragraphs "**Optical Index Modulation**" and "**Remote Radio Head**" of Section 3.5.1.2.

STBC and DM As shown in Fig. 3.11, this module consists of a laser bank performing STBC encoding, radio carrier modulation and optical direct modulation. Again, we use an eight-TA SM-STBC scheme as an example for illustration. More specifically, the classic modulated symbol S is assigned to the STBC and DM (SD) block of Fig. 3.11 for STBC processing[7], where S_1 and S_2 are the STBC symbols transmitted to a pair of STBC-activated TAs of RRH1 of Fig. 3.11. Then, as shown in Fig. 3.11, S_1 and S_2 are carried by a RF of frequency f_{RF} via carrier modulation, followed by the LD's direct modulation, whose spectra is shown in Stage 1 and Stage 2 of Fig. 3.14. The optical bandpass filters (OBPFs) of the SD then retain each side-band containing either S_1 or S_2 to form a new ODSB, as shown in Stage 3 of Fig. 3.14 using an optical combiner, where S_1 and S_2 are modulated to each side-band of the new ODSB of stage 3 of Fig. 3.14, where we will refer to the ODSB carrying S_1 and S_2 as ODSB-STBC signal for distinguishing them from our DD-MZM side-band selection process in Section 3.5.1.2. Again, the side-band described in the DD-MZM side-band selection can be viewed as a single ODSB-STBC signal, because the ODSB-STBC signal of Stage 3 of Fig. 3.14 is shifted away from an optical carrier and becomes its side-band, as shown in Stage 5 of Fig. 3.14. Then, the resultant ODSB of Stage 3 seen in Fig. 3.14 is fed into the optical index mapping block for side-band selection.

[6]For 2M-TA system, b_{21} represents 1-bit information, while b_{22} represents $(\log_2(\mathrm{M}) - 1)$-bit information.

[7]In this example, only single SD module is required for connecting a single RRH. However, the data transmitted to each RRH corresponds to each SD seen in Fig. 3.11.

Side-band central wavelength	Corresponding TA index	PS index	TFG index
λ_1	(TA1, TA2)	1	1
λ_2	(TA3, TA4)	1	0
λ_3	(TA5, TA6)	0	0
λ_4	(TA7, TA8)	0	1

Table 3.2: The A-RoF aided eight-TA SM-STBC mapping scheme. Phase Shifting Index, -$\pi/2$ (bit 1); $\pi/2$ (bit 0). Drive Frequency Index, f_{drive_1} (bit 0); f_{drive_2} (bit 1).

Optical Index Mapping This module performs the main function of optical index mapping, where the optical index is characterised both by the phase-difference between the drive signal fed into each arm of the DD-MZM and by the DD-MZM's drive frequency, where the locations of the ODSB generated in Stage 3 of Fig. 3.14 are mapped to different pairs of TAs in Fig. 3.11. The optical index mapping is mainly performed via changing the phase difference by either $\pi/2$ or $-\pi/2$ between the signal driving the two arms of the DD-MZM and via tuning the drive frequency f_{drive} [116].

Based on our previous experimental feasibility study of the RoF aided twin-antenna SM using side-band selection [28], we are capable of extending our design to any arbitrary number of TAs to support multiple SM schemes. More specifically, the side-band location relies on both the drive frequency controlled by b_{21} and on the phase shifting tuned by b_{22}, as shown in Fig. 3.11. As verified experimentally and analysed in the literature [116, 28], a phase difference of either $\pi/2$ or -$\pi/2$ between the two drive frequencies of the DD-MZM is capable of moving the ODSB-STBC signal to either the upper side-band or to the lower side-band of the optical carrier of the MZM, while changing the drive frequencies is capable of shifting away the ODSB-STBC signal from the optical carrier of DD-MZM by a frequency spacing of f_{drive}.

Again, considering an eight-TA based SM-STBC scheme, b_{21} is used for controlling the TFG, where the architecture is shown in Fig. 3.15, shifting the side-band to different frequencies. In our system, we use a flexible TFG, which is evolved from our previously proposed TFG of [19]. As shown in Fig. 3.15, the MZM driven by an unmodulated drive frequency of 15 GHz is invoked for generating a multi-wavelength signal. Following the WDM-Demux and b_{21}-controlled DSP block of Fig. 3.15 selecting the beating wavelength, the spectra containing λ_a and λ_b is retained and converted to the specific radio frequency of f_{drive}. Explicitly, if the drive signal $f_{drive_1} = 30$ GHz of Fig. 3.15

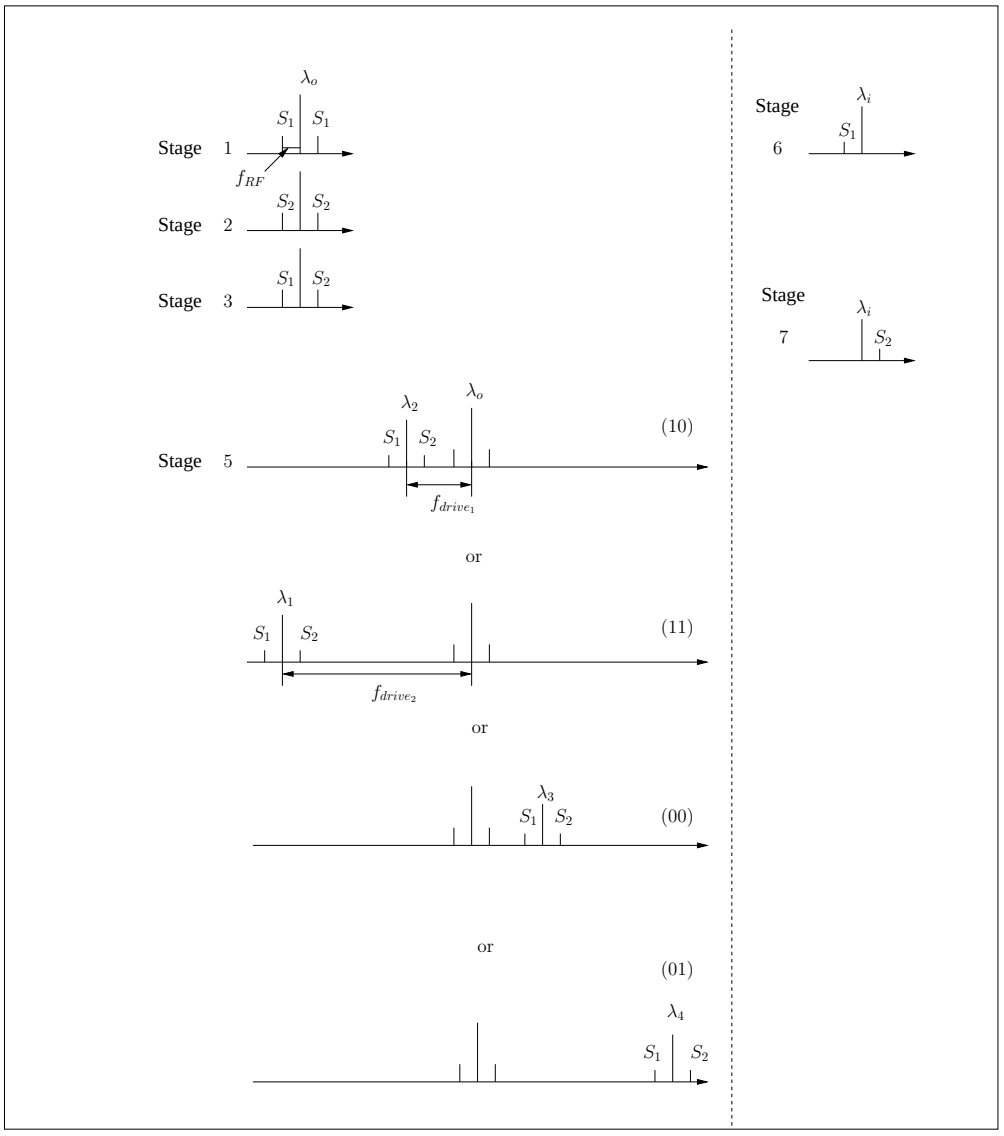

Figure 3.14: Spectrum evolution for 1-RRH scheme (Each stage corresponds to the stage of Fig. 3.11). Note that Stage 4 of Fig. 3.11 is not involved here because it only reflects the value of f_{drive}.

is required, given the relationship of $\lambda_b - \lambda_a = \lambda_3 - \lambda_2$, f_{drive} can be flexibly tuned by b_{21}, which results in a tunable frequency generator. Note that tunable commercial microwave generator can also be used in our system. However, we advocate the above-mentioned TFG as a more flexible and low-cost design. On the other hand, during each STBC symbol period, b_{22} flips the PS to either $\pi/2$ or -$\pi/2$ for shifting the ODSB-STBC signal modulated into the optical carrier after the DD-MZM process of Fig. 3.11 to be either the lower side-band or the upper side-band, as shown in Stage 5 of Fig. 3.14. The directly modulated ODSB signal of Stage 3 in Fig. 3.11 feeds a dual-drive MZM for

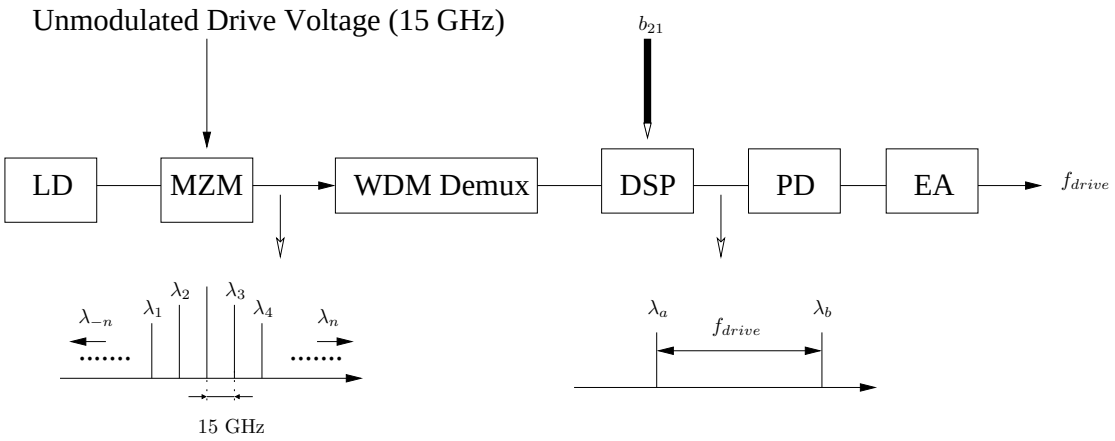

Figure 3.15: Tunable frequency generator.

side-band selection driven by a pair of RF signals having a frequency of either f_{drive_1} or f_{drive_2}, as shown in Stage 5 of Fig. 3.14 selected by b_{21} with a phase-difference of either $\pi/2$ or -$\pi/2$ controlled by b_{22}.

To clarify the optical index modulation process, for example, as shown in Fig. 3.11, $(b_{22}, b_{21}) = (1, 0)$ or $(1, 1)$ or $(0, 0)$ or $(0, 1)$ is used for side-band selection, where each combination corresponds to a side-band transmission in a SM-STBC symbol period[8], mapped to (TA1, TA2), (TA3, TA4), (TA5, TA6) and (TA7, TA8) of RRH1 of Fig. 3.11. The specific mapping rule conceived for an eight-TA SM-STBC system is shown in Table 3.2. After Stage 5 of Fig. 3.11, a power splitter is invoked before fiber transmission to serve multiple RRHs, where each fiber strand links the CU to a RRH.

Remote Radio Head As described above, the SM-STBC mapping and digital processing as well as radio carrier modulation are centralised in the CU of Fig. 3.11. The compact RRHs are responsible for the radio functions such as amplification, O/E conversion, RF filtering and transmission. More explicitly, at the fiber's receiver side, an EDFA is utilised for amplifying the optical signal, followed by a WDM Demultiplexer to filter the corresponding wavelength for the sake of TA mapping. The main components of the side-band to SM-STBC TA mapping operations are shown in the demodulation and side-band mapping (D&SBM) block of Fig. 3.11. As shown in Fig. 3.11, we invoke an FBG to separate the side-band of the ODSB-STBC signal obtained in Stage 3 of Fig. 3.14, which carries the STBC symbols S_1 and S_2. As seen at Stage 6 of

[8]In Alamouti's code, a SM-STBC symbol period refers to two symbol periods.

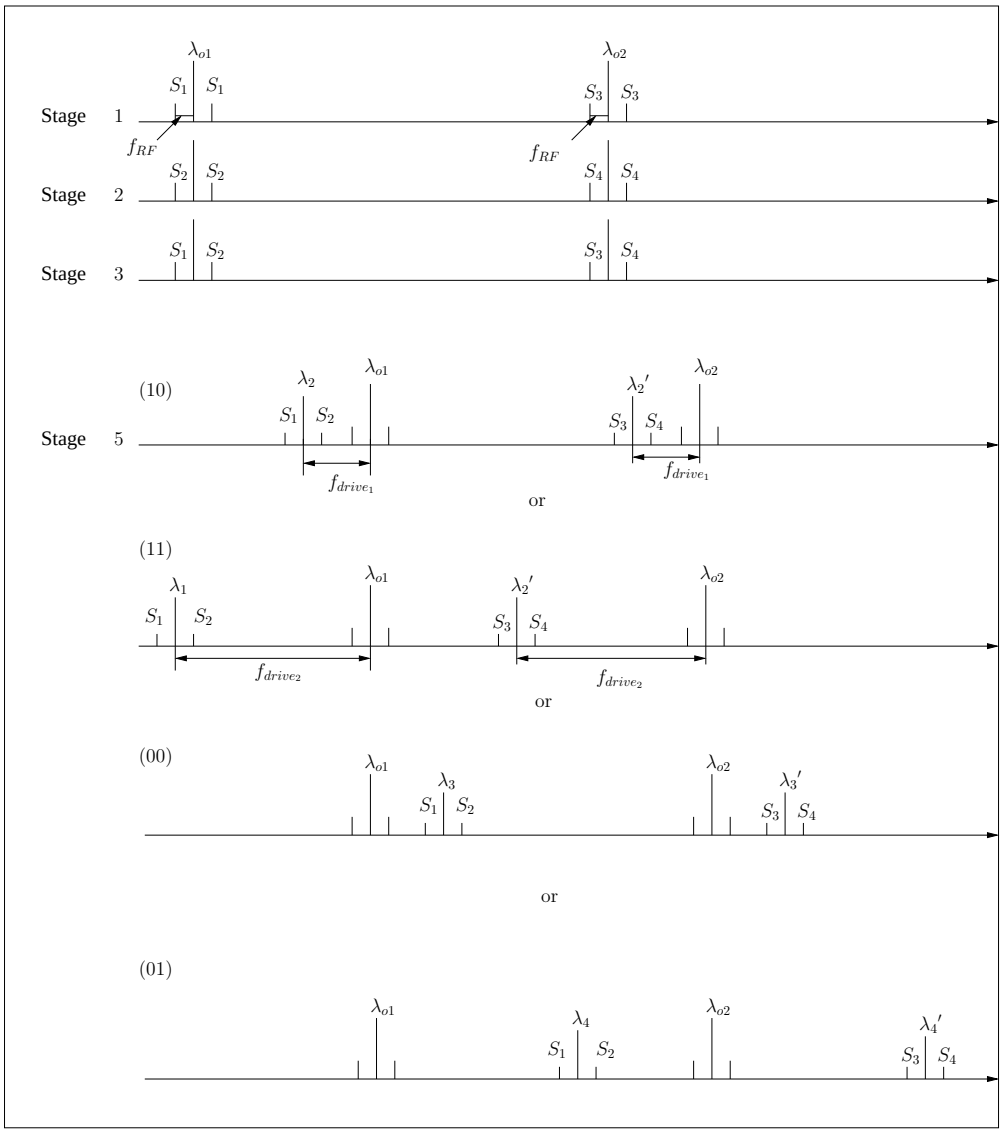

Figure 3.16: Spectrum evolution for 2-RRH scheme (Each stage corresponds to the stage of Fig. 3.11). Note that Stage 4 of Fig. 3.11 is not involved here because it only reflects the value of f_{drive}.

Fig. 3.14, the lower side-band of λ_i carrying S_1 reflected by the FBG and the upper side-band of λ_i carrying S_2 transmitting through the FBG feed the PDs used for the O/E conversion. Then the resultant signal is passed through an electronic bandpass filter (EBPF) for retaining the desired frequency, followed by an electronic amplifier for boosting the signal to the specific power level required for radio transmission. Lastly, the recovered RF signal f_{RF} carrying S_1 and S_2 is fed into the corresponding pair of TAs, while the remaining inactive antennas radiate negligible low-power noises and the phase noise imposed by the optical and electronic devices.

Fig. 3.14 shows spectral evolution process of the optical signal. Stages 1, 2 and 3 of Fig. 3.14 give the direct modulated ODSB, where S_1 and S_2 are carried by the lower side-band and the upper side-band in Stage 3 of Fig. 3.14. Then, the ODSB signal carrying both S_1 and S_2 feed the Optical Index Mapping module detailed above, where the (b_{22}, b_{21})-selected side-band formed by a single ODSB-STBC signal is transmitted by tuning the frequency of the TFG and PS of Fig. 3.11 during each SM-STBC symbol period. The mapping rule conceived for the example of an eight-TA scheme is seen at Stage 5 of Fig. 3.14 and described in Table 3.2. The fiber-based fronthaul then conveys the optical signal of Stage 5 in Fig. 3.14 to the RRHs, where a WDM-Demux block transports each side-band to each TA after O/E conversion. Stages 6 and 7 of Fig. 3.14 show that each optical signal carrying S_1 and S_2 is separated by the FBG, where S_1 and S_2 feed a pair of TAs. Thus, because only a single ODSB-STBC signal carrying the STBC symbols is transmitted during each STBC symbol period, the WDM-Demux of Fig. 3.11 becomes capable of filtering the specific wavelength in one of the ports, while no data is transmitted from the other ports, hence facilitating the mapping of the side-band index to a specific antenna index using a set of passive optical components.

Furthermore, our system is scalable, where any RRH can be activated by appropriately adjusting the number of activated SD_RRHs of the SD block in Fig. 3.11. To elaborate a little further, Fig. 3.16 portrays the spectral evolution, when a CU serves two RRHs. In this scheme, two SD modules, namely SD_RRH1 and SD_RRH2, are assigned the particular sets of STBC symbols S_1, S_2 and S_3, S_4 carried by λ_{o1} and λ_{o2} respectively, where the STBC symbols S_1 and S_2 are transmitted to RRH1, while S_3 and S_4 are forwarded to RRH2. As shown at Stage 5 of Fig. 3.16, the side-band selection of the two RRHs are consistent, meaning that several RRHs can be jointly controlled merely using a single Optical Index Mapping module. At RRH2, we apply the same architecture, where the WDM de-multiplexed wavelengths are λ_1', λ_2', λ_3' and λ_4'. Hence, a twin-RRH scheme can be readily implemented by adjusting the SD configuration. This configuration inspires our adaptive design, which will be detailed in Section 3.5.2. Next, our simulation results are presented.

Parameter	Value
Channel coding	Convolutional code
Throughput 4×2	1.5 Gbps (BPSK-1RRH) 2.5 Gbps (BPSK-2RRH) 2.5 Gbps (QPSK-1RRH) 4.5 Gbps (QPSK-2RRH)
Throughput 8×2	2 Gbps (BPSK-1RRH) 3 Gbps (BPSK-2RRH) 3 Gbps (QPSK-1RRH) 5 Gbps (QPSK-2RRH)
LD central wavelength	1550 nm (1 RRH) 1550 nm and 1547.2 nm (2 RRHs: frequency spacing 350 GHz)
RF signal	10 GHz
LD power	1 mW
Drive frequency (MZM)	30 GHz
Fiber type	SSMF+DCF
Fiber length	20 km (15 km SSMF and 5 km DCF)
Channel model	Split-step Fourier method
Modulation type	BPSK and QPSK
Wireless channel	Rayleigh fading channel
Wireless detection	ML detection
Number of TAs	four or eight each RRH
Simulation environment	MATLAB

Table 3.3: Simulation parameter.

3.5.1.3 System Simulation

In this section, our simulation results are discussed under two different scenarios. Firstly, we support a user by a single RRH, while relying on an eight-TA SM-STBC scheme. Then, we will increase the number of RRHs, which supports the user, to two, without changing the configuration of the CU as well as the RRHs. Similar to the channel model introduced in Section 3.5.1.1, the wireless channel is the classic statistical SM-STBC model with A-RoF impairments, as shown below:

$$\mathbf{Y} = \alpha \circ \mathbf{HX} + \mathbf{N}, \tag{3.2}$$

where α is the A-RoF-induced distortion[9], and $\mathbf{H}$ is the wireless MIMO channel matrix, both of which have a size of $(N_r \times N_{TA})$. Furthermore, $\circ$ represents the Hadamard product. Here, $\mathbf{H}$ has independent and identically distributed (i.i.d) entries with uniform

[9]The distortion is jointly caused by the effects of the A-RoF components, such as fiber's dispersion, fiber's non-linearity, the phase noises of other components, the OBPF's signal leakage and optical noises

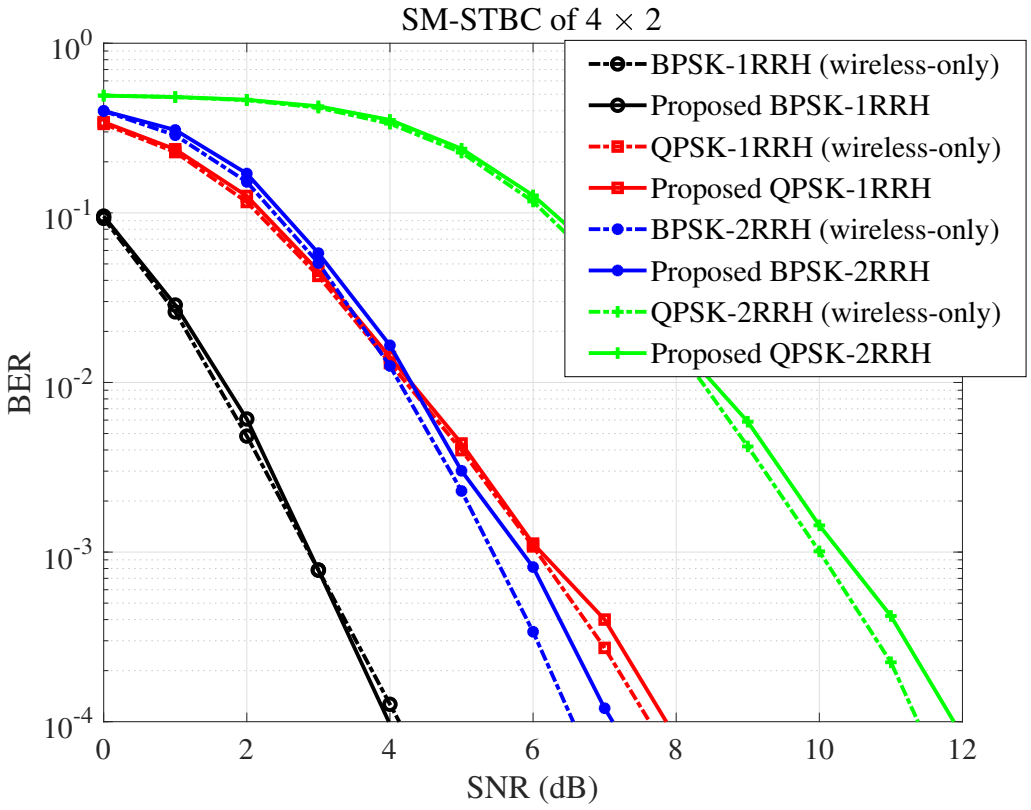

Figure 3.17: BER performance for four TAs and two receive antennas using the schematic of Fig. 3.11 and parameters of Table 3.3.

phase distribution and complex Gaussian distributed amplitude having a mean of 0 and a variance of 1, yielding $\mathcal{CN}$ ~(0,1). $\mathbf{N}$ is the Gaussian noise distributed as $\mathcal{CN}$ ~(0,σ^2). At the wireless receiver, ML detection is used for jointly detecting the antenna index and the classic modulated symbols.

Furthermore, we simulate a SSMF of 15 km and a DCF of 5 km, using the popular split-step Fourier method [90]. The A-RoF parameters used are listed in Table 3.3. In this section, we consider two scenarios, where single-RRH SM-STBC scheme and two-RRH multiplexing SM-STBC scheme are simulated for the proposed C-RAN system. Explicitly, depending on the specific wireless channel conditions, the user can either communicate by invoking a single RRH using our SM-STBC scheme or with the aid of two RRHs, while multiplexing the signals transmitted from both RRHs, where we use ML detection for both cases. In our proposed A-RoF aided C-RAN shown in Fig. 3.11, the SD block is used for switching the connection between the single-RRH SM-STBC and two-RRH multiplexing SM-STBC arrangements. For example, if the user is connected

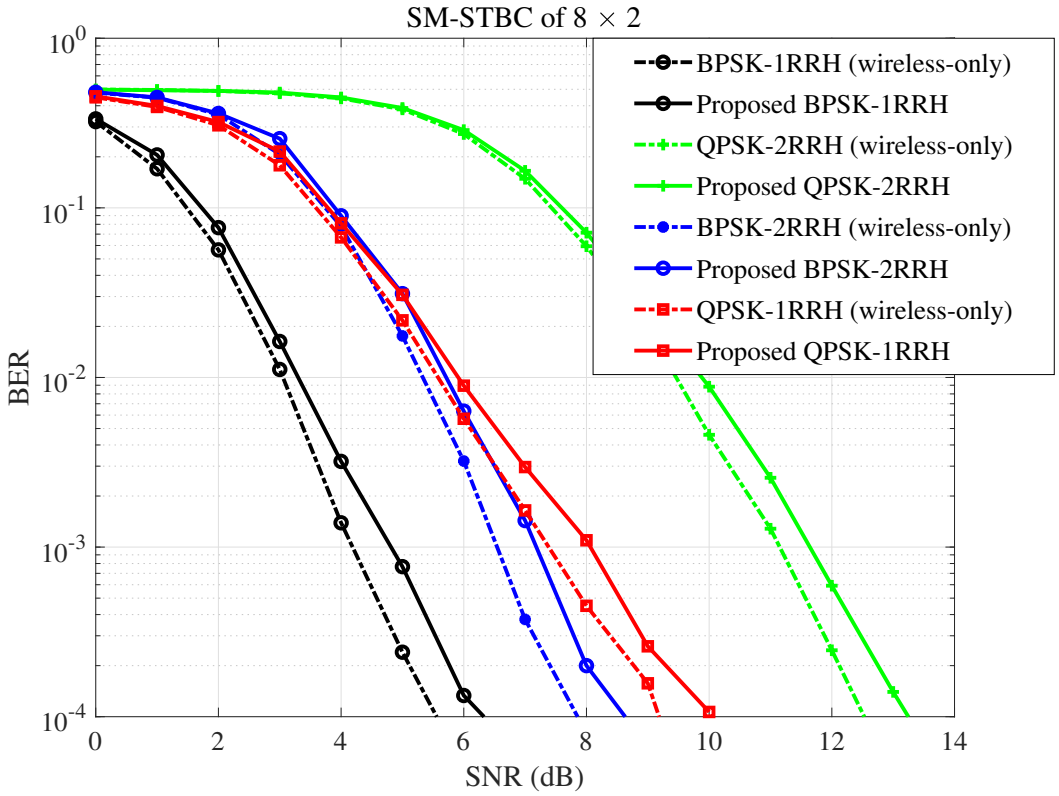

Figure 3.18: BER performance for eight TAs and two receive antennas using the schematic of Fig. 3.11 and parameters of Table 3.3.

to two RRHs, the C-RAN-DSP tends to assign the classic modulated bit sequence b_1 to SD_RRH1 and SD_RRH2 of Fig. 3.11, thus the signals will be transmitted from both RRH1 and RRH2, multiplexing the SM-STBC signals from each RRH to the same user.

We firstly investigate the SM-STBC scheme using four TAs and two RAs (4×2) schemes, while a pair of TAs transmit the modulated symbols during each STBC symbol period. Moreover, BPSK and QPSK are considered for both the single-RRH SM-STBC and two-RRH multiplexing SM-STBC arrangements. Thus, any of the four configurations shown in Table 3.3 may be activated by our proposed system. Moreover, the joint throughput after a half-rate convolutional code (CC) is halved. Note that, after the CC process, the modulated symbol rate of the single-RRH scheme is 1 Gsymbol/s[10] while that of the twin-RRH scheme is 2 Gsymbol/s[11], and the bit rate controlling the optical index is 0.5 Gbps for all the cases. Explicitly, we use a constraint length of 7 and the

[10]Corresponding bite rate: 1 Gbps for BPSK and 2 Gbps for QPSK.
[11]Corresponding bit rate: 2 Gbps for BPSK and 4 Gbps for QPSK.

generator polynomials of (171,133) (in octal), as shown in Table 3.3 in our proposed system simulation.

To verify that our A-RoF aided system performance is not unduly degraded by the optical link compared to the wireless-only scheme, namely where only wireless transmission relied upon, Fig. 3.17 shows a modest BER performance of the four configurations, where the scheme operating with A-RoF shows a negligible BER degradation of less than 1 dB compared to that of wireless-only scheme. This modest degradation is imposed by the residual interference introduced by the muted antennas.

Furthermore, our system is eminently scalable. Hence, we also investigate an (8×2) scheme for the sake of increasing the data rate, as seen in Fig. 3.18 that the BER performance difference between the proposed A-RoF-aided system and the (8×2) wireless-only scheme is higher than that of the (4×2) scheme comparison characterised in Fig. 3.17. This is because when more antennas are applied, more interference is inflicted, which degrades BER performance.

Next, relying on the system schematic of Fig. 3.11, we will discuss the benefits of invoking the KNN learning algorithm for transceiver adaptation and compare it to the classic threshold adaptation based benchmarker.

3.5.2 Learning Assisted Transceiver Adaptation

In Section 3.5.1, we proposed a C-RAN system based on an A-RoF link, where the SM concept is combined with STBC and the signals are processed optically. Furthermore, we discussed that our C-RAN system is scalable of adapting the number of RRHs supporting a user. Similarly, the choice of the modulation technique employed can also be adapted by the SD and C-RAN-DSP module of Fig. 3.11, depending on the power of the signal received by the user from the RRH.

3.5.2.1 Adaptation of the Proposed C-RAN

To elaborate further, observe in Fig. 3.11, if a user was served by a single RRH and then the system switches to the twin-RRH mode, the C-RAN-DSP will assign the STBC

symbols to SD_RRH1 and SD_RRH2 instead of SD_RRH1 only. Thus, as shown at Stage 3 of Fig. 3.16, a pair of ODSB-STBC signals are transmitted to the DD-MZM of Fig. 3.11 for side-band selection, as detailed in Section 3.5.1. Then the transmitted optical signal is mapped to separate single-mode fibers in order to serve individual RRHs. At the RRH, we invoke the same configuration, except for the demultiplexed wavelengths of the WDM-Demux module, where in the example of Fig. 3.16, we use λ_1, λ_2, λ_3, λ_4 at RRH1, while λ'_1, λ'_2, λ'_3, λ'_4 at RRH2. Thus, our proposed system is capable of supporting multiple RRH connections by adjusting the configuration of the SD block of Fig. 3.11.

Hence, we are able to design a system, where the number of RRHs supporting a user can be adapted in order to vary the data rate, while meeting a particular target performance threshold. Hence, we assume the following scenarios:

1. The user is supported by a single-RRH using SM-STBC along with the modulation formats of either BPSK or QPSK.

2. The user is supported by a pair of RRHs transmitting multiplexed signal using SM-STBC using the modulation formats of either BPSK or QPSK.

3.5.2.2 Learning Model and Results

We amalgamate our proposed adaptive C-RAN system with a learning technique for improving the achievable data rate of the system, which relies on the classification algorithm. The rationale of the choice behind the KNN algorithm is that most classification algorithms require an explicit functional mapping between the feature set and the classifiers. The feature set in our solution includes the SNR and the BER, while the classifiers are constituted by the number of RRHs connected to a single user, associated with different modulations techniques. Explicitly, for the single RRH case we invoke SM-STBC and for the 2-RRH scenario we invoke SM-STBC and spatial multiplexing. Unfortunately, there is a paucity of information about the functional mapping between the two. Therefore, a KNN classification algorithm is invoked in this section, which removes the need for a functional mapping [119]. The KNN algorithm consists of two stages, namely training and testing. During the training phase, the samples containing the information,

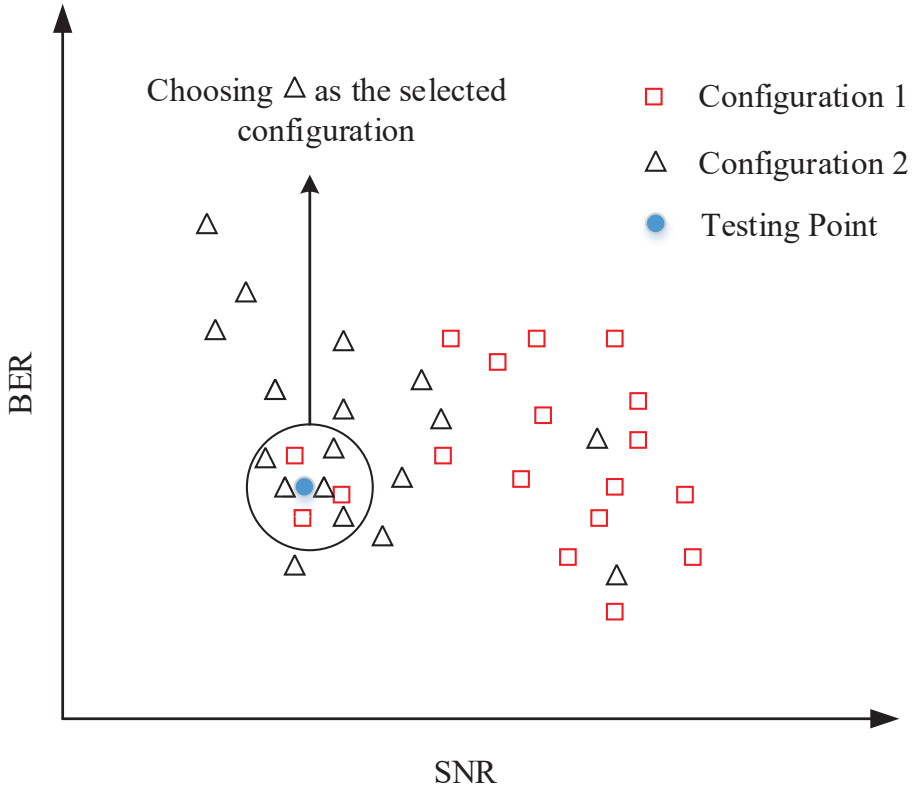

Figure 3.19: Stylized portrayal of the KNN algorithm.

such as the instantaneous SNR and its corresponding BER, is collected over different channel realisations. Then, in the testing phase, we have to decide about the class that is to be employed for attaining a high data rate as well as meeting the target BER. The BER vs SNR relationship may be observed in the stylized illustration of Fig. 3.19, where depending on the prevalent SNR, we select the transceiver mode capable of satisfying the BER requirement.

The conventional threshold adaptation relies on the BER vs SNR relationship and the SNR values meeting the target BER. For example, let us consider the results of Fig. 3.18. Assuming that the target at BER= 10^{-3} defines SNRs, the points of intersection of the horizontal line at the BER of 10^{-3}, where the transmission mode reconfiguration has to take place [120]. By contrast, the KNN classification relies on the training data. For example, as shown in Fig. 3.19, we aim for switching between Configuration 1 and Configuration 2, which are represented by squares □ and triangles △. The testing point

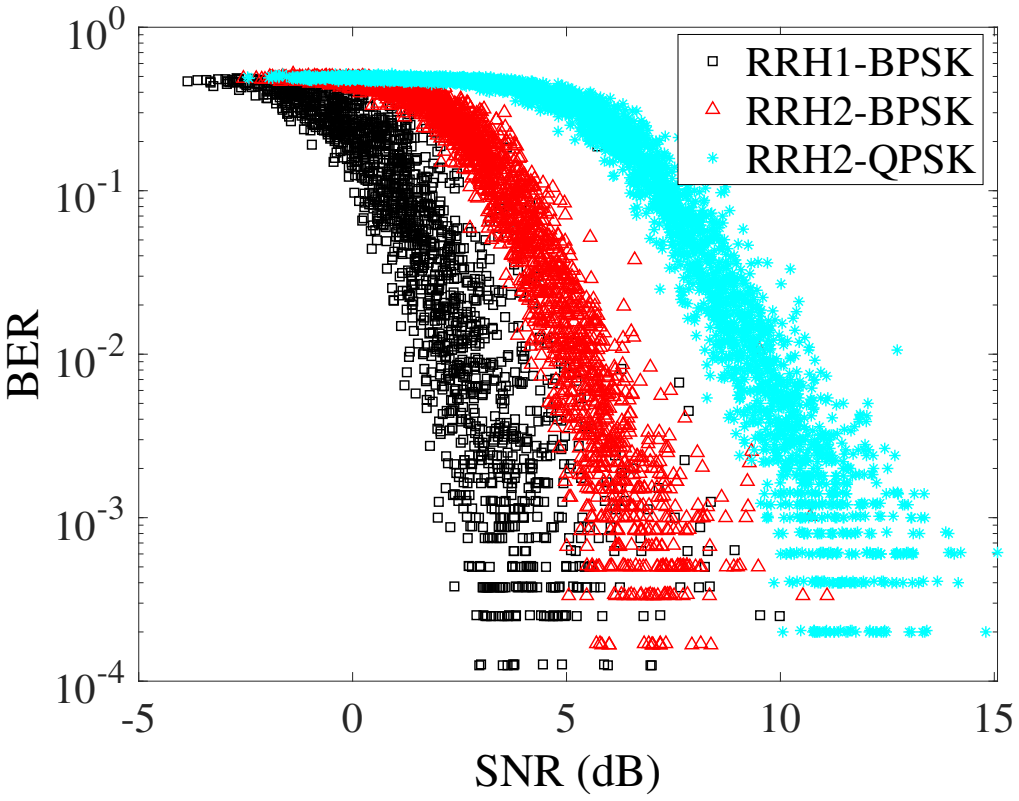

Figure 3.20: Stored training data.

of Fig. 3.19 is the centroid used for representing the symbols encircled, which determines the specific configuration activated. Compared to the conventional adaptation relying on a threshold adaptation, the KNN classification assisted adaptation achieves a higher throughput.

As mentioned in Section 3.5.1, our RoF aided SM-STBC is capable of flexibly switching between the single-RRH and twin-RRHs aided configuration, thus under the control of the KNN algorithm.

As discussed in Section 3.5.1, given our fixed symbol rate, which corresponds to a fixed maximum RF modulated bandwidth, the BER performance of the BPSK-2RRH scheme becomes slightly better than that of QPSK-1RRH. Thus, we consider the following three configurations or classes for our adaptation technique based on the SM-STBC scheme (8×2) to verify the feasibility of controlling our adaptive C-RAN system by the KNN algorithm, while employing a convolutional code having a code rate of $1/2$, a constraint

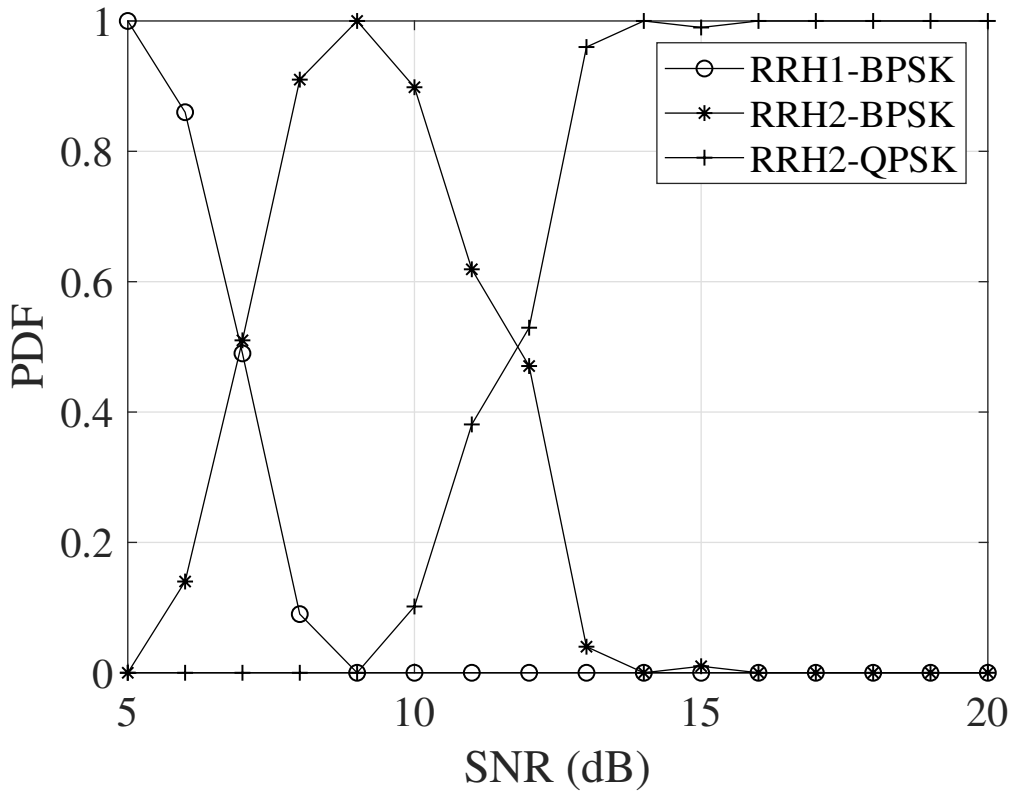

Figure 3.21: Probability distribution function after KNN algorithm using the schematic of Fig. 3.11 and parameters of Table 3.3.

length of 7 and generator polynomials of (171,133) (in octal). The following are the three configurations used in our adaptive system:

1. 2 Gbps BPSK-1RRH;
2. 3 Gbps BPSK-2RRH;
3. 5 Gbps QPSK-2RRH;

Again, the simulations rely on the training phase and the testing phase. In the training phase, we store the training data associated with the pair of features $\{BER, SNR\}$, namely the BER and the instantaneous post-processing SNR for each channel realisation associated with a different noise level. Hence, in our system, we store 300 training symbols for each of the 20 noise levels considered. Fig. 3.20 shows the training data stored for the above-mentioned scenarios, where the squares, triangles and stars denote

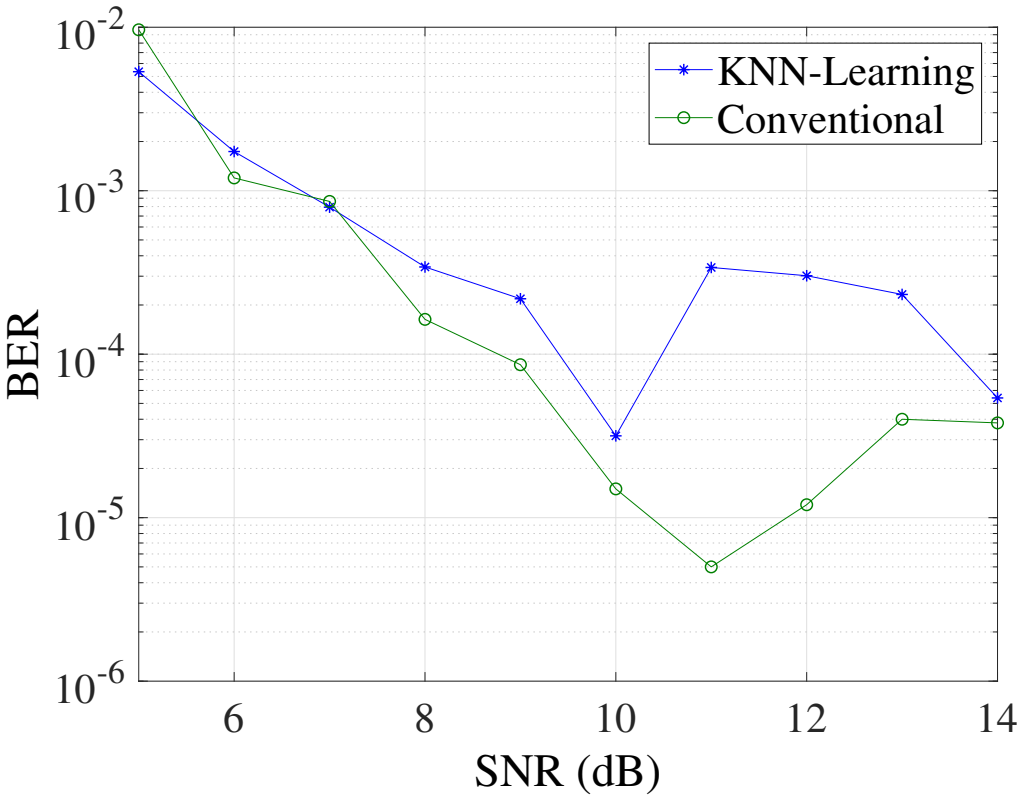

Figure 3.22: BER comparison between KNN algorithm aided adaptation and the conventional adaptation using the schematic of Fig. 3.11 and parameters of Table 3.3.

schemes representing the BPSK-1RRH, BPSK-1RRH and QPSK-2RRH schemes, respectively. The target BER of our system is 10^{-3} and the testing point is $\{10^{-3}, M\}$, where M denotes the real instantaneous post-processing SNR.

Thus, we compare the total number of each class encircled and determine which class (configuration) is used for that specific time slot. We performed Monte-Carlo simulations, where 100 frames each containing 8000 bits were used for each instantaneous post-processing SNR. Then, we obtained the probability density function (PDF) of the three classes tested, which is seen in Fig. 3.21. For example, around 7 dB around, we have a similar probability of choosing RRH1-BPSK and RRH2-BPSK. Upon increasing the SNR, the probability of the RRH1-BPSK mode is increased, while that of the RRH2-BPSK mode tends to zero upon approaching 9 dB. Then, the RRH2-QPSK mode shows increasingly high probability beyond 9 dB, while at 16 dB, the RRH2-BPSK probability tends to zero.

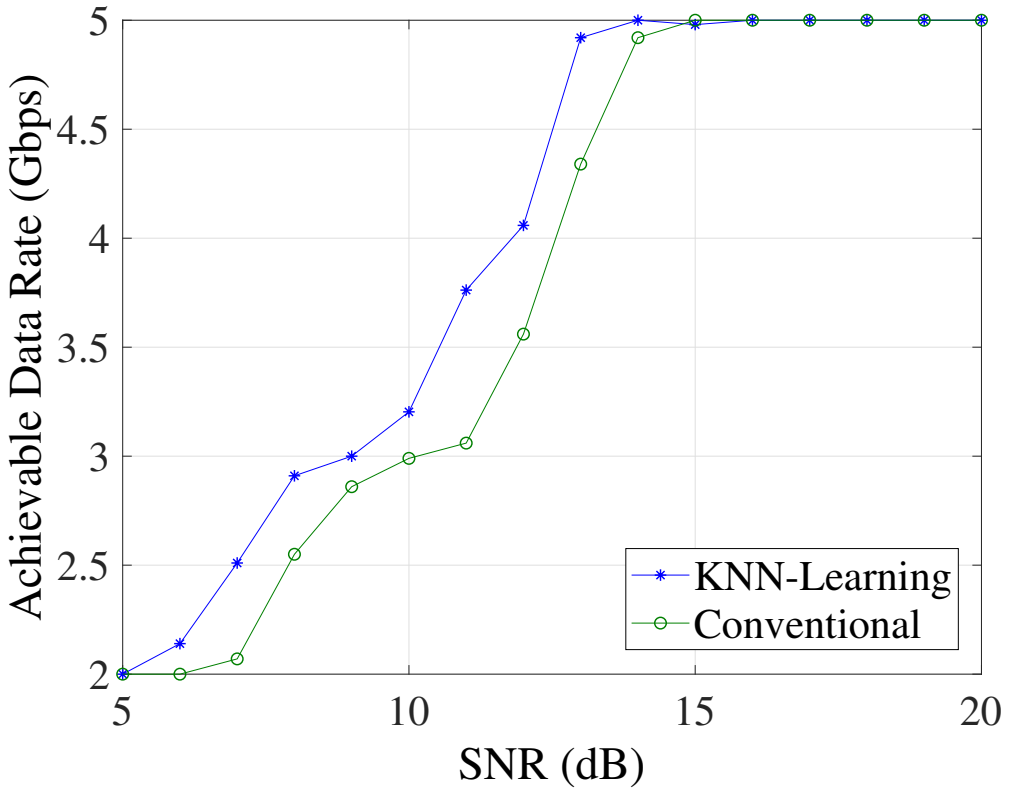

Figure 3.23: Data rate comparison between KNN algorithm aided adaptation and the conventional adaptation using the schematic of Fig. 3.11 and parameters of Table 3.3.

Fig. 3.22 shows that our KNN-learning algorithm is indeed capable of maintaining a BER below 10^{-3}. Compared to the classic threshold based adaptation [120], we show in Fig. 3.23 that the KNN assisted user adaptation improves the achievable data rate. Although, we observe in Fig. 3.22 that the BER performance of the conventional threshold adaptation is superior to that of our KNN-assisted solution, both techniques are capable of attaining target BER performance. Explicitly, the KNN-based learning algorithm achieves a higher throughput, because it does not maintain an unnecessarily low BER- it rather encourages the activation of higher-throughput modes.

3.6 Summary and Conclusions

Inspired by the popularity of both the SM and C-RAN concepts of next-generation mobile communication, we intrinsically amalgamated the SM philosophy, with our A-RoF

aided C-RAN system. Explicitly, we briefly reviewed the background of A-RoF aided C-RAN and SM in Section 3.1. In Section 3.3, we listed our new contributions. Then, in Section 3.4, we designed an all-optical processing based A-RoF-aided SM scheme. An experimental verification of the novel A-RoF-aided twin-antenna SM system has also been provided. SM encoding was carried out in the optical domain and our centralised RoF-aided SM encoding relying on the MZM's side-band selection was characterised both by simulations and by experiments. This design is also eminently suitable for small-cell fronthaul solutions. The experimental results show that our 2 Gbps system exhibits only marginally degraded BER performance compared to its pure wireless counterpart operating without an A-RoF link, while benefiting from centralised SM encoding and RAP switch removal. Bearing in mind that SM is not capable of achieving transmit diversity gain, in Section 3.5 we further extended our single side-band selection concept proposed in Section 3.4 to a generalized SM aided adaptive C-RAN system. Explicitly, we proposed an A-RoF aided SM-STBC scheme using optical side-band selection and further extended it to an adaptive C-RAN system, where any arbitrary number of transmitter antennas can be driven by a single MZM. In our proposed system, the power thirsty ADC, DAC and the actively-powered switches of a conventional system are eliminated, resulting in an energy-efficient and cost-efficient mobile access network, where the BER performance of this A-RoF aided solution is only marginally degraded compared to the conventional wireless SM-STBC scheme. Moreover, by taking advantage of the flexibly selectable number of RRHs of the proposed A-RoF aided C-RAN system, we invoked the KNN algorithm for intelligently adapting both the number of selected RRHs and the modulation format, showing that the achievable data rate exceeded that of the classic threshold adaptation.

Next, inspired by Chapter 2 and the solution conceived in this chapter, where beamforming and SM are invoked for A-RoF aided C-RAN systems, in the next chapter, we will propose a multi-functional-MIMO system, where a joint millimeter wave (mmWave) upconversion and A-RoF aided beamforming as well as SM and multi-set space-time shift keying assisted A-RoF are investigated.

Chapter 4

Analogue Radio Over Fiber Aided MF-MIMO

In Chapters 2 and 3, we proposed an analogue radio over fiber (A-RoF) network design technique and conceived a pair of multiple-input-multiple-output (MIMO) schemes, namely beamforming and spatial modulation (SM). As described in Chapters 2 and 3, our design aim is to optically process the MIMO schemes in a central unit (CU).

More explicitly, in Chapter 2 we invoked A-RoF techniques after appropriately shifting the phase of the RF signals carried by optical wavelengths in order to arrange for wireless beamforming without using radio frequency (RF) phase shifters. More explicitly, we proposed a fiber-non-linearity aided phase-shifting scheme, which was then invoked in a cloud/centralised radio access network (C-RAN) relying on small-cell sectorization. This may be deemed to be a cost-efficient beamforming system in comparison to the traditional RF phase-shifting aided scheme. To elaborate a little further, the benefit of our proposed system is that it eliminates the power-thirsty RF phase-shifter from the A-RoF aided C-RAN system advocated.

Then, in Chapter 3, we conceived an A-RoF aided C-RAN system relying on a SM-like concept, where we were able to dispense with the power-thirsty switches. Furthermore, an adaptive C-RAN relying on a SM-like concept was also proposed, which was flexible enough for accommodating an arbitrary number of transmitter antennas.

Based on the concepts conceived in Chapters 2 and 3, here we introduce more sophisticated multiple-antenna techniques, amalgamating both beamforming and diversity aided and SM-assisted MIMO schemes combined with millimeter wave (mmWave) upconversion using A-RoF. As a benefit, we arrive at a sophisticated multi-functional MIMO (MF-MIMO) scheme [121][1]. Recall that we proposed a joint SM and space-time block coding (STBC) system in Section 3.5, which is a dual-functional MIMO system, which evolved from Section 3.4 focusing on our side-band selection based SM-like concept conceived for an adaptive C-RAN system design. In this chapter, the dual-functional MIMO concept of Section 3.5 is evolved further into a general A-RoF aided MF-MIMO design for the C-RAN fronthaul downlink. Recall from Chapter 1 that the A-RoF aided MF-MIMO signal processing is constituted by the carrier modulation and electro-to-optic (E/O) conversion. Moreover, we generate mmWave carrier using a combination of a Mach-Zehnder modulator (MZM) and an optical interleaver housed in E/O conversion block and Optical filtering/WDM Demux block of Fig. 4.1, respectively, which we will elaborate on the process in Section 4.4.2.1.

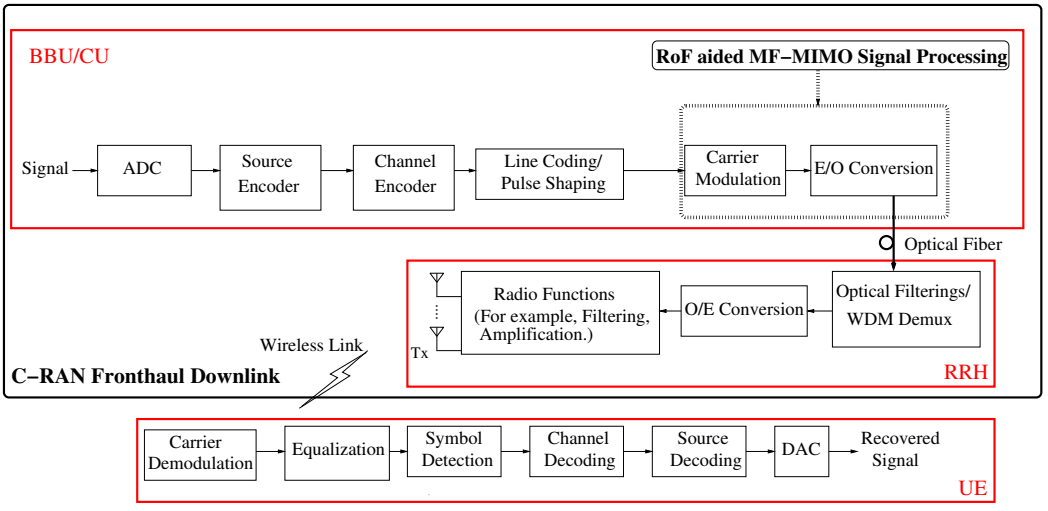

Figure 4.1: A-RoF aided MF-MIMO for C-RAN Downlink.

4.1 Background

Owing to the popularity of flawless multimedia services supported by the ubiquitous smartphones, cellular networks are approaching their capacity, especially in densely

[1]MF-MIMO is an aggregate of two or more than two multiple-antenna supported techniques.

populated areas [2, 9]. Small cells are capable of overcoming the network capacity shortage with the aid of cell-spliting, which results in high-quality wireless coverage within a small cell radius [31, 12, 122]. A-RoF techniques are capable of supporting small cell deployment using centralised processing, where the small cell base stations (BSs) are connected using fiber [12] and only low-complexity optical-to-electronic (O/E) conversion and RF amplification are required at the small-cell base station [16, 123]. A simplified schematic of the A-RoF-aided small cell system is shown in Fig. 4.2, where a single CU supports several remote small-cell radio heads. This architecture is potentially capable of reducing the overall cost of the network [1, 16]. As shown in Fig. 4.2, the CU is responsible for centralised digital processing, while the remote radio heads (RRHs) are used for radio transmission, including O/E conversion, filtering, amplification and transmission from the transmitter antenna arrays (TAAs). This architecture is also applicable to the popular C-RAN concept [101, 124], where a CU[2] carries out all the baseband signal processing [23], serving multiple low-complexity and low-cost RRHs. The A-RoF transmissions [12, 19] to the RRHs invoked by C-RAN [1] are also capable of supporting the emerging small-cell technologies [125, 1].

Moreover, mmWave carrier frequencies naturally lend themselves to small cell creation owing to the associated short propagation range, thus reducing the inter-cell interference [126, 2]. However, traditional all-electronic mmWave processing requires radio frequency (RF) mixers, which tend to degrade the link's performance [15]. We circumvent this problem with the aid of A-RoF techniques which are capable of dispensing with high frequency mixers and demonstrate that optical upconversion to mmWave frequencies is capable of matching the performance of its all-electronic counterpart [15]. This is achieved by exploiting the MZM's non-linearity, the fiber's non-linearity and the photo-detector's non-linearity for optical up-conversion [15]. Moreover, multi-frequency mmWave wavelength up-conversion techniques using four-wave mixing in a semiconductor optical amplifier have been proposed in [127, 128], which aim for improving the capacity and for reducing the interchannel interference. Additionally, the optical generation of multiple-frequency mmWave signals using tunable optical frequency combs has been proposed in [129] for mitigating the crosstalk between the various optical network elements involved. Furthermore, a beneficial combination of De-multiplexers and MZMs

[2]In the C-RAN literature the CU and baseband unit (BBU) terminologies are used interchangeably [1].

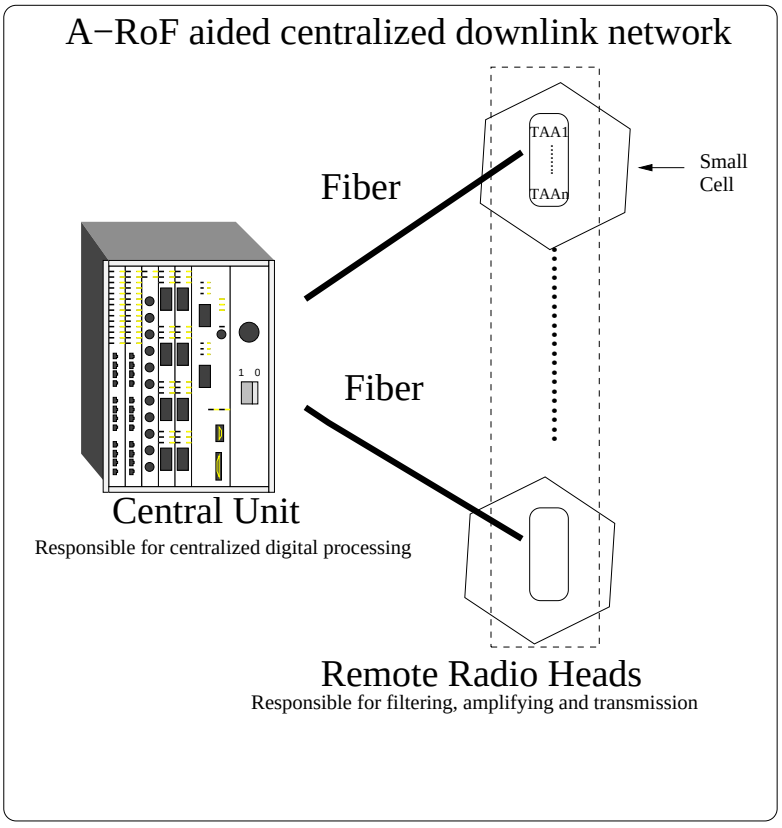

Figure 4.2: A-RoF aided centralised downlink network. The Central Unit performs centralised digital processing and radio modulation, while the Remote Radio Head carries out filtering, amplification and radio transmission.

has been proposed in the context of a passive optical network [130] for supporting the photonic generation of 60/120 GHz signals. By contrast, in this treatise we exploit the MZM's non-linearity combined with an OIL for optical upconversion and flexible beamforming.

On the other hand, as a key technique of reducing the inter-channel interference and of increasing the signal-to-interference-plus-noise ratio (SINR) of mmWave signals, beamforming may be invoked to compensate for the short propagation range of mmWave communications and hence for achieving an SINR gain [37]. Furthermore, A-RoF aided beamforming relying on all-optical processing is capable of substantially reducing the complexity of our MF-MIMO configuration, which is designed to combine the gains of spatial diversity, multiplexing and beamforming techniques, by avoiding the employment of phase shifters used in traditional electronic beamforming [19].

Let us now elaborate a little further on SM and its generalized version referred to

as MF-MIMO [8], namely space-time shift keying (STSK) and multi-set STSK (MS-STSK). SM is a low-cost MIMO technique, where one out of M transmit antennas is activated to transmit a single classic quadrature amplitude modulation/phase shift keying (QAM/PSK) symbol. Hence, in SM, in addition to the classic modulated bits, $log_2 M$ implicit antenna index based information bits are conveyed[3] [105]. SM is capable of striking a compelling trade-off between Bell Lab's Layered Space-Time (BLAST) and Alamouti's STBC, whilst relying on a reduced number of RF chains. Its further benefits are its ability to use a single-antenna based maximum likelihood (ML) detection scheme and the mitigation or elimination of inter-channel interference [108, 115]. Additionally, STSK constitutes a generalization of SM, where one out of say M number of dispersion matrices is activated for implicitly conveying $log_2 M$ bits, which can attain both diversity and multiplexing gains [115, 131]. Based on intrisincally amalgamating the philosophy of both SM and STSK, the concept of MS-STSK was proposed in [106] as a further generalized architecture, which is capable of striking a beneficial design trade-off between the achievable multiplexing and diversity gains [106]. In the next section, we will provide a brief review of wireless MF-MIMO techniques.

4.2 A Brief Review of Wireless MF-MIMO

As discussed in Chapter 1, MIMO schemes are capable of simultaneously achieving beamforming, multiplexing and diversity gain depending on the specific choices of the multiple-antenna techniques invoked, as shown in Fig. 1.5. Thus, in order to make the most of the MIMO techniques conceived for achieving a high data rate as well as attaining a low bit error ratio (BER), the MF-MIMO term is invoked for describing the amalgamation of two or more MIMO schemes [121]. The concept of MF-MIMO has been widely researched during the past two decades [121]. As early as 1991, Tarokh *et al.* [132] suggested a joint Vertical-Bell Laboratories Layered Space-Time (V-BLAST) and STBC scheme, where by partitioning the transmitter antennas into small individual groups with each carrying out independent STBC operations, their scheme became capable of providing diversity gain as well as multiplexing gain. Then, Jongren *et al.* [133] proposed combining conventional beamforming and orthogonal STBC (OSTBC) in the presence

[3]We refer to the antenna selection index in SM as the implicit information.

of imperfect channel knowledge, where significant SNR gains were shown both over conventional OSTBC and over conventional beamforming. Furthermore, El-Hajjar *et al.* [134] designed layered steered space-time codes (LSSTC), where the merits of V-BLAST, analogue beamforming (ABF) and OSTBC were combined to achieve a high spectral efficiency, a high SNR gain and a high diversity gain at a low detection complexity.

On the other hand, MF-MIMO signals can also be digitally processed. A linear dispersion code (LDC) was proposed by Hassibi and Hochwald in [135] which was then further developed by Heath *et al.* [136] for guaranteeing satisfactory BER performance, where appropriately designed dispersion matrices were utilised for generating independent space-time coding (STC) symbols. The scheme in [136] achieved both a multiplexing and a diversity gain, hence yielded both a high capacity and a low BER. Later, in order to strike a flexible trade-off between the diversity and the multiplexing gain, Sugiura *et al.* [137] amalgamated the concepts of LDC and SM for creating the concept of space-time shift keying (STSK) schemes, which was based on activating one out of several dispersion matrices at a time. Moreover, Basar *et al.* [138] proposed another MF-MIMO scheme amalgamating SM and Alamouti's STBC by activating a pair of antennas, aiming for providing a diversity gain, which the single-transmitter SM can not support. Inspired by the STSK scheme and antenna selection scheme of SM, Hemadah *et al.* [106] proposed a multi-set STSK (MS-STSK) scheme, which subsumes STSK, while benefiting from the SM's antenna combination selection for transmitting extra implicit antenna-index based bits, achieving both a higher data rate and a lower BER than conventional STSK.

4.3 New Contributions

In this chapter, we consider MF-MIMO concept in the context of A-RoF aided small-cell based C-RAN from the perspective of system design for achieving a compelling performance vs cost trade-off, where the following problems are considered:

- **Problem 1:** MF-MIMO tends to rely on complex digital signal processings, which would impose very high cost in densely populated areas, where numerous small cells are used.

- **Problem 2:** Currently, the state-of-the-art mmWave carriers are proposed for small-cell systems for reducing the inter-cell interference as a benefit of their otherwise undesirable high pathloss. However, they rely on costly high-frequency generators [139] and mmWave mixers, which may degrade the performance of the wireless link [15].
- **Problem 3:** Analogue beamforming (BF) is a RF phase-shifting based technique for creating a directional beam towards the desired user and nulls towards the interferers. They have the benefit of improving the SNR gain [37], but imposes a high insertion loss on each RF phase-shifter.

Thus, in this chapter, we have integrated these wireless MIMOs with the A-RoF aided C-RAN fronthaul concept for conceiving a cost- and energy- efficient mobile access network for centralised MIMO signal processing to address Problem 1. Furthermore, Problem 2 is solved by using optical up-conversion of mmWave signals, without the need for the large-scale deployment of the costly mmWave generators at the myriads of small-cell BS [139]. Then, the RF phase shifter potentially imposing a high-insertion loss presented by Problem 3 will be replaced by a single chirped fiber Bragg grating (CFBG), which is capable of delaying, i.e. phase shifting, the optical signals for steering the beam. Again, based on the above-mentioned solutions, Fig. 4.3 shows our proposed MF-MIMO arrangement, where the SM/MS-STSK and BF concepts are combined for achieving both diversity as well as multiplexing and beamforming gains.

In our A-RoF system's downlink, RF signals are transmitted over the optical fiber from the CU to the RRH, where the centralised baseband processing is carried out. Then, the photo-detected signal is transmitted by the antennas without the need for electronic processing in the baseband, such as modulation, digital-to-analogue (DAC) or analogue-to-digital (ADC) [15, 12]. In this section, we propose an A-RoF system relying on centralised processing aided SM and MS-STSK combined with all-optical beamforming, while simultaneously achieving optical up-conversion to mmWave carrier frequencies.

In the proposed A-RoF network, the SM and MS-STSK information is modulated onto the two side-bands of an optically modulated signal in the CU of Fig. 4.2, which is up-converted from a frequency of 3 GHz to a mmWave frequency by pure optical

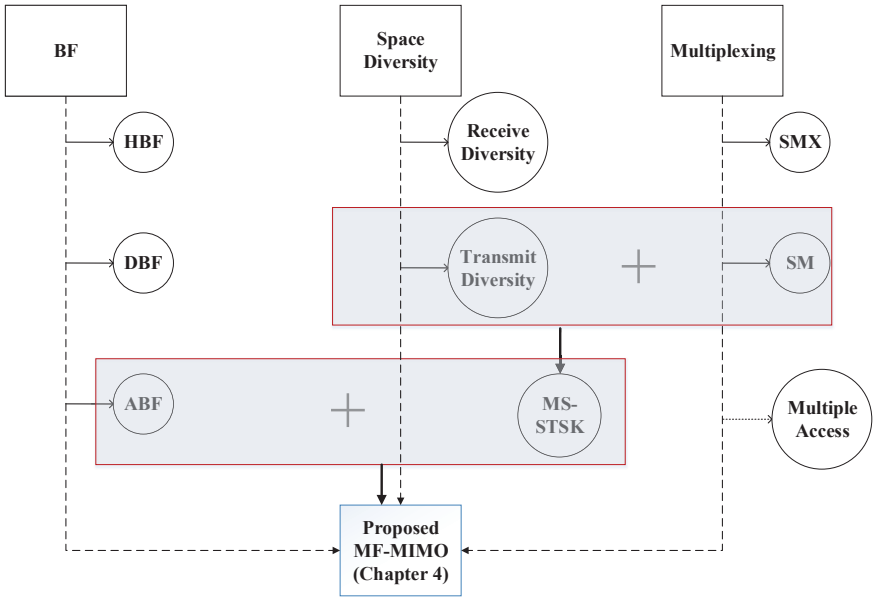

Figure 4.3: Proposed MF-MIMO arrangement. (Note that we rely on analogue beamforming, unless we explicitly refer to either hybrid or digital beamforming.)

processing utilising a MZM and an optical interleaver (OIL). The side-band containing the implicit information[4] is decoded by the RRH of Fig. 4.2. Furthermore, tunable optically aided beamforming can be achieved using optical FBG, which introduces a linear relationship between the time delays and the optical wavelengths by reflecting different wavelengths from different locations inside the FBG discussed in [37, 140]. Moreover, the SM/MS-STSK signals are transmitted over a dispersion-shifted fiber (DSF), which exibits a low dispersion in our proposed wavelength region [13]. This is used for mitigating the dispersion effects imposed on the optical fiber aided beamforming.

Thus, compared to a conventional cellular architecture, where the RF and baseband signal processing are integrated into a base station [1], our proposed design is capable of concentrating the digital baseband processing in the CU. Hence the complexity of the RRH is reduced to that of low-cost filtering, switching and amplification [141] Against the above backdrop, the novel contributions of this chapter are summarised as follows:

[4] In MS-STSK, the implicit information refers to the antenna selection index and dispersion matrix index information.

1. **Intelligent centralised-processing aided A-RoF network design**: We propose a sophisticated A-RoF network for supporting low-complexity SM or MS-STSK combined with all-optical beamforming and up-conversion to mmWave carrier frequencies. More explicitly, all-optical SM/MS-STSK processing is combined with beamforming in the mmWave spectral band. To the best of our knowledge, this is the first time that optical fiber aided analogue beamforming using CFBG is conceived for mmWave communications.

2. **Optical processing aided SM/MS-STSK encoding scheme**: We propose an architecture for carrying both implicit antenna-index-based information and classically modulated information by SM/MS-STSK intrinsically amalgamated with optical processing. Again, this avoids the ADC and RF carrier modulation at the RRH. Instead, an optically up-converted mmWave signal carries the SM and MS-STSK symbols, which are then fed into linear uniform arrays for beamforming, hence requiring no additional electronic signal processing at the RRHs.

The rest of the chapter is organised as follows. Section 4.4 presents the A-RoF aided SM-BF encoding network, where the proposed model is presented and discussed. Then, in Section 4.5, the A-RoF aided MS-STSK-BF scheme is introduced and analysed, followed by our conclusions in Section 5.6. Note that SM is a special case of MS-STSK, we invoke SM firstly for better demonstrating our system.

4.4 A-RoF Network Design for SM-BF

In this section, we propose an all-optical processing aided MF-MIMO [142] system, where SM/MS-STSK, optical upconversion and optical fiber aided beamforming were amalgamated. In A-RoF networks, most of the digital processing is carried out in the CU of Fig. 4.2. In this contribution, we propose a novel A-RoF network carrying SM symbols, which can be used both for the mobile fronthaul or backhaul.

In the proposed network, after the optical aided SM encoding, the SM information is transmitted over the DSF, where the signal is up-converted to a mmWave carrier frequency and linearly time-delayed signals are attained with the aid of FBGs for

achieving an angularly selective beamforming effect. In this section, we first present the conventional SM electronic encoding design and then we discuss the proposed system architecture and its performance.

4.4.1 Conventional Electronic SM

Fig. 4.4 shows the conventional SM encoding process using N_t transmit antennas, where the input bits are partitioned into two streams. The first stream is used for activating one out of the N_t transmit antennas, while the second stream is used for modulating a classical QAM/PSK symbol[5], as shown in Fig. 4.4. Hence, the transmitted symbol implicitly carries the selected antenna index information.

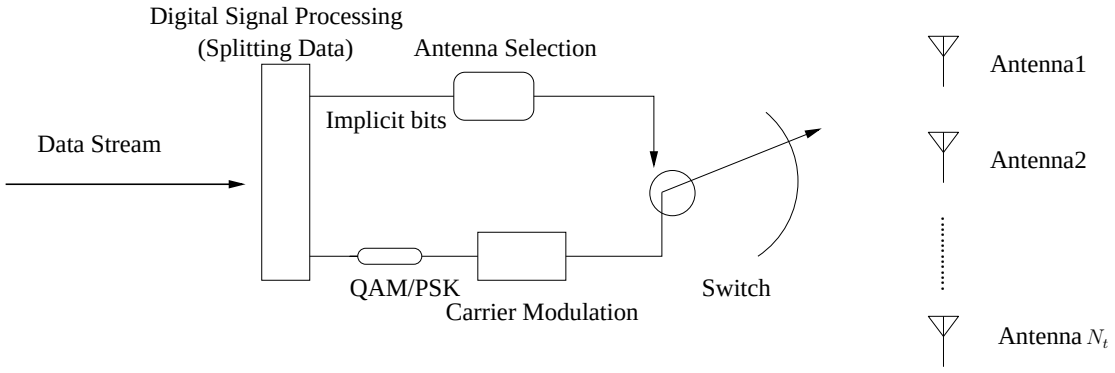

Figure 4.4: Conventional electronic SM encoding scheme used by the base stations of the conventional cellular architecture.

In the traditional architecture, SM encoding is carried out at each BS, adding extra cost and complexity to the small-cell system [1]. By contrast, in our proposed design, the digital processing is concentrated to the CU, as detailed in the following sections. To elaborate a little further, our proposed A-RoF-aided SM design is capable of confining the SM encoding to a single CU, hence substantially easing the burden imposed on small-cell base stations.

4.4.2 Proposed A-RoF-aided SM-BF Design

Upon introducing optical fiber aided beamforming and optical up-conversion, our system transmits the SM symbols using a mmWave carrier and all-optical processing, relying on

[5]In this chapter, we term data symbol for transmission as classic modulated symbol.

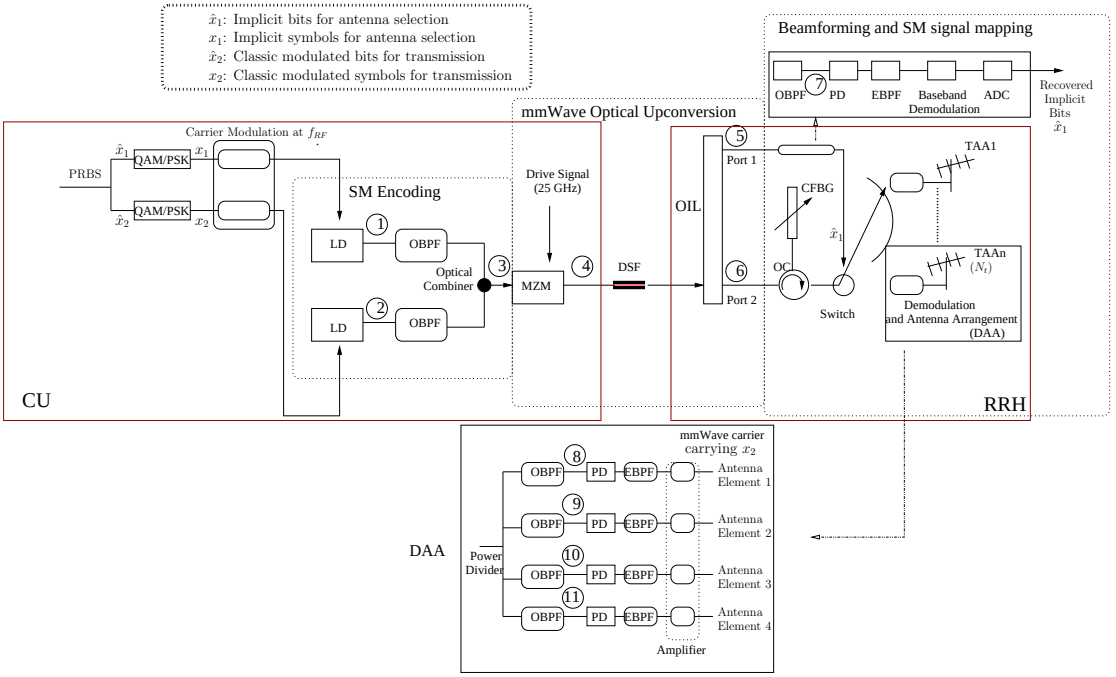

Figure 4.5: A centralised A-RoF aided SM encoding scheme. The CU performs digital modulation, carrier modulation, E/O conversion and SM encoding, while the RRH implements the radio functions (filtering, O/E conversion, photo-detection, amplifying and radio transmission), as well as SM implicit data recovery and SM switching.

the RRHs of Fig. 4.2. Figs. 4.5 and 4.6 highlight the operation of our A-RoF aided SM system and the corresponding spectral-domain manipulations. In the following, we will detail the signal processing in our system of Fig. 4.5, while referring to the corresponding spectral-domain manipulations seen in Fig. 4.6[6].

SM encoding: Similar to the conventional electronic SM encoding scheme, a pseudorandom binary sequence (PBRS) is generated and split into two streams that convey the antenna selection bits $\hat{x}_1$ as well as the classic modulated bits $\hat{x}_2$. Then, as shown in Fig. 4.5, we map the implicit antenna-index bits to a $2^L - QAM/PSK$ scheme, where 2^L represents the number of transmitter antenna elements of each antenna array of Fig. 4.5. Similarly, the classic modulated bits are conveyed by $2^M - QAM/PSK$ symbols according to the system requirements. Note in the interest of explicit clarity that in contrast to the conventional electronic SM encoding scheme, in our amalgamated optical/RF system both SM streams are conveyed by QAM/PSK symbols over the fiber.

[6]The circled numbers of Fig. 4.5 correspond to the numbers in Fig. 4.6.

This ensures that they have the same symbol rate during their transmission in the A-RoF link. For example, if a PRBS block of the bits $b_1...b_3$ is transmitted, b_1, b_2 are used for the implicit antenna-index bits as $\hat{x}_1$ for activating one out of four antenna elements, while b_3 is used for classic BPSK modulated bits for optical transmission as $\hat{x}_2$. To ensure that b_3 is conveyed by the b_1, b_2-based antenna element after the A-RoF link, b_1, b_2 are conveyed by a quadrature phase shift keying (QPSK) symbol.

Afterwards, both types of SM symbols are carried by a RF frequency of f_{RF} and fed into a pair of LDs for direct modulation, as shown in Fig. 4.5. The two LDs are directly modulated by x_1 and x_2 to generate a pair of wideband signals, respectively, as shown at ① and ② of Fig. 4.6. Then, the left side-band of ① carrying x_1 and the right side-band of ② carrying x_2 are retained by the optical bandpass filters (OBPFs) and combined to a new ODSB signal using an optical combiner, as shown in Fig. 4.5 and marked by ③ of Fig. 4.6.

Thus, SM encoding relies on optical double side-band (ODSB) modulation associated with an RF frequency of f_{RF}, where both the implicit symbols x_1 used for antenna selection and the classic modulated symbols x_2 are mapped to one of the side-bands, each using a combination of laser diodes (LDs) and OBPFs.

mmWave optical upconversion: Afterwards, optical modulation is employed using the MZM of Fig. 4.5, where, as demonstrated at ④ of Fig. 4.6, the drive voltage of the MZM can be appropriately tuned in order to copy the ODSB signal carrying x_1 and x_2 to multiple wavelengths. This will result in multi-wavelength signals that can be transmitted over mmWaves, by beneficially exploiting the MZM's non-linearity[7] [19]. Then, the multi-wavelength ODSB signal is transmitted over a DSF at the zero-dispersion wavelength in the vicinity of 1550 nm [13], for the sake of mitigating the dispersion effects, whilst aiming for a constant time-delay. As shown in Fig. 4.5, optical up-conversion is applied using an OIL, as illustrated in Fig. 4.7. The multi-wavelength signal at the fiber's output is fed into the OIL, where the two outputs of Fig. 4.7 provide the beat frequencies representing the mmWave frequency carrying x_2 and the RF frequency f_{RF} carrying x_1, respectively. For example, if a multi-wavelenth signal of the

[7] In Fig. 4.6, we portrayed the comb-like signals for the sake of showing the spectral evolution in our system design in a stylized format. In fact, the amplitude of the corresponding wavelengths relies on both the harmonics' order and on the switching voltage as well as on the amplitude of the MZM's drive voltage, which will be analysed in Section 4.4.2.1.

ODSBs having the center frequencies of λ_1, λ_2 and λ_3, shown in Fig. 5 is fed into the OIL, Port 1 of the OIL retains the optical carrier and the left side-band of λ_2 as well as the right side-bands of λ_1 and λ_3 while Port 2 outputs the remaining spectrum. The OIL acts as a periodic filter, which splits the spectrum for generating a set of appropriately beating frequencies after the PDs of the 'Beamforming and SM signal mapping' block of Fig. 4.5, generating the RF and mmWave frequencies in our proposed system. Generally, Port 1 retains the optical carrier and the left side-bands of λ_{2n} as well as the right side-bands of λ_{2n-1}, while Port 2 outputs the right side-bands of λ_{2n} as well as the optical carrier and the left side-bands of λ_{2n-1}. The corresponding spectra of Port 1 and Port 2 are shown at ⑤ and ⑥ of Fig. 4.6.

Beamforming and SM signal mapping: Following the OIL, the antenna selection bits $\hat{x}_1$ are recovered after passing the signal gleaned at Port 1 of Fig. 4.5 through the OBPF, PD, electronic bandpass filter (EBPF), baseband demodulation and the ADC components, where the OBPF retains the spectrum of ⑦ of Fig. 4.6, the PD achieves the O/E conversion, the EBPF obtains the f_{RF} RF signal and the ADC converts the analogue RF signal to digital symbols for SM switching. The photo-detected RF signal used for antenna selection appears at f_{RF}. On the other hand, the output of Port 2 is fed into a tunable chirped FBG, which imposes a linear time delay on each wavelength by reflecting different wavelength from different locations.

The time-delayed multi-wavelength signal carrying x_2 is then transmitted by the activated antenna, where the photo-detectors of the Demodulation and Antenna Arrangement (DAA) block of Fig. 4.5 receive the corresponding time-delayed wavelengths and then convert them to a mmWave signal having a frequency of $(f_{RF} + f_{drive})$. Therefore, the mmWave signals of the DAA associated with the linear time delays are passed on to the corresponding transmitter antenna array (TAA), whose index has been decoded after the photo detection stage of Fig. 4.5.

More specifically, as shown in Fig. 4.6, the spectra at ① and ② represent the directly modulated ODSB optical signals of the LDs of Fig. 4.5, where x_1 and x_2 are mapped to the side-bands having a center frequency of f_{RF}. Then, following the appropriate filtering by the OBPF after each LD of Fig. 4.5, we obtain a new ODSB, with x_1 being mapped to the left and x_2 to the right side-band, as shown at ③ of Fig. 4.6. The

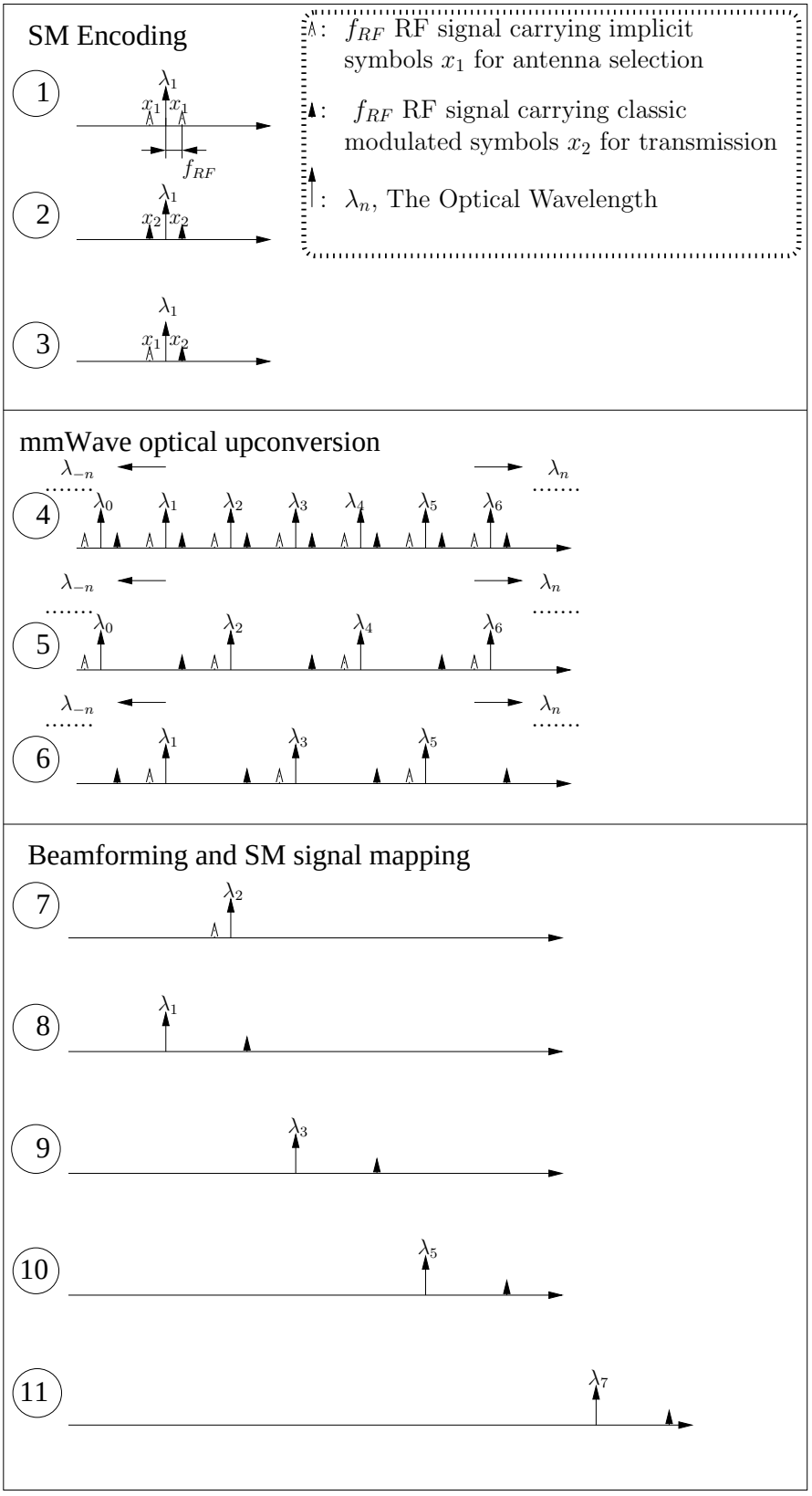

Figure 4.6: Spectral-domain charaterization of proposed system of Fig. 4.5.

ODSB signal is then converted to a multi-wavelength signal by beneficially exploiting the MZM's non-linearity of Fig. 4.5, resulting in the spectra at ④ of Fig. 4.6. The OIL of Fig. 4.5 is then used for appropriately filtering the spectrum to be utilised for mmWave generation and antenna-index bit recovery. The stages ⑤ and ⑥ show the spectrum of port 1 and port 2 of Fig. 4.5, where the corresponding frequencies will be processed in order to form stages ⑦, ⑧, ⑨, ⑩ and ⑪ of Fig. 4.6. The photo-detected RF signal after stage ⑦ is used for antenna selection, while those of ⑧, ⑨, ⑩ and ⑪ are used for mmWave signal generation. The details of these spectral shaping operations will be discussed in the following sections.

In contrast to the conventional SM encoding scheme of Fig. 4.4, our proposed system is capable of carrying the SM symbols encapsulated in a multi-wavelength optical signal over the optical fiber. At the fiber's output, the implicit antenna index bits are recovered, while the corresponding classic modulated symbols are modulated by a up-converted mmWave signal. Our design eliminates the need for both the ADC and the DAC at the RRH, which substantially reduces the cost and complexity of the RRH. The optically up-converted and beamformed mmWave signal can be directly fed into the TAA, without any additional electronic processing for modulation and demodulation, where the electronic filters and amplifiers are used for ensuring that the amplitudes of the mmWave signals emitted from each TAA element are appropriately adjusted. In the following, we detail both the rationale and mathematical model of our system regarding mmWave generation and beamforming.

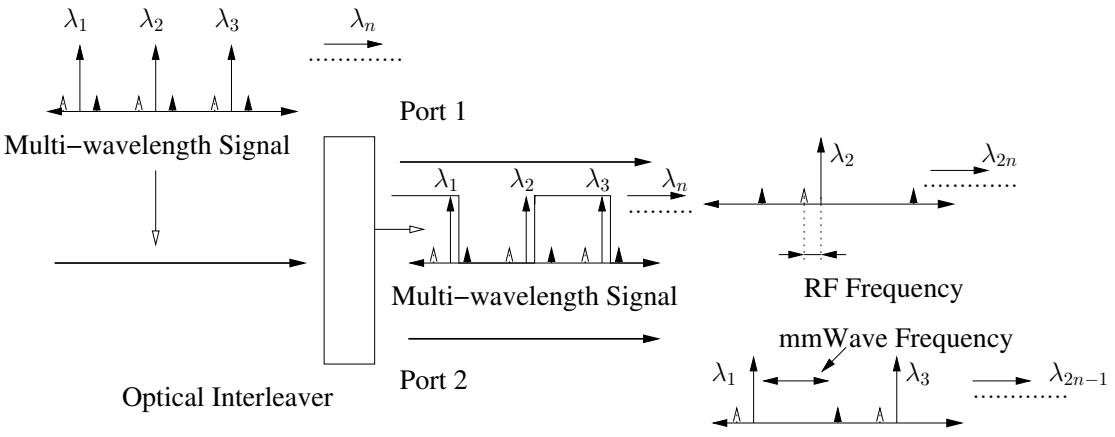

Figure 4.7: An optical interleaver.

4.4.2.1 mmWave Generation

As presented in the middle dashed box of Fig. 4.5, the MZM and OILs contribute to the mmWave signal generation. The harmonics generated by the MZM's non-linearity result in multiple wavelengths, where each wavelength carries a copy of the ODSB signal of ③ of Fig. 4.6[8]. Assuming that E_{in} is the ODSB input of the MZM, as detailed in [143], higher-order optical side-bands are generated relying on the voltage of the drive signal imposed on the MZM. The resultant optical signal is given by:

$$\begin{aligned} E_{MZM}(t) &= cos[\pm\frac{\pi}{4} + \frac{\pi V_{dr} cos(\omega_{LO})}{2V_\pi}]E_{in}(t) \\ &= \frac{E_{in}(t)}{\sqrt{2}}[J_0(\frac{\pi|V_{dr}|}{2V_\pi}) + 2\sum_{n=1}^{\infty}(-1)^n J_{2n}(\frac{\pi V_{dr}}{2V_\pi})cos(2n\omega_{LO}t) \\ &\pm 2\sum_{n=1}^{\infty}(-1)^n J_{2n-1}(\frac{\pi V_{dr}}{2V_\pi})cos((2n-1)\omega_{LO}t)], \end{aligned} \tag{4.1}$$

where the E_{MZM} is the output field of the MZM with a switching voltage of V_π, which induces a phase shift of π for each arm, while V_{dr} is the drive voltage of the angular center frequency of $\omega_{LO}/(2\pi)$. Here, $J_n(\frac{\pi V_{dr}}{2V_\pi})$ is the Bessel function of the first kind and order n, which determines both the number and the amplitude of the side-bands.

The resultant multi-wavelength ODSB signal carrying the RF of ω_{RF} is then fed into the OIL of Fig. 4.5, after transmission over the optical fiber, where the OIL removes some of the multi-wavelength signal frequencies. Explicitly, in the case of Port 2 of the OIL of Fig. 4.5, λ_1 associated with the left side-band, λ_3 with the right side-band as well as the right side-band of λ_2 and λ_4 are filtered out, as shown at ⑤ of Fig. 4.6. In this case, the beat frequency between λ_1 and the right side-band of λ_3 is photo-detected, which generates a frequency of $\omega_{RF} + \omega_{LO}$, namely 28 GHz in our design and completes the mmWave frequency generation. The up-converted frequency relies on the frequency ω_{rf} of the drive voltage imposed on the MZM of Fig. 4.5, which can be appropriately tuned in order to up-convert the signal to any desired frequency in the mmWave spectrum.

[8] λ_1 of Fig. 4.6 is the LD's optical carrier.

More specifically, if a RF signal of center frequency of 3 GHz is directly modulated by the LDs of Fig. 4.5, a multi-wavelength ODSB signal carrying a 3 GHz RF signal is then generated with the aid of a MZM's drive signal of 25 GHz, resulting in a wavelength spacing of 25 GHz among the neighbouring λ_n components. Then, as shown in stages ④, ⑤ and ⑥ of Fig. 4.6, the OIL of Fig. 4.5 removes some of the frequencies output by Port 1 and Port 2 of the OIL. Thus, on one hand, the output signal of Port 1 is filtered by the OBPF seen at ⑦ of Fig. 4.5. Then, after processing by the Beamforming and SM signal mapping block of Fig. 4.5, the beat frequency becomes 3 GHz, which is used for the implicit bits recovery of SM. On the other hand, following the transmission of the output signal of Port 2 of the OIL in the CFBG scheme of Fig. 4.5 for beamforming, the signal is fed into the DAA of Fig. 4.5, resulting in the time-delayed signals of stages ⑧, ⑨, ⑩ and ⑪ of Fig. 4.5. After the PD, the beat frequency obtained is the up-converted mmWave frequency of 28 GHz. The beamforming scheme will be further detailed in the next section.

4.4.2.2 Beamforming

Due to the short mmWave propagation range, we exploit our optical signal processing aided beamforming scheme to extend the propagation range of mmWave communications. In our design, beamforming is introduced by exploiting the constant time-delay difference between the neighbouring antenna elements of each transmitter, where the constant time delay difference is obtained with the aid of CFBG, which impose different time-delays on different wavelengths due to their different locations of reflection [140]. Furthermore, CFBG supports true-time delay based beamforming for wideband signals, which is achieved by avoiding the beam-squinting introduced by the popular phase shifting based beamforming scheme [37].

The signal generated at the output of the OIL of Fig. 4.5 is transmitted to an optical circulator (OC), which is a three-port component, where the time-delayed multi-wavelength signals reflected by CFBG are forwarded to one of the DAA block of Fig. 4.5. The time delay introduced by CFBG is linearly proportional to the transmitting wavelengths, which can be translated to a specific beamsteering direction [144]. Furthermore, the reflected frequency spectrum of the CFBG can be appropriately tuned to

control the time delay, thus adjusting the beamsteering direction [42]. Subsequently, the output of the OC is split into several branches shown in the DAA block of Fig. 4.5. As shown at ⑧, ⑨, ⑩, ⑪ of Fig. 4.6, the desired wavelength is retained with the aid of optical BPF in DAA of Fig. 4.5. Thus, each branch outputs the carrier associated with the same symbol but different delays. After the PD and electronic BPF of the DAA of Fig. 4.5, the delayed carriers are fed into the antenna array elements, which can be translated into different beamforming patterns according to the appropriately tuned time delay differences. We will demonstrate that our system is capable of both mmWave carrier generation and beamforming with the aid of the CFBG-induced time-delay as detailed mathematically in the following section.

4.4.3 Mathematical Model of Beamforming for Multi-wavelength Signals

Since the time-delay imposed by the CFBG is applied in the optical domain, there may be a delay-difference between the modulated optical signal and its corresponding photo-detected beat signal. In this section, we show mathematically that the time-delay differences between the photo-detected RF signals of the neighbouring antennas remain constant. As mentioned in Section 4.4.2, the RF signal is directly modulated by LDs and the input optical field of the MZM of Fig. 4.5 is formulated as:

$$E_{in}(t) = \sqrt{P_{Laser}} e^{j\omega_{oc}t}[1 + cos(\omega_{RF}t)], \tag{4.2}$$

where P_{Laser} is the LD's output power and ω_{oc} denotes the optical carrier's angular frequency corresponding to λ_1 of Fig. 4.6. The MZM output field expressed in Equation

(4.1) can be combined with Equation (4.2) to arrive at:

$$
\begin{aligned}
&E_{MZM}(t) \\
&\quad = cos(\pm\frac{\pi}{4} + \frac{\pi V_{dr} cos(\omega_{LO})}{2V_\pi}) E_{in}(t) \\
&\quad = \frac{\sqrt{P_{laser}}[1 + cos(\omega_{RF} t)] e^{j\omega_{oc} t}}{\sqrt{2}} [J_0(\frac{\pi |V_{dr}|}{2V_\pi}) \\
&\quad + 2\sum_{n=1}^{\infty} (-1)^n J_{2n}(\frac{\pi V_{dr}}{2V_\pi}) cos(2n\omega_{LO} t) \\
&\quad \pm 2\sum_{n=1}^{\infty} (-1)^n J_{2n-1}(\frac{\pi V_{dr}}{2V_\pi}) cos((2n-1)\omega_{LO} t)] \\
&\quad = \frac{\sqrt{P_{laser}} e^{j\omega_{oc} t}}{\sqrt{2}} [J_0(\frac{\pi |V_{dr}|}{2V_\pi})[1 + cos(\omega_{RF} t)] \\
&\quad + 2\sum_{n=1}^{\infty} (-1)^n J_{2n}(\frac{\pi V_{dr}}{2V_\pi}) [cos(2n\omega_{LO} t) \\
&\quad + \frac{cos((2n\omega_{LO} + \omega_{RF})t) + cos((2n\omega_{LO} - \omega_{RF})t)}{2}] \\
&\quad \pm 2\sum_{n=1}^{\infty} (-1)^n J_{2n-1}(\frac{\pi V_{dr}}{2V_\pi}) [cos((2n-1)\omega_{LO} t) \\
&\quad + \frac{cos(((2n-1)\omega_{LO} + \omega_{RF})t) + cos(((2n-1)\omega_{LO} - \omega_{RF})t)}{2}] \\
&\quad = \frac{\sqrt{P_{laser}}}{\sqrt{2}} [J_0(\frac{\pi |V_{dr}|}{2V_\pi})[e^{j\omega_{oc} t} + e^{j(\omega_{oc} + \omega_{RF})t}/2 \\
&\quad + e^{j(\omega_{oc} t - \omega_{RF} t)}/2] + 2\sum_{n=1}^{\infty} (-1)^n J_{2n}(\frac{\pi V_{dr}}{2V_\pi}) \\
&\quad \times [e^{j(\omega_{oc} + 2n\omega_{LO})t}/2 + e^{j(\omega_{oc} - 2n\omega_{LO})t}/2 \\
&\quad + \frac{e^{j(\omega_{oc} + 2n\omega_{LO} + \omega_{RF})t}/2 + e^{j(\omega_{oc} - 2n\omega_{LO} - \omega_{RF})t}/2}{2} \\
&\quad + \frac{e^{j(\omega_{oc} + 2n\omega_{LO} - \omega_{RF})t}/2 + e^{j(\omega_{oc} - 2n\omega_{LO} + \omega_{RF})t}/2}{2}] \\
&\quad \pm 2\sum_{n=1}^{\infty} (-1)^n J_{2n-1}(\frac{\pi V_{dr}}{2V_\pi}) \\
&\quad \times [\frac{e^{j(\omega_{oc} + (2n-1)\omega_{LO})t} + e^{j(\omega_{oc} - (2n-1)\omega_{LO})t}}{2} \\
&\quad + \frac{e^{j(\omega_{oc} + (2n-1)\omega_{LO} + \omega_{RF})t}/2 + e^{j(\omega_{oc} - (2n-1)\omega_{LO} - \omega_{RF})t}/2}{2} \\
&\quad + \frac{e^{j(\omega_{oc} + (2n-1)\omega_{LO} - \omega_{RF})t}/2 + e^{j(\omega_{oc} - (2n-1)\omega_{LO} + \omega_{RF})t}/2}{2}].
\end{aligned}
\tag{4.3}
$$

Thus, after the OIL and the DAA block of Fig. 4.5, we arrive at multiple mmWave

signals of the same frequency but having different time-delays. Here, the signal at the output of Port 2 after the OIL block of Fig. 4.5 can be expressed from Equation (4.4) as follows:

$$
\begin{aligned}
&E_{IL_{bottom}}(t) \\
&\quad = \frac{\sqrt{P_{laser}}}{\sqrt{2}}[J_0(\frac{\pi|V_{dr}|}{2V_\pi})(\frac{e^{j(\omega_{oc}-\omega_{RF})t}}{2} + e^{j\omega_{oc}t}) \\
&\quad + 2\sum_{n=1}^{\infty}(-1)^n J_{2n}(\frac{\pi V_{dr}}{2V_\pi}) \\
&\quad (\frac{e^{j(\omega_{oc}-2n\omega_{LO}-\omega_{RF})t} + e^{j(\omega_{oc}+2n\omega_{LO}-\omega_{RF})t}}{4} \\
&\quad + \frac{e^{j(\omega_{oc}+2n\omega_{LO})t} + e^{j(\omega_{oc}-2n\omega_{LO})t}}{2}) \\
&\quad \pm 2\sum_{n=1}^{\infty}(-1)^n J_{2n-1}(\frac{\pi V_{dr}}{2V_\pi}) \\
&\quad \frac{e^{j(\omega_{oc}-(2n-1)\omega_{LO}+\omega_{RF})t} + e^{j(\omega_{oc}+(2n-1)\omega_{LO}+\omega_{RF})t}}{4}].
\end{aligned} \tag{4.4}
$$

After the OIL, the beat frequency can be obtained by the DAA block seen at the bottom of Fig. 4.5, where the right side-band of even wavelength (λ_2 and λ_4...) and its neighbouring wavelengths' optical carrier (λ_1 and λ_3...) are retained and mapped to each line of the DAA block, as shown in Fig. 4.6. Thus, assuming that no time-delay scheme is applied, the resultant photo-detected signal of the top line of the DAA block of Fig. 4.5 is given as follows:

$$
\begin{aligned}
&E_{PD}(t) \\
&\quad \propto |E_{IL}(t)|^2 \\
&\quad = |\frac{\sqrt{P_{laser}}}{\sqrt{2}}[J_0(\frac{\pi|V_{dr}|}{2V_\pi})\frac{e^{j\omega_{oc}t}}{2} \mp 2J_1(\frac{\pi V_{dr}}{2V_\pi}) \\
&\quad \frac{e^{j(\omega_{oc}+\omega_{LO}+\omega_{RF})t}}{2}]|^2 \\
&\quad = \frac{P_{laser}}{8}[J_0^2(\frac{\pi|V_{dr}|}{2V_\pi}) + 4J_1^2(\frac{\pi V_{dr}}{2V_\pi}) \mp 4J_0(\frac{\pi V_{dr}}{2V_\pi})J_1(\frac{\pi V_{dr}}{2V_\pi}) \\
&\quad \times cos(\omega_{LO}+\omega_{RF})t].
\end{aligned} \tag{4.5}
$$

In order to achieve the desired beamforming effect, having an identical time-delay

difference between neighbouring wavelengths is required. Thus, in terms of the first line of DAA shown in Fig. 4.5, which feeds the signal to antenna element 1 of each TAA, the CFBG applies the time-delay t_1 to the optical carrier λ_1 and t_2 to λ_2's right side-band x_2 upon introducing $\Delta t = t_2 - t_1$. The corresponding photo-detected beat signal is expressed as follows:

$$
\begin{aligned}
&E_{PD_{delayed}}(t) \\
&\quad \propto |E_{IL_{delayed}}(t)|^2 \\
&\quad = |\frac{\sqrt{P_{laser}}}{\sqrt{2}}[J_0(\frac{\pi|V_{dr}|}{2V_\pi})\frac{e^{j\omega_{oc}(t-t_1)}}{2} \mp 2J_1(\frac{\pi V_{dr}}{2V_\pi}) \\
&\quad \frac{e^{j(\omega_{oc}+\omega_{LO}+\omega_{RF})(t-t_2)}}{2}]|^2 \\
&\quad = \frac{P_{laser}}{8}[J_0^2(\frac{\pi|V_{dr}|}{2V_\pi}) + 4J_1^2(\frac{\pi V_{dr}}{2V_\pi}) \mp 4J_0(\frac{\pi V_{dr}}{2V_\pi})J_1(\frac{\pi V_{dr}}{2V_\pi}) \\
&\quad \times cos((\omega_{LO}+\omega_{RF})(t-t_2) + \omega_{oc}(t_1-t_2))] \\
&\quad = \frac{P_{laser}}{8}[J_0^2(\frac{\pi|V_{dr}|}{2V_\pi}) + 4J_1^2(\frac{\pi V_{dr}}{2V_\pi}) \mp 4J_0(\frac{\pi V_{dr}}{2V_\pi})J_1(\frac{\pi V_{dr}}{2V_\pi}) \\
&\quad \times cos((\omega_{LO}+\omega_{RF})(t-t_2-\frac{\omega_{oc}\Delta t}{\omega_{LO}+\omega_{RF}}))].
\end{aligned} \tag{4.6}
$$

Similarly, assuming that the delay t_3 is applied to the optical carrier λ_3 of ⑥ of Fig. 4.6 , while t_4 to the right side-band of λ_4 and that $\Delta t = t_2 - t_1 = t_4 - t_3$, the photo-detected signal of the second line of DAA block of Fig. 4.5, which is fed into the antenna element 2 of each TAA of Fig. 4.5 becomes:

$$
\begin{aligned}
&E_{PD_{delayed_2}}(t) \\
&\quad \propto |\frac{\sqrt{P_{laser}}}{\sqrt{2}}[-2J_2(\frac{\pi V_{dr}}{2V_\pi})\frac{e^{j(\omega_{oc}+2\omega_{LO})(t-t_3)}}{2} \pm 2J_3(\frac{\pi V_{dr}}{2V_\pi}) \\
&\quad \frac{e^{j(\omega_{oc}+3\omega_{LO}+\omega_{RF})(t-t_4)}}{2}]|^2 \\
&\quad = \frac{P_{laser}}{8}[4J_2^2(\frac{\pi|V_{dr}|}{2V_\pi}) + 4J_3^2(\frac{\pi V_{dr}}{2V_\pi}) \mp 8J_2(\frac{\pi V_{dr}}{2V_\pi})J_3(\frac{\pi V_{dr}}{2V_\pi}) \\
&\quad \times cos((\omega_{LO}+\omega_{RF})(t-t_4) + (\omega_{oc}+2\omega_{LO})(t_3-t_4))] \\
&\quad = \frac{P_{laser}}{8}[4J_2^2(\frac{\pi|V_{dr}|}{2V_\pi}) + 4J_3^2(\frac{\pi V_{dr}}{2V_\pi}) \mp 8J_2(\frac{\pi V_{dr}}{2V_\pi})J_3(\frac{\pi V_{dr}}{2V_\pi}) \\
&\quad \times cos((\omega_{LO}+\omega_{RF})(t-t_4-\frac{(\omega_{oc}+2\omega_{LO})\Delta t}{\omega_{LO}+\omega_{RF}}))].
\end{aligned} \tag{4.7}
$$

Thus, following the same philosophy, the photo-detected signal of the third line of DAA of Fig. 4.5 is,

$$
\begin{aligned}
&E_{PD_{delayed_3}}(t) \\
&\quad \propto \frac{P_{laser}}{8}[4J_4^2(\frac{\pi|V_{dr}|}{2V_\pi}) + 4J_5^2(\frac{\pi V_{dr}}{2V_\pi}) \mp 8J_4(\frac{\pi V_{dr}}{2V_\pi})J_5(\frac{\pi V_{dr}}{2V_\pi}) \\
&\quad \times cos((\omega_{LO}+\omega_{RF})(t - t_6 - \frac{(\omega_{oc}+4\omega_{LO})\Delta t}{\omega_{LO}+\omega_{RF}}))], \qquad (4.8)
\end{aligned}
$$

where the delay t_5 is applied to the optical carrier λ_5 of ⑥ of Fig. 4.6, while t_6 is applied to the right side-band of λ_6 and $\Delta t = t_2 - t_1 = t_4 - t_3 = t_6 - t_5$.

By comparing Equations (4.6), (4.7) and (4.8), it becomes clear that there exists some delay between each photo-detected output signal and for antenna element of each DAA, the delay will not be exactly the same. However, the time delay difference of the photo-detected signals fed into neighbouring antenna elements of the DAA block of Fig. 4.5 will be constant. Specifically, due to the linear relationship between the time-delay and the wavelengths, we obtain $\Delta t = t_2 - t_1 = t_4 - t_3 = t_6 - t_5$ and $t_2 - t_4 = t_4 - t_6$. The time-delay difference of the output signals between antenna element 1 and antenna element 2 of the DAA block of Fig. 4.5 is $(t_4 - t_2) + \frac{2\omega_{LO}\Delta t}{\omega_{LO}+\omega_{RF}}$, while for antenna element 2 and antenna element 3 is $(t_6 - t_4) + \frac{2\omega_{LO}\Delta t}{\omega_{LO}+\omega_{RF}}$. Thus, the time difference remains constant for each neighbouring antenna element of each TAA of Fig. 4.5.

Hence, we have shown mathematically that our beamforming signal generation is capable of maintaining a constant time-delay difference between the neighbouring photo-detected mmWave frequencies fed into different antenna elements. Thus, our all-optical design is capable of supporting beamforming, while simultaneously implementing mmWave upconversion.

4.4.4 Beamforming Results

In our system, a 30 mm CFBG is used for introducing the delay required at the different wavelengths in order to support beamsteering. The time-delay imposed on the different wavelengths when the total chirp of the grating period of CFBG is set to 1.05 nm, which represents the difference between the first period and the last period in the CFBG. Our

simulations were carried out by using the OPTGRATING software and the delay vs wavelength and frequency is shown in Fig. 4.8, where the wavelength range spans from 1549 nm to 1551 nm.

Thus, the spectral width, which is refered to as the spectral range of reflected wavelength and changes with the total chirp [47], determines the time-delay difference as a function of frequency spacing. Proposed by [47], the total spectral width as well as total chirp can be adjusted by tuning a supported beam's deflection, resulting in a linear time-delay difference vs spectral width.

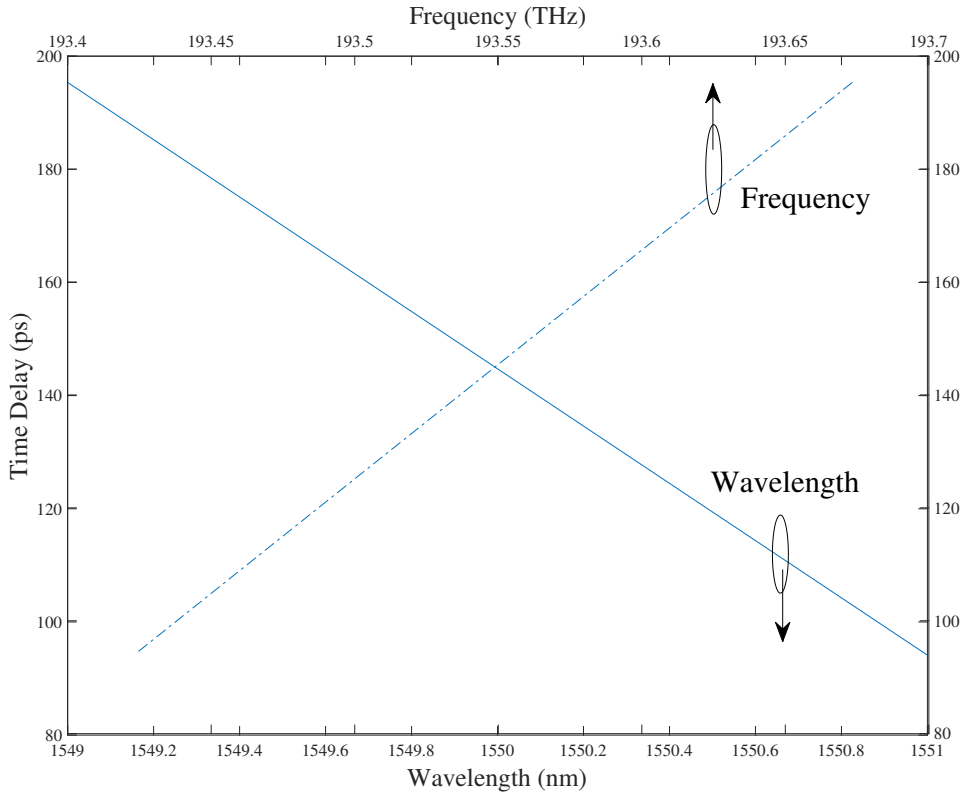

Figure 4.8: Linear time delay vs wavelength and frequency of CFBG with the total chirp of 1.05 nm.

Furthermore, as analysed in Section 4.4.3, the CFBG facilitates a constant time-delay difference of $(t_4 - t_2) + \frac{2\omega_{LO}\Delta t}{\omega_{LO}+\omega_{RF}}$, where Δt is the time-delay difference for a 28 GHz spacing and $t_4 - t_2$ is a time-delay difference at a 50 GHz spacing. Thus, according to the linear relationship seen in Fig. 4.8 and 4.9, the time-delay difference between the adjacent antenna elements is 77.6 ps, when a total chirp of 1.05 nm is applied. Then, by changing the total chirp of the tunable CFBG of Fig. 4.5, we obtain the corresponding

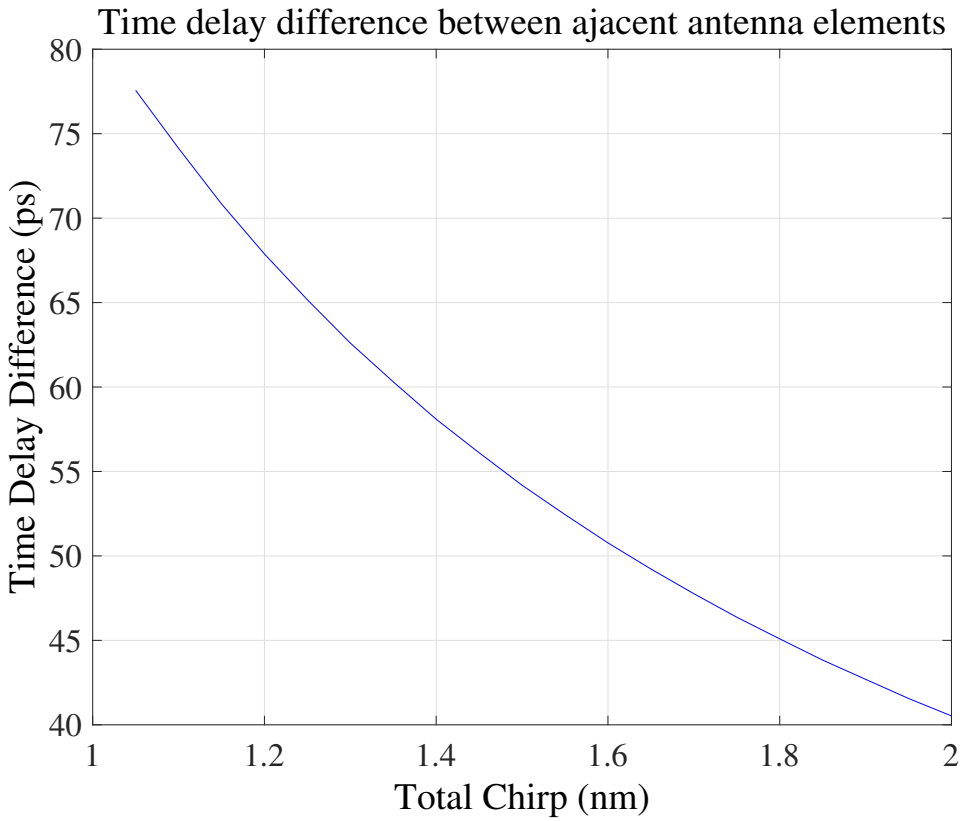

Figure 4.9: Total chirp vs time delay difference.

relationship between the total chirp and the time-delay difference regarding our design as shown in Fig. 4.9, where the time-delay difference range spans from 77.6 ps to 40.6 ps, when increasing the total chirp from 1.05 nm to 2.05 nm with a step-size of 0.05 nm. Then, according to the time-delay difference range, we obtain a beam coverage range of almost 360°, as shown in Fig. 4.10.

4.4.5 System Performance Results and Discussions

In this section we analyse the performance of our SM system employing A-RoF combined with all-optical beamforming and up-conversion to mmWave frequency. We compare our proposed system to the conventional SM system operating without A-RoF in the context of a single-RRH for verifying our centralised design philosophy, which only imposes an almost negligible performance degradation. However, before discussing the results, let us first consider the MIMO channel model after the fiber transmission and study its effect on the system's performance.

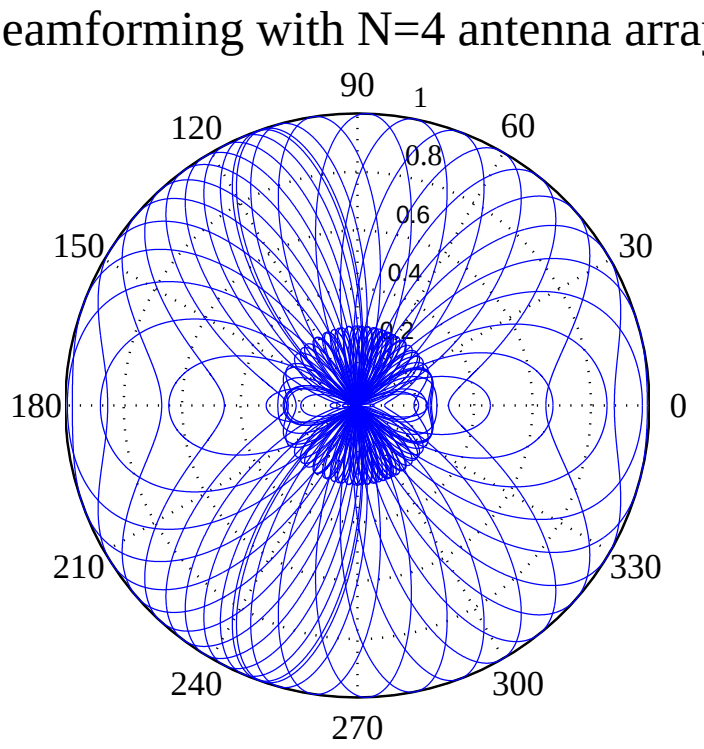

Figure 4.10: Beamforming pattern.

In conventional MIMO systems employing N_t transmit antennas and N_r receive antennas, we model the received signal using $\mathbf{Y} = \mathbf{HX}+\mathbf{n}$, where $\mathbf{Y}$ represents the received symbol vector of size $(N_r \times 1)$, $\mathbf{H}$ is the MIMO channel matrix of size $(N_r \times N_t)$, $\mathbf{X}$ denotes the transmitted symbol vector of size $(N_t \times 1)$ and $\mathbf{n}$ is a $(N_r \times 1)$-element additive white Gaussian noise (AWGN) vector. However, during its fiber-based transition, the symbol vector $\mathbf{X}$ is affected by the fiber impairments, such as fiber attenuation, chromatic dispersion and fiber non-linearity in addition to the noise imposed by photo detection [13]. Hence, in our system we model the SM based MIMO transmission after fiber-based transmission as follows:

$$\mathbf{Y} = \mathbf{H}\alpha\mathbf{X} + \mathbf{n}, \tag{4.9}$$

where α includes the effect of the fiber impairments and optical noise, while $\mathbf{n}$ includes the effect of the AWGN imposed by the RF circuits. Note that the channel state information now includes the wireless channel fading as well as the fiber impairments and

these are jointly estimated at the receiver. In other words, the receiver will estimate $\mathbf{H}\alpha$.

Furthermore, in the proposed system, the beamsteering direction has to be known at the transmitter and this problem has been widely discussed in the literature, where several accurate angle of departure (AoD) estimation techniques have been proposed [145, 146]. Based on the above-mentioned design, we simulated our A-RoF network and compared the BER of the received signal to that of its equivalent electronic SM counterpart dispensing with A-RoF transmission. Table 4.1 summarises the parameters used in our system. The bit rate given is the joint bit rate of implicit bits and classic modulated bits, where, for example, a classic modulated BPSK scheme of 1 Gbps can achieve a joint bit rate of 2 Gbps for two-antenna SM and 3 Gbps for four-antenna SM. The MS-STSK scheme applies the bit rate similarly, which is detailed in [121].

Parameter	Value
Bit rate	2 Gbps (2-antenna SM) 3 Gbps (4-antenna SM)
RF signal	3 GHz
LD center wavelength	1550 nm
LD power	1 mW
Drive frequency (MZM)	25 GHz
Achieved mmWave frequency	28 GHz
MZM mode	Push-pull mode
Fiber type	DSF
Fiber length	10 km
Channel model	Split-step Fourier method
Modulation type	BPSK
Wireless channel	Rayleigh fading channel
Wireless detection	ML detection
Beamforming type	4 antenna elements
Simulation environment	MATLAB

Table 4.1: Simulation parameter.

An RF signal having a 3 GHz carrier is directly modulated by the LDs of Fig. 4.5, while a drive frequency of 25 GHz is used by the MZM. This allows up-converting the 3 GHz signal to a mmWave signal of 28 GHz. The resultant frequency depends on the specific combination of the RF and the drive frequency of the MZM. Owing to the utilisation of the DSF, where the zero-dispersion wavelength is in the vicinity of 1550 nm, the proposed design is capable of mitigating the fiber dispersion hence achieving an

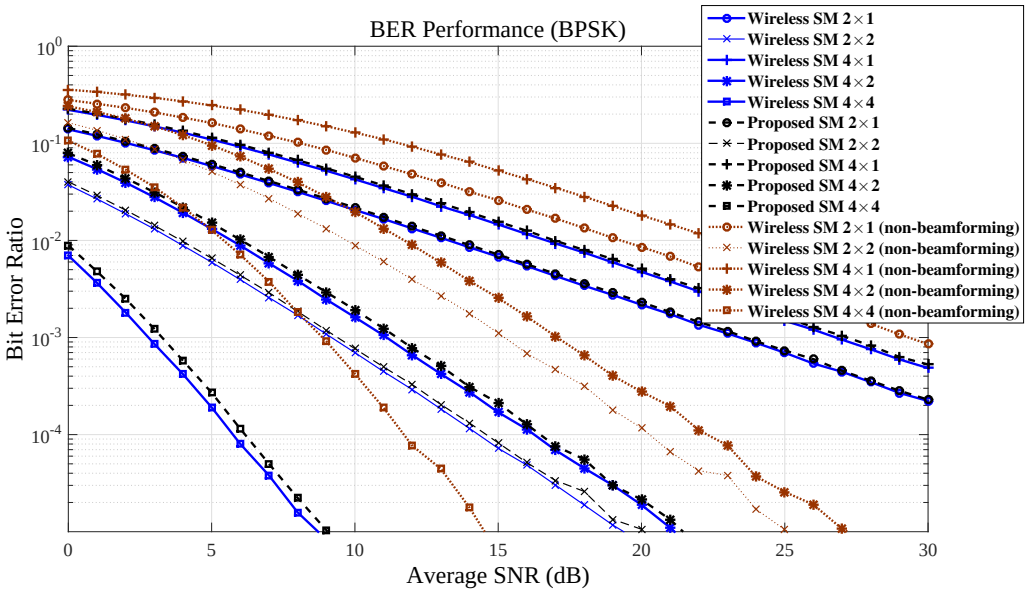

Figure 4.11: The BER performance of our SM scheme compared to that of the conventional electronic SM scheme using the parameters summarised in Table 4.1.

improved beamforming performance. We employed 4 elements per TAA for the sake of showing the benefits of beamforming.

In order to show that our proposed A-RoF system has a minimal impact on the BER performance compared to that of the conventional SM system, we transmit our mmWave signal over the wireless channel and then compare the performance of the two systems. The beamformed mmWave SM signal obtained after A-RoF transmission is impaired by the mmWave wireless channel [126]. Fig. 4.11 shows the BER performance of $(N_t \times N_r)$=(2×1), (2×2), (4×1), (4×2) and (4×4) MIMO systems operating both with and without A-RoF, while analogue beamforming is employed at the transmitter and receiver. Again, four-element TAAs are employed for attaining beamforming in our simulated system.

In the conventional electronic SM encoding scheme of Section 4.4.1, the antenna selection is based on implicitly conveyed symbols. In our proposed system, we modulate the implicit symbol and the classically modulated symbol onto each side-band of the ODSB signal generated by the LDs of Fig. 4.5.

Furthermore, we applied the implicit bits to a 2^L-PSK/QAM modulation scheme,

where 2^L also represents the number of antenna elements, while the classic modulated bits on BPSK format. Then, before feeding the antennas, the corresponding 2^L-PSK/QAM symbols are recovered and then the implicit bits will select the activated antenna transmitting the up-converted mmWave signals carrying the modulated BPSK symbols. Thus, the implicit bits of the 2-antenna SM scheme are carried in the left side-band of Fig. 4.5 as a BPSK symbol, while for the 4-antenna case, they are modulated as QPSK. The bit rate of the classic BPSK modulated bits is 1 Gbps, while the BPSK implicit bits convey a bit rate of 1 Gbps, and the QPSK implicit bits support a bit rate of 2 Gbps, hence achieving a multiplexed bits rate of 2 Gbps for our 2-antenna SM and 3 Gbps for 4-antenna SM.

As shown in Fig. 4.11, when no optical amplifier is used, the BER performance of our proposed system shows a slight degradation, which is caused by the fiber's attenuation, non-linearity and optical noise. This degradation can be readily mitigated by introducing an optical amplifier, as shown in the next section in the context of MS-STSK. Moreover, in Fig. 4.11, the BER performance of wireless systems dispensing with beamforming is shown, where a 6 dB SNR gain is achieved by beamforming using $N = 4$ antenna arrays.

As observed in Fig. 4.11, by employing lower-complexity RRHs, our proposed SM scheme shows a slight BER degradation in comparison to the conventional SM scheme. In the following scheme, we incorporate MS-STSK into our system, which is a generalized architecture subsuming both SM and STSK.

4.5 A-RoF Network Design for MS-STSK-BF

In this section, the MS-STSK scheme is intrinsically amalgamated with our A-RoF downlink combined with all-optical beamforming and upconversion to a mmWave frequency for transmission over the mmWave wireless channel.

4.5.1 Conventional MS-STSK Schemes

MS-STSK was proposed in [106] as a generalization of SM and STSK, where the data bit sequence is partitioned into three streams that convey the antenna selection, the

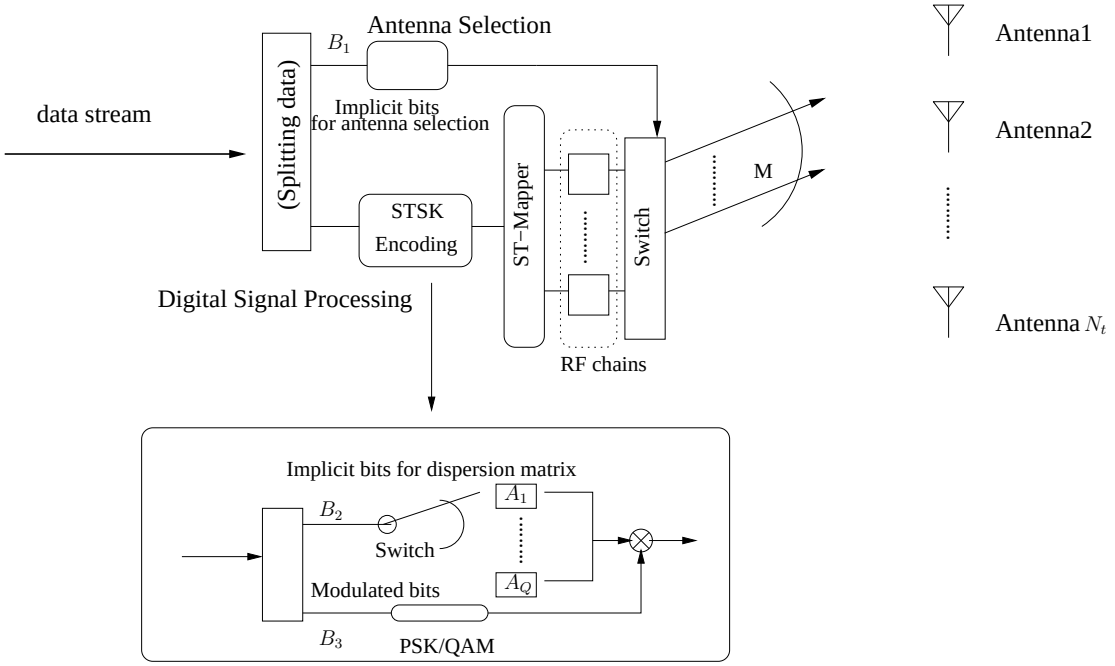

Figure 4.12: Conventional electronic MS-STSK encoding scheme employed at the base stations of the conventional cellular architecture.

dispersion matrix selection and the PSK/QAM modulated symbol. As shown in Fig. 4.12, the data stream is divided into three parts: the bit stream B_1 is used for antenna selection, while the bit streams B_2 and B_3 are used for STSK encoding. In STSK encoding, $B_2 = log_2 Q$ bits are used for selecting one out of Q dispersion matrices, while B_3 is represented by the PSK/QAM symbol. The output of the STSK encoder is transmitted using N_{RF} RF chains, which are switched to a specific combination of N_{RF} out of the N_t antennas with the aid of the antenna selection unit. Hence, the B_1 and B_2 bit streams of Fig. 4.12 are implicitly conveyed over the activated antenna combination (AC) index and the dispersion matrix selected, respectively.

The MS-STSK scheme is capable of utilising a compelling diversity and multiplexing trade-off [106]. As mentioned above, MS-STSK can be introduced into our system by imposing a slight extra complexity on the RRH compared to the A-RoF-aided SM design of Fig. 4.5. In this section, we denote the MS-STSK system as MS-STSK(N_t,M,N_r,T,Q,$\mathcal{L} - PSK/QAM$), where each symbol is characterised in Table 4.2. In the following section, we will discuss our A-RoF-aided MS-STSK design.

Parameter	Representation
N_t	Transmitter antenna
M	STSK space dimension
Nr	Receive antenna
Q	Number of dispersion matrix
T	STSK time slots
$\mathcal{L}$	PSK/QAM constellation size

Table 4.2: MS-STSK symbol notations.

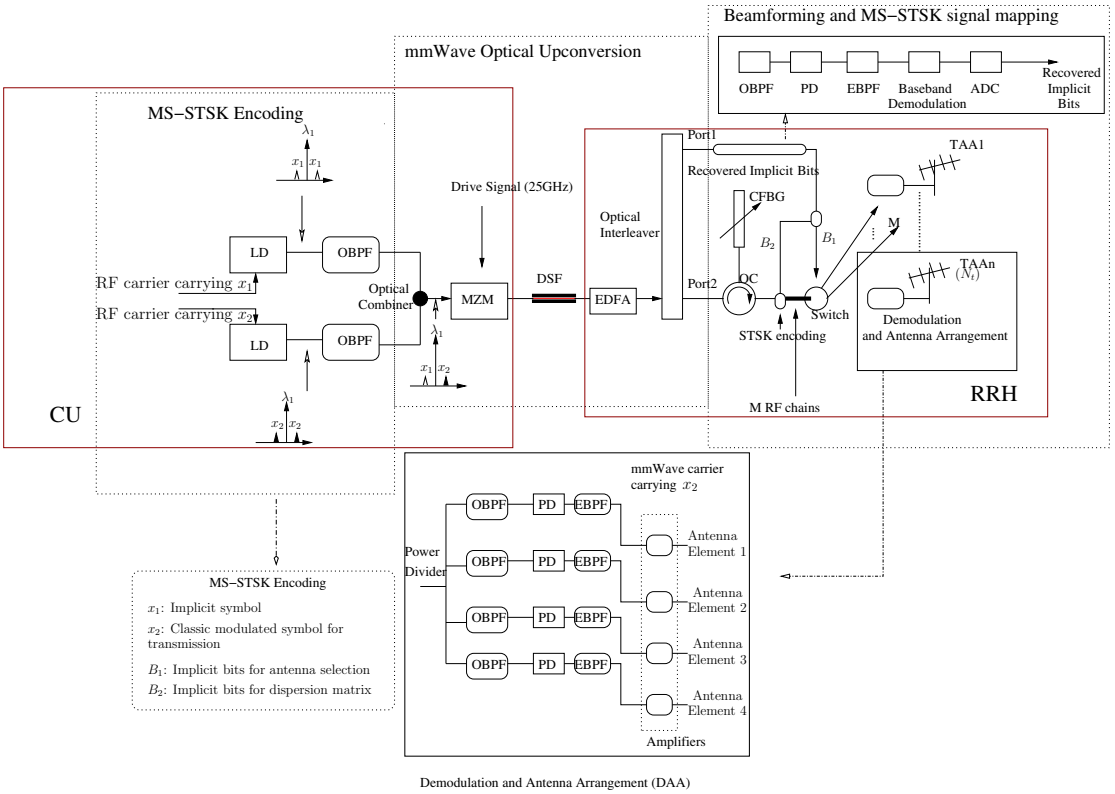

Figure 4.13: A centralised A-RoF aided MS-STSK network. The CU implements digital modulation, carrier modulation, E/O conversion and MS-STSK encoding, while the RRH carries out the radio functions (filtering, O/E conversion, photo-detection and amplifying radio transmission), as well as MS-STSK implicit data recovery and MS-STSK switching.

4.5.2 Proposed A-RoF-aided MS-STSK-BF Designs

The MS-STSK design is further extended and improved from the SM design proposed in Section 4.4, as shown in Fig. 4.13. Three changes have been made in the A-RoF aided MS-STSK system compared to the SM counterpart of Fig. 4.5.

1. The x_1 implicit symbols carry the bits B_1 and B_2 of both the selected AC and of

the dispersion matrix, rather than only of the antenna selection information of SM, which is mapped to the left side-band of the ODSB signals generated before the MZM of Fig. 4.13. Here, the B_1 and B_2 bits are concatenated and then mapped to x_1.

2. If the number of implicit bits containing B_1 and B_2 is L_{MS}, then the symbols carrying the implicit bits would be mapped to $2^{L_{MS}} - PSK/QAM$ alphabet. Thus, the implicit bits convey both the information for antenna selection and the dispersion matrix selection. Hence, more implicit bits are conveyed by MS-STSK and therefore a larger constellation size is required to transmit the implicit bits of MS-STSK over the optical fiber, which is more susceptible to both fiber impairments and to optical noise. We invoked an erbium-doped fiber amplifier (EDFA) before the OIL of Fig. 4.13 in order to mitigate these effects by improving the optical SNR.

3. Furthermore, in the RRH of Fig. 4.13, the recovered implicit bits are split into the B_1 and B_2 streams, which represent the antenna selection bits and the dispersion matrix selection bits, respectively. Then, the classic modulated symbol carried by the up-converted mmWave signal is multiplied by the dispersion matrix selected and then transmitted over the AC selected, while beamforming is introduced by CFBG, which was discussed in Section 4.4.

Our A-RoF-aided MS-STSK scheme constitutes an extension of the A-RoF-aided SM scheme discussed in Section 4.4. As shown in Fig. 4.13, the ODSB modulated by x_1 and x_2 is up-converted to a mmWave frequency, and an optically aided beamforming scheme based on the CFBG philosophy of [47] is created. Thus, we adjusted the A-RoF network conceived for SM to include MS-STSK by adding a few extra components, such as an EDFA and the dispersion matrix selection scheme of Fig. 4.13. Next, we present our simulation results and related discussion to verify our system.

Parameter	Value
Bit rate	5 Gbps (BPSK system) 10 Gbps (16QAM system)
RF signal	3 GHz
LD center wavelength	1550 nm
LD power	0.1 mW
Drive frequency (MZM)	25 GHz
Achieved mmWave frequency	28 GHz
MZM mode	Push-pull mode
Fiber type	DSF
Fiber length	10 km
Channel model	Split-step Fourier method
Modulation type	BPSK/16QAM
EDFA gain	20 dB
Wireless channel	Rayleigh fading channel
Wireless detection	ML detection
Beamforming type	4 antenna elements
Simulation environment	MATLAB

Table 4.3: Simulation parameters.

4.5.3 System Simulation Results and Discussions

Let us now consider an MS-STSK (4,2,2,2,4,BPSK) system based on the design depicted in Fig. 4.13. The simulation parameters are shown in Table 4.3. Due to the larger number of implicit bits of MS-STSK than that of our SM scheme, a higher order modulation scheme such as 16QAM is required, which is more susceptible to fiber non-linearity. The LD power is reduced to 0.1 milliWatt (mW) for the sake of mitigating the effect of non-linearity-induced-phase shifts.

Before being mapped to the two side-bands of the ODSB scheme shown in Fig. 4.13, the implicit bits used for the MS-STSK scheme of Fig. 4.13 are mapped to the 16QAM symbols x_1, where two bits are used for selection of a dispersion matrix and the other two bits are used for the antenna selection. Finally, the classic modulated symbols x_2 are BPSK symbols. Using the same data set for the dispersion matrix as in [106], Fig. 4.14 shows the BER performance of the conventional electronic MS-STSK both with and without beamforming using $N = 4$ antenna arrays and of our proposed A-RoF-aided MS-STSK system. The comparisons are based on (4×4), (4×2) and (4×1) MIMO schemes, where analogue beamforming using four antenna elements is employed. It is clearly observed that there is only a minor BER degradation, when our

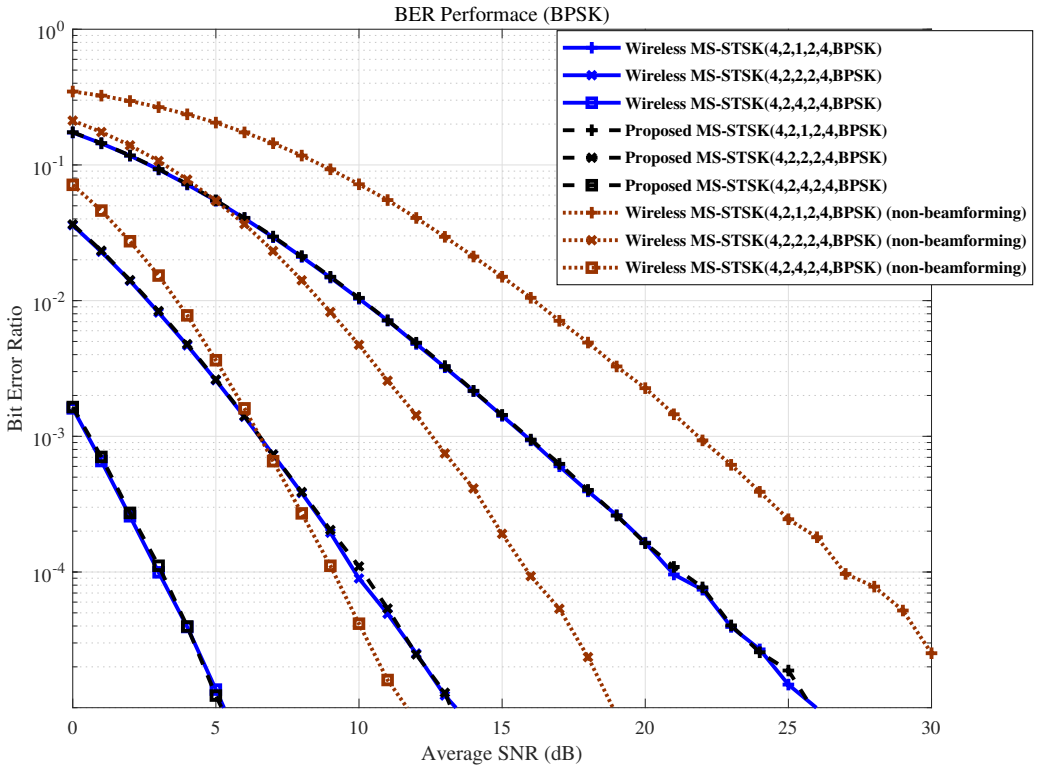

Figure 4.14: BER performance of the conventional electronic MS-STSK and of our proposed MS-STSK scheme for 5 Gbps BPSK modulated signal using the parameters summarised in Table 4.3.

fiber network is invoked. Moreover, recall from Fig. 4.11, that without EDFA, there is still a modest degradation in BER performance. However, owing to the requirement of using a higher-order fiber-modulation for MS-STSK, which is more susceptible to fiber impairments, the proposed MS-STSK system relies on an EDFA having a 20 dB gain in order to compensate for the degradation. Additionally, observe in Fig. 4.14 that the beamforming aided system has a 6 dB beamforming gain.

Furthermore, to verify that our system is scalable and suitable for high data rates, we mapped the classic modulated bits to a 16QAMs while invoking another 16QAM scheme for the implicit bits, transmitting a 10 Gbps signal using the same MS-STSK scheme as above. As discussed above, 16QAM is more susceptible than BPSK to the fiber impairment, hence an EDFA of 26 dB gain is invoked. Fig. 4.15 shows our comparison of the (4×4), (4×2) and (4×1) MS-MTSK MIMO schemes. Given that only a modest degradation is observed, we conclude that our SM/MS-STSK A-RoF network benefits

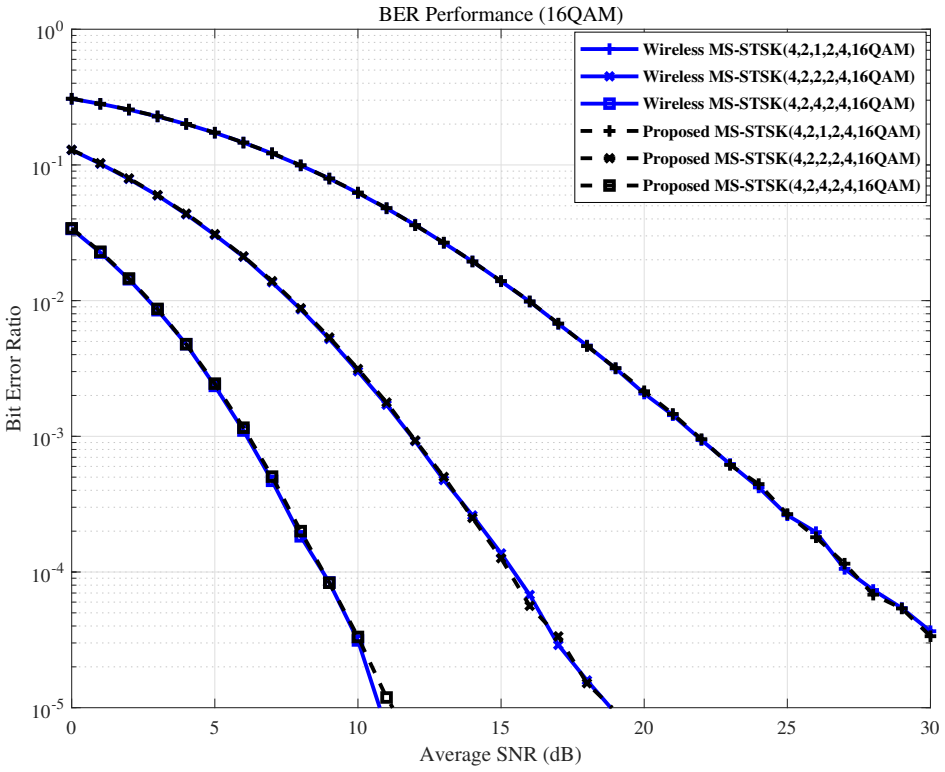

Figure 4.15: BER performance of the conventional electronic MS-STSK and of our proposed MS-STSK scheme for 10 Gbps 16QAM using the parameters summarised in Table 4.3.

from all-optical processing, whilst avoiding the ADC-and-DAC-related complexity in the RRH of Fig. 4.13.

MS-STSK is a general scheme subsuming both SM and STSK, where space-time coding can be included, leading increased flexibility to our proposed system. Additionally, the beamforming solely relies on CFBG and the corresponding wavelengths, as discussed in Section 4.4.

4.6 Conclusions

In this chapter, we firstly presented a rudimentary introduction to the underlying MF-MIMO, C-RAN, A-RoF and mmWave communications concept in Section 4.1, where we demonstrated the potential of amalgamating A-RoF aided MF-MIMO with C-RAN for cost-efficient C-RAN design. Then in Section 4.2, a brief review of wireless MF-MIMO

schemes was provided, while we ended up with our introduction of MS-STSK techniques. Section 4.3 revealed the problems imposed by the wireless MF-MIMO schemes in the context of small-cell based C-RANs, which may be circumvented by centrally processing the beamforming and SM/MS-STSK whilst relying on optical solutions. Then, in Section 4.4, we firstly proposed an A-RoF aided SM-BF downlink, where SM is combined with BF implemented by relying on a centralised processing solution. In the proposed network, most of the digital processing of the baseband SM is carried out by the CU. In this context, the implicitly carried bits of SM, such as the antenna index selection and dispersion matrix selection bits, are recovered by the RRHs of our A-RoF network for creating a MF-MIMO arrangement. Again, A-RoF-aided techniques were invoked for achieving optical processing aided beamforming and optical up-conversion to a mmWave carrier frequency. Then, in Section 4.5, we demonstrated that the A-RoF techniques conceived may also be applied to MS-STSK and are capable of generating the MS-STSK-BF signal with the aid of optically up-converted mmWave signals and beamforming without using any electronic oscillators, mixers or phase-shifters.

Furthermore, our A-RoF-aided system's BER performance is similar to that of the conventional all-electronic SM/MS-STSK scheme. However, this design is capable of substantially reducing the complexity of the RRH, when intrinsically amalgamated with SM or MS-STSK. Additionally, as seen in Fig. 4.15, we achieved a bit rate of 10 Gbps for 16QAM and 10 km DSF in our MS-STSK fiber-based A-RoF network. Again, the BER performance is only marginally eroded, compared to the conventional solution relying on electronic component. In the previous three chapters, we introduced A-RoF aided MIMO schemes in the outdoor communication scenarios, namely small cell and C-RANs. In the next chapter, we will further exploit and develop our optical centralised processing aided MF-MIMO concept in the context of indoor environments.

Chapter 5

Analogue Radio Over Plastic Optical Fiber Communications

CHAPTERS 2-4 have been dedicated to radio over single-mode glass optical fiber (GOF) communications, which are widely used for outdoor communications. Given the increasing industrial attention focused on cost-efficient plastic optical fiber (POF) solutions [10], in this chapter, we will focus our attentions on the radio over plastic optical fiber (RoPOF) aided multi-functional multiple-input-multiple-output (MF-MIMO) designs. Again, our goal is that of combining beamforming and transmitter diversity, where mode division multiplexing [147] (MDM) can be invoked for multi-user communications. Since in this chapter POF is used as the transmission medium, we will briefly portray the state-of-the-art in POF and its applications in communications as well as its channel model, which will be subsequently applied in the system proposed in this chapter. Then, we will proceed by discussing our proposed analogue RoPOF (A-RoPOF) aided MF-MIMO design conceived for indoor environments.

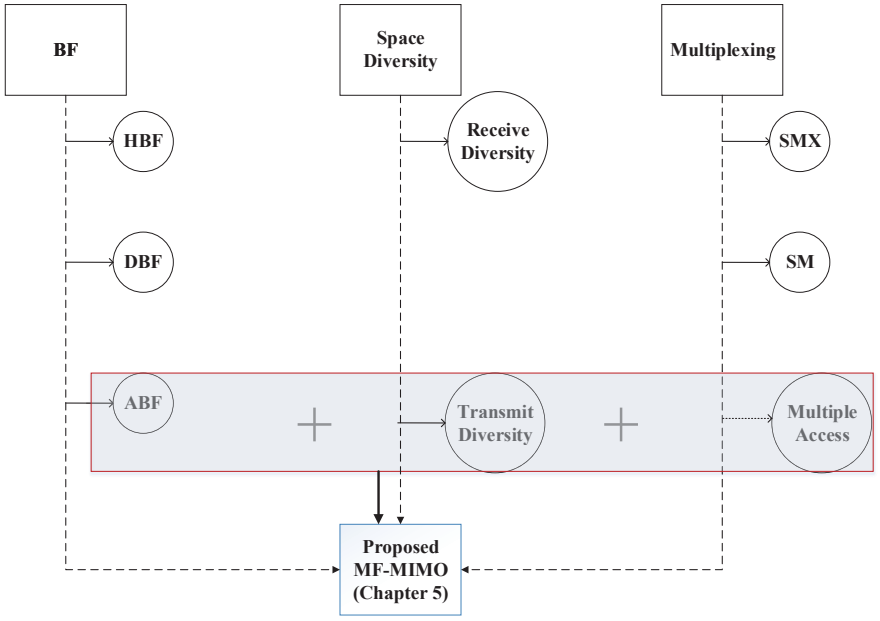

Figure 5.1: Proposed MF-MIMO arrangement investigated in this chapter. (Note that we refer to beamforming as analogue beamforming in the in-text content unless we specify it to hybrid or digital beamforming.)

5.1 Plastic Optical Fiber Background of POF

The wide-ranging application of the Internet accompanied by the popularity of smart phones, tablets and PCs has penetrated our daily life, but requires a hitherto to unprecedented bandwidth to transmit vast amounts of data. To meet this challenge, the second-generation GSM system followed by 3G based on WCDMA and then the 4G LTE system have offered increasingly more convenient Internet 'surfing'. Outdoor communication has significantly benefited from these advances in communication techniques and the pace of development remains rapid both in terms of theory and in hardware techniques. However, there is strong quantitative evidence that most of the tele-traffic is initiated in and destined for indoor communication networks. Wi-Fi is clearly a popular candidate for indoor communication systems. However, its limited bandwidth and its low transmission distance render this technique inadequate for satisfying all the future demands, when for example low-latency high-resolution video streaming is required.

The ubiquitous single-mode GOF (SM GOF) is eminently suitable for long-reach outdoor communications, both in the backhaul and fronthaul network, as a benefit of its wide bandwidth, low attenuation and low dispersion compared to multi-mode

GoF (MM GOF). On the other hand, MM GOF is popularly deployed in short-range communications for striking an attractive cost-performance trade-off, for example in local area networks (LANs), as a benefit of its overall cabling cost advantage over SM GOF, including that of fiber connectors and of optical transceivers.

In the context of short-range fiber links, POF may be capable of outperforming MM GOF, when considering its installation cost, owing to its larger core size leading to compelling ease in handling and connecting without the need for a professional engineer [10, 148, 11].

Thus, it is promising to investigate RoPOF aided indoor communications. Compared to silicon fibers, such as the standard single-mode fiber, which is routinely used in core and access networks [149], large core POF may be preferred for indoor networks, since it provides a low-cost solution. Hence, RoPOF solutions combine the advantages of POF with those of wireless technology for supporting high data rate communications by offering a high bandwidth for users [6]. However, the limited bandwidth caused by the associated large core constitutes an impediment. Hence, researchers have attempted to improve it by conceiving the most appropriate modulation format [150]. Next, prior to outlining our contributions on the A-RoPOF aided MF-MIMO schemes, we will review the applications of POF in hybrid mobile communications by investigating its most suitable modulation type aiming for extending its attainable bitrate-length product.

5.2 A Brief Review of POF Communications

POF predates GOF, since it was developed by Dupont as early as 1977, but its development was overtaken by GOF owing to the high attenuation of POF [148]. However, there is continued interest in short-distance LANs supporting the indoor user ends (UEs), where the low-installation cost of POF is promising [11]. Hence in this section, we briefly review the family of POF based indoor communication systems in terms of the type of the modulation schemes, and categorise them into baseband and passband modulation.

5.2.1 Baseband Modulation

During data transmission in the POF, baseband digital modulations schemes, such as non-return-to-zero (NRZ) [151], on-off-keying (OOK) [152] and pulse-amplitude-modulation (PAM) [153] have been used.

5.2.1.1 Non-return-to-zero Techniques

Non-return-to-zero (NRZ) modulation is commonly used both in wireless and wireline communication for baseband transmission. Explicitly, a binary '1' is represented by a positive voltage, while a binary '0' by a negative voltage [154]. However, in the context of RoPOF communications, binary information is mapped to optical pulses, where '1' is represented by a pulse of light while '0' by the absence of a pulse.

In [151], a 10.7 Gbps NRZ system was conceived for transmission over a graded-index POF (GI-POF) which had a length of 220 m.

5.2.1.2 On-off Keying

OOK is the simplified form of amplitude shift keying (ASK). In ASK, the digit '1' is represented by the carrier having a higher amplitude, while digit '0' is represented by the carrier exibiting a lower amplitude. The difference between OOK and ASK is that in OOK '0' is transmitted when the amplitude of the carrier wave is zero. Thus, when it is 'on', a '1' is transmitted while 'off' represents '0' [154].

Generally, the bandwidth limitation of POF results in a limited fiber length of less than 100 m [152]. However, by using maximum likelihood sequence estimation equaliser (MLSE) based equalisation and forward error correction (FEC) in the OOK scheme, a 10 Gbps system was capable of reliably operating over a 220 m GI-POF [151]. However, the MLSE equaliser imposes a high complexity. Thus, in [152], OOK modulation relying on a fractionally-spaced feed-forward equaliser and decision feedback equaliser (DFE) was shown to attain a rate of 10 Gbps over a stretch of 300 m GI-POF [152]. As a further development, by amalgamating differential phase shift keying (DPSK) and OOK, a 40 Gbps system communicating over a distance of 100 m using POF was realised [155].

Furthermore, RZ OOK [155] results in an error free transmission for GI-POF. Finally, OOK combined with a DFE-aided receiver [156] was shown to achieve a data rate of 2.5 Gbps over a distance of 50 m step-index multi-core POF (SI-MCPOF).

5.2.1.3 Pulse Amplitude Modulation

In pulse amplitude modulation (PAM), the information symbols are mapped to the amplitude of the signal. According to [157]:

$$s(t) = \sum_{k=-\infty}^{\infty} a_k g(t - kT), \tag{5.1}$$

where a_k denotes the pulse amplitude and $g(t)$ is the band-limited pulse shape, which specifies the baseband signalling waveform.

Let us now briefly elaborate on the application of PAM in POF based indoor communications, where 2-PAM, 4-PAM and 8-PAM are used depending on the specific system design. Compared to 2-PAM, multi-level PAMs schemes, such as 4-PAM and 8-PAM, are more spectral-efficient at the cost of sacrificing the power efficiency [153]. 4-PAM modulation combined with fractionally-spaced blind equalisation at the receiver [158] was shown to be capable of achieving a 1.25 Gbps transmission rate over a 50 m SI-POF. However, the attainable remained limited owing to relatively severe non-linear distortions. In [159], a low-complexity equalizer was invoked for mitigating the distortion.

8-PAM was also investigated as a means of improving POF based communications. Specifically, a 3 Gbps system using 8-PAM over a 25 m SI-POF was characterised in [153], which invoked factionally-spaced equalizer relying on both the feed forward and decision feedback sections, for mitigating both the noise and the inter-symbol interference.

5.2.1.4 Baseband Orthogonal Frequency Division Multiplexing/ Discrete Multitone Modulation

Orthogonal frequency division multiplexing (OFDM) was standardised for the 4th generation wireless communication, which relies on orthogonal sub-carriers, each transmitting

at a low rate, hence it becomes immune to inter-symbol interference communication system. Thus, by invoking OFDM in the POF system, both the modal dispersion as well as the chromatic dispersion and the polarisation mode dispersion are potentially mitigated. Therefore, discrete multitone modulation (DMT), which is a baseband version of OFDM, is indeed attractive for POF based communication systems [150].

DMT is widely used in the digital subscriber copper line (xDSL). In the DMT scheme, the bits are mapped to the real and imaginary parts of each sub-carrier and then the conjugate complex version of it is copied to the negative frequencies. Hence the resultant time-domain signal at the output of DMT after inverse fast-Fourier transform (IFFT) based modulation becomes real-valued.

Let us now review the DMT-based system in the context of the POF based communcation system. The DMT cocept is also suitable for the POF based system by introducing the ubiquitous cyclic prefix (CP) for mitigating the dinstinctive modal dispersion [160] in combination with applying bit-loading for improving the data rate and for reducing the bit error ratio (BER) [161]. Further details of adaptive bit-loading can be found in [162].

Despit its benefits, DMT also has its limitations, such as its high peak-to-average-power ratio (PAPR) which is mitigated by the authors of [163].

In a nutshell, the real-valued output and the adaptive allocation of data bits to each sub-carrier make it a cost-effective and power-efficient modulation scheme for POF systems [161, 164, 165]. The combination of CP and parallel transmission regime of DMT overcome the bandwidth limitation imposed by the deleterious effects of modal dispersion, while the rate-adaptive bit loading relying on Chow's algorithm [165] efficiently allocates the bits to each sub-carrier with the goal of maximizing the bit rate.

Baseband modulation presents a simplified solution for wireline communication with the ignorance of setting up higher frequency conversion while passband modulation offers more bandwidth, which is also investigated in POF communications. Next, we provide a brief review of the passband modulation aided POF communications.

5.2.2 Passband Modulation

5.2.2.1 Multi-band Orthogonal Frequency Division Multiplexing Ultra-wideband Systems

The ultra-wideband (UWB) signal has been defined as having at least 500 MHz bandwidth or a fractional bandwidth of at least 20% of center frequency according to the U.S. Federal Communication Commission (FCC) [166]. The UWB system concept relies on the inherent assumption that its signal overlaps with other services operating within the same band at a much higher power. Conversely, the UWB signal has to have a sufficiently low power spectral density (PSD) to avoid penetrating the other higher power signals within its band. Hence, the FCC has set up a maximum UWB emission limit ranging from 3.1 GHz to 10.6 GHz. There are two popular techniques of generating the UWB signal: impulse radio ultra-wideband (IR-UWB) and multiband OFDM ultra-wideband (MB-OFDM UWB) [167].

IR-UWB may be deemed to be the more traditional methodology, where a short-duration Gaussian impulse is generated [168]. The resultant IR-UWB signal satisfied the strict FCC spectrum mask during its transmission over a 100 m GI-POF [168].

An alternative UWB signal generation method is constituted by MB-OFDM, which relies on partitioning the UWB signal into several sub-bands, with each band consisting of an appropriately selected number of sub-carriers [169]. A so-called time-frequency coding techniqeus was invoked, where each sub-band's information was transmitted in a different time-slot for ensuring that they experienced stastitically independent impairments [167].

Thus, MB-OFDM UWB may also be deemed to constitute a promising modulation technique, albeit its high PAPR remains an impediment. Finally, it is worth mentioning in closing that as a compelling application, the distinction of cable television signal (CATV) has also been reported in the literature [170].

In a nutshell, the modulation schemes shown in Fig. 5.2 have briefly touched upon including some of the popular baseband modulation (NRZ, OOK, PAM and DMT) schemes, and passband modulation arrangements (MB-OFDM UWB and IR-UWB),

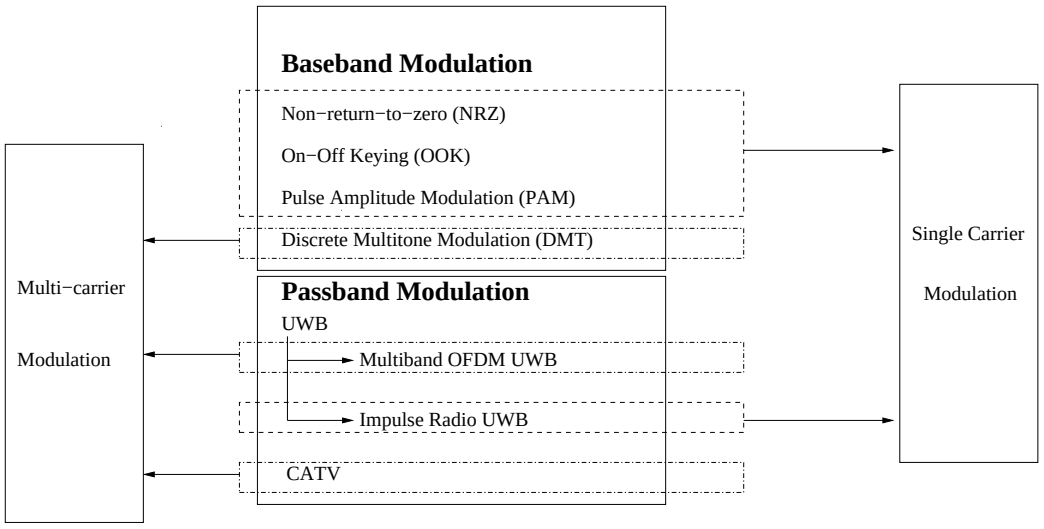

Figure 5.2: Modulation scheme.

which belongs either to the single carrier (NRZ, OOK, PAM and IR-UWB) modulation or to the multi-carrier modulation (DMT, MB-OFDM UWB) family. In conclusion, observe in Table 5.1 that DMT exhibits the best performance, when considering bitrate-length product metric.

Let us now consider the POF channel in the next section.

Techniques	Bitrate-Length Product	
	Graded-Index	Step-Index
NRZ	10.7 Gbps for 220 m [151]	1.25 Gbps for 100 m [171]
OOK	40 Gbps for 100 m [155]	2.5 Gbps for 25 m [156]
PAM	10 Gbps for 300 m(PAM+OOK) [152]	3 Gbps for 25 m [153]
DMT	51.8 Gbps for 100 m [172]	10 Gbps for 25 m [156]
UWB	4.48 Gbps for 50 m [149]	———
CATV	2.5 Gbps for 25 m [173]	———

Table 5.1: POF modulation techniques and their performance.

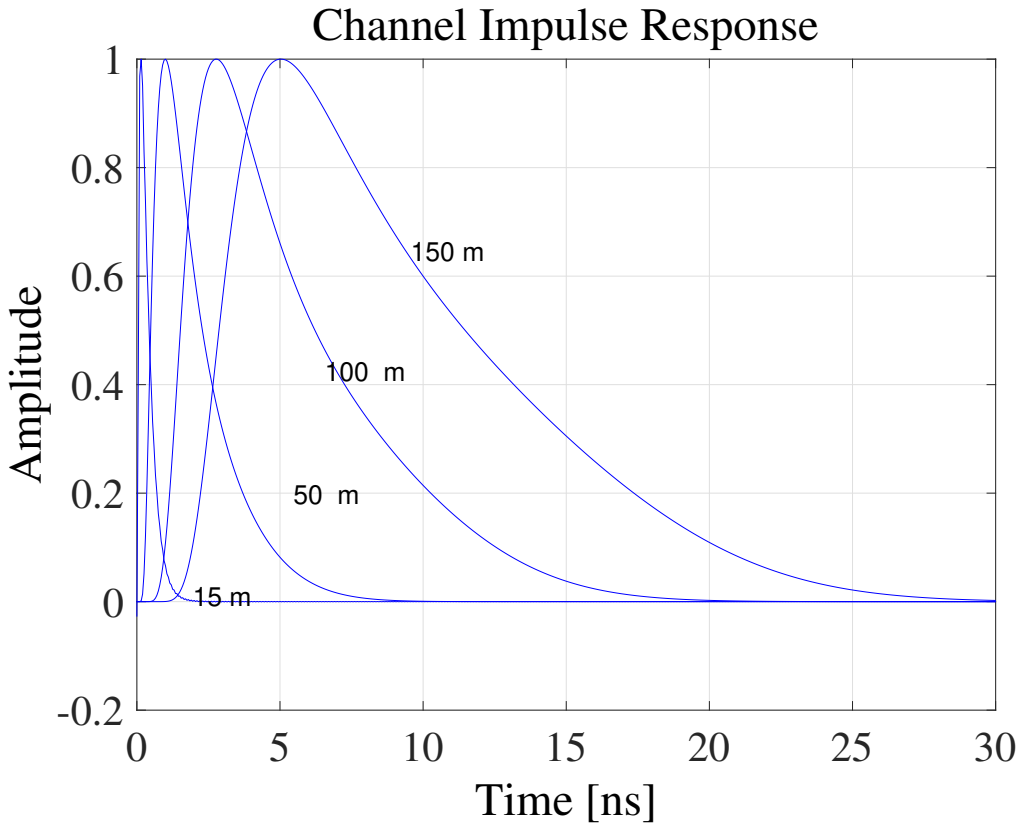

Figure 5.3: Channel impulse responses (CIR) of the fiber lengths.

5.3 Channel Modelling

Accurate channel modelling is required for POF based simulations. The plastic fiber has a large multi-mode core. Numerous impairments degrade the POF channel, such as its imperfect refractive index, mode coupling, differential mode attenuation, modal dispersion, chromatic dispersion, angular diffusion and non-linear effect, etc. Here, we simply use the CIR of different fiber length for characterising our channel, along with the corresponding frequency response as shown in Figs. 5.3 and 5.4, respectively.

5.4 Novel Contributions

POF may be deemed to be a suitable candidate for future indoor communication systems, since it provides a low-cost solution to indoor communications due to its convenient installation [24]. However, POF techniques are in their infancy, like silicon was decades ago, which motivated our research. When reaching maturity, POF may even replace

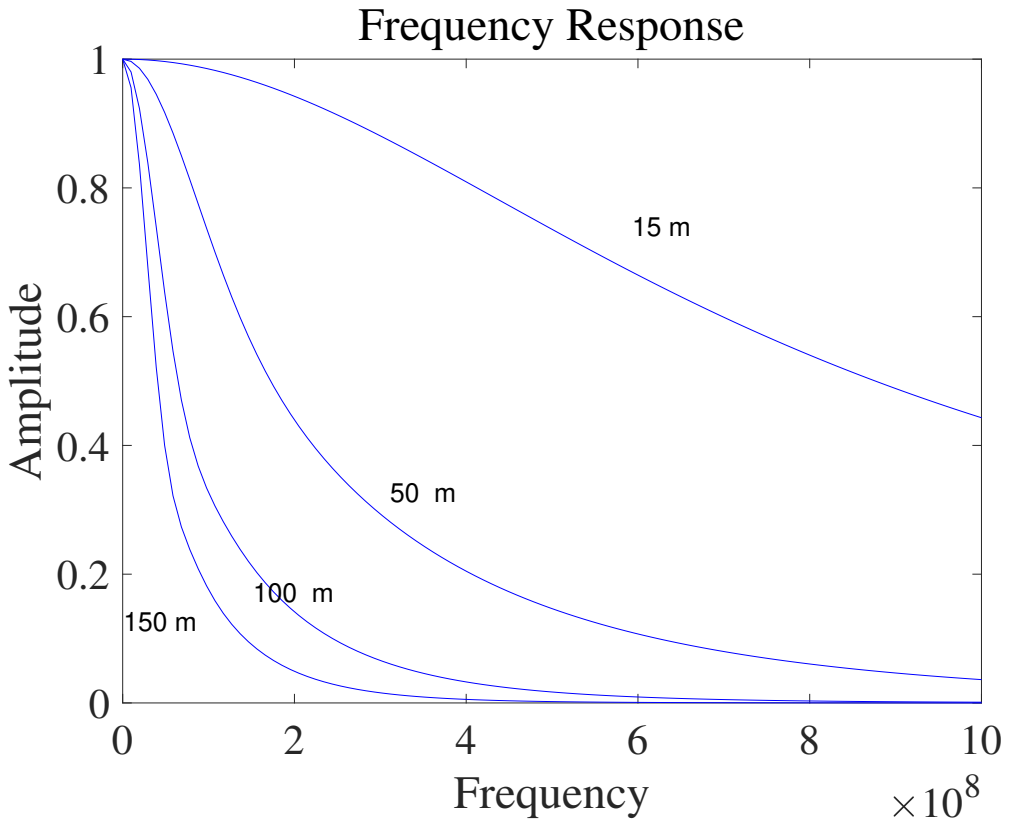

Figure 5.4: Frequency response.

the plastic insulation of mains-wiring. On a similar note, MIMO systems constitute promising techniques, since both diversity as well as multiplexing and beamforming gains can be attained in order to reduce the effect of multi-path fading and to increase both the channel capacity and signal-to-noise ratio (SNR) gains [142, 174]. Furthermore, the standardisation of different MIMO techniques including transmitter beamforming in the IEEE 802.11 family used for Wi-Fi [175] motivates the implementation of the MIMO techniques in the indoor environment. Hence, we aim for designing an all-optical processing aided MF-MIMO assisted indoor system, which achieves both diversity as well as beamforming gains and supports multiple users relying on all-optical processing by the POF, while minimising the number of electronics components and processing cost [6].

A number of challenges are imposed by the current MF-MIMO aided indoor networking techniques, which can be summarised as follows:

1. State-of-the-art beamforming techniques mainly rely on invoking phase shifters in the transceiver, which impose a high insertion loss [37].

2. Numerous phase-shifters are needed for beamforming in large-scale MF-MIMO systems, such as layered steered space-time codes (LSSTC) and layered steered space-time spreading (LSSTS) [174, 133].

3. Since each MZM can only modulate a single RF signal, hence multiple optical modulators are required for transmitter diversity or multiplexing techniques, such as space-time block coding (STBC) [2] and their number is proportional to the number of transmitters, which potentially results in high complexity [176].

The first challenge can be tackled by using fiber optical solutions, such as a chirped fiber Bragg grating (CFBG) [44], relying on the wavelength-dependent time delay imposed by CFBG. Therefore, the complexity of the MF-MIMO configuration can be substantially reduced by avoiding bulky phase shifters [44]. The optical solution is capable of reducing the loss imposed by an electronic phase shifter and significantly simplifies the wireless beamforming [37].

As for the third challenge, a single optical double side-band (ODSB) modulation solution was proposed in [99] for simplifying the system by encoding the related pair of signals into two different side-bands of an ODSB signal using optical up-conversion. However, no beamforming can be realised using the architecture of [99], unless we expand the same architecture to an increased number of antenna elements.

Therefore, we propose the all-optical processing aided downlink architecture of Fig. 5.5 conceived for an indoor environment, which amalgamates both STBC and beamforming by exploiting the non-linearity of the Mach-Zehnder modulator (MZM) and of the CFBG in order to address all three of the above mentioned challenges. We propose STBC as an example of a transmitter diversity scheme, noting that our system is quite flexible and hence it is also readily applicable to other sophisticated MIMO techniques, such as V-BLAST [142], spatial modulation or space-time shift keying (STSK) [106]. Combining STBC and beamforming has been proposed in the literature [142, 174, 133], where it was shown that the combination of these two techniques attains a better BER performance than each of the individual techniques [142, 174, 133]. Additionally, based

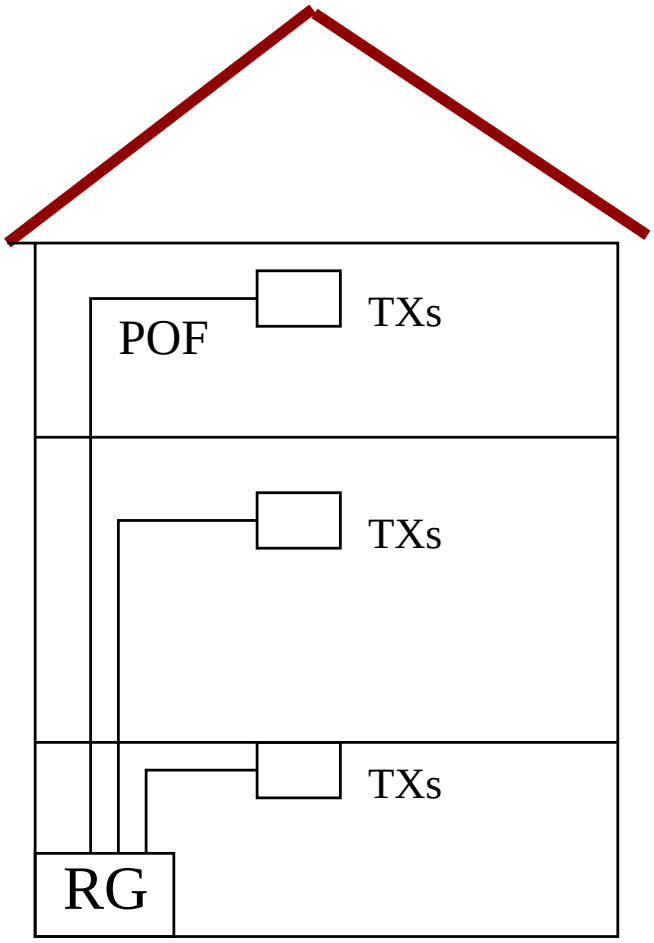

Figure 5.5: A FITH architecture based on POF. TXs: Transmitters, RG: Residential Gateway, POF: Plastic Optical Fiber.

on the capacity analysis presented in [177], in non-line-of-sight channels, the combination of the two techniques provides a higher capacity than each individual technique. The beamforming employed in this section is analog beamforming, which requires the knowledge of the angle of departure (AoD) at the transmitter. The AoD can be estimated using the techniques reported in [146, 145]. On the other hand, STBC requires the knowledge of the channel impulse response at the receivers, which can be estimated as reported in [178].

In order to generate the twin-antenna aided STBC symbols [2] whilst relying on a single wavelength, we will use a combination of two laser diodes (LDs) and a pair of optical bandpass filters. Their output signal will be fed into a MZM. Then the MZM copies the STBC signals to multiple wavelengths by exploiting the non-linearity of MZM

[15]. The wavelengths can be tuned by a frequency-controllable MZM drive signal in order to control the beamsteering angle. These signal processing operations will be carried out by the residential gateway (RG) of Fig. 5.5 (the link between the access and the in-home network). Afterwards, a POF is invoked for supporting a multi-user system in each floor of Fig. 5.5 by relying on the MDM principle [179], where each mode is capable of carrying the STBC symbols of a different user. Then, by exploiting the time delay of CFBG and by invoking the appropriate photo detection (PD) and demodulation, a beamforming angular range of approximately 150° can be achieved for each transmitted signal corresponding to each STBC symbol.

Our contributions can be summarised as follows:

1. The MF-MIMO principle can be readily supported by optical fiber based processing without requiring a large number of phase shifters and multiple optical modulators, hence substantially reducing the complexity of wireless beamforming systems additionally supporting the STBC.

2. We design a novel tunable microwave generator based on the MZM's non-linearity for controlling the beamforming pattern, whilst also providing a less costly alternative in comparison to the state-of-the-art commercial microwave generators.

3. By conveniently controlling the number of side-bands with the aid of the MZM's non-linearity, the system becomes quite scalable and it is capable of supporting larger antenna arrays for the sake of achieving narrower beams.

4. MDM is implemented within a POF for supporting multiple users, where the multiple STBC signals of different users can be readily mapped to different modes.

The rest of the chapter is organised as follows. In Section 5.5, the proposed system architecture will be presented, while our performance results are discussed in Section 5.5.4, followed by our conclusions in Section 5.6.

5.5 Proposed System Model

In this section, we propose a multi-user system for the downlink of an in-home network, where each user's signal is encoded as a 2×1 STBC signal modulated onto a double side-band optical carrier and transmitted over POF. Each signal of the STBC can be beamsteered by using all-optical processing. Thus, the system of Fig. 5.6 can be expanded to support multi-user applications by simply copying the same design and transmitting the different users' signals in different modes of the POF using MDM, which is shown in Fig. 5.7. To further detail the rationale of our proposed system, we

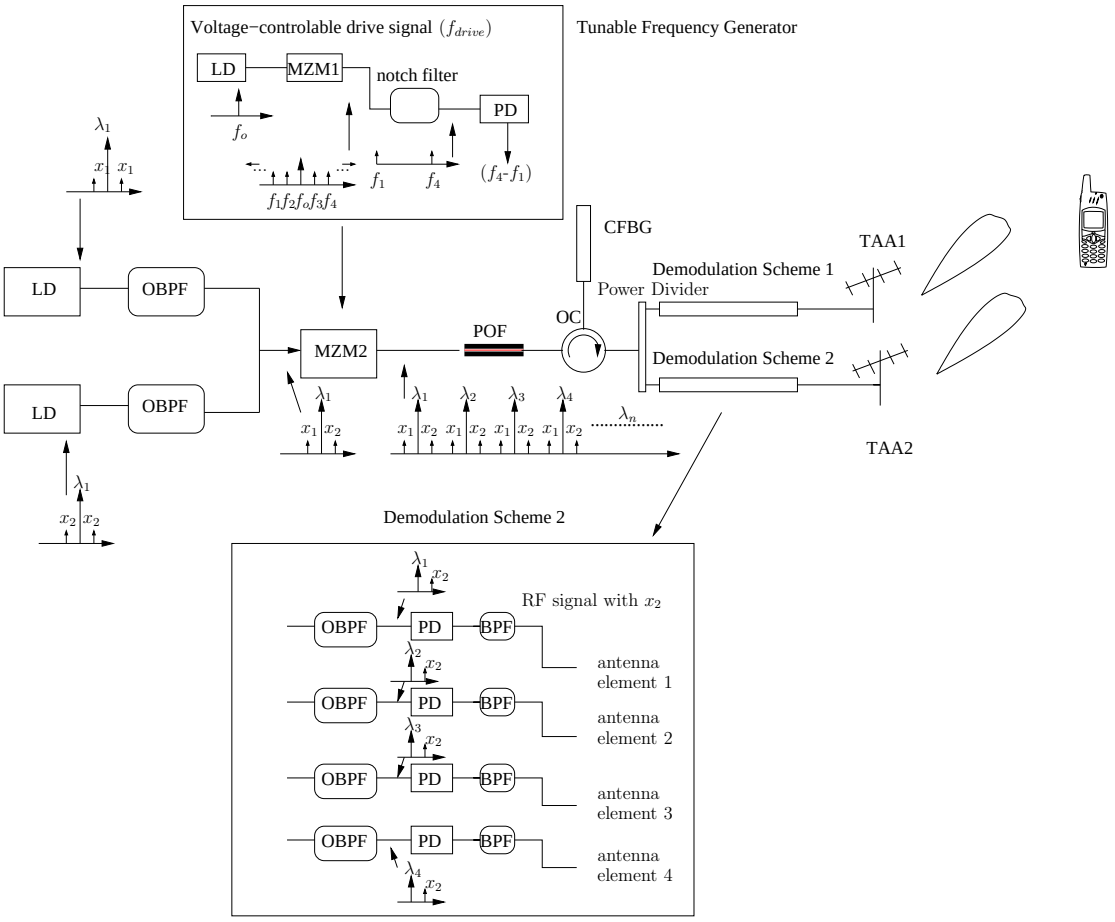

Figure 5.6: Proposed system model based on a single user.

will simply describe a single-user model and characterise the spectrum of the signal at each processing stage in the network.

As shown in Fig. 5.6, a modulated ODSB signal is generated by exploiting two direct-modulated LDs, with each bandlimited by an optical bandpass filter (OBPF). Using the

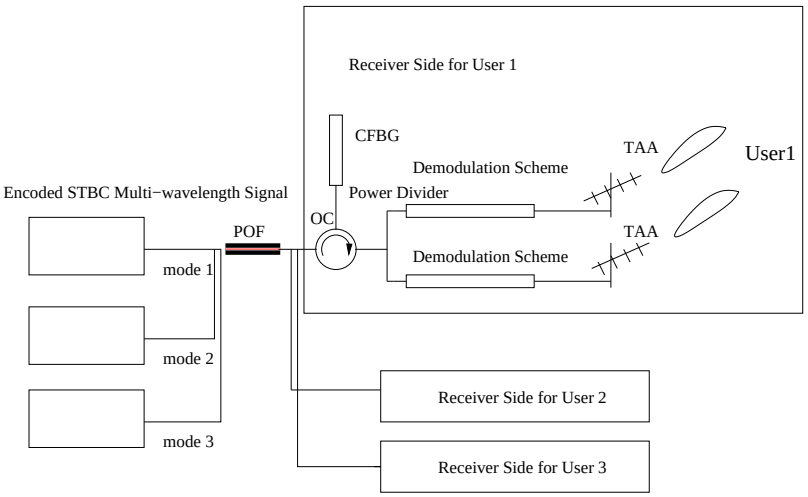

Figure 5.7: A multi-user system.

OBPFs of Fig. 5.6, the upper side-band of the upper LD and the lower side-band of the lower LD are removed, while the remaining side-bands are combined. Then, the combined signal, which contains the data streams x_1 and x_2 in the separate side-bands is fed into the MZM2 of Fig. 5.6. Here, the pair of data streams x_1 and x_2 correspond to the pair of symbols transmitted from the two antennas of the Alamouti scheme, with x_1 fed into transmitter antenna array 1 (TAA1) and x_2 fed into transmitter antenna array 2 (TAA2) as shown in Fig. 5.6 [2].

In our design, we generate a multi-wavelength signal for supporting beamforming as motivated below. In order to realise directional beamsteering, when employing linear uniform arrays, each element requires differently delayed signals, where the time delay difference between the neighbouring elements must be constant. Since CFBG imposes a linear time delay on the carrier, it can be invoked for the beamforming scheme by exploiting the time delay difference of the different-wavelength carriers in CFBG. Thus, a multi-wavelength signal carrying the same signal at each wavelength having a constant wavelength-spacing is required, whilst guaranteeing a constant time delay difference between neighbouring elements.

Here, the higher order side-bands introduced by the non-linearity of MZM2 seen in Fig. 5.6 can generate a multi-wavelength signal, and each wavelength carries a set of STBC signal. The STBC signal is transmitted as ODSB and copied to different wavelengths. Then, the multi-wavelength signal generated for each user is transmitted in a single mode of the POF, while the different users' signals are transmitted in different

modes. The CFBG of Fig. 5.6 seen at the output of the POF provides the different wavelengths of the multi-wavelength signal associated with different delays, thus offering beamforming for the same signal after PD and demodulation.

As demonstrated in Fig. 5.6, after the CFBGs, the delayed wavelengths will be power-divided into two different demodulation schemes (DSs), where each one contains several branches. The number of branches depends on the number of antenna elements. As shown in the bottom box of Fig. 5.6, in each branch of DS 2, the multi-wavelength signal is split by an OBPF to retain half of the optical carrier having the corresponding wavelength and the right side-band which is modulated by x_2. By contrast, in DS 1, the left side-band is filtered out. Thus, during the demodulation, the delayed photo-detected signal is categorised into one of two groups and it is mapped to two antennas according to the filtered-out side-bands. For each antenna, we arrange for a linearly increasing time delay after the photo detection of each wavelength, which is then exploited for beamsteering [37]. The desired beamsteering direction is determined by using explicit beamforming feedback, where a beamforming weight matrix containing the phase information for each antenna element is sent back from the desired users to the TAAs [180]. Then, in our design, this information is fed back over the fiber to the tunable frequency generator of Fig. 5.6 through the POF, where the corresponding driving frequencies are applied. Explicitly, the AoD can be accurately estimated using classic techniques reported in the literature, such as the direction search for the largest gain used in the IEEE 802.11ad standard [146], the Kalman filter based tracking algorithm presented in [146] and the path search techniques using different beamwidths [145]. Additionally, several channel estimation technniques have been proposed for STBC in the literature, including closed-form blind channel estimation [178]. Then, the AoD information can be sent back to the tunable frequency generator to adjust the corresponding beamsteering angles.

Consequently, the specific pair of data streams modulated using STBC and carried by the same radio frequency (RF) will be beamsteered. Additionally, to appropriately tune the beamsteering direction, a tunable microwave generator used as the drive signal is imposed on the MZM2 for the sake of controlling the spacing of each wavelength, hence indirectly resulting in an adjustable beamforming pattern. The multi-wavelength generation, tunable microwave generator and the multi-user system design will be described

in the following sections.

5.5.1 MZM-aided Multi-wavelength Generation

As shown in Fig. 5.6, the multi-wavelength signal is generated with the aid of the MZM's non-linearity, where the ODSB appears at every wavelength [15]. This is arranged for ensuring that different wavelengths experience different delays in the CFBG and hence beamforming can be achieved for each STBC signal, which is a benefit of the CFBG-induced-time-delay of each wavelength. Here, we briefly introduce the physical rationale for this process.

The RF signal is directly modulated by laser, which can be formulated as:

$$E_{dm} = \sqrt{P_{laser}} e^{j2\pi f_{oc} t} [1 + cos(2\pi f_{RF} t)], \tag{5.2}$$

where E_{dm} is the output field of the direct-modulated LD that operates at an optical power of P_{laser} and an optical frequency of f_{oc}, which is modulated by a RF signal of frequency f_{RF}.

As detailed in [143], higher-order optical side-bands can be generated based on the voltage of the drive signal imposed on the MZM, which results in the optical signal as [15]:

$$\begin{aligned} E_{MZM} & \\ &= cos(\pm\frac{\pi}{4} + \frac{\pi V_{dr} cos(\omega_{LO})}{2V_\pi}) E_{dm}(t) \\ &= \frac{E_{dm}(t)}{\sqrt{2}} [J_0(\frac{\pi |V_{dr}|}{2V_\pi}) + 2\sum_{n=1}^{\infty} (-1)^n J_{2n}(\frac{\pi V_{dr}}{2V_\pi}) cos(2n\omega_{LO} t) \\ &\pm 2\sum_{n=1}^{\infty} (-1)^n J_{2n-1}(\frac{\pi V_{dr}}{2V_\pi}) cos((2n-1)\omega_{LO} t)], \end{aligned} \tag{5.3}$$

where the E_{MZM} is the output field of MZM2 seen in Fig. 5.6 having a switching voltage of V_π, which imposes a phase shift of π for each arm of the MZM, while V_{dr} is the drive voltage having the center angular frequency of $w_{LO}/(2\pi)$. Finally, $J_n(\frac{\pi V_{dr}}{2V_\pi})$ is the Bessel function of the first kind and order n, which determines the number of side-bands.

The multi-wavelength signal generated is attributed to the changing of side-bands, which rely on V_{dr}. Thus, copies of ODSB can be readily obtained by simply tuning the voltage of the drive signal. However, to achieve convenient beamsteering tunability, in the following section a novel tunable microwave generator capable of generating the drive signal of MZM2 seen in Fig. 5.6 is described.

5.5.2 Tunable Frequency Generator

In our system, CFBG is used for adjusting the time-delay imposed on the optical carriers, which can then be exploited for beamsteering [69]. This requires multiple wavelengths carrying the same signal and hence we utilise a MZM to create the multi-wavelength signal mentioned in Section 5.5.1. However, for tuning the beamsteering direction and meet the minimum wavelength spacing requirement of 12.5 GHz to avoid inter-channel crosstalk in optical transmission [13], a tunable microwave generator is required for the MZM's drive signal. Thus, we created the low-complexity tunable frequency generator of Fig. 5.6 relying on another MZM modulator. Similar to the analysis in Section 5.5.1, the higher-order side-bands resulting from the MZM's non-linearity combined with a voltage-controllable drive signal will create a drive-voltage-dependent optical signal.

As depicted in Fig. 5.6, a four-side-band signal is generated by MZM1, where the optically modulated output signal is filtered by a notch filter (optical band stop signal) to retain merely the leftmost and rightmost side-bands, denoted here by f_1 and f_4. Thus, after photo detection, the frequency of the demodulated RF signal will be twice that of the left/right-most side-band. In the example of Fig. 5.6, $(f_4 - f_1)$ is the output used for the drive signal of MZM2, which depends on the drive signal of MZM1 and on the number of the side-bands generated. Explicitly, the edge side-bands rely on the amplitude variation of the drive voltage, which will then control the frequencies generated by photo detection. A tunable lower frequency generator can be used for generating microwave frequency. Thus, compared to commercially available microwave generators, this is a more cost-efficient solution for providing tunable frequencies.

5.5.3 MDM Based Multi-user Design

POF is referred to as a multi-mode fiber [24] and can be used for the currently fast developing fiber technique of MDM [147]. MDM is a technique coupling different signals into different modes of multi-mode fiber. Here, we use POF as a mode division multiple access channel. As shown in Fig. 5.7, each user's data feeds one of the modes of POF and shares the same receiver design, while each user can tune its own angle independently. Thus, the beam pattern can be adjusted and avoid interference while supporting multiple users thanks to our system's flexibility of independent tuning processes for different users.

To verify our proposed system, we consider twin-antenna based STBC modulation and each of the two STBC antenna arrays is equipped with four beamforming elements, as seen in Figure 5.6 and detailed in the following section.

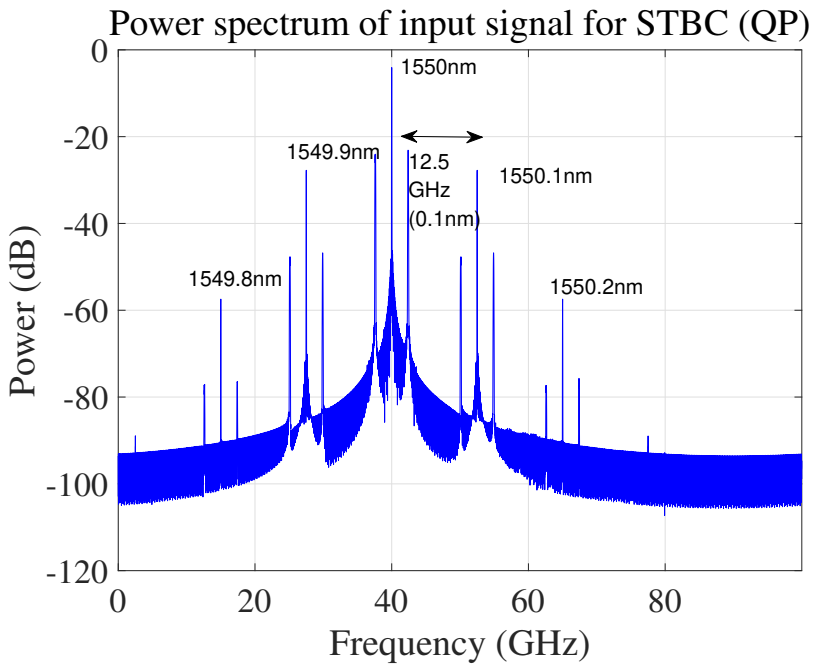

Figure 5.8: MZM aided multi-wavelength generation.

5.5.4 Simulation Results

In this section, we consider a system to support the Wi-Fi spectrum of 2.4 GHz, where each user is supported by MF-MIMO transmission intrinsically combining twin-antenna STBC and beamforming. We consider beamforming using four antenna elements per

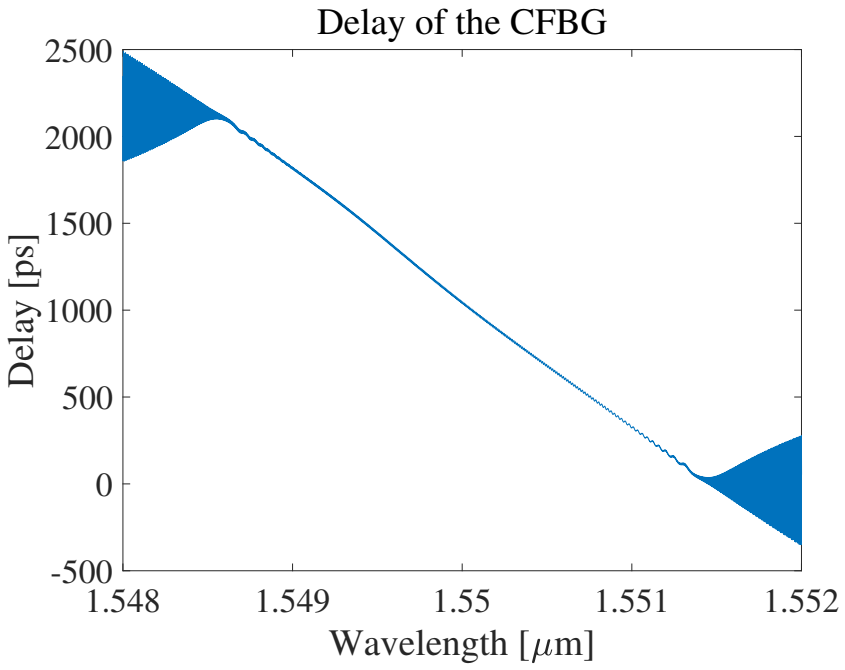

Figure 5.9: Time delay of CFBG.

Parameter	Value
RF signal	2.4 GHz
LD center wavelength	1550 nm
Drive frequency (MZM)	12.5 GHz
MZM mode	Push-pull mode
Fiber type	POF
Fiber length	40 m
Channel model	Power flow equation
CFBG length	22cm
Diversity employed	STBC
Modulation type	DBPSK
Simulation environment	MATLAB

Table 5.2: Simulation parameter.

antenna array. Table 5.2 shows the simulation parameters, where after STBC encoding [2], the differential binary phase shift keying (DBPSK) STBC signal is direct-modulated by two separate LDs. The MZM is based on the quadrature point and operates in the push-pull mode [15]. Furthermore, $\frac{\pi V_{dr}}{2V_{\pi}}$ is set to 0.13, where the third side-band can be ignored, due to the low power level, as shown in Fig. 5.8.

In Fig. 5.8, we opted for 40 GHz (1550 nm) as the center frequency for the simulations and a wavelength spacing of 12.5 GHz is used. It is shown in Fig. 5.8 that the same pair of STBC signal is modulated to the ODSBs carried by different wavelengths. A short

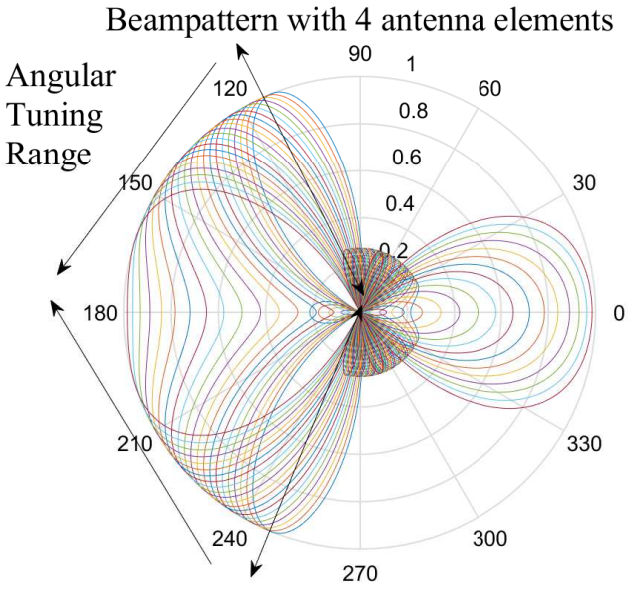

Figure 5.10: Beamforming pattern.

POF of 40 m is simulated based on Mateo's power flow equation detailed in [179] and discussed in Section 5.3, which is suitable for MDM, where the multi-wavelength signal is coupled into one of the mode in the POF. A 22 cm CFBG is used for introducing the delay required at the different wavelengths in order to impose the specific time delay required for beamsteering. The time delay imposed on the different wavelengths is simulated by using the OPTIGRATING software [181] as shown in Figure 5.9, where the delay is a linear function of the wavelengths ranging from 1549 to 1551 nm.

Arranging for a constant wavelength-spacing guarantees the required equal time delay difference of neighbouring wavelengths due to the linear time delay of the CFBG, as shown in Fig. 5.9. This introduces a linearly increasing time delay between the adjacent elements of each antenna, hence resulting in beamsteering in the wireless transmitter. Here, according to the gradient of the linear part shown in Fig. 5.9, we can readily obtain the time delay for the wavelength spacing of 0.1 nm (12.5 GHz) as 78 ps.

To control the beamsteering direction, the tunable range of frequencies in Fig. 5.6 spans from 12.5 GHz to 31.5 GHz with a step size of 1 GHz. This correponds to a time delay difference ranging from of 78 ps to 200 ps, with a step size of approximately 6 ps. This allows us to tune the beamforming pattern of a four-element antenna, as shown in

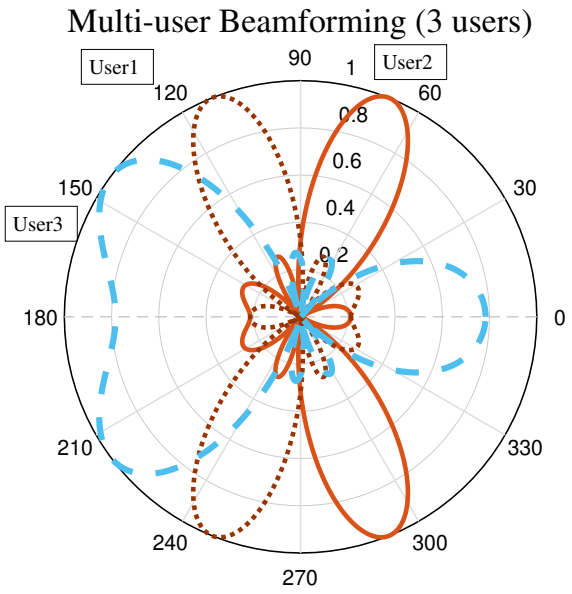

Figure 5.11: A multi-user system beampattern (N=4 antenna elements).

Fig. 5.10, where the beamforming pattern of each step changes from the right to left in a very small step. It is clearly shown in Fig. 5.10 that the beamsteering angular range is upto 150°, which is suitable for indoor transmissions.

The system is scalable, where by carefully tuning the drive signal voltage of MZM2, the number of wavelengths will be changing, adapting itself to different antenna sizes. For example, more than two side-bands can be obtained by the MZM-aided multi-wavelength generation mentioned in Section 5.5, narrowing the beams and thus increasing the propagation range.

Additionally, MDM introduced by POF is capable of supporting multiple user transmissions, as shown in Fig. 5.7, where user 1, 2 and 3 share the same architecture before the POF of Fig. 5.6. User 1, 2 and 3 encode different sets of STBC signals with the aid of the same architecture and these signals are transmitted in different modes of the POF through MDM. At the receiver side of POF, the demodulation is the same as that of the single-user system of Fig. 5.6. In order to show how the different users' signals can be tuned using the proposed architecture, Figs. 5.11 and 5.12 show different beams for three users. In the example of Figs. 5.11 and 5.12, three users are located at angles of 110°, 70° and 140°, which correspond to time delay differences of 78 *ps*, -78 *ps* and

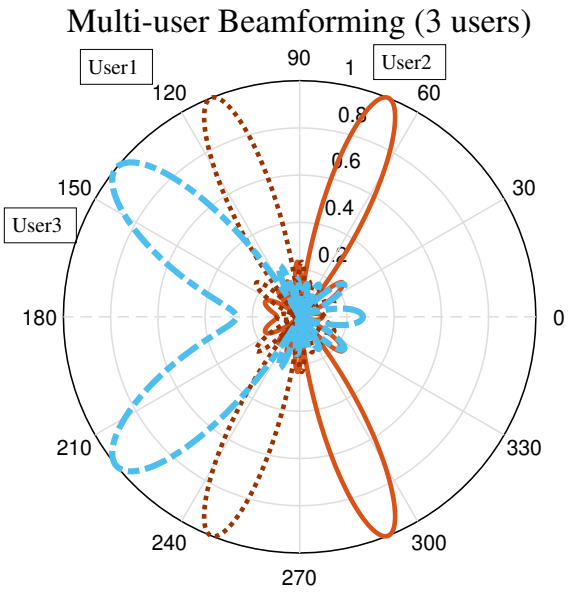

Figure 5.12: A multi-user system beampattern (N=7 antenna elements).

162 *ps*. Fig. 5.11 shows the beams, when N=4 antenna elements are used, while Fig. 5.12 shows the beams, when N=7 antenna elements are employed.

5.6 Conclusions

In this chapter, we focused on our attention on the RoPOF aided MF-MIMO assisted indoor environment. In Section 5.1, we introduced the low-cost POF in the context of short-distance indoor communications. Then, in Section 5.2, we briefly reviewed the recently developed POF based indoor communication systems, including their modulation format and concluded that DMT is suitable for communication in the limited bandwidth of the large-core POF. Furthermore, in Sections 5.4 and 5.5, a novel all-optical processing aided multi-functional wireless MIMO system was designed by exploiting the MZM's non-linearity and CFBG, where a POF was used for supporting a multi-user system. Furthermore, the ODSB-encoded STBC signal was realised by using a combination of two LDs and two BPFs, where the associated multi-wavelength generation is based on the MZM's non-linearity. Our design achieved a beamforming angular range of upto 150° with a small time delay step of 6 ps, which may be deemed suitable for indoor communications.

Chapter 6

Conclusions and Future Research

In this thesis, we have designed a range of cost-efficient high-performance communication systems, where we combined the benefits of analogue radio over fiber (A-RoF) and the popular multiple-input-multiple-output (MIMO) concept for conceiving centralised system designs. More explicitly, we proposed several MIMO aided A-RoF designs. In Table 6.1, we characterised each system by its MIMO type, fiber type and length as well as the application scenarios.

	MIMO type	Fiber type and length	Applications
Chapter 2	Analogue beamforming	Glass SMF (10km)	C-RAN
Chapter 3	SM	Glass SMF (20km)	C-RAN
Chapter 4	MF-MIMO (BF, Diversity, SM)	Glass SMF (10km)	C-RAN
Chapter 5	MF-MIMO (BF, Diverisity, SDM)	POF (40m)	Indoor DAS

Table 6.1: The outline of system design each chapter. SM: Spatial Modulation, MF-MIMO: Multi-functional MIMO, BF: Beamforming, SDM: Space Division Multiplexing, SMF: Single-Mode Fiber, POF: Plastic Optical Fiber, C-RAN: Cloud/Centralised Radio Access Networks, DAS: Distributed Antenna System.

In this chapter, we will summarise each chapter in Section 6.1, followed by our potential future work ideas regarding this area in Section 6.2.

6.1 Thesis Summary

In this section we summarise this thesis chapter by chapter.

- **Chapter 1**: This chapter reflected in the fundamental questions: " *What motivates our research?*" in Section 1.1, where A-RoF were designed for cost-saving and MIMO techniques were harnessed for performance-improvement. In Section 1.2, for the sake of presenting our proposed system in the following chapters, some background knowledge was provided. Explicitly, the RoF concept was described and categorised as digitised and analogue RoF, namely D-RoF and A-RoF, where we opted for A-RoF. Then, the family of MIMO schemes including beamforming, diversity and multiplexing arrangements were introduced, leading to the combined concept of multi-functional-MIMO (MF-MIMO) schemes. In Section 1.2.3, we briefly reviewed the A-RoF based centralised networks, where the concepts of A-ROF-assisted low-cost cloud/centralised radio access network (C-RAN) and multi-mode fiber based indoor system were highlighted. Furthermore in Section 1.3, the novel contributions of this thesis were listed for each chapter linked to each publication.

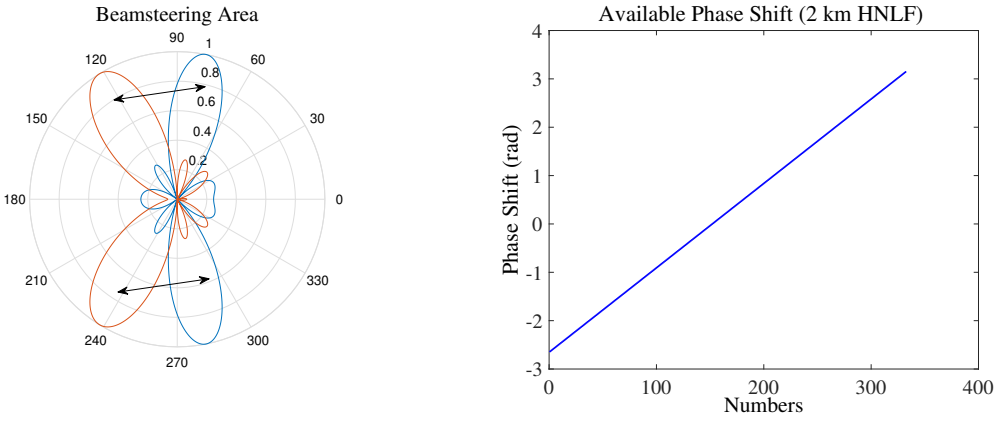

Figure 6.1: Left Figure: beam pattern of the 10 Gbps system, Right Figure: attainable phase shifts with HNLFs fiber length of 2 km (Section 2.4).

- **Chapter 2:** The system designed in this chapter invokes A-RoF for optical processing aided beamforming. In Section 2.1, we addressed the question of " *Why do we need the optical processing aided beamforming?*", demonstrating the fact that it is capable of dispensing with the electronic phase shifter required for conventional analogue beamforming. Then, in Section 2.2, the phased array aided beamforming basics were reviewed. Subsequently, in Section 2.3, a comprehensive review of A-RoF aided beamforming was provided. Then, in Section 2.4, we proposed a wireless beamforming system design beneficially exploiting the potentially

hostile fiber-non-linearity, replacing the power-thirsty electronic phase-shifters and realising convenient cellular sectorization, as shown in the left graph of Fig 6.1. Furthermore, an adaptive C-RAN system appropriately selecting the number of connected remote radio heads (RRHs) and relying on the proposed A-RoF aided beamforming scheme was proposed, which is characterised in the right graph of Fig. 6.1. Finally, we concluded the whole chapter in Section 2.5.

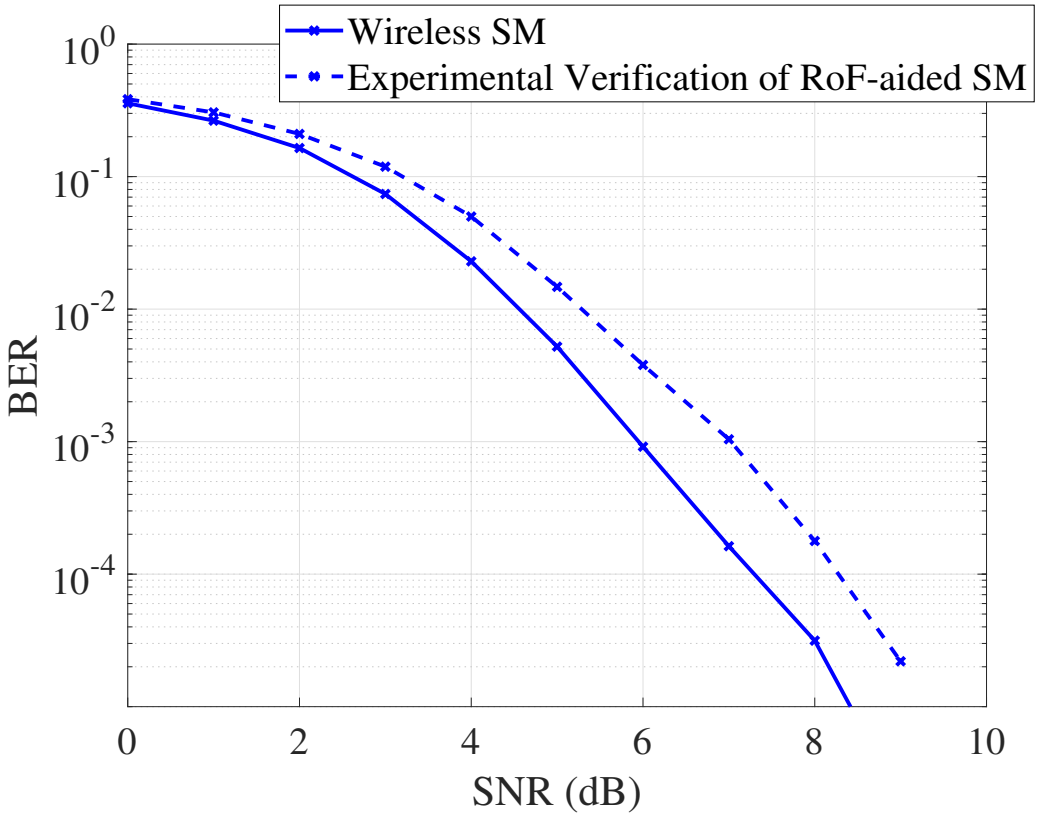

Figure 6.2: Experimental verification of the BER of proposed A-RoF-aided twin-antenna SM BER performance (Section 3.4).

- **Chapter 3:** In contrast to the beamforming aided A-RoF system of Chapter 2, this chapter aims for conceiving the spatial modulation (SM) aided A-RoF techniques for enhancing the attainable system throughput. In Section 3.1, the relevant background of A-RoF based centralised networks and the benefits of wireless SM were discussed for imposing both the spectral efficiency and energy efficiency. Then, in Section 3.2, the development of SM in wireless communications was briefly reviewed. In Section 3.3, we highlighted our contributions based on amalgamating

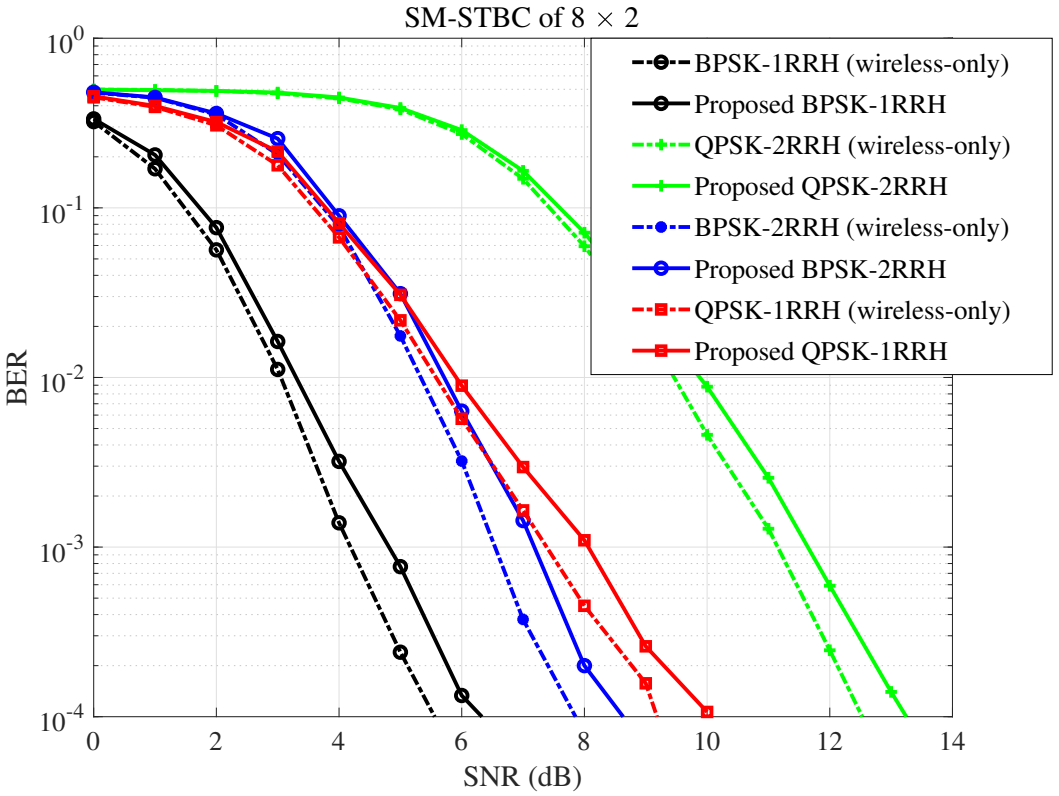

Figure 6.3: BER performance for an eight transmit antennas and two receive antennas system (Section 3.5).

SM with A-RoF for a low-cost high-efficiency C-RAN system. In Section 3.4, a feasibility study of using Mach-Zehnder modulator (MZM) side-band selection for the SM scheme's antenna mapping was demonstrated experimentally. However, only a two-antenna transmitter was considered. The experimental results demonstrated that the 2 Gbps system conceived only imposed as little as 1 dB signal-to-noise ratio (SNR) degradation at the BER of 10^{-4} compared to its counterpart operating without the A-RoF link, while benefiting from centralised SM encoding and requiring no RRH switches. Again, we show the bit error ratio (BER) performance attained in Fig. 6.2. Furthermore, the system proposed in Section 3.5 was inspired by the above experimental study, where any arbitrary number of antennas were employable by our SM design. This scheme was also amalgamated by Alamouti's space-time block coding (STBC) arrangement in an A-RoF aided adaptive C-RAN system, which was capable of flexibly adapting both the modulation format and the number of RRHs connected. We showed the corresponding BER performance

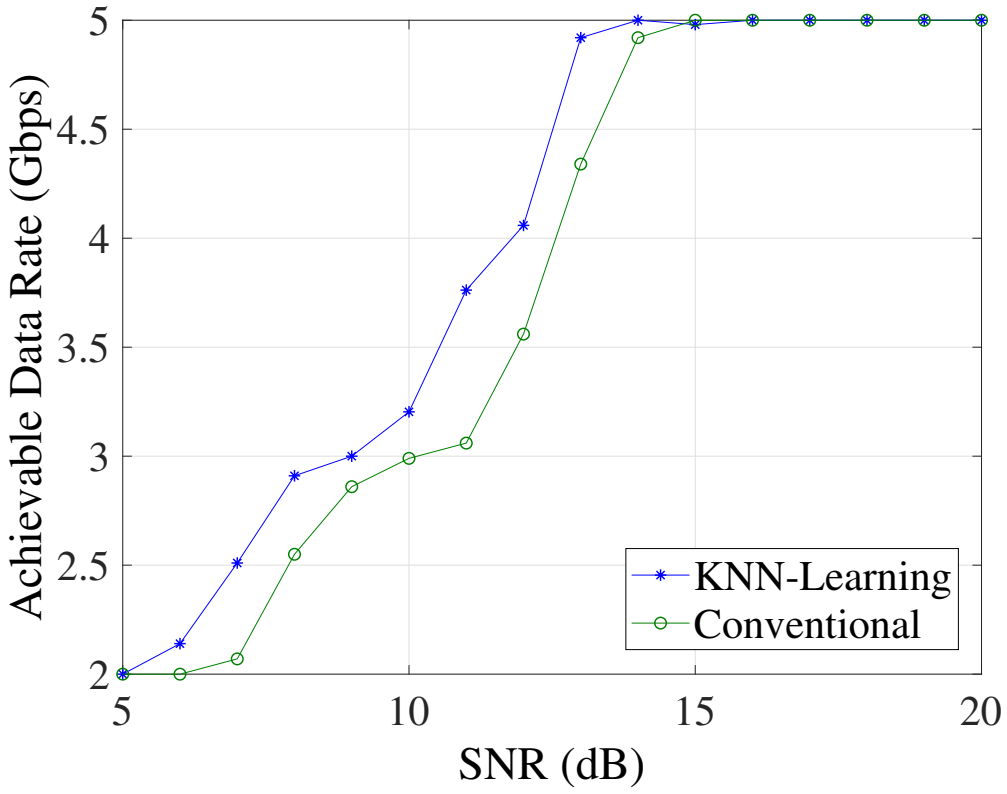

Figure 6.4: Data rate comparison (Section 3.5).

in Fig. 6.3, where the systems with A-RoF and without A-RoF were characterised, showing less than 1 dB disparity. Furthermore, in the context of the proposed C-RAN system detailed in Section 3.5, a learning assisted transceiver adaptation regime was introduced for increasing the channel capacity, which we characterised in Fig. 6.4. Section 3.6 concluded the chapter.

- **Chapter 4:** This chapter employed the MF-MIMO concepts in the A-RoF aided centralised system for the sake of achieving MIMO gains. In this chapter, combined beamforming, diversity and SM gains were achieved by the A-RoF aided C-RAN system equipped with only a single optical transceiver. In Section 4.1, we presented the relevant background both on the A-ROF and on the optical mmWave upconversion, while a brief review of wireless MF-MIMO system was provided in Section 4.2. Then, a pair of novel A-RoF aided MF-MIMO designs were proposed for both SM-BF and SM-MS-STSK in Sections 4.4 and 4.5, respectively, where most of the signal processing was carried out by a CU, while beamforming, diversity-oriented

transmission and reception as well as SM were simultaneously and centrally processed by our proposed A-RoF system. The structure of the systems proposed in Sections 4.4 and 4.5 are similar. The simulation results given by Figs. 4.11, 4.14 and 4.15 compare the A-RoF system to that employing SM-BF and MS-STSK that dispensing with A-RoF transmissions, where we see only a negligible BER degradation imposed by the A-RoF link. Finally, the conclusions of this chapter were provided in Section 4.6.

- **Chapter 5:** Whilst the above chapters were focused on outdoor communication design, this chapter conceived an indoor distributed antenna system (DAS) scenario, where we invoked a radio over plastic optical fiber (RoPOF) aided MF-MIMO design for data transmission. In Section 5.1, the background of POF aided indoor communications was reviewed briefly. In Section 5.2, we reviewed the state-of-the-art RoPOF aided indoor communication systems from the perspective of modulation formats, where we showed that multitone modulation (DMT) performed the best, when considering the bitrate-length product. Then in Section 5.3, we briefly touched upon the POF channel. Then, in Section 5.5, we proposed an A-RoPoF aided MF-MIMO system for the indoor DAS, where amalgamated beamforming, diversity and space division multiplexing (SDM) schemes were implemented using optical processing. The proposed system was further shown to be able to support multi-user communications, thanks to its beamforming function. Finally, Section 5.6 concluded this chapter.

6.2 Future Research

In this section, we propose some future research ideas:

1. **Digitised RoF (D-RoF) aided SM:** The system proposed in Chapter 3 is susceptible to optical impairments which introduces a BER error floor unless channel coding is invoked. With the advent of D-RoF [18], we expect an improved performance.

2. **Optical processing aided beamforming by exploiting the different delays of MMF modes:** Explicitly, the MMF introduces different delays for each

mode and the resultant phase shifts can be exploited for generating beamforming patterns. However, the effects of mode coupling and fiber bending should be considered. More specifically, an accurate multi-mode channel model has to be conceived for the sake of characterising the associated delay and coupling behaviour. Furthermore, the feasibility of flexibly controlling the multi-mode fiber's differential delay has to be explored.

3. **OFDM-aided A-RoMMF:** It is worth investigating whether the OFDM is capable of reducing the modal dispersion of MMF for the sake of improving the channel capacity attained.

4. **Mode division multiplexing (MDM) based MIMO-aided A-RoMMF:** MDM designed for multi-mode fiber is said to be the next revolutionary technique following the conception of laser, low-loss silica fiber, optical amplifiers and WDM in the optical communication history. How to mitigate the impact of mode coupling and of mode delay are only some of the issues which have to be considered in our future research, especially when considering wireless MIMO signal processing.

5. **A-RoF aided hybrid beamforming system with mmWave up-conversion:** Eliminating the analogue phase-shifter, as in the A-RoF aided beamformer of Chapter 2, the A-RoF assisted analogue beamforming can also be combined with digital beamforming. Furthermore, using cost-efficient mmWave optical upconversion techniques, an A-RoF aided hybrid beamformer conceived for mmWave communications may be expected to outperform its wireless DSP counterparts in terms of both energy-efficiency and cost-reduction.

6. **Indoor POF vs indoor power line communications (PLC) and copper-based communications:** A comparison among these techniques is essential for the future indoor communications. POF may also be manufactured as the electronic insulation of the mains power line and they could be combined for attaining a beneficial diversity gain.

Bibliography

[1] A. Checko, H. L. Christiansen, Y. Yan, L. Scolari, G. Kardaras, M. S. Berger, and L. Dittmann, "Cloud RAN for mobile networks——a technology overview," *IEEE Communications Surveys Tutorials*, vol. 17, pp. 405–426, First Quarter 2015.

[2] A. Goldsmith, *Wireless communications*. Cambridge university press, 2005.

[3] S. Lien, S. Shieh, Y. Huang, B. Su, Y. Hsu, and H. Wei, "5G new radio: Waveform, frame structure, multiple access, and initial access," *IEEE Communications Magazine*, vol. 55, pp. 64–71, June 2017.

[4] E. Dahlman, G. Mildh, S. Parkvall, J. Peisa, J. Sachs, Y. Seln, and J. Sköld, "5G wireless access: requirements and realization," *IEEE Communications Magazine*, vol. 52, pp. 42–47, Dec. 2014.

[5] A. Alexiou, "Wireless world 2020: Radio interface challenges and technology enablers," *IEEE Vehicular Technology Magazine*, vol. 9, pp. 46–53, March 2014.

[6] Y. Shi, M. Morant, C. Okonkwo, R. Llorente, E. Tangdiongga, and A. Koonen, "Multistandard wireless transmission over SSMF and large-core POF for access and in-home networks," *IEEE Photonics Technology Letters*, vol. 24, pp. 736–738, May 2012.

[7] Y. Li, I. A. Hemadeh, M. El-Hajjar, and L. Hanzo, "Radio over fiber downlink design for spatial modulation and multi-set space-time shift-keying," *IEEE Access*, vol. 6, pp. 21812–21827, March 2018.

[8] M. D. Renzo, H. Haas, A. Ghrayeb, S. Sugiura, and L. Hanzo, "Spatial modulation for generalized MIMO: Challenges, opportunities, and implementation," *Proceedings of the IEEE*, vol. 102, pp. 56–103, Jan. 2014.

[9] L. Hanzo, H. Haas, S. Imre, D. O'Brien, M. Rupp, and L. Gyongyosi, "Wireless myths, realities, and futures: From 3G/4G to optical and quantum wireless," *Proceedings of the IEEE*, vol. 100, pp. 1853–1888, May 2012.

[10] P. Polishuk, "Plastic optical fibers branch out," *IEEE Communications Magazine*, vol. 44, pp. 140–148, Sept. 2006.

[11] Y. Koike and M. Asai, "The future of plastic optical fiber," *NPG Asia Materials*, vol. 1, p. 22, Oct. 2009.

[12] V. Thomas, M. El-Hajjar, and L. Hanzo, "Performance improvement and cost reduction techniques for radio over fiber communications," *IEEE Communications Surveys Tutorials*, vol. 17, pp. 627–670, Second Quarter 2015.

[13] G. P. Agrawal, *Fiber-optic communication systems*, vol. 222. John Wiley & Sons, 2012.

[14] W. Way, R. Wolff, and M. Krain, "A 1.3-m 35-km fiber-optic microwave multicarrier transmission system for satellite earth stations," *Journal of Lightwave Technology*, vol. 5, pp. 1325–1332, Sept. 1987.

[15] V. A. Thomas, M. El-Hajjar, and L. Hanzo, "Millimeter-wave radio over fiber optical upconversion techniques relying on link nonlinearity," *IEEE Communications Surveys Tutorials*, vol. 18, pp. 29–53, First Quarter 2016.

[16] D. Novak, R. B. Waterhouse, A. Nirmalathas, C. Lim, P. A. Gamage, T. R. Clark, M. L. Dennis, and J. A. Nanzer, "Radio-over-fiber technologies for emerging wireless systems," *IEEE Journal of Quantum Electronics*, vol. 52, pp. 1–11, Jan. 2016.

[17] D. Novak and R. Waterhouse, "Advanced radio over fiber network technologies," *Optics Express*, vol. 21, pp. 23001–23006, Sept. 2013.

[18] P. A. Gamage, A. Nirmalathas, C. Lim, D. Novak, and R. Waterhouse, "Design and analysis of digitized RF-over-fiber links," *Journal of Lightwave Technology*, vol. 27, pp. 2052–2061, June 2009.

[19] Y. Li, M. El-Hajjar, and L. Hanzo, "Joint space-time block-coding and beamforming for the multiuser radio over plastic fiber downlink," *IEEE Transactions on Vehicular Technology*, vol. 67, pp. 2781–2786, March 2018.

[20] N. J. Gomes, M. Morant, A. Alphones, B. Cabon, J. E. Mitchell, C. Lethien, M. Csörnyei, A. Stöhr, and S. Iezekiel, "Radio-over-fiber transport for the support of wireless broadband services," *Journal of Optical Networking*, vol. 8, pp. 156–178, Feb. 2009.

[21] S. Yang and L. Hanzo, "Fifty years of MIMO detection: The road to large-scale MIMOs," *IEEE Communications Surveys Tutorials*, vol. 17, pp. 1941–1988, Fourth Quarter 2015.

[22] L. Hanzo, O. Alamri, M. El-Hajjar, and N. Wu, *Near-capacity multi-functional MIMO systems: sphere-packing, iterative detection and cooperation*, vol. 4. John Wiley & Sons, 2009.

[23] M. Peng, C. Wang, V. Lau, and H. V. Poor, "Fronthaul-constrained cloud radio access networks: Insights and challenges," *IEEE Wireless Communications*, vol. 22, pp. 152–160, April 2015.

[24] A. Koonen and E. Tangdiongga, "Photonic home area networks," *Journal of Lightwave Technology*, vol. 32, pp. 591–604, Feb. 2014.

[25] D. Visani, M. N. Petersen, F. Sorci, L. Tarlazzi, P. Faccin, and G. Tartarini, "In-building wireless distribution in legacy multimode fiber with an improved RoMMF system," *IEEE Microwave and Wireless Components Letters*, vol. 22, pp. 598–600, Nov. 2012.

[26] N. J. Gomes, A. Das, A. Nkansah, M. Mjeku, and D. Wake, "Multimode fiber-fed indoor wireless networks," in *2006 International Topical Meeting on Microwave Photonics*, pp. 1–4, Oct. 2006.

[27] Y. Li, S. Ghafoor, K. Satyanarayana, M. El-Hajjar, and L. Hanzo, "Analogue wireless beamforming exploiting the fiber-nonlinearity of radio over fiber based c-rans," *IEEE Transactions on Vehicular Technology*, pp. 1–1, Jan. 2019.

[28] Y. Li, Q. Yang, I. A. Hemadeh, M. El-Hajjar, C.-K. Chan, and L. Hanzo, "Experimental characterization of the radio over fiber aided twin-antenna spatial modulation downlink," *Optics Express*, vol. 26, pp. 12432–12440, May 2018.

[29] Y. Li, K. Satyanarayana, M. El-Hajjar, and L. Hanzo, "Analogue radio over fiber aided mimo design for the learning assisted adaptive c-ran downlink," *IEEE Access*, vol. 7, pp. 21359–21371, Feb. 2019.

[30] I. Ahmed, H. Khammari, A. Shahid, A. Musa, K. S. Kim, E. D. Poorter, and I. Moerman, "A survey on hybrid beamforming techniques in 5G: Architecture and system model perspectives," *IEEE Communications Surveys Tutorials*, vol. 20, pp. 3060–3097, Fourth Quarter 2018.

[31] S. Rangan, T. S. Rappaport, and E. Erkip, "Millimeter-wave cellular wireless networks: Potentials and challenges," *Proceedings of the IEEE*, vol. 102, pp. 366–385, March 2014.

[32] H. Subbaraman, M. Y. Chen, and R. T. Chen, "Photonic crystal fiber-based true-time-delay beamformer for multiple RF beam transmission and reception of an X-band phased-array antenna," *Journal of Lightwave Technology*, vol. 26, pp. 2803–2809, Aug. 2008.

[33] J. Andrews, S. Buzzi, W. Choi, S. Hanly, A. Lozano, A. Soong, and J. Zhang, "What will 5G be?," *IEEE Journal on Selected Areas in Communications*, vol. 32, pp. 1065–1082, June 2014.

[34] R. A. Minasian and K. E. Alameh, "Optical-fiber grating-based beamforming network for microwave phased arrays," *IEEE Transaction on Microwave Theory and Techniques*, vol. 45, pp. 1513–1518, Aug. 1997.

[35] L. Xu, R. Taylor, and S. R. Forrest, "The use of optically coherent detection techniques for true-time delay phased array and systems," *Journal of Lightwave Technology*, vol. 13, pp. 1663–1678, Aug. 1995.

[36] A. Pizzinat, P. Chanclou, F. Saliou, and T. Diallo, "Things you should know about fronthaul," *Journal of Lightwave Technology*, vol. 33, pp. 1077–1083, March 2015.

[37] Z. Cao, Q. Ma, A. B. Smolders, Y. Jiao, M. J. Wale, C. W. Oh, H. Wu, and A. M. J. Koonen, "Advanced integration techniques on broadband millimeter-wave beam steering for 5G wireless networks and beyond," *IEEE Journal of Quantum Electronics*, vol. 52, pp. 1–20, Jan. 2016.

[38] M. Longbrake, "True time-delay beamsteering for radar," in *IEEE National Aerospace and Electronics Conference (NAECON)*, pp. 246–249, July 2012.

[39] B. Ortega, J. Cruz, J. Capmany, M. Andres, and D. Pastor, "Analysis of a microwave time delay line based on a perturbed uniform fiber Bragg grating operating at constant wavelength," *Journal of Lightwave Technology*, vol. 18, pp. 430–436, March 2000.

[40] S. Blais and J. Yao, "Photonic true-time delay beamforming based on superstructured fiber Bragg gratings with linearly increasing equivalent chirps," *Journal of Lightwave Technology*, vol. 27, pp. 1147–1154, May 2009.

[41] A. Molony, L. Zhang, J. A. Williams, I. Bennion, C. Edge, and J. Fells, "Fiber Bragg-grating true time-delay systems: discrete-grating array 3-b delay lines and chirped-grating 6-b delay lines," *IEEE Transaction on Microwave Theory and Techniques*, vol. 45, pp. 1527–1530, Aug. 1997.

[42] J. Yao, J. Yang, and Y. Liu, "Continuous true-time-delay beamforming employing a multiwavelength tunable fiber laser source," *IEEE Photonics Technology Letters*, vol. 14, pp. 687–689, May 2002.

[43] H. Rideout, J. Seregelyi, and J. Yao, "A true time delay beamforming system incorporating a wavelength tunable optical phase-lock loop," *Journal of Lightwave Technology*, vol. 25, pp. 1761–1770, July 2007.

[44] V. Italia, M. Pisco, S. Campopiano, A. Cusano, and A. Cutolo, "Chirped fiber Bragg gratings for electrically tunable time delay lines," *IEEE Journal of Selected Topics in Quantum Electronics*, vol. 11, pp. 408–416, March 2005.

[45] H. Zmuda, R. A. Soref, P. Payson, S. Johns, and E. Toughlian, "Photonic beamformer for phased array antennas using a fiber grating prism," *IEEE Photonics Technology Letters*, vol. 9, pp. 241–243, Feb. 1997.

[46] B. Ortega, J. Cruz, J. Capmany, M. Andres, and D. Pastor, "Variable delay line for phased-array antenna based on a chirped fiber grating," *IEEE Transaction on Microwave Theory and Techniquess on*, vol. 48, pp. 1352–1360, Aug. 2000.

[47] Y. Liu, J. Yang, and J. Yao, "Continuous true-time-delay beamforming for phased array antenna using a tunable chirped fiber grating delay line," *IEEE Photonics Technology Letters*, vol. 14, pp. 1172–1174, Aug. 2002.

[48] Y.-G. Han, J. Lee, and S. Lee, "Continuously tunable photonic microwave true-time delay based on tunable chirped fibre Bragg grating," *Electronics Letters*, vol. 42, pp. 811–812, July 2006.

[49] D. Hunter, M. Parker, and J. Dexter, "Demonstration of a continuously variable true-time delay beamformer using a multichannel chirped fiber grating," *IEEE Transaction on Microwave Theory and Techniques*, vol. 54, pp. 861–867, Feb. 2006.

[50] B. Zhou, X. Zheng, X. Yu, H. Zhang, Y. Guo, and B. Zhou, "Optical beamforming networks based on broadband optical source and chirped fiber grating," *IEEE Photonics Technology Letters*, vol. 20, pp. 733–735, May 2008.

[51] A. Molony, L. Zhang, J. Willlams, I. Bennion, C. Edge, and J. Fells, "Fiber Bragg grating networks for time-delay control of phased-array antennas," in *Summaries of papers presented at the 1996 Conference on Lasers and Electro-Optics*, pp. 244–245, IEEE, June 1996.

[52] G. A. Ball, W. Glenn, and W. Morey, "Programmable fiber optic delay line," *IEEE Photonics Technology Letters*, vol. 6, pp. 741–743, June 1994.

[53] B. Ortega, J. L. Cruz, J. Capmany, M. V. Andrés, and D. Pastor, "Analysis of a microwave time delay line based on a perturbed uniform fiber Bragg grating operating at constant wavelength," *Journal of Lightwave Technology*, vol. 18, pp. 430–436, March 2000.

[54] D. B. Hunter, M. E. Parker, and J. L. Dexter, "Demonstration of a continuously variable true-time delay beamformer using a multichannel chirped fiber grating," *IEEE Transaction on Microwave Theory and Techniques*, vol. 54, pp. 861–867, Feb. 2006.

[55] B. Zhou, X. Zheng, X. Yu, H. Zhang, Y. Guo, and B. Zhou, "Optical beamforming networks based on broadband optical source and chirped fiber grating," *IEEE Photonics Technology Letters*, vol. 20, pp. 733–735, Sept. 2008.

[56] R. Bonjour, S. A. Gebrewold, D. Hillerkuss, C. Hafner, and J. Leuthold, "Ultra-fast tunable true-time delay using complementary phase-shifted spectra (CPSS)," in *2015 Optical Fiber Communication Conference*, p. W2A.67, Optical Society of America, March 2015.

[57] G.-Y. Lee, Y.-B. Choi, J.-D. Shin, and B.-G. Kim, "4-b true time-delay feeder using MEMS switches for linear phased-array antennas," in *2002 Optical Fiber Communication Conference and Exhibit*, pp. 738–740, March 2002.

[58] O. Raz, S. Barzilay, R. Rotman, and M. Tur, "Fast switching and wideband photonic beamformer with flat RF response and squintless scan performance," in *2007 Conference on Optical Fiber Communication and the National Fiber Optic Engineers Conference*, pp. 1–3, March 2007.

[59] V. S. Ilchenko and A. B. Matsko, "Optical resonators with whispering-gallery modes-Part II: applications," *IEEE Journal of Selected Topics in Quantum Electronics*, vol. 12, pp. 15–32, Jan. 2006.

[60] M. Fakharzadeh, S. Chaudhuri, and S. Safavi-Naeini, "Optical beamforming with tunable ring resonators," in *2008 IEEE Antennas and Propagation Society International Symposium*, pp. 1–4, July 2008.

[61] T. Mengual, B. Vidal Rodriguez, C. Stoltidou, S. Blanch, J. Martí, L. Jofre, I. McKenzie, and J. M. Del Cura, "Optical beamforming network with multibeam capability based on a spatial light modulator," in *2008 Optical Fiber Communication Conference*, p. JThA71, Optical Society of America, Feb. 2008.

[62] T. H. Barnes, T. Eiju, K. Matsuda, H. Ichikawa, M. R. Taghizadeh, and J. Turunen, "Reconfigurable free-space optical interconnections with a phase-only

liquid-crystal spatial light modulator," *Applied Optics*, vol. 31, pp. 5527–5535, Sept. 1992.

[63] B. Vidal, T. Mengual, C. Ibanez-Lopez, and J. Marti, "Optical beamforming network based on fiber-optical delay lines and spatial light modulators for large antenna arrays," *IEEE Photonics Technology Letters*, vol. 18, pp. 2590–2592, Dec. 2006.

[64] M. Hirano, T. Nakanishi, T. Okuno, and M. Onishi, "Silica-based highly nonlinear fibers and their application," *IEEE Journal of Selected Topics in Quantum Electronics*, vol. 15, pp. 103–113, Jan. 2009.

[65] A. Loayssa, S. Galech, and F. Lahoz, "Broadband microwave photonic phase-shifter based on stimulated Brillouin scattering," in *The 18th Annual Meeting of the IEEE Lasers and Electro-Optics Society*, pp. 839–840, Oct. 2005.

[66] Y. Dong, H. He, W. Hu, Z. Li, Q. Wang, W. Kuang, T. H. Cheng, Y. J. Wen, Y. Wang, and C. Lu, "Photonic microwave phase shifter/modulator based on a nonlinear optical loop mirror incorporating a Mach-Zehnder interferometer," *Optics Letters*, vol. 32, pp. 745–747, April 2007.

[67] W. Li, W. H. Sun, W. T. Wang, and N. H. Zhu, "Optically controlled microwave phase shifter based on nonlinear polarization rotation in a highly nonlinear fiber," *Optics Letters*, vol. 39, pp. 3290–3293, June 2014.

[68] K. Satyanarayana, M. El-Hajjar, P. H. Kuo, A. Mourad, and L. Hanzo, "Adaptive transceiver design for C-RAN in mmwave communications," *IEEE Access*, vol. PP, pp. 1–1, Nov. 2017.

[69] C. A. Balanis, *Antenna theory: analysis and design*, vol. 1. John Wiley & Sons, 2005.

[70] S. Blais and J. Yao, "Photonic true-time delay beamforming based on superstructured fiber Bragg gratings with linearly increasing equivalent chirps," *Journal of Lightwave Technology*, vol. 27, pp. 1147–1154, May 2009.

[71] S. Garakoui, E. Klumperink, B. Nauta, and F. van Vliet, "Phased-array antenna beam squinting related to frequency dependency of delay circuits," in *2011 41st European Microwave Conference (EUMC)*, pp. 1304–1307, Oct. 2011.

[72] E. Chan and R. Minasian, "Photonic RF phase shifter and tunable photonic RF notch filter," *Journal of Lightwave Technology*, vol. 24, pp. 2676–2682, July 2006.

[73] D. Adams and C. Madsen, "A novel broadband photonic RF phase shifter," *Journal of Lightwave Technology*, vol. 26, pp. 2712–2717, Aug. 2008.

[74] E. H. Chan, W. Zhang, and R. A. Minasian, "Photonic RF phase shifter based on optical carrier and RF modulation sidebands amplitude and phase control," *Journal of Lightwave Technology*, vol. 30, pp. 3672–3678, Dec. 2012.

[75] X. Wang, E. H. W. Chan, and R. A. Minasian, "All-optical photonic microwave phase shifter based on an optical filter with a nonlinear phase response," *Journal of Lightwave Technology*, vol. 31, pp. 3323–3330, Oct. 2013.

[76] B. Vidal, T. Mengual, C. Ibanez-Lopez, and J. Marti, "Optical beamforming network based on fiber-optical delay lines and spatial light modulators for large antenna arrays," *IEEE Photonics Technology Letters*, vol. 18, pp. 2590–2592, Dec. 2006.

[77] R. Wilson, M. Lewis, and P. Sample, "Developments in coherent beamforming for compact phased array antennas," in *2001 International Topical Meeting on Microwave Photonics*, pp. 4–pp, IEEE, Jan. 2001.

[78] U. Efron, *Spatial light modulator technology: materials, devices, and applications*, vol. 47. CRC Press, 1994.

[79] J. Corral, J. Marti, and J. Fuster, "Optical beamforming network based on chirped fiber gratings continuously variable true-time-delay lines," in *1998 IEEE MTT-S International Microwave Symposium Digest*, vol. 3, pp. 1379–1382, IEEE, June 1998.

[80] J. Corral, J. Marti, and J. Fuster, "Effects of optical modulation on continuously variable millimeter-wave delay lines based on optical fiber gratings," in *1999 IEEE*

MTT-S International Microwave Symposium Digest, vol. 3, pp. 1117–1120, IEEE, June 1999.

[81] B. Ortega, J. L. Cruz, J. Capmany, M. V. Andrés, and D. Pastor, "Variable delay line for phased-array antenna based on a chirped fiber grating," *IEEE Transaction on Microwave Theory and Techniques*, vol. 48, pp. 1352–1360, Aug. 2000.

[82] B. Vidal, D. Madrid, J. L. Corral, V. Polo, A. Martinez, J. H. Den Besten, F. Soares, J. Marti, and M. K. Smit, "Photonic true-time delay beamformer for broadband wireless access networks at 40 GHz band," in *2002 IEEE MTT-S International Microwave Symposium Digest*, vol. 3, pp. 1949–1952, June 2002.

[83] K. O. Hill and G. Meltz, "Fiber Bragg grating technology fundamentals and overview," *Journal of Lightwave Technology*, vol. 15, pp. 1263–1276, Aug. 1997.

[84] F. Zeng, J. Yao, and T. Yeap, "Dispersion effects and implementation errors on uniform fiber Bragg grating based true-time-delay beamforming networks," in *Proceedings of the 2003 International Topical Meeting on Microwave Photonics*, pp. 337–340, Sept. 2003.

[85] P. Q. Thai, A. Alphones, and D. R. Lim, "Optical beamforming using chirped fiber grating: Criticality of group delay ripple," in *2009 International Topical Meeting on Microwave Photonics*, pp. 1–4, IEEE, Oct. 2009.

[86] P. Q. Thai, A. Alphones, and D. Lim, "Limitations by group delay ripple on optical beam-forming with chirped fiber grating," *Journal of Lightwave Technology*, vol. 27, pp. 5619–5625, Dec. 2009.

[87] D. Mogilevtsev, T. A. Birks, and P. S. J. Russell, "Group-velocity dispersion in photonic crystal fibers," *Optics Letters*, vol. 23, pp. 1662–1664, Nov. 1998.

[88] D. G. Rabus, *Integrated ring resonators*. Springer, 2007.

[89] T. S. Rappaport, *Wireless communications: principles and practice*, vol. 2. prentice hall PTR New Jersey, 1996.

[90] G. P. Agrawal, *Nonlinear fiber optics*. Academic press, 2007.

[91] G. P. Agrawal, "Nonlinear fiber optics: its history and recent progress," *JOSA B*, vol. 28, pp. A1–A10, Dec. 2011.

[92] J. Leibrich and W. Rosenkranz, "Efficient numerical simulation of multichannel WDM transmission systems limited by XPM," *IEEE Photonics Technology Letters*, vol. 15, pp. 395–397, March 2003.

[93] M. Hirano, T. Nakanishi, T. Okuno, and M. Onishi, "Silica-based highly nonlinear fibers and their application," *IEEE Journal of Selected Topics in Quantum Electronics*, vol. 15, pp. 103–113, Jan. 2009.

[94] K. Satyanarayana, M. El-Hajjar, P. H. Kuo, A. Mourad, and L. Hanzo, "Dual-function hybrid beamforming and transmit diversity aided millimeter wave architecture," *IEEE Transactions on Vehicular Technology*, vol. PP, pp. 1–1, March 2017.

[95] L. Provost, C. Finot, K. Mukasa, P. Petropoulos, and D. J. Richardson, "Generalisation and experimental validation of design rules for self-phase modulation-based 2R-regenerators," in *2007 Optical Fiber Communication Conference and Exposition and The National Fiber Optic Engineers*, pp. 1–3, Optical Society of America, March 2007.

[96] B. Peng, S. Priebe, and T. Kurner, "Effects of phase shift errors on the antenna directivity of phased arrays in indoor terahertz communications," in *2014 11th International Symposium on Wireless Communications Systems (ISWCS)*, pp. 355–359, Aug. 2014.

[97] M. Mohamed, X. Zhang, B. Hraimel, and K. Wu, "Analysis of frequency quadrupling using a single Mach-Zehnder modulator for millimeter-wave generation and distribution over fiber systems," *Optics Express*, vol. 16, pp. 10786–10802, July 2008.

[98] D.-I. Yeom, E. C. Magi, M. R. Lamont, L. Fu, and B. J. Eggleton, "Low-threshold supercontinuum generation in dispersion engineered highly nonlinear chalcogenide fiber nanowires," in *2008 Conference on Optical Fiber communication/National Fiber Optic Engineers*, pp. 1–3, IEEE, March 2008.

[99] V. A. Thomas, M. El-Hajjar, and L. Hanzo, "Single ODSB radio-over-fiber signal supports STBC at each RAP," *IEEE Communications Letters*, vol. 19, pp. 1331–1334, May 2015.

[100] H. Yang, Y. He, J. Zhang, Y. Ji, W. Bai, and Y. Lee, "Performance evaluation of multi-stratum resources optimization with network functions virtualization for cloud-based radio over optical fiber networks," *Optics Express*, vol. 24, pp. 8666–8678, April 2016.

[101] M. Peng, K. Zhang, J. Jiang, J. Wang, and W. Wang, "Energy-efficient resource assignment and power allocation in heterogeneous cloud radio access networks," *IEEE Transactions on Vehicular Technology*, vol. 64, pp. 5275–5287, Nov. 2015.

[102] C. Liu, L. Zhang, M. Zhu, J. Wang, L. Cheng, and G. K. Chang, "A novel multi-service small-cell cloud radio access network for mobile backhaul and computing based on radio-over-fiber technologies," *Journal of Lightwave Technology*, vol. 31, pp. 2869–2875, Sept. 2013.

[103] R. Irmer, H. Droste, P. Marsch, M. Grieger, G. Fettweis, S. Brueck, H. P. Mayer, L. Thiele, and V. Jungnickel, "Coordinated multipoint: Concepts, performance, and field trial results," *IEEE Communications Magazine*, vol. 49, pp. 102–111, Feb. 2011.

[104] N. Ishikawa, S. Sugiura, and L. Hanzo, "50 years of permutation, spatial and index modulation: From classic RF to visible light communications and data storage," *IEEE Communications Surveys Tutorials*, vol. 20, pp. 1905–1938, Third Quarter 2018.

[105] R. Y. Mesleh, H. Haas, S. Sinanovic, C. W. Ahn, and S. Yun, "Spatial modulation," *IEEE Transactions on Vehicular Technology*, vol. 57, pp. 2228–2241, July 2008.

[106] I. A. Hemadeh, M. El-Hajjar, S. Won, and L. Hanzo, "Multi-set space-time shift-keying with reduced detection complexity," *IEEE Access*, vol. 4, pp. 4234–4246, June 2016.

[107] Y. Chen, L. Wang, Y. Ai, B. Jiao, and L. Hanzo, "Performance analysis of NOMA-SM in vehicle-to-vehicle massive MIMO channels," *IEEE Journal on Selected Areas in Communications*, vol. 35, pp. 2653–2666, Dec. 2017.

[108] C. X. Wang, F. Haider, X. Gao, X. H. You, Y. Yang, D. Yuan, H. M. Aggoune, H. Haas, S. Fletcher, and E. Hepsaydir, "Cellular architecture and key technologies for 5G wireless communication networks," *IEEE Communications Magazine*, vol. 52, pp. 122–130, Feb. 2014.

[109] Y. A. Chau and S.-H. Yu, "Space modulation on wireless fading channels," in *Proceedings of IEEE 54th Vehicular Technology Conference (VTC Fall 2001)*, vol. 3, pp. 1668–1671 vol.3, 2001.

[110] S. Sugiura, S. Chen, and L. Hanzo, "Generalized space-time shift keying designed for flexible diversity-, multiplexing- and complexity-tradeoffs," *IEEE Transactions on Wireless Communications*, vol. 10, pp. 1144–1153, April 2011.

[111] P. Yang, Y. Xiao, L. Li, Q. Tang, Y. Yu, and S. Li, "Link adaptation for spatial modulation with limited feedback," *IEEE Transactions on Vehicular Technology*, vol. 61, pp. 3808–3813, Oct. 2012.

[112] Y. Bian, X. Cheng, M. Wen, L. Yang, H. V. Poor, and B. Jiao, "Differential spatial modulation," *IEEE Transactions on Vehicular Technology*, vol. 64, pp. 3262–3268, July 2015.

[113] D. A. Basnayaka and H. Haas, "Spatial modulation for massive MIMO," in *2015 IEEE International Conference on Communications (ICC)*, pp. 1945–1950, June 2015.

[114] F. Wu, L. L. Yang, W. Wang, and Z. Kong, "Secret precoding-aided spatial modulation," *IEEE Communications Letters*, vol. 19, pp. 1544–1547, Sept. 2015.

[115] S. Sugiura, S. Chen, and L. Hanzo, "A universal space-time architecture for multiple-antenna aided systems," *IEEE Communications Surveys Tutorials*, vol. 14, pp. 401–420, Second Quarter 2012.

[116] G. Smith, D. Novak, and Z. Ahmed, "Technique for optical SSB generation to overcome dispersion penalties in fibre-radio systems," *Electronics Letters*, vol. 33, pp. 74–75, Jan. 1997.

[117] M. Xue, S. Pan, and Y. Zhao, "Optical single-sideband modulation based on a dual-drive MZM and a 120 hybrid coupler," *Journal of Lightwave Technology*, vol. 32, pp. 3317–3323, Oct. 2014.

[118] J. Jeganathan, A. Ghrayeb, and L. Szczecinski, "Spatial modulation: optimal detection and performance analysis," *IEEE Communications Letters*, vol. 12, pp. 545–547, Aug. 2008.

[119] R. O. Duda and P. E. Hart, "Pattern classification and scene analysis," *A Wiley-Interscience Publication, New York: Wiley*, 1973.

[120] M. El-Hajjar, S. Zummo, and L. Hanzo, "Near-instantaneously adaptive cooperative uplink schemes based on space-time block codes and V-Blast," in *2007 IEEE 65th Vehicular Technology Conference - VTC2007-Spring*, pp. 2200–2204, April 2007.

[121] I. A. Hemadeh, M. El-Hajjar, and L. Hanzo, "Hierarchical multi-functional layered spatial modulation," *IEEE Access*, vol. 6, pp. 9492–9533, Feb. 2018.

[122] J. M. B. Oliveira, H. M. Salgado, and M. R. D. Rodrigues, "A new MSE channel estimator optimized for nonlinearly distorted faded OFDM signals with applications to radio over fiber," *IEEE Transactions on Communications*, vol. 62, pp. 2977–2985, Aug. 2014.

[123] S. Z. Pinter and X. N. Fernando, "Estimation and equalization of fiber-wireless uplink for multiuser CDMA 4G networks," *IEEE Transactions on Communications*, vol. 58, pp. 1803–1813, June 2010.

[124] V. N. Ha, L. B. Le, and N. D. Dao, "Coordinated multipoint transmission design for cloud RANs with limited fronthaul capacity constraints," *IEEE Transactions on Vehicular Technology*, vol. 65, pp. 7432–7447, Sept. 2016.

[125] G. S. D. Gordon, M. J. Crisp, R. V. Penty, and I. H. White, "Experimental evaluation of layout designs for 3×3 MIMO-enabled radio-over-fiber distributed antenna systems," *IEEE Transactions on Vehicular Technology*, vol. 63, pp. 643–653, Feb. 2014.

[126] T. Rappaport, S. Sun, R. Mayzus, H. Zhao, Y. Azar, K. Wang, G. Wong, J. Schulz, M. Samimi, and F. Gutierrez, "Millimeter wave mobile communications for 5G cellular: It will work!," *IEEE Access*, vol. 1, pp. 335–349, May 2013.

[127] Y. Xiang, C. Chen, C. Zhang, and K. Qiu, "Wired/wireless access integrated RoF-PON with scalable generation of multi-frequency MMWs enabled by polarization multiplexed FWM in SOA," *Optics Express*, vol. 21, pp. 1218–1225, Jan. 2013.

[128] C. Zhang, L. Wang, and K. Qiu, "Proposal for all-optical generation of multiple-frequency millimeter-wave signals for RoF system with multiple base stations using FWM in SOA," *Optics Express*, vol. 19, pp. 13957–13962, July 2011.

[129] Y. Xiang, N. Jiang, C. Chen, C. Zhang, and K. Qiu, "Wired/wireless access integrated RoF-PON with scalable generation of multi-frequency MMWs enabled by tunable optical frequency comb," *Optics Express*, vol. 21, pp. 19762–19767, Aug. 2013.

[130] C. Zhang, C. Chen, and K. Qiu, "Hybrid bidirectional radio-over-fiber-based orthogonal frequency division multiple access-passive optical network supporting 60/120 GHz using offset quadrate phase shift keying," *Optical Engineering*, vol. 54, pp. 096–108, Sept. 2015.

[131] S. Sugiura, S. Chen, and L. Hanzo, "Coherent and differential space-time shift keying: A dispersion matrix approach," *IEEE Transactions on Communications*, vol. 58, pp. 3219–3230, Nov. 2010.

[132] V. Tarokh, A. Naguib, N. Seshadri, and A. R. Calderbank, "Combined array processing and space-time coding," *IEEE Transactions on Information Theory*, vol. 45, pp. 1121–1128, May 1999.

[133] G. Jongren, M. Skoglund, and B. Ottersten, "Combining beamforming and orthogonal space-time block coding," *IEEE Transactions on Information Theory*, vol. 48, pp. 611–627, March 2002.

[134] M. El-Hajjar, O. Alamri, J. Wang, S. Zummo, and L. Hanzo, "Layered steered space-time codes using multi-dimensional sphere packing modulation," *IEEE Transactions on Wireless Communications*, vol. 8, pp. 3335–3340, July 2009.

[135] B. Hassibi and B. Hochwald, "Linear dispersion codes," in *Proceedings of the 2001 IEEE International Symposium on Information Theory (IEEE Cat. No.01CH37252)*, p. 325, 2001.

[136] R. W. Heath and A. J. Paulraj, "Linear dispersion codes for MIMO systems based on frame theory," *IEEE Transactions on Signal Processing*, vol. 50, pp. 2429–2441, Oct. 2002.

[137] S. Sugiura, S. Chen, and L. Hanzo, "Space-time shift keying: A unified MIMO architecture," in *2010 IEEE Global Telecommunications Conference (GLOBECOM)*, pp. 1–5, Dec. 2010.

[138] E. Basar, U. Aygolu, E. Panayirci, and H. V. Poor, "Space-time block coded spatial modulation," *IEEE Transactions on Communications*, vol. 59, pp. 823–832, March 2011.

[139] J. Yao, "Microwave photonics," *Journal of Lightwave Technology*, vol. 27, pp. 314–335, Feb. 2009.

[140] T. Erdogan, "Fiber grating spectra," *Journal of lightwave technology*, vol. 15, pp. 1277–1294, Aug. 1997.

[141] H. Chettat, L. M. Simohamed, Y. Bouslimani, and H. Hamam, "RoF networks : A comprehensive study," in *2008 3rd International Symposium on Wireless Pervasive Computing*, pp. 495–498, May 2008.

[142] M. El-Hajjar and L. Hanzo, "Multifunctional MIMO systems: A combined diversity and multiplexing design perspective," *Wireless Communications, IEEE*, vol. 17, pp. 73–79, April 2010.

[143] S. Ghafoor and L. Hanzo, "Reduced dispersion duplex DQPSK radio-over-fiber communications using single-laser-based multiple side-bands," in *2011 IEEE International Conference on Communications (ICC)*, pp. 1–5, June 2011.

[144] J. Corral, J. Marti, S. Regidor, J. Foster, R. Laming, and M. Cole, "Continuously variable true time-delay optical feeder for phased-array antenna employing chirped fiber grating," *IEEE Transactions on Microwave Theory and Techniques*, vol. 45, pp. 1531–1536, Aug. 1997.

[145] A. Alkhateeb, O. E. Ayach, G. Leus, and R. W. Heath, "Channel estimation and hybrid precoding for millimeter wave cellular systems," *IEEE Journal of Selected Topics in Signal Processing*, vol. 8, pp. 831–846, Oct. 2014.

[146] C. Zhang, D. Guo, and P. Fan, "Tracking angles of departure and arrival in a mobile millimeter wave channel," in *2016 IEEE International Conference on Communications (ICC)*, pp. 1–6, May 2016.

[147] D. J. Richardson, J. M. Fini, and L. E. Nelson, "Space-division multiplexing in optical fibres," *Nature Photonics*, vol. 7, pp. 354–362, May 2013. Review.

[148] I. Mollers, D. Jager, R. Gaudino, A. Nocivelli, H. Kragl, O. Ziemann, N. Weber, T. Koonen, C. Lezzi, A. Bluschke, and S. Randel, "Plastic optical fiber technology for reliable home networking: overview and results of the EU project POF-all," *IEEE Communications Magazine*, vol. 47, pp. 58–68, Aug. 2009.

[149] H. Yang, Y. Shi, W. Wang, C. Okonkwo, H. van den Boom, A. Koonen, and E. Tangdiongga, "Wimedia-compliant uwb transmission over 1 mm core diameter plastic optical fibre," *Electronics Letters*, vol. 46, pp. 434–436, March 2010.

[150] J. Yu, D. Qian, M. Huang, Z. Jia, G. Chang, and T. Wang, "16 Gbit/s radio OFDM signals over graded-index plastic optical fiber," in *2008 34th European Conference on Optical Communication*, pp. 1–2, Sept. 2008.

[151] S. Lee, F. Breyer, S. Randel, B. Spinnler, I. Polo, D. van den Borne, J. Zeng, E. de Man, H. van den Boom, and A. Koonen, "10.7 Gbit/s transmission over 220 m polymer optical fiber using maximum likelihood sequence estimation," in *2007 Conference on Optical Fiber Communication and the National Fiber Optic Engineers Conference*, pp. 1–3, March 2007.

[152] F. Breyer, S. Lee, S. Randel, and N. Hanik, "Comparison of OOK- and PAM-4 modulation for 10 Gbit/s transmission over up to 300 m polymer optical fiber," in *2008 Conference on Optical Fiber communication/National Fiber Optic Engineers Conference*, pp. 1–3, Feb. 2008.

[153] L. Geng, J. Wei, R. Penty, I. White, and D. Cunningham, "3 Gbit/s LED-based step index plastic optical fiber link using multilevel pulse amplitude modulation,"

in *Optical Fiber Communication Conference and Exposition and the National Fiber Optic Engineers Conference (OFC/NFOEC)*, pp. 1–3, March 2013.

[154] B. Sklar, *Digital communications*, vol. 2. Prentice Hall NJ, 2001.

[155] S. Nuccio, L. Christen, X. Wu, S. Khaleghi, O. Yilmaz, A. Willner, and Y. Koike, "Transmission of 40 Gb/s DPSK and OOK at 1.55 μ m through 100 m of plastic optical fiber," in *2008 34th European Conference on Optical Communication*, pp. 1–2, Sept. 2008.

[156] C. Okonkwo, E. Tangdiongga, H. Yang, D. Visani, S. Loquai, R. Kruglov, B. Charbonnier, M. Ouzzif, I. Greiss, O. Ziemann, R. Gaudino, and A. Koonen, "Recent results from the EU POF-PLUS project: Multi-Gigabit transmission over 1 mm core diameter plastic optical fibers," *Journal of Lightwave Technology*, vol. 29, pp. 186–193, Jan. 2011.

[157] M. Schwartz, W. Bennett, and S. Stein, "Communication systems and techniques," *IEEE Communications Magazine*, vol. 34, pp. 9–11, May 1996.

[158] F. Breyer, S. Lee, S. Randel, and N. Hani, "PAM-4 signalling for gigabit transmission over standard step-index plastic optical fibre using light emitting diodes," in *2008 34th European Conference on Optical Communication*, pp. 1–2, Sept. 2008.

[159] I. Djordjevic, "LDPC-Coded OFDM transmission over graded-index plastic optical fiber links," *IEEE Photonics Technology Letters*, vol. 19, pp. 871–873, June 2007.

[160] H. Yang, S. Lee, E. Tangdiongga, F. Breyer, S. Randel, and A. Koonen, "40-Gb/s transmission over 100m graded-index plastic optical fiber based on discrete multitone modulation," in *2009 Conference on Optical Fiber Communication - incudes post deadline papers*, pp. 1–3, March 2009.

[161] Y. Shi, C. Okonkwo, D. Visani, E. Tangdiongga, and T. Koonen, "Distribution of broadband services over 1-mm core diameter plastic optical fiber for point-to-multipoint in-home networks," *Journal of Lightwave Technology*, vol. 31, pp. 874–881, March 2013.

[162] L. Hanzo, M. Münster, B. Choi, and T. Keller, *OFDM and MC-CDMA for broadband multi-user communications, WLANs and broadcasting.* John Wiley & Sons, Jan. 2005.

[163] S. Karabetsos, E. Pikasis, T. Nikas, A. Nassiopoulos, and D. Syvridis, "DFT-spread DMT modulation for 1-Gb/s transmission rate over 100 m of 1-mm SI-POF," *Photonics Technology Letters, IEEE*, vol. 24, pp. 836–838, May 2012.

[164] S. Lee, F. Breyer, S. Randel, D. Cardenas, H. van den Boom, and A. Koonen, "Discrete multitone modulation for high-speed data transmission over multimode fibers using 850-nm VCSEL," in *2009 Conference on Optical Fiber Communication - incudes post deadline papers*, pp. 1–3, March 2009.

[165] P. Chow, J. Cioffi, and J. Bingham, "A practical discrete multitone transceiver loading algorithm for data transmission over spectrally shaped channels," *IEEE Transactions on Communications*, vol. 43, pp. 773–775, Feb. 1995.

[166] H. Xu, W. Zhang, and L. Yang, "Wireless localization and ranging with ultra-wideband signals," in *2011 IEEE International Conference on Ultra-Wideband (ICUWB)*, pp. 580–584, Sept. 2011.

[167] A. Batra, J. Balakrishnan, and A. Dabak, "Multi-band OFDM: a new approach for UWB," in *Proceedings of the 2004 International Symposium on Circuits and Systems*, vol. 5, pp. 365–368 Vol.5, May 2004.

[168] S. Abraha, H. Yang, E. Tangdiongga, and A. Koonen, "Novel generation and transmission of FCC-compliant impulse radio ultra wideband signals over 100-m GI-POF," in *2009 International Topical Meeting on Microwave Photonics*, pp. 1–4, Oct. 2009.

[169] C. Lethien, C. Loyez, J.-P. Vilcot, R. Kassi, N. Rolland, C. Sion, and P.-A. Rolland, "Review of glass and polymer multimode fibers used in a wimedia ultrawideband MB-OFDM radio over fiber system," *Journal of Lightwave Technology*, vol. 27, pp. 1320–1331, May 2009.

[170] C.-H. Chang, H.-S. Su, H.-H. Lu, P.-C. Peng, and H.-W. Hu, "Integrating fiber-to-the-home and POF in-door routing CATV transport system," *Journal of Lightwave Technology*, vol. 28, pp. 1864–1869, June 2010.

[171] F. Breyer, S. C. J. Lee, S. Randel, and N. Hanik, "1.25 Gbit/s transmission over up to 100 m standard 1 mm step-index polymer optical fibre using FFE or DFE equalisation schemes," in *2007 33rd European Conference and Ehxibition of Optical Communication (ECOC)*, pp. 1–2, Sept. 2007.

[172] E. Tangdiongga, H. Yang, S. Lee, C. Okonkwo, H. van den Boom, S. Randel, and A. Koonen, "Low-cost and high-capacity short-range optical interconnects using graded-index plastic optical fiber," in *2010 Conference on Optical Fiber Communication (OFC), collocated National Fiber Optic Engineers Conference (OFC/NFOEC)*, pp. 1–3, March 2010.

[173] H.-C. Peng, H.-S. Su, H.-H. Lu, C.-Y. Li, P.-C. Peng, S.-H. Wu, and C.-H. Chang, "Hybrid CATV/16-QAM OFDM in-building networks over SMF and GI-POF transport," *Optics Express*, vol. 19, pp. 9575–9581, May 2011.

[174] L. Hanzo, M. El-Hajjar, and O. Alamri, "Near-capacity wireless transceivers and cooperative communications in the MIMO era: Evolution of standards, waveform design, and future perspectives," *Proceedings of the IEEE*, vol. 99, pp. 1343–1385, Aug. 2011.

[175] J. Kim and I. Lee, "802.11 WLAN: history and new enabling MIMO techniques for next generation standards," *IEEE Communications Magazine*, vol. 53, pp. 134–140, March 2015.

[176] I. S. Amiri, S. E. Alavi, N. Fisal, A. S. M. Supa'at, and H. Ahmad, "All-optical generation of two IEEE802.11n signals for 2 × 2 MIMO-RoF via MRR system," *IEEE Photonics Journal*, vol. 6, pp. 1–11, Dec. 2014.

[177] B. Friedlander and S. Scherzer, "Beamforming versus transmit diversity in the downlink of a cellular communications system," *IEEE Transactions on Vehicular Technology*, vol. 53, pp. 1023–1034, July 2004.

[178] S. Shahbazpanahi, A. B. Gershman, and J. H. Manton, "Closed-form blind MIMO channel estimation for orthogonal space-time block codes," *IEEE Transactions on Signal Processing*, vol. 53, pp. 4506–4517, Dec. 2005.

[179] J. Mateo, M. A. Losada, I. Garcés, and J. Zubia, "Global characterization of optical power propagation in step-index plastic optical fibers.," *Optics Express*, vol. 14, pp. 9028–9035, Oct. 2006.

[180] "IEEE standard for information technology–Telecommunications and information exchange between systems local and metropolitan area networks–Specific requirements - Part 11: wireless LAN medium access control (MAC) and physical layer (PHY) specifications," *IEEE Std 802.11-2016 (Revision of IEEE Std 802.11-2012)*, pp. 1–3534, Dec. 2016.

[181] "Fiber Bragg Grating", *Optiwave,* 2017. [Online]. Available: https://optiwave.com/resources/applications-resources/optical-grating-fiber-bragg-grating/. [Accessed: 14-March-2017].

Glossary

3G	3rd Generation
4QAM	4 Quadrature Amplitude Modulation
5G	5th Generation
16QAM	16 Quadrature Amplitude Modulation
A-RoF	Analogue Radio over Fiber
ABF	Analogue Beamforming
AC	Antenna Combination
ADC	Analogue-to-digital Conversion
AI	Artificial Intelligence
AoD	Angle of Departure
ASK	Amplitude Shift Keying
ASI	Antenna Selection Information
AWG	Arbitrary Waveform Generator
AWGN	Additive White Gaussian Noise
BBU	Baseband Unit
BER	Bit Error Ratio
BF	Beamforming
BLAST	Bell Lab's Layer Space-time
BPSK	Binary Phase Shift Keying
BS	Base-station
BSL	Bit Splitter
CATV	Cable Television
CAPEX	Capital Expenditure
CCI	Co-channel Interference

CDMA	Code Division Multiple Access
C-RAN	Cloud/Centralised Radio Access Network
CFBG	Chirped Fiber Bragg Grating
CIR	Channel Impulse Response
CM	Carrier Modulation
CoMP	Coordinated Multi-point
CP	Cyclic Prefix
CU	Central Unit
DAC	Digital-to-analogue
DAA	Demodulation and Antenna Arrangement
DAS	Distributed Antenna System
DBPSK	Differential Phase Shift Keying
DCF	Dispersion-compensation Fiber
DD-MZM	Dual-drive Mach-Zehnder Modulator
D-RoF	Digitised Radio over Fiber
Demux	Demultiplexer
DFE	Decision Feedback Equaliser
DSF	Dispersion-shifted Fiber
DSM	Differential Spatial Modulation
DSP	Digital Signal Processing
DMT	Discrete Multitone
EA	Electronic Amplifier
EBPF	Electronic Bandpass Filter
EE	Energy Efficiency
EFDM	Explicit Finite-difference Method
EDFA	Erbium-doped Fiber Amplifier
EMD	Equilibrium Mode Distribution
EOM	Eletrooptic Modulator
E/O	Electro-to-optic
EVM	Error Vector Magnitude
FBG	Fiber Bragg Grating
FCC	Federal Communication Commission

FEC	Forward Error Correction
FFT	Fast Fourier Transform
FITH	Fiber In the Home
FWM	Four Wave Mixing
GI-POF	Graded-index Plastic Optical Fiber
GOF	Glass Optical Fiber
HBF	Hybrid Beamforming
HNLF	Highly Non-linear Fiber
ICI	Inter-channel Interference
IFDM	Implicit Finite-difference Method
IFFT	Inverse Fast Fourier Transform
IoT	Internet of Things
KNN	K-nearest Neighbourhood
LAN	Local Area Networks
LD	Laser Diode
LDC	Linear Dispersion Code
LSSTC	Layered Steered Space-time Codes
LSSTS	Layered Space-time Spreading
MEMS	Micro Electro Mechanical Systems
MF-MIMO	Multi-functional Multiple-input-multiple-output
MI	Modulation Index
MIMO	Multiple-Input-multiple-output
MITP	Minimum Transmission Point
ML	Maximum Likelihood
MLSE	Maximum Likelihood Sequence Estimation
mmWave	Millimeter Wave
MS-STSK	Multi-set Space-time Shift Keying
MZM	Mach-Zehnder Modulator
MDM	Mode Division Multiplexing
NRZ	None-return-to-zero
OBPF	Optical Bandpass Filter
OC	Optical Circulator

OCS	Optical Carrier Suppression
ODSB	Optical Double side-Band
OFDM	Orthogonal Frequency Division Multiplexing
O/E	Optic-to-electro
OIL	Optical Interleaver
OOK	On-off Keying
OPEX	Operational Expenditure
OSSB	Optical Single Side-band
OSTBC	Orthogonal Space-time Block Coding
PAA	Phased Array Antenna
PAM	Pulse Amplitude Modulation
PAL-SLM	Parallel Spatial Light Modulator
PAPR	Peak-to-average-ratio
PCF	Photonic Crystal Fiber
PD	Photo Detection
PLC	Power Line Communications
POF	Plastic Optical Fiber
PRBS	Pseudorandom Binary Sequence
PS	Phase Shifter
PSD	Power Spectral Density
PSE	Phase Shift Error
PTTD	Photonic True Time Delay
QAM/PSK	Quadrature Amplitude Modulation/ Phase Shift Keying
QPSK	Quadrature Phase Shift Keying
RF	Radio Frequency
RG	Residential Gateway
RoF	Radio over Fiber
RoPOF	Radio over Plastic Optical Fiber
RRH	Remote Radio Head
Rx	Receiver
SBS	Stimulated Brillouin Scattering

SDM	Space Division Multiplexing
SDMA	Space Division Multiple Access
SE	Spectral Efficiency
SINR	Signal-to-interference-plus-noise Ratio
SI-POF	Step-index Plastic Optical Fiber
SLM	Spatial Light Modulator
SM	Spatial Modulation
SMF	Single-mode Fiber
SMX	Spatial Multiplexing
SNR	Signal-to-noise Ratio
SNIR	Signal-to-noise-plus-interference Ratio
SPM	Self-phase Modulation
SSK	Space Shift Keying
SSD	Steady State Mode Distribution
SSFM	Symmetric Split-step Fourier Method
STBC	Space-time Block Coding
STC	Space-time Code
STSK	Space-time Shift Keying
TA	Transmitter Antenna
TAA	Transmitter Antenna Arrays
TFG	Tunable Frequency Generator
TO	Thermo-optic
TTD	True Time Delay
Tx/TX	Transmitter
UWB	Ultra-wideband
V-BLAST	Vertical-Bell Laboratories Layered Space-time
WDM	Wavelength Division Multiplexing
XPM	Cross-phase Modulation